

Polarisation Reversal in Ferroelectric PVDF and PZT Films

THÈSE N° 4097 (2008)

PRÉSENTÉE LE 13 JUIN 2008

À LA FACULTE SCIENCES ET TECHNIQUES DE L'INGÉNIEUR

LABORATOIRE DE CÉRAMIQUE

PROGRAMME DOCTORAL EN SCIENCE ET GÉNIE DES MATÉRIAUX

ÉCOLE POLYTECHNIQUE FÉDÉRALE DE LAUSANNE

POUR L'OBTENTION DU GRADE DE DOCTEUR ÈS SCIENCES

PAR

Roman GYSEL

Diplomierter Werkstoff-Ingenieur ETH
de nationalité suisse et originaire de Wilchingen (SH)

acceptée sur proposition du jury:

Prof. I. Botsis, président du jury
Prof. N. Setter, Dr A. Tagantsev, directeurs de thèse
Prof. M. A. Ionescu, rapporteur
Dr E. Soergel, rapporteur
Prof. J. Trodahl, rapporteur



ÉCOLE POLYTECHNIQUE
FÉDÉRALE DE LAUSANNE

Suisse
2008

Contents

Abstract	v
Résumé	vii
1 Preface	1
1.1 Ferroelectricity and Applications	1
1.2 Goal of the Thesis	1
1.3 Ferroelectric Materials	1
1.4 Outline of the Thesis	2
2 Theoretical Background and State of Art	5
2.1 Ferroelectricity	5
2.1.1 Historical Background	5
2.1.2 Phenomenological Theory	5
2.1.3 Thermodynamic Theory	6
2.1.4 Phase Transitions	6
2.1.5 Dielectric Properties	9
2.1.6 Domains	11
2.1.7 Piezoelectricity	12
2.1.8 Critical Size for Ferroelectricity	13
2.2 Ferroelectric Materials	14
2.2.1 Thin Films	14
2.2.2 Lead Zirconate Titanate, Barium Titanate — Perovskite Ferroelectrics	15
2.2.3 Ferroelectric Polymers	16
2.3 Polarisation Reversal	25
2.3.1 Introduction and Overview	25
2.3.2 Experimental Findings	26
2.3.3 Nucleation — the Landauer Model	28
2.3.4 Domain Wall Motion	30
2.3.5 Summary	32
2.4 Kinetics of the Polarisation Reversal	34
2.4.1 Introduction	34
2.4.2 Switching Model Based on Sideways-Growth and Coalescence of Domains	34
2.4.3 Polarisation Reversal in Thin Ferroelectric Films	36
2.4.4 Polarisation Reversal in Thin Films	38
2.5 Polarisation Reversal in Ferroelectric Polymers	40
2.5.1 Rotation of the Molecular Chain	40
2.5.2 Kinetics of the Polarisation Reversal in PVDF	44

2.6	Macroscopic Characterisation Methods of the Polarisation Reversal	49
2.6.1	Polarisation Hysteresis Loops	49
2.6.2	Piezoelectric Loops	50
2.6.3	Pulse Switching Technique	53
2.6.4	Dielectric Characterisation	54
2.7	Domain Imaging Methods	56
2.7.1	Surface Decoration Methods	56
2.7.2	Selective Etching Methods	56
2.7.3	Optical Methods	56
2.7.4	Electron Microscopy	56
2.7.5	Scanning Probe Microscopy	57
3	Microscopic Characterisation of the Polarisation Reversal	61
3.1	Piezoelectric Force Microscopy	61
3.1.1	Working Principle of PFM	62
3.1.2	Instrumentation for PFM	64
3.1.3	Possible Experimental Configurations	70
3.2	Combination of PFM with Short Pulse Technique	71
3.3	Cross-sectional PFM	72
3.3.1	Statement of the Problem	72
3.3.2	Idea for Our Approach	73
3.3.3	Sample Preparation	74
3.3.4	Probe-Sample Contact	83
3.3.5	Experimental Method and Technique	84
3.3.6	Set of Acquired Data	87
3.3.7	Discussion	90
3.4	Summary	93
4	Experimental Results of Cross-Sectional PFM	95
4.1	Experimental Details	95
4.2	Results	96
4.3	Discussion	102
4.3.1	Polarisation Reversal Mechanism	102
4.3.2	Surface-Stimulated Nucleation	104
4.4	Summary	108
5	Polarisation Reversal in Ferroelectric Polymers	109
5.1	Introduction	109
5.2	Fabrication and Methods	110
5.2.1	Film Deposition	110
5.2.2	Deposition and Structuring of Top Electrodes	110
5.3	Annealing and Morphology	111
5.4	Polarisation Reversal	115
5.4.1	Methods	115
5.5	Results	117
5.5.1	Piezoelectric Properties	117
5.5.2	Polarisation Reversal and Temperature	118
5.5.3	Permittivity and Temperature	119
5.5.4	Polarisation Reversal Kinetics	119

5.6	Discussion	128
5.6.1	Dielectric Properties vs. P – E hysteresis	128
5.6.2	Switching Mechanism and Polarisation Reversal Dynamics	131
5.7	Summary	136
6	Switching Properties in Applications — Ferroelectric Transistors	137
6.1	Working Principle	137
6.1.1	Ferroelectric Memories	137
6.1.2	Field Effect Transistors	139
6.1.3	Ferroelectric Field Effect Transistors	141
6.1.4	Difficulties in the Realisation of Ferroelectric FET	143
6.2	Integration of Organic Ferroelectrics into Transistors	147
6.2.1	Advantages of the Organic Ferroelectrics in Transistors	147
6.2.2	Drawbacks of the Organic Ferroelectrics in Transistors	148
6.3	Literature Review on FET with Organic Gate Electrodes	149
6.4	Ferroelectric Field Effect Transistor Fabrication	150
6.4.1	Device Design	151
6.4.2	Fabrication Details	151
6.5	Experimental Results	151
6.5.1	Polarisation Reversal in Transistor Structure	151
6.5.2	“On”/“Off” Drain Current Ratio and Retention	157
6.5.3	Properties of the Transistor without a Ferroelectric Gate	159
6.6	Discussion	160
6.6.1	Polarisation Loops and Switching Curves	160
6.6.2	Required Polarisation for the “On” State of the Transistor	161
6.6.3	Mechanism of Drain Current Relaxation	161
6.6.4	Retention Loss — Semi-Quantitative Description	164
6.7	Summary	166
	Conclusions and Outlook	167
	Bibliography	169
	Acknowledgements	187
	List of Publications	189
	Curriculum Vitae	191

Abstract

Ferroelectrics are characterised by a spontaneous polarisation that can be reversed by an external electric field. The stability of the polarisation states and the possibility for controlled switching between the states render ferroelectric materials very attractive for memory applications, in which polarisation states are associated to a binary information “0” or “1”. Fast, dense, and reliable data storage has gained enormous importance in our information technology based society. In this context, the fundamental physics of ferroelectric materials attracted great interest with the ultimate goal of reaching memory elements with shortest access times and highest densities.

Two model systems of ferroelectric materials were studied in this thesis on the polarisation reversal: an inorganic, classical perovskite and an organic polymer. Despite the fundamental structural differences between lead zirconate titanate $[\text{Pb}(\text{Zr},\text{Ti})\text{O}_3]$ and the investigated polyvinylidene fluoride-trifluoroethylene $[\text{P}(\text{VDF-TrFE})]$ copolymer, the switching kinetics in these materials can be described by a similar formalism.

Our approach of a combination of macroscopic and microscopic techniques enables an insight into the mechanisms of the polarisation reversal and allows for a better understanding of macroscopic effects governed by mechanisms occurring on the nanoscale. The experimental techniques developed for the ferroelectric capacitor structures have been successfully applied for studying a first hybrid PVDF/silicon ferroelectric transistor for non-volatile information storage.

The major accomplishments of this thesis are the following:

- (i) We demonstrated for the first time a piezoelectric scanning probe study on the cross section of ferroelectric thin films. In combination with switching pulses, this allowed us to directly image the polarisation reversal in ferroelectric films quasi-dynamically. The utility of cross-sectional domain imaging as a powerful tool for the study of the polarisation reversal in ferroelectrics has been corroborated. The apparent contradiction between observations interpreted as a fast sideways growth and the classical scenario of a fast forward growth could be explained by an oblique polarisation direction with respect to the film plane. A surface-stimulated nucleation of reverse domains, with preference on the electrode with a negative potential was observed. It was interpreted in terms of a built-in field due to a depletion layer at the ferroelectric-electrode interface.
- (ii) A combination of microscopic and macroscopic methods used for the first time in organic ferroelectric thin films enabled a better insight into polarisation reversal of the copolymer of vinylidene fluoride and trifluoroethylene $\text{P}(\text{VDF-TrFE})$. The polarisation reversal was found to be impeded by a restricted domain growth. This limits the applicability of the conventional Kolmogorov-Avrami model as well as the nucleation-limited switching model with a broad distribution of nucleation times.

We demonstrated that an interface-adjacent passive layer may impact on the switching properties and gives rise to a retardation of the polarisation reversal. Furthermore, an extraordinary dielectric constant increase was observed in the films with a passive layer due to an additional domain wall contribution.

- (iii) We fabricated for the first time a hybrid silicon/ferroelectric polymer ferroelectric single transistor memory element with non-volatile operation. The observed difference of the polarisation reversal kinetics of the ferroelectric in the simple capacitor and in the transistor structure was explained by the gate oxide buffer layer in the transistor. Our previously developed tools and approaches enabled a better understanding of retention loss mechanism. A semi-quantitative retention model was suggested that explains the observed exponential retention loss.

The investigation of relevant fundamental aspects of ferroelectric materials and the development of novel characterisation techniques in this work can be of interest for further development of non-volatile memory devices.

key words: ferroelectric, polarisation reversal, thin film, scanning probe microscopy, non-volatile memory, transistor, PZT, lead zirconate titanate, PVDF, polyvinylidene fluoride.

Resumé

Les matériaux ferroélectriques sont caractérisés par une polarisation spontanée qui peut être basculée par un champ électrique externe. La stabilité des états de polarisation et la possibilité de contrôler leur inversion font des ferroélectriques des matériaux très intéressants pour les dispositifs informatiques de stockage, le code binaire pouvant être représenté par ces états de polarisation. Le stockage de données rapide, dense et fiable est d'une énorme importance dans notre société actuelle, où la technologie de l'information tient une place prépondérante. Dans ce contexte, le temps nécessaire au basculement de la polarisation, la taille minimale des domaines ferroélectriques, ainsi que la connaissance des matériaux ferroélectriques sur le plan de la physique fondamentale sont d'un grand intérêt.

Cette thèse, ayant pour thème principal le basculement de la polarisation dans des couches minces ferroélectriques, a eu pour objet d'étude deux types de matériaux : un composé inorganique de perovskite classique et un polymère organique. Malgré les différences structurelles fondamentales entre le titano-zirconate de plomb $[\text{Pb}(\text{Zr},\text{Ti})\text{O}_3]$ et le polyfluorure de vinylidène $[\text{P}(\text{VDF}-\text{TrFE})]$, la cinétique du basculement peut être décrite par un formalisme similaire.

Notre approche combinant des techniques macro- et microscopiques permet une observation plus approfondie des mécanismes sous-jacents au basculement de la polarisation et améliore la compréhension des effets macroscopiques contrôlés par des processus à l'échelle nanométrique. Les techniques expérimentales développées pour l'étude des structures des condensateurs ferroélectriques ont pu être appliquées avec succès lors de l'étude d'un premier transistor hybride en PVDF/silicium servant au stockage des informations non-volatiles.

Ci-dessous figurent les principaux apports de cette thèse :

- (i) Notre étude constitue la première démonstration de l'utilisation de la microscopie à réponse piézoélectrique sur la section transversale de couches minces ferroélectriques. La combinaison de cette technique avec une tension pulsée nous a permis d'observer directement et de façon quasi dynamique le basculement de la polarisation. L'utilité de l'imagerie sur une section transversale en tant qu'outil puissant pour l'étude de l'inversion de la polarisation ferroélectrique a été démontrée. L'apparente contradiction entre la conclusion d'une croissance transversale rapide et le scénario classique d'une croissance rapide en direction de la polarisation a été expliquée par une inclinaison de la direction de la polarisation. Une nucléation stimulée à la surface des domaines inversés, avec préférence sur l'électrode de potentiel négatif, a été observée et expliquée.
- (ii) Une combinaison de méthodes micro- et macroscopiques a été appliquée pour la première fois à des couches minces de polymère ferroélectrique, ce qui a permis de mieux comprendre le phénomène de basculement de la polarisation. Nous avons

observé que le basculement de la polarisation a été ralenti par la croissance entravée des domaines. Cela limite la possibilité d'appliquer le modèle classique de Kolmogorov-Avrami ainsi que le modèle de basculement limité par la nucléation qui consiste en une large distribution des temps de nucléation. Par ailleurs, nous avons expliqué de quelle manière une couche passive adjacente à l'interface peut avoir un impact sur les propriétés de basculement et induire une décélération de l'inversion de la polarisation. De plus, une hausse extraordinaire de la constante diélectrique a été observée en présence d'une couche mince passive en raison de la contribution des murs de domaines.

- (iii) Nous avons fabriqué pour la première fois un élément de mémoire ferroélectrique consistant en un transistor non-volatil de silicium et d'un polymère ferroélectrique. La différence observée de la cinétique du basculement de la polarisation entre la structure de simple condensateur et celle du transistor a été expliquée par la couche d'oxyde intégrée dans la grille du transistor. Nos outils développés précédemment ont permis une meilleure compréhension du mécanisme de la perte de rétention. Un modèle semi-quantitatif de la perte de rétention exponentielle a été proposé.

L'étude des aspects fondamentaux des matériaux ferroélectriques et le développement de nouvelles méthodes de caractérisation mis en évidence par ce travail de recherche présentent un intérêt pour le développement futur d'éléments de mémoire non-volatiles.

mots-clés : ferroélectrique, basculement de polarisation, couche mince, microscopie à champ proche, mémoire non volatile, transistor, PZT, titano-zirconate de plomb, PVDF, polyfluorure de vinylidène.

Chapter 1

Preface

1.1 Ferroelectricity and Applications

Ferroelectrics are a class of materials that are distinguished by a reversible spontaneous polarisation. This polarisation can be reversed by the application of an external electric field and researchers were soon infatuated by the idea of using opposite stable polarisation state for memories. The information in such applications must naturally be controllable and detectable for writing and reading information. In this context, the many aspects of the polarisation reversal process are of great interest: important are mainly write (and read) time, size limits to allow for high information densities, endurance for lifetime and security reasons. Such aspects are crucial for ferroelectrics in memory applications, but additionally, ferroelectrics represent a valuable model system for fundamental physical studies.

Apart from memory applications, the piezoelectric effect inherent to ferroelectrics is used in many applications. Piezoelectric sensors and actuators can be found in all macroscopic dimensions to mechanical micro- and possibly soon nanoscopic systems (MEMS and NEMS). Typical products are piezoelectric inkjet printers, sonar systems, medical ultrasound imaging systems, acceleration sensors, “smart” sport devices like tennis racquets, skis, and others. However, piezoelectricity is only used in this thesis to characterise the polarisation state in the studied ferroelectric samples.

1.2 Goal of the Thesis

The scope of this thesis is to get a better understanding of the mechanisms of polarisation reversal in model systems of ferroelectrics in the form of thin films. The transfer of the fundamental findings should help to improve memory applications. Finally, the experimental character of this thesis is underlined by the development of novel characterisation tools and methods.

1.3 Ferroelectric Materials

Not many years are left until studies on ferroelectric materials have been conducted for one century. BaTiO_3 and $\text{Pb}(\text{Zr},\text{Ti})\text{O}_3$, which crystallise in a perovskite structure, were in the focus of this research due to their advantageous properties in terms of high piezoelectric coefficients, high dielectric constants, and the convenient paraelectric to ferroelectric

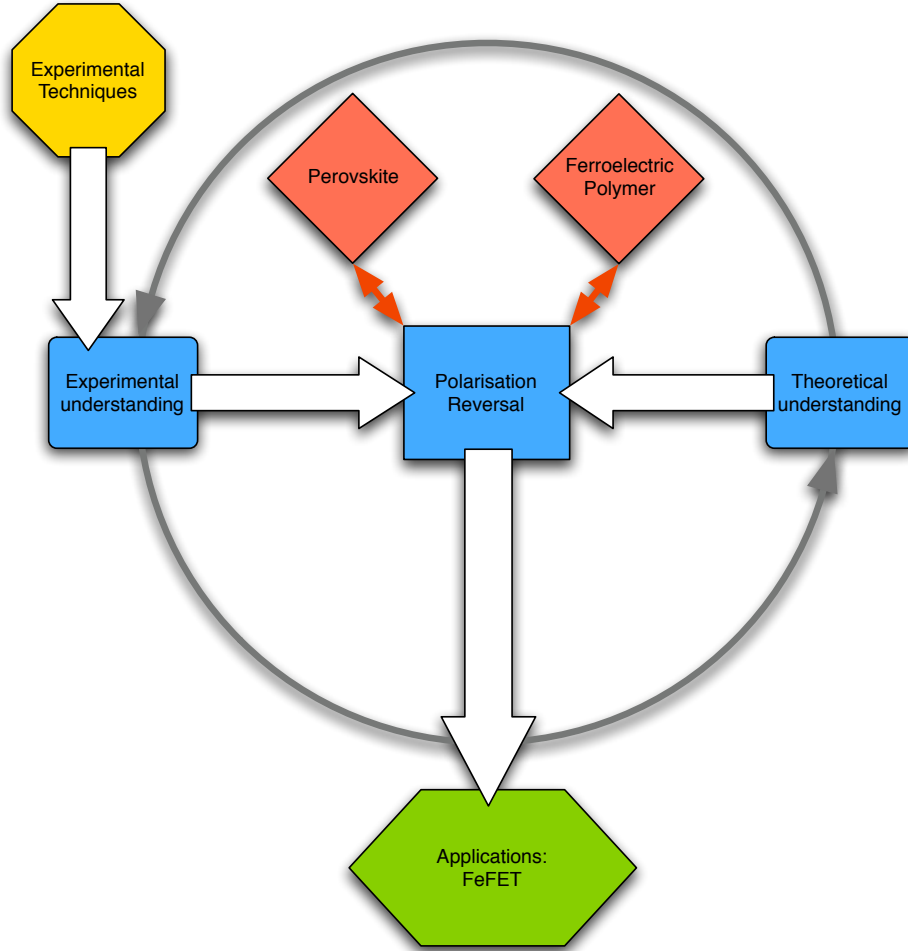


Figure 1.1: This thesis deals mainly with experimental investigation of the polarisation reversal of ferroelectrics, the development of new techniques, and the utilisation of the results in an application.

transitions points for many applications. Besides the traditional perovskite ferroelectrics, the class of polymer ferroelectrics have emerged. The fundamental structural differences within the spectrum of available combinations of properties defined by specific applications.

1.4 Outline of the Thesis

The field of activities in this thesis is illustrated in figure 1.1. The development of experimental methods was required for the experimental study of polarisation reversal. Experimental results were compared to existing models in order to get a better understanding of the polarisation reversal. Thin films of organic $[P(VDF-TrFE)]$ and inorganic $[Pb(Zr,Ti)O_3]$ ferroelectric materials were studied and the better suited material was then integrated in a ferroelectric field effect transistor (FeFET).

Basics on ferroelectricity are discussed in a first part of chapter 2. In the second part, two model ferroelectric materials are introduced, the well-known $Pb(Zr,Ti)O_3$ and

the organic polymer of vinylidene fluoride (PVDF). The focus is clearly on the lesser known PVDF polymers, namely its structural features and the nature of ferroelectricity are discussed. A literature review on the kinetics of polarisation reversal is given in a third part of chapter 2. An introduction of experimental techniques concludes chapter 2.

Chapter 3 focuses on microscopic methods. A novel technique developed during this thesis is introduced.

The experimental results as an outcome of the developed technique are presented in chapter 4. It covers imaging of a stepwise polarisation reversal on the cross section of a $\text{Pb}(\text{Zr,Ti})\text{O}_3$ film.

A comprehensive set of results on organic ferroelectrics, $\text{P}(\text{VDF-TrFE})$, its dielectric properties, and polarisation reversal kinetics are discussed in chapter 5.

Advantages of the integration of the ferroelectric copolymer into a memory applications and the experimental realisation of such devices are described in chapter 6.

The last chapter contains the main conclusions and an outlook.

Chapter 2

Theoretical Background and State of Art

2.1 Ferroelectricity

2.1.1 Historical Background

Ferroelectric materials have attracted the interest of engineers and scientists during the past nine decades due to their multiple interesting properties in terms of applications. Ferroelectric materials possess the ability to convert mechanical to electric energy via the so-called piezoelectricity (derived from the Greek word “piezein” meaning to press). Furthermore, they can transduce heat energy, i.e. a temperature change, into an electrical signal. A property that is called pyroelectricity (derived from the Greek word “pyr” for fire).

Pierre and Jacques Curie [[Curie and Curie, 1880](#)] discovered the piezoelectric effect in 1880. It took however almost another half of a century, until ferroelectricity — named in analogy to iron and its ferromagnetic effect — was discovered by J. Valasek [[Valasek, 1921](#)] in Rochelle salt in 1921. Probably the best studied ferroelectric material, BaTiO_3 , was discovered more than 20 years later, in about 1943 — curiously at the same time and independently — in the USA, the USSR, and Japan by von Hippel and co-workers, Wul and Goldman, and Ogawa, respectively [[Mitsui et al., 1976](#)].

The development of higher quality materials paved the road to applications for ferroelectrics. Apart from piezoelectric (see section [2.1.7](#)) and pyroelectric applications, ferroelectrics were foreseen for memory applications. They were already realised and presented in detail by Anderson in 1952 [[Anderson, 1952](#)].

2.1.2 Phenomenological Theory

Phenomenological theories treat the macroscopic properties of a material as a continuum. A sufficient number of variables is used to describe a stimulus and its response. By means of thermodynamics, relations between the stimulus and the response can be expressed. Such a treatment for ferroelectrics is named after its founders: Landau-Ginzburg-Devonshire (LGD) [[Lines and Glass, 1977](#), [Devonshire, 1949](#), [Devonshire, 1954](#)] and is presented briefly in the following two sections.

2.1.3 Thermodynamic Theory

Thermodynamic potentials are used as a basis to describe the coupling of different properties in dielectrics.

The reversible change of the internal energy dU due to the performed work and the heat transfer of the system, i.e. due to small changes of the strain dx , of the dielectric displacement dD , and the entropy dS can be written as:

$$dU = TdS + X_{ij}dx_{ij} + E_idD_i \quad (2.1)$$

with the temperature T , the stress X_{ij} , and the electric field E_i .

The elastic Gibbs free energy potential is a convenient thermodynamic potential for many experimental situations reads:

$$dG = -SdT - x_{ij}dX_{ij} + E_idP_i \quad (2.2)$$

We use an expansion of the elastic Gibbs function ΔG according to the work of Haun for PbTiO_3 [Haun et al., 1987]:

$$\begin{aligned} \Delta G = & a_1(P_1^2 + P_2^2 + P_3^2) + a_{11}(P_1^4 + P_2^4 + P_3^4) \\ & + a_{12}(P_1^2P_2^2 + P_2^2P_3^2 + P_3^2P_1^2) + a_{111}(P_1^6 + P_2^6 + P_3^6) \\ & + a_{112}[P_1^4(P_2^2 + P_3^2) + P_2^4(P_1^2 + P_3^2) + P_3^4(P_1^2 + P_2^2)] + a_{123}(P_1^2P_2^2P_3^2) \\ & - \frac{1}{2}s_{11}(X_1^2 + X_2^2 + X_3^2) - s_{12}(X_1X_2 + X_2X_3 + X_3X_1) - \frac{1}{2}s_{44}(X_4^2 + X_5^2 + X_6^2) \\ & - Q_{11}(X_1P_1^2 + X_2P_2^2 + X_3P_3^2) - Q_{12}[X_1(P_2^2 + P_3^2) + X_2(P_1^2 + P_3^2) \\ & + X_3(P_1^2 + P_2^2)] - 2Q_{44}(X_4P_2P_3 + X_5P_1P_3 + X_6P_1P_2) , \end{aligned} \quad (2.3)$$

where the a_i , a_{ij} , and a_{ijk} are the dielectric stiffness and higher-order stiffness coefficients at constant stress, s_{ij} is the elastic compliance coefficient at constant polarisation, and Q_{ij} is the cubic electrostrictive constant in polarisation (Voigt) notation.

2.1.4 Phase Transitions

Most materials exist in different phases, described by the minima of their thermodynamic potential. The transition between two phases can occur in a discontinuous or continuous way. This is shown here by using the elastic Gibbs free energy potential ΔG introduced in equation (2.3). The equilibrium state of the system is defined as the global minimum of the potential and we are thus interested in the minima of the used potential.

During the cubic ($P_1 = P_2 = P_3 = 0$) to tetragonal ($P_1 = P_2 = 0$ and $P_3 \neq 0$) phase transition in, for example, PbTiO_3 or BaTiO_3 , the potential ΔG of a mechanically free sample reduces to:

$$\Delta G = \frac{1}{2}\alpha_1P_3^2 + \frac{1}{4}\alpha_2P_3^4 + \frac{1}{6}\alpha_3P_3^6, \quad (2.4)$$

with the coefficients $\alpha_1 = 2a_1$, $\alpha_2 = 4a_{11}$, and $\alpha_3 = 6a_{111}$. These coefficients are in general temperature dependent. The evolution of a first to a second order phase transition can then be explained by the sign of α_2 . For stability reasons, the condition $\alpha_3 > 0$ is required.

For a positive parameter α_2 and $\alpha_1 > 0$, there is a single minimum at $P = 0$, this is called the paraelectric phase and there is no spontaneous polarisation. If $\alpha_1 < 0$, there are two minima at $P \neq 0$, i.e. a spontaneous polarisation emerges, as illustrated in figure 2.1(a).

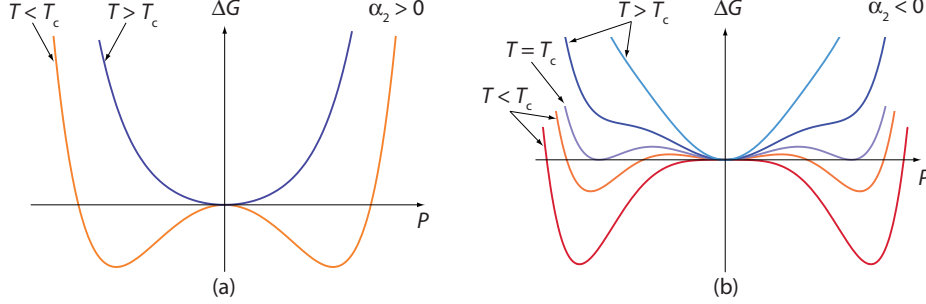


Figure 2.1: The thermodynamic potential ΔG as a function of the polarisation P for a second (a), $\alpha_2 > 0$, and first order (b), $\alpha_2 < 0$, phase transition.

A relation between the electric field and the polarisation can be found by differentiation of equation (2.4) with respect to P :

$$\frac{\partial \Delta G}{\partial P} = E = \alpha_1 P + \alpha_2 P^3 + \alpha_3 P^5. \quad (2.5)$$

In the above equation of states, α_1 can be identified as the reciprocal permittivity in the non-polar phase. Devonshire assumed in his phenomenological considerations a linear dependence of the parameter α_1 on the temperature, with a positive constant β . This leads to the well-known Curie-Weiss law [cp. equation (2.12)] for $T > T_C = T_0$:

$$\alpha_1 = \frac{1}{\varepsilon_0 \varepsilon} = \beta (T - T_0), \quad (2.6)$$

where ε is the dielectric constant of the material in the paraelectric state and ε_0 the dielectric vacuum permittivity.

T_C is the phase transition point in the case of $\alpha_2 > 0$. For $\alpha_1 < 0$ and thus for temperatures below T_C , the material is in the ferroelectric phase. It can be seen from equation (2.5) at zero field and for $\alpha_3 = 0$ that the polarisation increases continuously with decreasing temperature:

$$P_s^2 = -\frac{\alpha_1}{\alpha_2}. \quad (2.7)$$

Solutions of equation (2.5) are plotted in a P - E graph in figure 2.2 for the conditions $T > T_C = T_0$ ($\alpha_1 > 0$), $T = T_C$, and $T < T_C$. Above the Curie temperature, the polarisation is oriented in the direction of an applied electric field and equals 0 at zero field. Below the Curie temperature, the polarisation shows a hysteresis behaviour.

The coercive field E_c is the field at zero polarisation in the ferroelectric phase, $P(E_c) = 0$; with $\frac{\partial E}{\partial P} = 0$ as shown in figure 2.2. With equation (2.5) and neglecting the last term $\alpha_3 P^5$, we can write:

$$\frac{\partial E}{\partial P} = \alpha_1 + 3\alpha_2 P(E_c)^2 = 0. \quad (2.8)$$

It can be seen from equation (2.7) that $[P(E_c)]^2 = \frac{1}{3}P_s^2$. With this relation and the substitution of α_2 from equation (2.8), equation (2.5) (still neglecting the third term) can be used to estimate the thermodynamic coercive field:

$$E_c = \alpha_1 \frac{1}{3\sqrt{3}} P_s \approx 0.2 \frac{P_s}{\epsilon \epsilon_0}, \quad (2.9)$$

where α_1 is replaced by the permittivity at zero field [equation (2.6)] in the right side of the above equation.

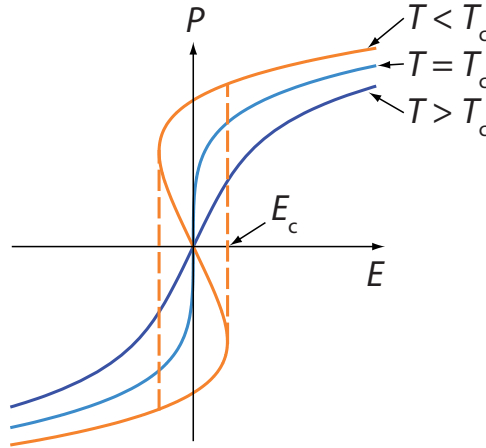


Figure 2.2: The P - E relation according to equation (2.5) results in a hysteresis loop for $T < T_C$.

For a negative parameter α_2 , it can be seen in figure 2.1(b) that a phase transition takes places at $\alpha_1 > 0$. It follows that the phase transition or the Curie temperature T_C differs from the Curie-Weiss temperature T_0 in the relation for the reciprocal isothermal permittivity as described by equation (2.6).

In this case, polarisation and permittivity become discontinuous functions of the temperature as is illustrated in figure 2.3(b).

The phase transitions can thus be distinguished by the derivative of the order parameter¹. If the order parameter changes abruptly at the Curie point and the first derivative is not continuous, the phase transition is of *first order*. If the change of the order parameter through the Curie point is smooth and a discontinuity is observed in the second derivative, the phase transition is of *second order*.

¹The order parameter in ferroelectrics is usually the polarisation.

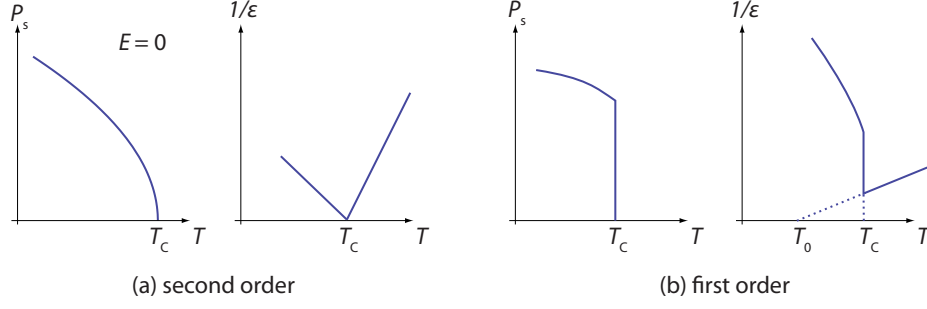


Figure 2.3: Polarisation and permittivity behaviour for a second (a) and first (b) order phase transition.

Discontinuous *first-order phase transitions* are characterised by a temperature hysteresis, because the transition cannot occur in thermodynamic equilibrium (infinitely slow).

Continuous *second-order phase transitions* generally involve smooth displacements in the unit cell changing the crystal symmetry [Strukov and Levanyuk, 1998]. As a consequence, no temperature hysteresis occurs during the phase transition².

2.1.5 Dielectric Properties

Basics

In linear dielectrics, the polarisation, P_i , is proportional to the applied electric field, E_j , with the second rank tensor named dielectric susceptibility, χ_{ij} :

$$P_i = \chi_{ij} E_j \quad (2.10)$$

The dielectric displacement D_i is then defined as:

$$D_i = \varepsilon_0 E_i + P_i = (\varepsilon_0 \delta_{ij} + \chi_{ij}) E_j = \varepsilon_0 \varepsilon_{ij} E_j, \quad (2.11)$$

with the (scalar) dielectric vacuum permittivity ε_0 , δ_{ij} is Kronecker's symbol with $\delta_{ij} = 1$ for $i = j$ and otherwise $\delta_{ij} = 0$. ε_{ij} is the *relative dielectric permittivity* or *dielectric constant*.

Phase Transition Behaviour

The dielectric constant is typically very high in ferroelectric materials around the phase transition between the paraelectric and the ferroelectric phase. The origin lies in the delicate balance between microscopic forces, which keep the material in the paraelectric or ferroelectric phase. This balance of forces is rather fragile and upon the application of an electric field, the restoring forces are relatively weak resulting in a high dielectric constant [Tagantsev et al., 2003].

If we rewrite equation (2.6), we get the so-called *Curie-Weiss law* in the common form:

²This is due to the fact that there are no metastable states, as can be seen, e.g. in figure 2.1

$$\varepsilon = 1 + \frac{C}{T - T_0} \approx \frac{C}{T - T_0}, \quad (2.12)$$

where C and T_0 are the Curie constant and the Curie-Weiss temperature, respectively. The dielectric constant increases to a maximum at the Curie point T_C as shown in figure 2.4(b).

It was experimentally found that the magnitude of the Curie constant C indicates the type of the phase transition, with values around 10^5 K for the displacive and 10^3 K for the order-disorder type.

An example of a ferroelectric with a first order phase transition is BaTiO_3 , one of second order LiNbO_3 . The ferroelectric copolymers of VDF and TrFE reveal both, first ($> 50\%$ of VDF) and second order ($< 50\%$ of VDF) paraelectric-ferroelectric transitions depending on the composition of the copolymer [Tashiro, 1995], p. 143. This copolymer is further discussed in section 2.2.3.

In addition to the ferroelectric-paraelectric, other phase transitions occur in typical perovskite ferroelectrics. Barium titanate, BaTiO_3 , with a high-temperature perovskite structure (see section 2.2.2) undergoes three transitions from the paraelectric centrosymmetric cubic (C) to the ferroelectric tetragonal (T) to the orthorhombic (O) and finally to the rhombohedral (R) structure as illustrated in figure 2.4(a). All the structures described are near-cubic, nevertheless, according to the lattice distorted in different directions, the macroscopic polarisation direction changes from the $\langle 100 \rangle$ direction along a cube edge via the $\langle 110 \rangle$ in the orthorhombic phase to the body diagonal in the rhombohedral $\langle 111 \rangle$ direction. The dimensional changes of the lattice during the phase transitions are associated with anomalies in the dielectric, elastic, thermal, piezoelectric, and other properties [Strukov and Levanyuk, 1998].

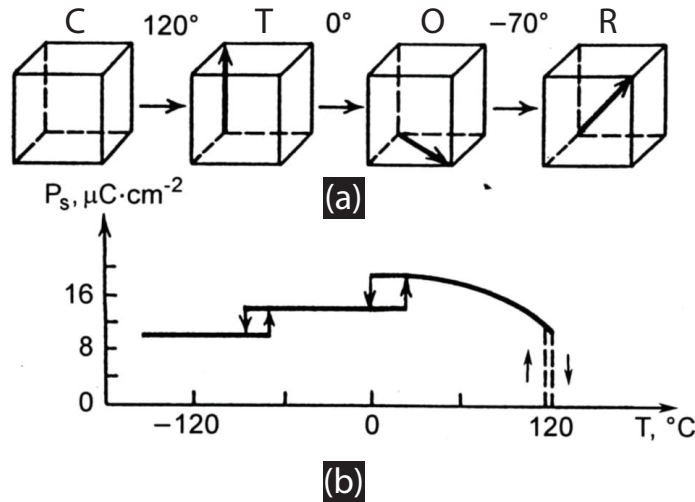


Figure 2.4: Phase transitions in BaTiO_3 and the polarisation directions associated for the each phase indicated in the quasi-cubic lattice (a), the spontaneous polarisation as a function of temperature (b) [original illustration from [Strukov and Levanyuk, 1998], p. 21].

2.1.6 Domains

Regions of parallel polarisation direction are called *domains*. The above considerations are valid for the most simple case of monodomain single crystal ferroelectrics. However, in a ferroelectric crystal plate or a thin film with the polarisation perpendicular to the plate or film surface, the bound charges of the polarisation induce a very high electric field opposite to the polarisation. This so-called *depolarisation* field can be high enough to impede ferroelectricity. The ferroelectric sample can however break up into *domains* of anti-parallel polarisation to stabilise the ferroelectric phase by a reduction of the depolarisation field.

Relaxation of mechanical stresses may act as another reason for the appearance of domains. Stress relaxation is possible due to different lattice parameters with respect to the polarisation direction, e.g. a 90° rotation of the polarisation is associated with stress or strain on a macroscopic scale in the tetragonal phase due to $a \neq c$, with the the lattice constants perpendicular, a , and parallel to the polarisation direction, c . The mechanical constraints on the domain structure are usually referred to as *clamping effects*.

The depolarisation field and elastic stress are the main reasons for the presence of domains in ferroelectrics. The first effect is in general stronger for crystals, whereas the latter dominates many thin ferroelectric films [Setter et al., 2006]. A domain pattern in a BaTiO₃ single crystalline sample is displayed in figure 2.5.

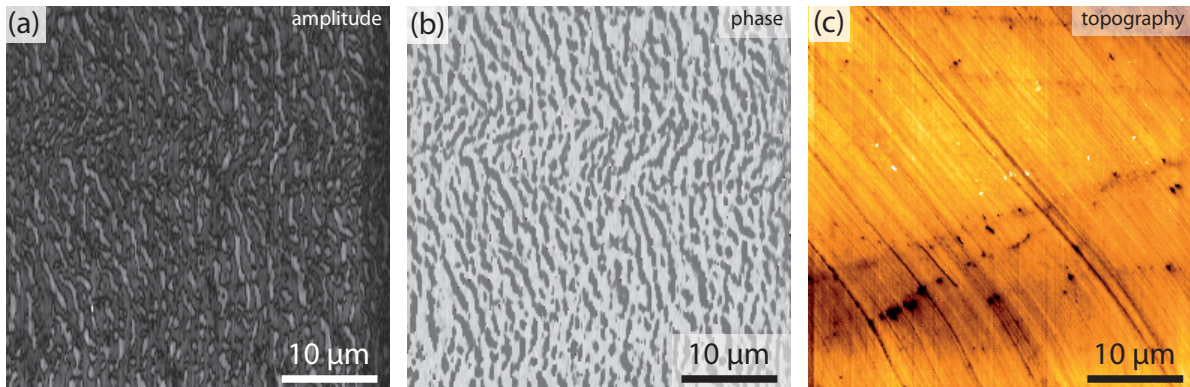


Figure 2.5: A tiger hidden behind a smooth surface? No, the domain pattern of a polished, unpoled BaTiO₃ single crystal (001)-face is imaged by piezoelectric force microscopy. The piezoelectric activity [black means no activity in image (a), a PFM “amplitude image”, see chapter 3], domains with antiparallel polarisation directions [PFM “phase image”, (b)], and the topography [AFM, (c)] are shown; the three images were recorded simultaneously.

The interfaces between domains are called domain walls. They are important, because they can define a lower limit for the minimal domain size and thus the information density in memory devices. Domain walls in ferromagnetic materials, which are presently used for hard drives are much wider than domain walls in ferroelectrics with the resulting disadvantages in terms of information density. The domain walls can be termed according to the angular difference of the polarisation direction in the separated domains; most common are 180° , 90° , and 60° -domain wall.

A ferroelectric with more than a single domain, is in a *polydomain* state. In the case of a polydomain state, extrinsic and intrinsic contributions to the material parameters, like dielectric constant, piezoelectric coefficient etc, can be distinguished. The intrinsic con-

tributions can be calculated from the thermodynamical potential as discussed. Extrinsic contributions in ferroelectrics are often due to domain-related effects [Damjanovic, 1998]. Domain walls can contribute to the permittivity due to their motion in an electric ac field. A domain wall motion is associated with a polarisation change in the sample. In the case of a 180° domain wall, we can write:

$$\Delta P = \alpha P_s + (1 - \alpha)(-P_s), \quad (2.13)$$

where ΔP and α are the polarisation variation and the volume ratio of the positive polarisation direction, respectively. The polarisation variation due to domain wall motions gives rise to a contribution to the dielectric constant under the influence of an ac field [equation (2.10)].

2.1.7 Piezoelectricity

Piezoelectric materials are sensitive to mechanical stress in terms of polarisation. A stress applied to a piezoelectric material produces a charge density $\vec{D} \cdot \vec{n}$ on the faces of a capacitor, with the normal vector \vec{n} , due the variation of the dielectric displacement. The linear relationship between mechanical stress X_{kl} and D_i ,

$$D_i = d_{ijk} X_{jk}, \quad (2.14)$$

is named the *direct piezoelectric effect* with the piezoelectric coefficients written in a third-rank tensor d_{ijk} .

The *converse piezoelectric effect* is — as well as the direct — very interesting from the point of view of applications. Upon the application of an electric field, a piezoelectric material changes its shape and volume. This can be described similarly to equation (2.14):

$$x_{ij} = d_{kij} E_k, \quad (2.15)$$

with the strain tensor x_{ij} , the electric field E_i , and the piezoelectric coefficients in the tensor d_{ijk} .

The electro-mechanical field response can be found from the introduced thermodynamic potential in equation (2.3). If we take only the lowest order terms, we can write for the tetragonal case with $P_1 = P_2 = 0$:

$$E_3 = \frac{\partial \Delta G}{\partial P_3} = a_1 P_3 - 2Q_{11} X_1 P_3 - 2Q_{12} X_2 P_3 - 2Q_{44} (X_4 P_2 P_3 + X_5 P_1 P_3). \quad (2.16)$$

The first term is the dielectric and the second and third are the piezoelectric response. The piezoelectric coefficient g_{in} is then:

$$g_{33} = -\frac{\partial E_3}{\partial X_3} = -\frac{\partial^2 \Delta G}{\partial X_3 \partial P_3} = 2Q_{11} P_3, \quad (2.17)$$

$$g_{31} = g_{32} = 2Q_{12} P_3, \quad g_{15} = g_{24} = 2Q_{44} P_3. \quad (2.18)$$

Using the relationship between the piezoelectric coefficients for different experimental situations $d_{im} = \varepsilon_0 \varepsilon_{ij} g_{jm}$, the piezoelectric coefficients d for a constant electric field can be written in the matrix notation as:

$$d_{33} = \varepsilon_0 \varepsilon_{33} Q_{11} P_3, \quad d_{31} = d_{32} = \varepsilon_0 \varepsilon_{33} Q_{12} P_3, \quad d_{15} = g_{24} = \varepsilon_0 \varepsilon_{11} Q_{44} P_3. \quad (2.19)$$

Since the direct piezoelectric and the converse piezoelectric effect are two different effects, one might expect different coefficients; nevertheless, they are identical as is shown in the following two equations:

$$g_{in}^{\text{direct}} = -\frac{\partial E_i}{\partial X_n} = -\frac{\partial^2 \Delta G}{\partial X_n \partial P_i}, \quad (2.20)$$

$$g_{in}^{\text{converse}} = \frac{\partial x_n}{\partial P_i} = -\frac{\partial^2 \Delta G}{\partial P_i \partial X_n}. \quad (2.21)$$

The piezoelectric coefficients can be either positive or negative and the sign of the response depends on the sign of the perturbation, i.e. the direction of the electric or mechanical field. This is important for piezoelectric force microscopy (see section 3.1). The number of independent elements of the piezoelectric coefficient d is reduced from 27 to 18 by the symmetry of the stress and strain tensors ($d_{ijk} = d_{ikj}$). The crystal symmetry of the material plays a crucial role in the piezoelectric effect: centrosymmetric point groups do not allow any element in the piezoelectric tensor to differ from zero and in non-centrosymmetric point groups, symmetry elements may decrease the number of independent elements.

In a short notation, the coefficients d_{ijk} (tensor form) can be written as d_{im} (matrix form) according to equation (2.22).

$$\begin{pmatrix} d_{11} & d_{12} & d_{13} & d_{14} & d_{15} & d_{16} \\ d_{21} & d_{22} & d_{23} & d_{24} & d_{25} & d_{26} \\ d_{31} & d_{32} & d_{33} & d_{34} & d_{35} & d_{36} \end{pmatrix} = \begin{pmatrix} d_{111} & d_{122} & d_{133} & 2d_{123} & 2d_{113} & 2d_{112} \\ d_{211} & d_{222} & d_{233} & 2d_{223} & 2d_{213} & 2d_{212} \\ d_{311} & d_{322} & d_{333} & 2d_{323} & 2d_{313} & 2d_{312} \end{pmatrix} \quad (2.22)$$

2.1.8 Critical Size for Ferroelectricity

With the trend to very thin films and the technical abilities to produce small ferroelectric structures, the question of critical size for ferroelectricity gained in significance for practical applications and experimental research (compare to section 2.4.3 as well) [Spaldin, 2004, Shaw et al., 2000]. Researchers have observed a lower Curie temperature and a reduced polarisation upon the size reduction of ferroelectrics and extrapolation of the data suggested a critical size for ferroelectricity. Phenomenological theories [Wang et al., 1995, Chew et al., 2003] were supplemented recently by *ab-initio* simulations by different groups [Junquera and Ghosez, 2003, Chew et al., 2003]. General statements about a critical size for ferroelectricity are difficult because calculated values are valid only for the studied systems with specific electrodes and misfit strains, which induce a shift of the transition temperature [Junquera and Ghosez, 2003].

A critical thickness limit as small as the size of three unit cells, hence a thickness of 12 Å, has been found [Gerra et al., 2006] using first-principles calculations for BaTiO₃ with SrRuO₃ electrodes. This theoretical limit is possible due to *in-situ* screening of the polarisation in SrRuO₃ electrodes.

Experimental results agree with such a small critical size. Using synchrotron x-ray radiation, ferroelectricity was shown in films, which were only three unit cells thick (1.2 nm, PbTiO_3 on SrTiO_3) [Fong et al., 2004].

Ferroelectric polymers are an interesting model system for the study of critical size, because they can be deposited as ultrathin films by for instance the *Langmuir-Blodgett* (LB) technique. Fundamental phenomena such as the coercive field [Ducharme et al., 2000], phase transitions, and ferroelectricity [Bune et al., 1998] were studied in high quality ultrathin (down to only 1 nm) LB films (see section 2.4.3).

2.2 Ferroelectric Materials

Ferroelectric materials exist in various compositions and forms. Single crystals of a material simplify studies of fundamental ferroelectric phenomena. The crystallographic orientation can be well controlled and intrinsic properties more easily accessed. However, single crystals are not an option for many applications, because their costs are high. Ceramic materials can be processed, shaped and manipulated more easily and are therefore preferred in many, e.g. piezoelectric, applications. The most widely used ferroelectric³, lead titanate zirconates, $\text{Pb}(\text{Zr,Ti})\text{O}_3$ (PZT) cannot even be grown in single crystal form (large enough to be useful).

Apart from single crystals and ceramics, ferroelectrics are commonly deposited and used in the form of thin films. In micro-electro-mechanical systems (MEMS), but also for memory applications with high information density, this form is the most important; it is shortly discussed below.

2.2.1 Thin Films

With the age of miniaturisation and computing, the interest in thin ferroelectric film grew fast. Thin films can be deposited in many different ways and consequently in many different phases and various degrees of perfection. The choice of a substrate is decisive for the quality of the films. Using appropriate single crystalline substrates, films can be grown with an orientation of the crystallographic axes that is fully controlled by the substrate. Such films are called *epitaxial*.

For more economic applications, methods were found to control the crystallographic orientation of the film and to achieve *textured* films with a preferential out-of-plane crystallographic orientation of the grains.

Important parameters for the control of film growth are the lattice spacing, the thermal expansion coefficients of the substrate and the film, the temperature of the deposition, the material supply, the annealing process and other, more deposition technique specific parameters. An effective way to control the texture of a film are buffer layers that initiate the growth of crystals on the substrate [Muralt et al., 1998].

In this thesis, sol-gel and spinning methods, Langmuir-Blodgett, sputtering, evaporation, and pulsed laser deposition (PLD) techniques were used to deposit ferroelectric films and electrodes.

³A lot of research is going on now to replace PZT by lead-free materials.

2.2.2 Lead Zirconate Titanate, Barium Titanate — Perovskite Ferroelectrics

Perovskite are pseudo-cubic structures with a chemical formula of the form ABO_3 . The class of perovskite ferroelectrics is the best studied and holds the record values for important ferroelectric properties. The origin of their ferroelectricity is based on the displacement of ions out of their symmetric position. In a simplified model of perovskite materials, the small Ti^{4+} ion, perfectly centred in the unit cell above the Curie temperature, moves to one of its equilibrium positions, which is slightly out-of-centre. This displacement during the phase transition has two consequences: the crystal symmetry changes from cubic (point group $m\bar{3}m$) to tetragonal ($4/mmm$) and due to the charge of the Ti atom, a polarisation can be attributed to the structure. Two possible and equivalent polarisation states are depicted in figure 2.6 of a $BaTiO_3$ unit cell⁴.

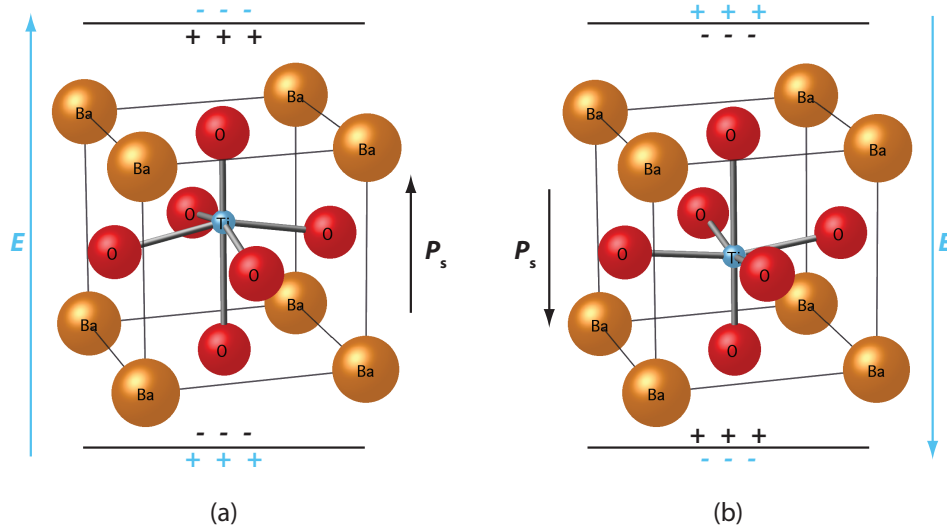


Figure 2.6: A perovskite unit cell ABC_3 , in the example $BaTiO_3$, is shown with the barium atoms on the corners, the oxygen atoms on the face centres, and the titanium in the centre of the unit cell. “Up” (a) and “down” (b) spontaneous polarisation P_s are shown with the electric field E to switch it to the respective polar direction (note that the polarisation state remains when the electric field is removed).

The polarisation can be switched to other directions by the application of an external electric field. The schematic representation in figure 2.6(a) shows, how the polarisation aligns with the electric field (which is parallel to one of the four-fold axes in the tetragonal system). The black solid lines in this image represent the electrodes that are needed to apply an electric field. The charges, symbolised by + and –, between the electrode are bound charges due to the spontaneous polarisation.

Lead zirconate titanate ($Pb(Zr_xTi_{1-x})O_3$, short: PZT) is the most used ferroelectric in applications and was also used in our experimental studies, described in chapter 4. The phase diagram of the solid solution of lead zirconate and lead titanate is shown in figure 2.7. The Zr-rich side of the phase diagram at room temperature is characterised by

⁴The crystal structure was visualised with the software CrystalMaker from *CrystalMaker Software Ltd.*

a rhombohedral, whereas the Ti-rich side by a tetragonal phase. Detailed discussions of this solid solution are available [Jaffe et al., 1971]. The polarisation direction is associated with the crystal symmetry as is illustrated in figure 2.4(a) and changes thus when phase boundaries are crossed.

The phase boundary and monoclinic phase region around a Zr/Ti ratio of 53/47 are technologically very important because many properties are at a maximum close to the phase transition.

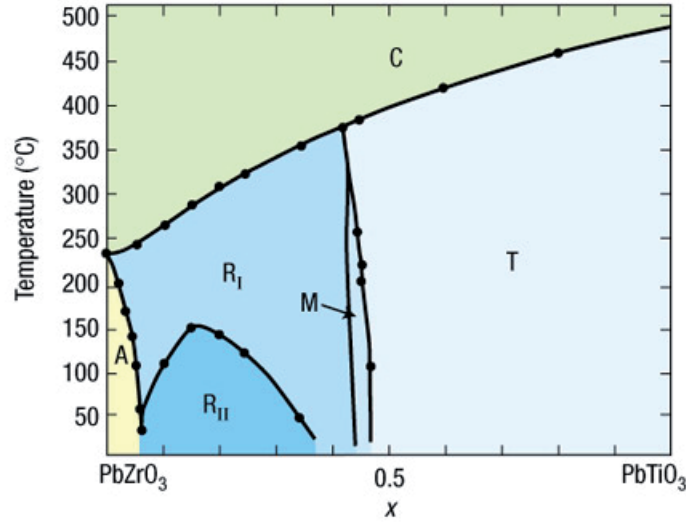


Figure 2.7: The phase diagram of the solid solution of lead titanate and lead zirconate (original illustration from [Rabe, 2002]). Most of the phases at room temperature are ferroelectric: T – titanium-rich tetragonal phase, M – monoclinic phase, R_I and R_{II} – high- and low-temperature zirconium-rich rhombohedral phase; the non-ferroelectric phases are: C – paraelectric cubic phase, A – antiferroelectric phase

2.2.3 Ferroelectric Polymers

Apart from the big class of ferroelectric oxides, ferroelectricity was discovered — but much later — in fundamentally different materials, namely in liquid crystals [Meyer et al., 1975] and polymers [Nakamura and Wada, 1971]. Due to the more complicated units constituting a crystal, these two materials have in general a more complex structure. Ions or atoms are stacked in the crystal lattice of oxide ferroelectrics and their order is repeated over large volumes, whereas polymers consist of macromolecules, which arrange in a lower symmetry and frequently with mixed amorphous and crystalline regions. Probably due to their higher complexity, ferroelectricity in these soft matter materials was discovered decades after the phenomena was known in ionic structures. Ferroelectricity was found for the first time in polyvinylidene fluoride (PVDF) two years after observing piezoelectric effects in this material [Kawai, 1969]. PVDF and its copolymers are still among the most prominent members of the organic ferroelectrics due to their high piezoelectric and pyroelectric coefficients.

Chemical Structure

In the molecule of PVDF, two hydrogen and two fluorine atoms are alternatively bonded to the carbon atoms of the polymer backbone. The structure of a molecule of PVDF is illustrated⁵ in figure 2.8.

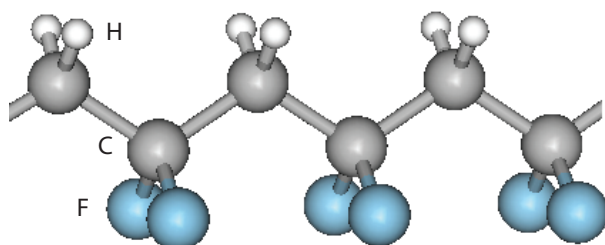


Figure 2.8: The chemical structure of polyvinylidene fluoride (PVDF) with the backbone of carbon atoms and fluoride and hydrogen atoms, which are regularly bonded to it.

The origin of the ferroelectricity of polymers are electric dipoles in the molecules, which can be inverted under the application of an electric field by molecular movements. The dipole is formed by the C–F and C–H bonds with an decreasing electronegativity from fluorine (F; electronegativity 3.98) over carbon (C; 2.55) to hydrogen (H; 2.20). Electrons are thus on average closer to F than to C resulting in a polar bond with an increase in negative charge δ^- on the fluorine side of the bond. The same is true — to a smaller extent — for the C–H bond, with a δ^+ on the H side of the bond as is depicted in figure 2.9.

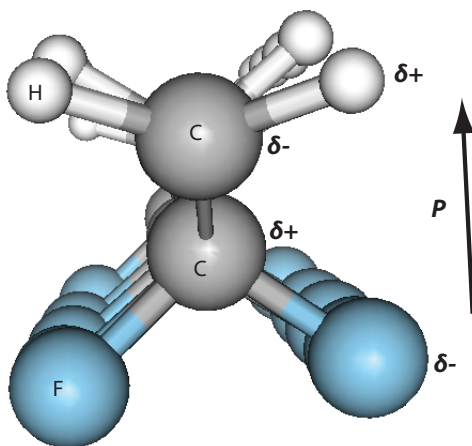


Figure 2.9: A view in the direction of the polymer axis of PVDF. The higher electronegativity of the F atom induces higher electron density between the F and C than the H and C bonds indicated by the δ^+ and δ^- symbols and a polar direction as indicated by P_s .

In order to understand ferroelectricity in PVDF, one has to understand the structure of the polymer on the level of the molecule and crystals.

⁵The chemical structures were visualised with the software MarvinSpace from ChemAxon.

Concerning the molecular level, one distinguishes between the configurational and the conformational structure of a molecule in macromolecular chemistry. Whereas the *conformation* of a molecule can be changed without breaking bonds but mainly by rotations, changes in the *configuration* involve breaking and reintroduction of bonds [Tieke, 1997].

The conformation of the macromolecules are designated with the *trans* (T) and *gauche* (G) terms. In order to understand the meaning of these terms, the sp^3 hybridisation of the C atoms have to be considered. In this tetrahedral geometry, bond angles between two C–C bonds are equal to 109.5° . In the case of PVDF and its $[-CH_2-CF_2-]_n$ elements, the chain is maximally stretched when the adjacent C atoms of both sides of a C–C bond are in the *trans* conformation, i.e. at the maximum distance from each other (under the condition of the given bond angles) as illustrated in figure 2.10(d). This corresponds to an angle of $\Phi = 0^\circ$ in the Newman projection as illustrated in figure 2.10(a).

Positions out of the *trans* conformation — as shown in figure 2.10(b,c) — with an energy minimum called *gauche* (b,c), and, more precisely, depending on the sense of the rotation, *gauche* (+) [abbrev. G] or *gauche* (–) [\bar{G} or G']. If $\Phi = 180^\circ$, one speaks of a *cis*-conformation.

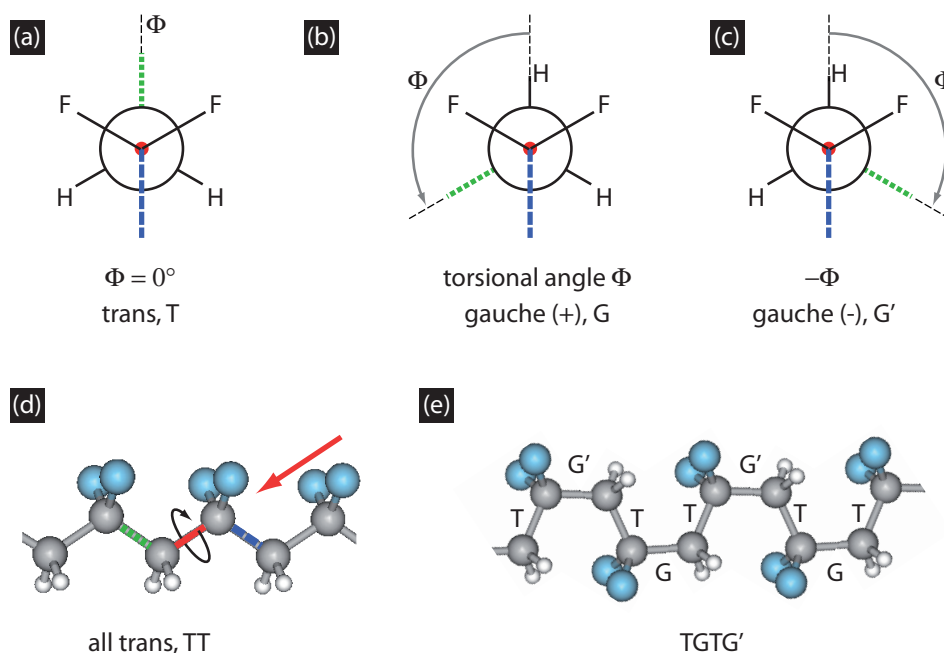


Figure 2.10: Different conformations of a PVDF macromolecule in the Newman projection. This projection is in direction of the arrow indicated in figure (d). The *trans* state of subsequent C–C bonds results in a maximally stretched chain (d). A combination of *trans* and *gauche* (+ and –) conformations would result in a TGTG' chain (e).

Polymers in the melt and in solution are also disordered with respect to the conformation. When they crystallise, the macromolecules can either keep the disordered conformation or crystallise in a regular conformation by the the described rotations. Van der Waals forces can stabilise three conformations in PVDF, which is rather exceptional for macromolecules: TT, TGTG', TTTGTTTG' (or T_3GT_3G'). The combination of *trans* and *gauche* conformations results in chains with a different intramolecular polarisation [Lovinger, 1983]. For an all-*trans*, TT, chain as shown in figure 2.10(d), the polarisation

is basically perpendicular to the chain direction, whereas it has an additional component along the chain in the TGTG' conformation [Lovinger, 1983].

Crystallographic Structure

Four experimentally found polymorphs of pure PVDF are listed in table 2.1. These phases are related to the conformations of the molecules (TT, TGTG, and T₃GT₃G'). The phase transformations between the polymorphs occur via macromolecular chain rotations and necessitate macroscopic treatments like stretching and heating (see e.g. in figure 6 in reference [Kepler and Anderson, 1992]).

Table 2.1: The polymorphs of PVDF. Data sources: [Tashiro, 1995, Hasegawa et al., 1972, Karasawa and Goddard III, 1992].

Names	conformation	type of dielectric	lattice parameters				space group	lattice
			a [Å]	b [Å]	c [Å]	β [°]		
Form I β	TT, all <i>trans</i> zig-zag	ferroel.	8.58	4.91	2.56		Cm2m, C _{2v}	b.c. ortho- rhombic
Form II α	TGTG' antiparallel	nonpolar,	4.96	9.64	4.62	90	P2 ₁ /c, C _{2h}	mono- clinic
Form II _p $\delta = \alpha_p$	TGTG' parallel	ferroel.	essentially the same as form II				P2 ₁ <i>cn</i> C	mono- clinic
Form III γ	T ₃ GT ₃ G' parallel	ferroel.	4.96	9.58	9.23	92.9	Cc, C _s	mono- clinic

The pure PVDF polymer crystallises from the melt in the nonpolar α -phase with chains in the TGTG' conformation as illustrated in figure 2.11(b). This most stable phase is also designated *form II*. Macroscopic stretching of the polymer sample can transform the α -phase into the polar β - or *form I*-phase with molecules in the all-*trans* (TT) conformation. The β -phase is most interesting because it is ferroelectric. Additional polymorphs that are of minor interest in this work are the γ and δ -phases.

The ferroelectric β -phase of PVDF is most important for us, but stretching in order to orient the macromolecules and to get this ferroelectric phase in thin films deposited on rigid substrate is not possible. Nevertheless, it was found that a compositional modification of the PVDF molecules favours the β -phase as described below.

The Copolymer of VDF and TrFE

The substitution of some hydrogen atoms by fluorine, or in other words the addition of trifluoroethylene (TrFE; $-\text{CF}_2-\text{CHF}-$) or tetrafluoroethylene (TeFE; $-\text{CF}_2-\text{CF}_2-$) to PVDF, induces a crystallisation of the copolymer in the polar β -phase as was found in 1968 [Lando and Doll, 1968].

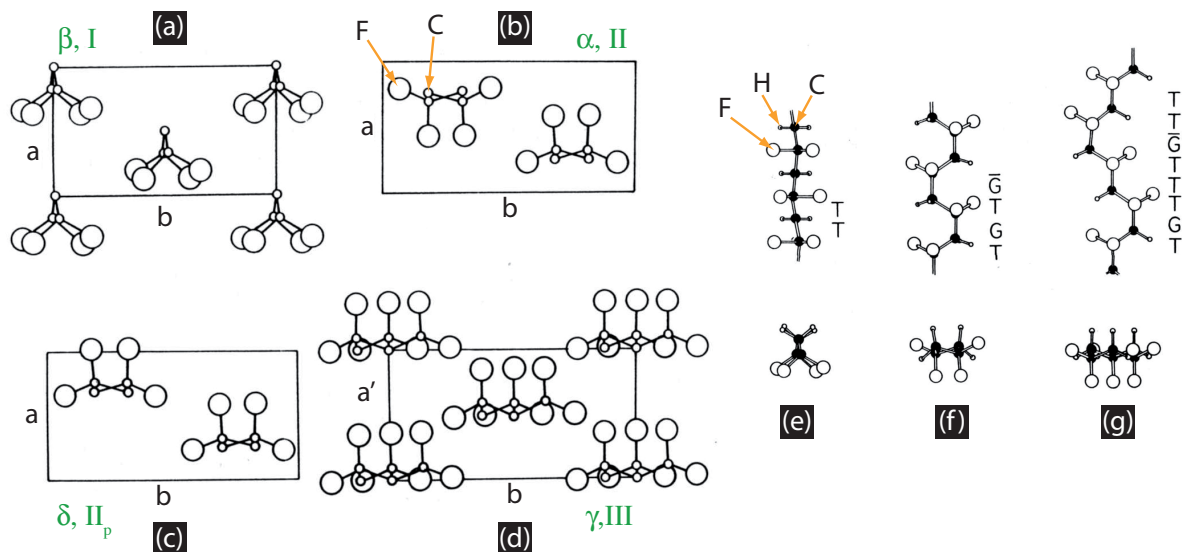


Figure 2.11: Unit cell of the β (a), α (b), δ (c), γ (d) phases of PVDF in an orthorhombic symmetry (from [Tashiro, 1995], p. 65-66), the H atoms are not shown. The conformation of the constituent molecules for the phases in (a-d) are given: TT (e), TGTG' (f), T_3GT_3G' (g).

Fluorine atoms (diameter of 0.270 nm) are slightly bigger than the space offered by the all-*trans* carbon backbone (0.256 nm). The carbon chains therefore prefer to slightly twist to the right or left instead of the all-*trans* conformation. In the case of a *gauche*-conformation, the H and F atoms approach each other which leads to some destabilisation of the structure. There is thus a competition of these two destabilisation effects between the all-*trans* and the *trans-gauche* conformations.

It turns out that replacing some hydrogen atoms with a diameter of 0.240 nm in the copolymer chain by the larger F atoms results in a more stable all-*trans* conformation, because the steric hindrance between F atoms in the *gauche*-conformation is stronger than between neighbouring atoms in the all-*trans* conformation [Furukawa, 1989] [compare to figure 2.11(e-g)]. This preference of the TT conformation then leads to the crystallisation in the ferroelectric β -phase.

The more stable TT conformation in the copolymer also results in increased crystallinity [Koga and Ohigashi, 1986]. The maximum crystallinity of pure PVDF is 50 % and may reach values up to 90 % in the copolymer.

The direct crystallisation from the melt or solution in the ferroelectric β -phase and the higher crystallinity are very important advantages of the copolymers over pure PVDF, since polarisation and polarisation-related effects, like piezoelectricity and pyroelectricity, augment with the degree of crystallinity.

In the polymerisation of the the copolymer, the sequence of the VDF and TrFE units is difficult to control and results consequently in a random order⁶, since the size of hydrogen and fluorine atoms are similar.

Three structural phases were found in P(VDF-TrFE):

⁶A random polymer has a random distribution of the units A and B in the polymer chain, e.g. AABABBBA... in contrast to regular unit distributions, e.g. ABAB... [Tieke, 1997] p. 146

- Low-temperature phase (LT)
- Cooled phase (CL)
- High-temperature phase (HT)

The low-temperature (LT) phase is similar to form I (β phase) in PVDF and ferroelectric. The paraelectric, high-temperature HT phase was observed — as indicated by the name — at higher temperatures [Tashiro et al., 1984], but only for copolymer compositions with a high enough TrFE composition as discussed in the next section.

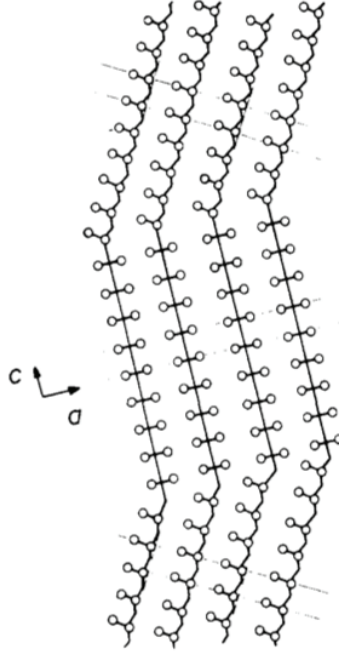


Figure 2.12: The suggested crystal structure of the cooled phase with crystalline segments that consist of molecules in the TT conformation and skews consisting of G conformations (original illustration from [Tashiro et al., 1984]).

The paraelectric phase was described in terms of a hexagonal structure with the space group $6/mmm$ [Ishibashi and Iwata, 2005, Tashiro, 1995], p. 107. The molecules in this structure are irregular in terms of the conformation (T, G, and G') and are dynamically rotated around the chain axis as illustrated in figure 2.13(a).

The CL phase forms after cooling copolymers with a TrFE composition of $> 30\%$; there are some uncertainties about its structure [Furukawa, 1989].

A structure for the CL phase was suggested [Tashiro et al., 1984] and is shown in figure 2.12 [Tashiro and Tanaka, 2006]. Segments of TT chains are arranged in parallel arrays, which are connected by boundaries of disordered *trans-gauche* bonds (not necessarily according to the skews shown in figure 2.12a). The torsional angle between *trans*-segments is 60° , and according to the polarisation direction, the adjacent arrays can thus be considered as 60° domains.

Ferroelectric Phase Transition

Upon cooling through the Curie temperature, the chains order from their random T, G, G' conformations of the high-temperature (HT) phase to the TT conformation of

the low-temperature (LT) phase. This corresponds to the transition of the hexagonal, $6/mmm$, symmetry in the HT to the orthorhombic low-temperature (β) phase with the space group $mm2$. The macromolecules are arranged along the c -direction as illustrated in figure 2.11(a,e). Due to the ordered dipoles, the LT phase is ferroelectric.

An experimental indication for the change of the conformation is the periodicity of the C atoms in the main chain. The maximum of the 001-peak moves to smaller angles in the x-ray pattern due to the stretching of the chain (to the TT conformation, monomer unit length changes from 2.30 Å to 2.56 Å) upon cooling and peaks associated with the intermolecular spacing — as shown in figure 2.13(c) — move to larger angles due to the decreasing distances.

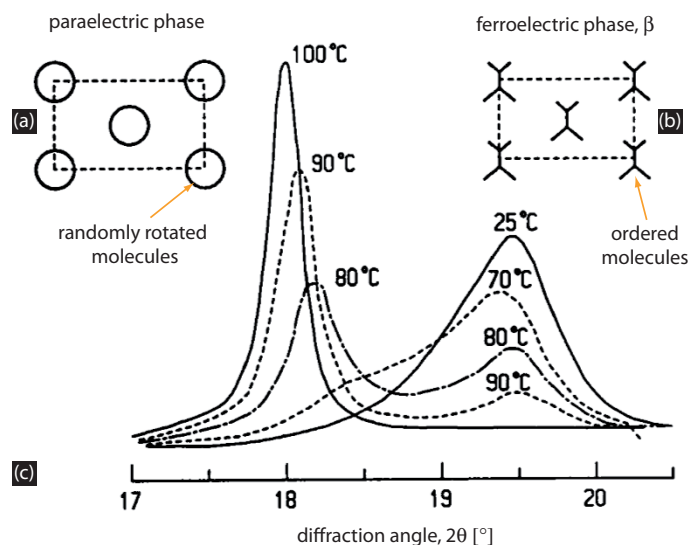


Figure 2.13: The transition from the hexagonal, $6/mmm$ symmetry of the paraelectric high-temperature (HT) copolymer phase (the macromolecules are projected into the paper plane; c direction) to the orthorhombic, $mm2$ symmetry of the ferroelectric low-temperature (LT) phase is associated with a contraction perpendicular to the chains as shown by the x-ray data (illustration taken from [Furukawa, 1989], x-ray data from [Lovinger et al., 1983])

This transition from the randomly distributed conformation and rotational order to the ordered, stretched arrangement of the macromolecules is of the *order-disorder type*.

The orthorhombic symmetry $mm2$ in the ferroelectric phase allows for six different domain states. Hence, 60° -domain walls can be expected.

In the case of pure PVDF, the paraelectric HT phase could not be observed, because the (estimated) Curie temperature is above the melting point of this polymer. This can be seen in the phase diagram of the copolymer for compositions between 0 to 100 % of VDF given in figure 2.14.

The HT phase appears with decreasing VDF content, i.e. substitution of H by F atoms and the ferroelectric-paraelectric phase transition between the regular LT and the disordered HT phases can be observed experimentally. The LT–HT phase transition shows a considerable hysteresis: a characteristic of a first order phase transition.

In a comprehensive study, Yagi synthesised the copolymer of P(VDF-TrFE) over the entire range of compositions and characterised their properties [Yagi et al., 1980].

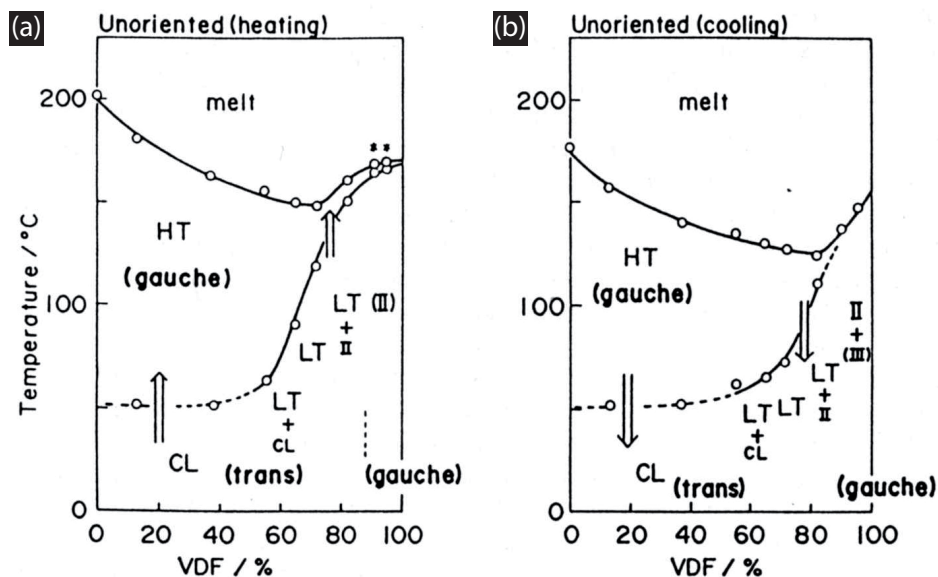


Figure 2.14: The phase diagram of the oriented (a) and unoriented (b) copolymer of P(VDF-TrFE) for cooling and heating for an increasing VDF composition given in mol % (original illustration from [Tashiro, 1995], p. 124). The VDF composition of all our films was 70 mol %.

The most interesting compositions consist of 50 – 80 % VDF due to their relatively well-defined Curie temperature, the stability of the β -phase, and the high crystallinity [Tajitsu et al., 1980].

We used a 70/30 mol % (65/35 weight %) composition of the P(VDF-TrFE) copolymer for all our experimental studies.

Morphology of the PVDF and P(VDF-TrFE Films)

After the discussion of the molecular and the crystallographic structure of PVDF and P(VDF-TrFE) ferroelectric polymers, their morphology in thin films is treated briefly in this section. The crystalline structure as described above applies to the crystalline regions in the thin films. These regions were described as lamellae, which are embedded in an amorphous matrix [Koga and Ohigashi, 1986, Ohigashi et al., 1992].

Structural analysis of the copolymer via transmission electron microscopy (TEM) is rather difficult. It was reported that the thinned samples become amorphous under the electron beam after a very short exposure time (of about 20 s). A lamellar structure with the chain orientation in the direction of the lamellae and the polarisation thus perpendicular was suggested [Park et al., 2006]. They used grazing-incidence x-ray diffraction (GIXD), SEM (shown in figure 2.15a) and polarised optical microscope techniques. Amorphous and crystalline regions could be observed in TEM as shown in figure 2.15(b) [El-Hami et al., 2003]. This group could see a diffraction pattern, but could not take dark field or high resolution images due to the damaging electron beam. Both groups found crystalline rods (lamellae) of about 50 nm and 300–500 nm width and length.

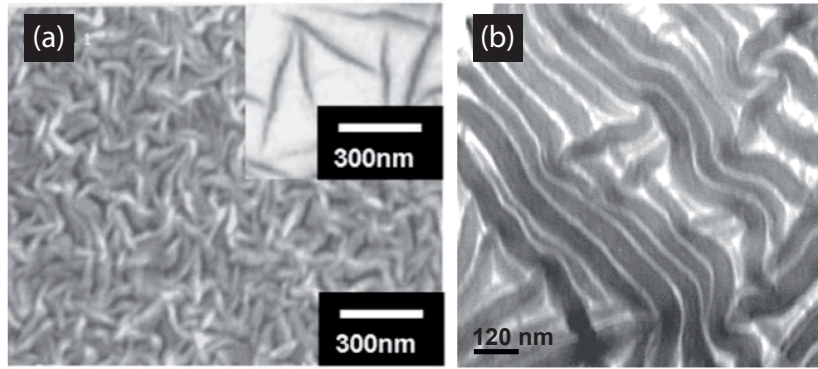


Figure 2.15: The morphology of an annealed VDF/TrFE copolymer 70 nm thick film on Al electrodes in (a) SEM and TEM images (inset), taken from [Park et al., 2006]. The TEM image (b) shows an annealed VDF/TrFE copolymer deposited on a NaCl substrate taken by El-Hami et al. [El-Hami et al., 2003]. The crystalline rods are embedded in an amorphous matrix.

2.3 Polarisation Reversal

2.3.1 Introduction and Overview

The main feature distinguishing ferroelectrics from other materials is the bistable nature of their polarisation state at zero field and the possibility of changing from one state to the other. This change is called *polarisation reversal* or *switching*.

Given a ferroelectric crystal, one can wonder in what way it reverses its polarisation. The following scenarios are conceivable in principle:

- (i) the polarisation switches simultaneously in all unit cells of the crystal;
- (ii) the polarisation switches independently in different regions of the crystal;
- (iii) the polarisation switches in a very small volume first, i.e. a nucleus, which then expands through the whole crystal;
- (iv) a combination of the above scenarios.

Simultaneous switching (i) has not been observed in ferroelectric materials — in contrast to ferromagnetic materials [Humphrey and Gyorgy, 1959].

Under exclusion of the possibility of simultaneous switching of all unit cells, the change from a poled state with a certain polarisation direction to a state of opposite polarisation direction entails an evolving domain pattern between the first and the final state.

The existence of domains was indeed reported already in the very early years of ferroelectric studies on Rochelle Salt, e.g. [Mueller, 1935]. However, not only the existence of domains and their walls, but also their motion was of interest.

The polarisation reversal in ferroelectric single crystals was reported to proceed through the expansion of switched regions, hence involving scenario (iii).

The questions as to whether regions in a crystal can reverse their polarisation independently, whether the polarisation reversal happens through single or many nuclei, or what kind of interactions between the regions were involved, attracted the interest of many researchers and are treated in numerous papers due to their direct impact on applications.

Experimental Methods

The study of the polarisation reversal mechanism is closely linked to available experimental techniques. Since the onset of the polarisation reversal in ferroelectrics involves potentially very small regions of nucleation, characterisation techniques to study the mechanisms should therefore have a corresponding spacial resolution (at least tens of nanometres). At the same time, this process can develop on very short time scales and requires accordingly very fast techniques, ideally with a time resolution in the order of nanoseconds, but at least microseconds.

An ideal domain imaging technique combining the required spatial and the desired time resolution is presently not available. Historically, techniques with sufficient time resolution were first obtained. Due to their low spatial resolution, we refer to these methods as *macroscopic techniques*. Generally, they measure global — or macroscopic — polarisation reversal effects, e.g. the switching current or switching charges, permittivity or even structural parameters, i.e. lattice spacing. The most common macroscopic methods are introduced briefly in chapter 2.6 of this thesis.

Macroscopic techniques allow conclusions about the polarisation reversal only in combination with appropriate, microscopic models. Such theoretical models are ideally based on microscopic observations.

For microscopic observations, a high spatial resolution and hence *microscopic techniques* are indispensable. Modern and traditional microscopic techniques are briefly introduced in section 2.7. Even though modern techniques are able to image domain patterns on a sufficiently small scale, they are usually not fast enough to follow the polarisation reversal directly.

Besides the high performance measurement techniques, high quality samples are essential for fundamental studies. A historic example are high grade BaTiO₃ crystals, which could only be grown thanks to a new crystal growth method developed by Remeika [Remeika and Jackson, 1954]. Their superior quality allowed for more detailed studies on the polarisation reversal than previously existing samples. The domain wall motions were observed by microscopic techniques with optical microscopes, but only for slow switching times and with a limited resolution. The historical observations are presented briefly in the next section.

In order to image fast polarisation reversal, switching pulses with a width smaller than the switching time of the ferroelectric can be applied, producing thus an “interrupted” switching. The domain wall motions can then be followed by repeated imaging of the instantaneous domain patterns.

Such an “interrupted switching” technique is also applied in combination with the developed PFM technique as described in chapters 3 and 4 as well as in the studies on ferroelectric polymers as presented in chapter 5.

After these remarks about the importance and the difficulties of the experimental study for the understanding of the polarisation reversal, we return back to the switching scenarios introduced above and the first studies on polarisation reversal.

2.3.2 Experimental Findings

A comprehensive body of results on polarisation reversal in ferroelectric crystals was reported in the 1950s by Merz working at Bell Labs in the USA and later at the RCA Company in Zürich. Merz used both microscopic and macroscopic techniques to observe the ferroelectric polarisation reversal. Macroscopically, he measured the switching current, i_{sw} , as a function of time, t , at constant voltage and for different temperatures [Merz, 1954].

The maximal switching current was determined from a switching current vs. time curve. The maximal switching current as a function of the applied electric field, E , followed an exponential law at low fields (below about 2 kV/cm for BaTiO₃) and a linear law at high fields [Fatuzzo and Merz, 1959].

$$i_{\text{sw}} \propto \begin{cases} e^{-\alpha/E} & \text{at low } E \\ (E - E_0) & \text{at high } E \end{cases} \quad (2.23)$$

The time taken for the switching current to return to zero in a $i_{\text{sw}}-t$ curve was called switching time by Merz⁷. The maximal switching current was inverse proportional to the switching time as shown in figure 2.16. The switching time t_s could then be written as:

⁷Further in the thesis, we will use a different definition for the switching time, as the time required to reverse half of the switchable polarisation.

$$t_s \propto \begin{cases} e^{\alpha/E} & \text{at low } E \\ 1/(E - E_0) & \text{at high } E \end{cases} \quad (2.24)$$

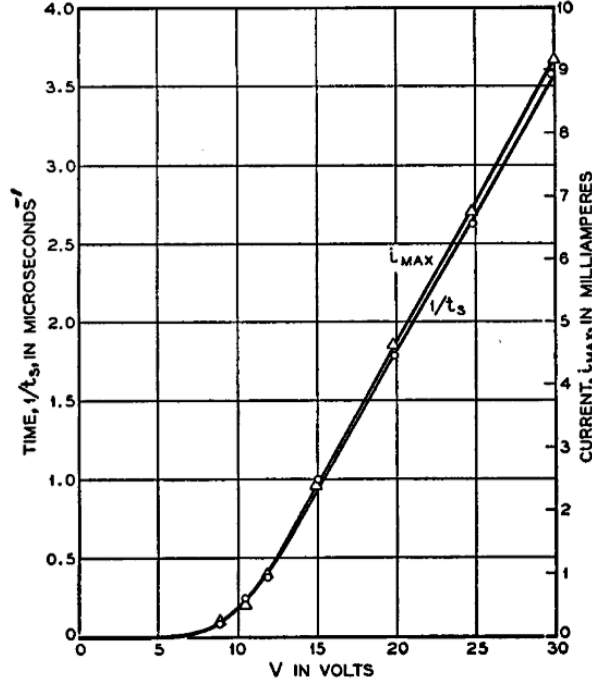


Figure 2.16: The field dependence of the maximal switching current and inverse switching time as published in the original work by Merz [Merz, 1956].

Merz suggested that the low- and high-field behaviour relate to different growth mechanisms. At low fields, the *thermally activated nucleation* is the limiting process for the polarisation reversal and the switching current therefore follows an exponential law. In the case of high fields, enough nuclei are provided and the polarisation is limited by the *expansion of domains*, i.e. the domain wall movement, with a linear field-dependence.

The domain expansion can be explained by a movement of domain walls to enlarge the domain volume. This domain wall motion was classified as *sideways* and as *forward* motion, with respect to the polarisation direction. In the case of a domain growth parallel to the direction of the polarisation, it was called forward growth, whilst an expansion perpendicular to the polarisation was called sideways.

Whereas in ferromagnetic materials, domain wall motion was found to be dominated by sideways motion of growing domains, Merz reported that this was not the case in the ferroelectric crystal. The appearance of domains of opposite polarisation direction was followed by forward growth. A sideways growth perpendicular to the polarisation direction was not observed [Merz, 1954].

Based on this observation, Merz deduced a weak coupling between neighbouring dipoles perpendicular to the dipole direction and concluded that the mechanism for the polarisation reversal differs significantly from the reversal in ferromagnetic materials.

Merz' interpretation concerning the field dependence of the nucleation was confirmed by Little's measurements on BaTiO₃ [Little, 1955]. She observed a threshold field for nucleation (of 2 kV/cm) and an increase in the number of appearing nuclei at higher fields.

Concerning the domain wall motion, she observed the appearance of spikes, as shown in figure 2.17. The spikes were reported to expand perpendicular to the polarisation direction, i.e. with a sideways motion. This observation was in contradiction to Merz, who claimed not to see any lateral expansion of the spike-shaped domains.

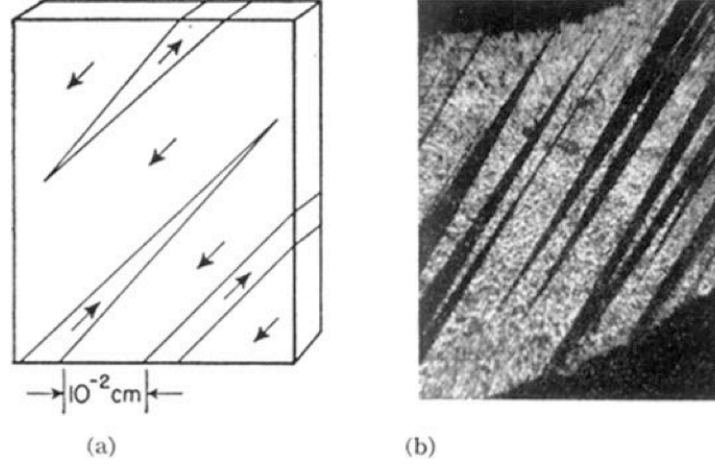


Figure 2.17: Appearing wedges of anti-parallel polarisation observed by Little [Little, 1955] in a (101)-oriented BaTiO_3 crystal with an optical method.

Apart from the exponential and linear time dependence of the switching time reported first by Merz at low fields and at higher fields, respectively, a power law for the switching time was found [Stadler and Zachmanidis, 1963] in the very large-field range in BaTiO_3 :

$$t_{\text{sw}} \propto E^{-n}, \quad (2.25)$$

with an exponent $n \approx \frac{3}{2}$.

To summarise, the polarisation reversal suggested by Merz and Little includes the following stages, illustrated also in figure 2.18:

nucleation, the first step, consist of the creation of small nuclei of inverse polarisation;

forward growth, the second step, in which the nuclei grow quickly in the direction of the polarisation;

sideways growth, the third step, with sideways expansion of the needle-like, forward-grown domains.

The slowest of the above mentioned stages is the most important in terms of kinetics, because it limits the switching rate and hence, determines the polarisation reversal time.

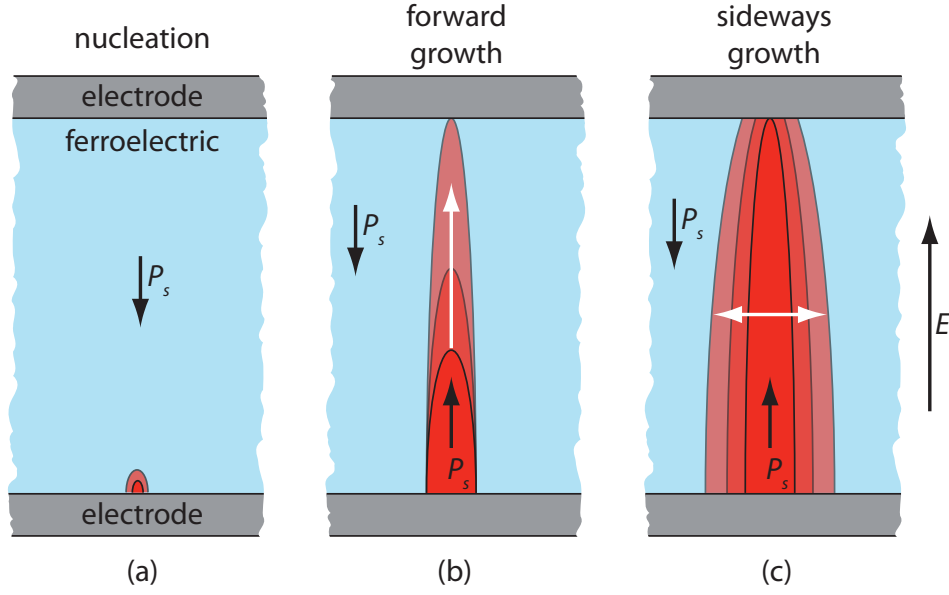


Figure 2.18: Schematic of the three growth stages with nucleation (a), forward (b), and sideways growth (c).

2.3.3 Nucleation — the Landauer Model

The problem of polarisation reversal, and more specifically nucleation, was treated theoretically in 1957 by Landauer [Landauer, 1957]. He considered a nucleus in the shape of a prolate semispheroid as shown in figure 2.19:

Landauer's model compares the energy gained upon polarisation reversal to the wall energy and the energy associated with the depolarising field.

$$\begin{aligned}
 U &= -U_{\text{bulk}} + U_{\text{surface}} + U_{\text{depol}} = \\
 &= -ar^2l + brl + c\frac{r^4}{l}, \\
 \text{with} \\
 a &= \frac{4\pi P_s E}{3}, \quad b = \frac{\pi^2}{\sigma}, \quad c = \frac{4\pi P_s^2}{3\epsilon_l \epsilon_0} \log\left(\frac{2l}{r}\right),
 \end{aligned} \tag{2.26}$$

where r , l , E , P_s , σ , ϵ_l , and ϵ_0 are the radius and the length of the half prolate spheroid, the applied electric field, the spontaneous polarisation, the surface energy of a 180° wall, the relative lattice dielectric constant of the ferroelectric, and the dielectric constant of vacuum.

The free energy of the nucleus can be calculated as a function of its size (r and l). At a critical size, the growth of the nucleus is favourable in terms of energy, i.e. analytically a saddle point is reached $\partial U/\partial l = 0$ and $\partial U/\partial r = 0$. The nucleus is thus unstable below and stable above the critical size.

A critical energy has to be provided thermally to create a nucleus of critical size. This critical energy for a thermally activated nucleus was calculated for parameters used by Merz, i.e. an applied field of 500 V/cm under the assumption of the energy of a 180°

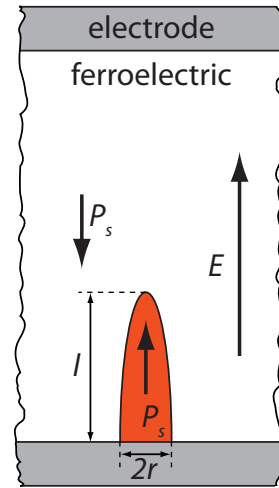


Figure 2.19: Schematic illustration of a nucleus in the shape of a prolate spheroid, which nucleated at the bottom electrode due to the application of an electric field E .

domain wall $\sigma = 7 \cdot 10^{-3} \text{ J/m}^2$ (this corresponds to about 0.007 eV per unit cell face). It resulted in a value of $E_N \approx 10^8 k_B T$ [Landauer, 1957].

The probability of nucleation for this thermally activated process is proportional to the Boltzmann factor $e^{-E_N/(k_B T)}$. With a critical energy 10^8 times $k_B T$, the probability for nucleation is evidently negligible. In another estimation for PZT and an electric field of 100 kV/cm, the activation energy is “only” $10^3 k_B T$, however, the nucleation probability from the Boltzmann factor is still only 10^{-430} and the waiting time is thus of the order of the lifetime of the universe [Tagantsev, 1997]!

Based on these calculations, a realistic nucleation probability can only be obtained by increasing the applied field considerably while keeping the other parameters constant. A higher critical field for nucleation would likewise result in considerably higher coercive fields⁸, which contradicts with experimental evidence.

Further Developments of the Landauer Model

Despite the critical energies and probabilities calculated above, nucleation does occur in real crystals at low electric fields. Numerous attempts have been made to explain the discrepancy between the necessary electric field for nucleation in theory and real ferroelectrics, the so-called *paradox of the coercive field*.

The numerical agreement (in the same order of magnitude) between the theoretical model and real crystals could however not improved sufficiently to bridge the orders of magnitude gap between theoretical and real critical energy values.

The manifestation of nucleation in real crystals was explained hypothetically with special effects that can lower the domain wall energy. Such effects are not taken into account in the simplified model of a perfect crystal. Lattice defects, screw dislocations [Nakamura, 1954], space charge layers at the crystal surfaces [Pruett, 1958], or remnants of reversed polarisation may serve as crystal inhomogeneities that lower the barrier for nucleation. Despite numerous general suggestions of defects as activation energy reducing agents, e.g. [Jona and Shirane, 1962], the defect type and the mechanism of their influence on nucleation were not specified.

Gerra et al. considered a ferroelectric-electrode interface, which favours one polarisation direction over the antiparallel one [Gerra et al., 2005]. An additional energy term for the interface energy, which depends on the polarisation direction was therefore added to the Landauer model in equation (2.26). This revised model showed a decrease of the nucleation barrier and even a complete suppression of the barrier at high enough fields.

A further interesting outcome of the model was the possibility of *cold-field nucleation*, i.e. a nucleation without thermal activation. This type of nucleation was deduced from observations of non-exponential temperature behaviour of the switching dynamics [Xu et al., 2001, Stolichnov et al., 2003, Astafiev et al., 2003].

The model demonstrates a way to explain formally the paradox of the coercive field, the non-diverging temperature dependence of the coercive field upon cooling, and the existence of favourable conditions for nucleation given by small inhomogeneities in the ferroelectric-electrode interfaces. The latter may even explain an exponentially wide spectrum of waiting times for nucleation (see section 2.4).

⁸The coercive field, E_c is the field at which about half of the switchable polarisation has reversed so that $P(E_c) = 0$.

2.3.4 Domain Wall Motion

Soon after the pioneering work of Merz, an important contribution to the understanding of domain wall motion in ferroelectric single crystals was made by Miller and Savage [Miller and Savage, 1958], [Miller and Savage, 1959]. They used a technique employing liquid electrodes and etching⁹ to directly visualise the domain wall movement in BaTiO₃ with an optical microscope. An exemplary photograph of a domain pattern prepared by such a technique is shown in figure 2.20.

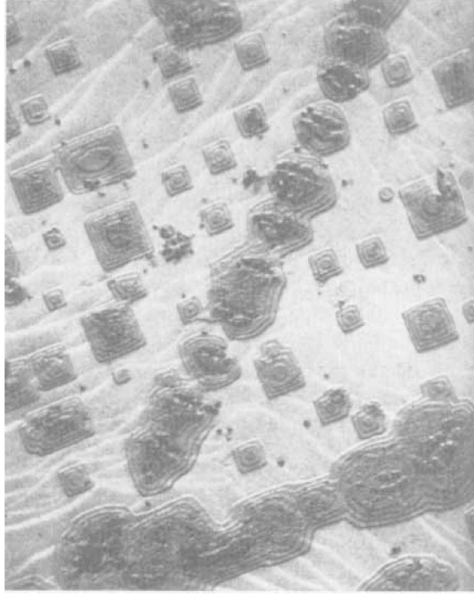


Figure 2.20: Photograph of an etched domain pattern of a BaTiO₃ crystal prepared by Stadler [Stadler and Zachmanidis, 1963] using the technique used by Miller and Savage.

They found that the polarisation of the crystal could be reversed by a single sideways-moving wall at low fields. The combination of the optical technique with switching current measurements established that the domain velocity followed an exponential law:

$$v_{\text{dw}} \propto e^{-\delta/E} . \quad (2.27)$$

The parameter δ was almost equal to the parameter α in the relation (2.23) for the switching current in the Merz law. The observed dependence of the switching current was thus related to the domain wall motion and not to the first step in the classical scenario, the nucleation process.

This contradiction could however be explained by a new model for the domain wall motion. Abe [Abe, 1959] as well as Miller and Weinreich [Miller and Weinreich, 1960, Miller and Savage, 1960] contributed to the idea of a nucleation next to an existing domain wall. The wall-adjacent nucleus grows then step-like over the domain wall resulting in an effective sideways motion of the domain wall as illustrated in figure 2.21. The limiting stage of such a domain wall motion was assumed to be the nucleation of new domains

⁹HF was used to reveal the c-domain structure and H₃PO₄ to remove the HF-etch pattern and to flatten the sample surface again.

next to existent domain walls. The analogy to an nucleation activation mechanism could therewith be explained.

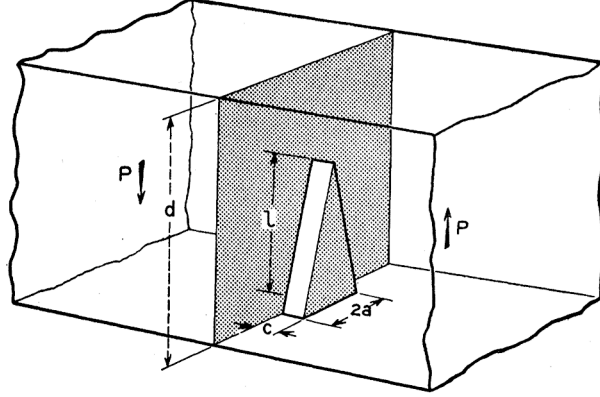


Figure 2.21: Sideways growth model with nucleation close to an existing domain wall by Miller and Weinreich [Miller and Weinreich, 1960]

The theory by Miller and Weinreich had however some shortcomings concerning the neglect of imaging forces from the electrode for the calculation of the depolarising field and the dimension of the domain wall. The nucleation probability would be proportional to the domain wall length, but Miller and Weinreich have not observed a dependence on the domain wall area [Stadler, 1992]. Burtsev and Chervonobrodov revised the Miller-Weinreich model and came up with a more correct description [Burtsev and Chervonobrodov, 1982]. With the optimisation of the nucleus' shape (not the triangular shape as shown in figure 2.21) in terms of the nucleation energy, more realistic values were obtained. The authors could further show that the domain wall motion is thermoactivated at low fields and a dissipative process at high fields yielding an exponential and a power law, respectively.

The results of Merz, who did not observe a sideways motion, were explained by a theory on the forward motion of ferroelectric domains [Molotskii, 2003]. Due to the fast velocity in the forward direction, the sideways expansion can hardly be seen at high electric fields.

More recent work on the field of polarisation reversal usually involved computer simulations and modern characterisation tools.

Using PFM and short pulses, a thickness dependent sideways domain wall motion was explained as a creep process [Tybell et al., 2002]. This was characterised by a wall velocity proportional to an exponential function of the inverse electric field. In the creep mechanism, the domain wall motion is controlled by defects.

In a recent paper, Shin et al. tried to bridge the gap between the experimental studies and *ab-initio* calculations [Shin et al., 2007]. They corrected the shortcomings of the Miller-Weinreich theory to obtain smaller critical nuclei sizes and more realistic (one to two orders of magnitude smaller) activation fields.

2.3.5 Summary

The domain reversal in ferroelectric crystal is characterised by three stages: nucleation, forward, and sideways growth. Sideways growth was found to be the rate limiting step in many cases; forward growth and nucleation appeared to happen in general faster. The domain wall velocity of the sideways growth as a function of the applied field was described

most generally by an exponential law. Such a behaviour was explained by a nucleation process in the vicinity of existing domain walls.

The exponential law for the switching time as a function of the applied electric field was found at small applied fields, where the thermal activation plays a crucial role. At the high-field regime a linear law was reported, which can be seen as the transition to the power law at yet higher fields.

Despite many years of research on the polarisation reversal in ferroelectrics, a clear picture of the detailed mechanisms of nucleation and domain wall motion is still missing and many important questions regarding the effects of crystal defects, electrodes, etc. are not answered yet.

It is clear that polarisation reversal is a complex process and that it needs better, i.e. fast and high resolution characterisation techniques, which can provide a basis for the improvement of the phenomenological models and understanding of the polarisation reversal mechanisms.

2.4 Kinetics of the Polarisation Reversal

2.4.1 Introduction

Time-related aspects of the polarisation reversal are treated in this section. According to the terminology stemming from chemistry, we call these switching rate studies *kinetics*.

What is the time required to switch a ferroelectric material? — A question of great interest, both from an application and from a fundamental point of view. The time needed to reverse the polarisation is related to the polarisation reversal mechanism, but also to the nature of ferroelectricity. Considering the difference in the structure of different ferroelectrics, e.g. PZT and PVDF as discussed in section 2.2, different mechanisms and switching times might be expected.

In the case of *perovskite ferroelectrics*, the spontaneous polarisation is related to the displacement of cations relative to the negatively charged oxygen polyhedra around them [Lines and Glass, 1977, Shirane et al., 1956, Cohen, 1992].

The structure of *ferroelectric polymer* PVDF consists not of ions and atoms connected by ionic or covalent-ionic bonds as in the perovskite crystals, but of polymer chains. The intramolecular bonds of the polymer chains are covalent, whereas the interchain bonds are H-bridges and van-der-Waals bonds.

Ionic displacements are required in the case of the perovskite for the polarisation reversal. In the case of the ferroelectric PVDF polymers, the polymer chain are rotated. The individual jump and rotation processes were expected to be very fast and of the order picoseconds in both materials. Lattice and polarisation responses on such time scales were measured with x-ray and very fast laser pulses in PZT [von Korff Schmising et al., 2007] and the chain rotation in PVDF polymers was estimated to happen of the order of ps [Dvey-Aharon et al., 1980].

However, polarisation reversal times were measured in many different samples, single crystals, ceramics, and thin films of different materials and were found to be orders of magnitude greater than picoseconds (reports on very fast reversals: [Larsen et al., 1991, Li et al., 2004]). From the discussion in section 2.3 about the presence of a potential barrier and the thermally activated process, it is clear that the polarisation reversal cannot occur synchronously in the whole specimen. It happens rather inhomogeneously. Mechanisms controlling the kinetics of such an inhomogeneous polarisation reversal will be discussed in the following subsections.

2.4.2 Switching Model Based on Sideways-Growth and Coalescence of Domains

Fatuzzo reported a model for the polarisation reversal kinetics in ferroelectric crystals [Fatuzzo, 1962]. About a decade later, this model was revisited by Ishibashi and Takagi [Ishibashi and Takagi, 1971, Ishibashi, 1996]. Their model was based on the theory by Kolmogorov [Kolmogorov, 1937] and Avrami [Avrami, 1939, Avrami, 1940, Avrami, 1941] and is frequently called Kolmogorov-Avrami model (KA). Independently from each other, Kolmogorov and Avrami described the kinetics of transformations between two phases. From the metastable (“supercooling”) state of a first order phase transition, the transformation to a more favourable state is hindered by an energy barrier. In the case of polarisation reversal in ferroelectrics, the energy barrier can be associated to the creation of a nucleus of a critical size. As soon as the critical size is reached — or the energy barrier

overcome —, it increases in volume. If there is not a single, but many nuclei, they grow unhindered until they coalesce. Subsequently, they expand further to complete the phase transformation.

Nuclei are expected to appear at electrode-ferroelectric interfaces. These interfaces are assumed to offer favoured conditions for the nucleation of new domains under the application of an electric field. Once they reach the critical size, they become stable and grow forward in the polarisation direction until they reach the opposite interface. Subsequently, the wedge-shaped domains expand sideways.

The KA model is basically a geometrical model, which takes the overlapping of joining domains into account. The fraction of reversed regions, $c_{KA}(t)$ as a function of the elapsed time t reads:

$$c_{KA} = 1 - \exp \left[\left(-\frac{t}{t_0} \right)^n \right], \quad (2.28)$$

where n is an exponent related to the dimensionality of the domain growth, as illustrated in figure 2.22. The time parameter t_0 is of the order of the time at which the first neighbouring nuclei coalesce and the polarisation reversal decelerates. The scenario discussed in the preceding paragraph corresponds to $n = 2$.

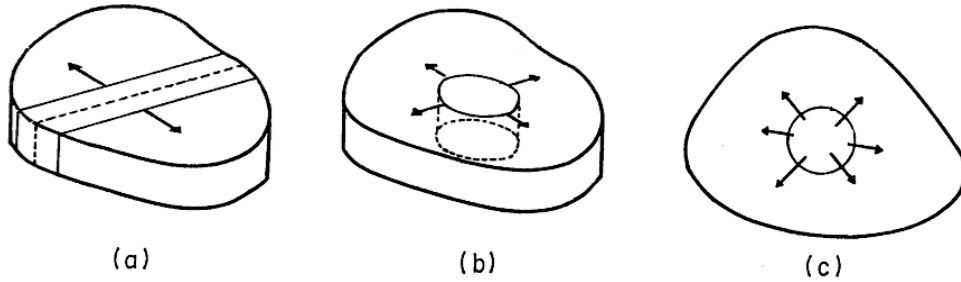


Figure 2.22: The one (a), two (b), and three (c) dimensional cases of the reversed domain shape and domain wall growth as explained in the original illustration in reference [Ishibashi and Takagi, 1971].

The number of appearing nuclei per unit length or area, respectively, and per unit time can be described by the nucleation probability $J(\tau)$ at a time τ . Two nucleation scenarios are usually distinguished.

Continuous nucleation, which corresponds to a case with a constant nucleation rate $J(\tau) = R$. The exponent is in this case $n = d + 1$ in equation (2.28), with the dimensionality d .

Instantaneous nucleation, in which the nucleation is δ -function-distributed and takes place only at $t = 0$. The exponent is here $n = d$.

The scenario with constant-rate nucleation was called the α -model after Kolmogorov. It can be associated with a *thermo-activated nucleation*. The β -model refers to the step-like nucleation and can be associated with a *cold-field nucleation*; it describes thus the immediate growth of the nuclei to the critical size as soon as the field is applied.

In a real system and due to the activation process, one can expect some waiting time until a nucleus of critical size appears. A model taking into account this issue was developed by Fatuzzo [Fatuzzo, 1962].

First, he derived a nucleation rate R as:

$$R = \frac{n_0}{\tau_0} \exp \left[-\frac{t}{\tau_0} \right] , \quad (2.29)$$

where n_0 and τ_0 represent the density of possible nucleation sites and the average waiting time for nucleation, respectively. He obtained for the two dimensional case the normalised switching polarisation $c(t)$ with $m = t/\tau_0$:

$$c(t) = 1 - \exp \left[-\left(\frac{\tau_0}{t_0} \right)^2 2 \left(\frac{m^2}{2} - m + 1 - e^{-m} \right) \right] . \quad (2.30)$$

Analysis of Fatuzzo's equation reveals that it describes the cross-over between the two limiting scenarios of the KA-model in equation (2.28):

- for $t \ll \tau_0$: corresponding to the α -model with the exponent $n = 3$,
- for $t \gg \tau_0$: corresponding to the β -model with the exponent $n = 2$.

If the electric field is increased, domain walls move faster to reverse the polarisation, and the switching curves shift to shorter times, as illustrated in figure 2.23(c) for the Fatuzzo model (dashed lines).

The slope of the switching curves is related to the exponent n in the KA model as shown in figure 2.23(a). A broader distribution of nucleation times is associated with an increase of the parameter τ_0 in the Fatuzzo model. The switching curve slope gets consequently smaller upon an increase of τ as illustrated in figure 2.23(b).

Both models are however oversimplified. The domain wall velocity is assumed to be constant, which is in general not true. The domain motion velocity may vary as a function of the local boundary curvature of the domain wall, defects, trapped charges, or other lattice inhomogeneities.

Despite the fact that the Fatuzzo or KA models are in good agreement with the switching kinetics observed in a number of single crystals [Lohse et al., 2001] and thin epitaxial films [Scott et al., 1989, So et al., 2005], they were not applicable to certain ferroelectric materials like polycrystalline thin films. A more appropriate model for polycrystalline films is discussed in section 2.4.4.

Even if the polarisation reversal in simple ferroelectrics¹⁰ is quite well understood on a phenomenological level, there is only limited understanding on a microscopic scale, i.e. interaction with dislocations, trapped charges, preferred nucleation sites etc. This limited knowledge is mainly due to the difficulties for its experimental investigation.

2.4.3 Polarisation Reversal in Thin Ferroelectric Films

Ferroelectricity was also observed in thin films (e.g. [Tomashpolski et al., 1974]). However, the polarisation hysteresis loops often differ in terms of their tilt and larger width. The

¹⁰'Simple ferroelectrics', in this context refers to single crystals with simple structures and to some extent epitaxial films.

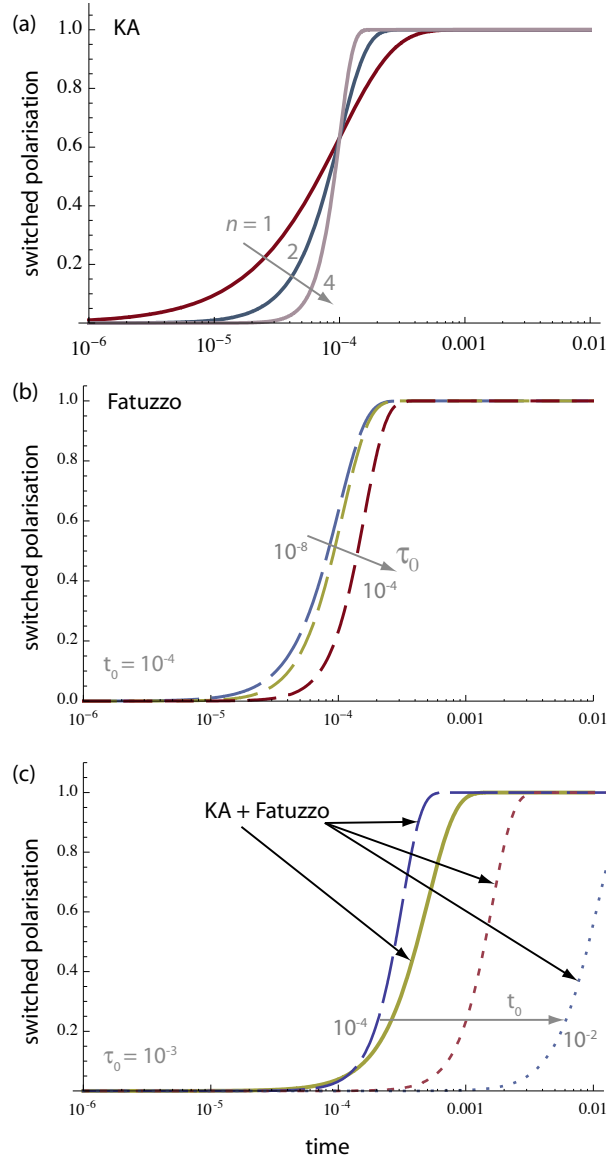


Figure 2.23: Illustration of the parameter influence and comparison of the Kolmogorov-Avrami (KA) and the Fatuzzo model: (a) KA, eq. (2.28), varying n ; (b) Fatuzzo, eq. (2.30), varying τ_0 ; (c) KA with $n = 2$ and Fatuzzo, varying t_0

loop width, characterised by the coercive field, may be ten times greater in thin films than in ceramic samples of the same composition. The loop tilt is usually more pronounced in thin films (see figure 2.24).

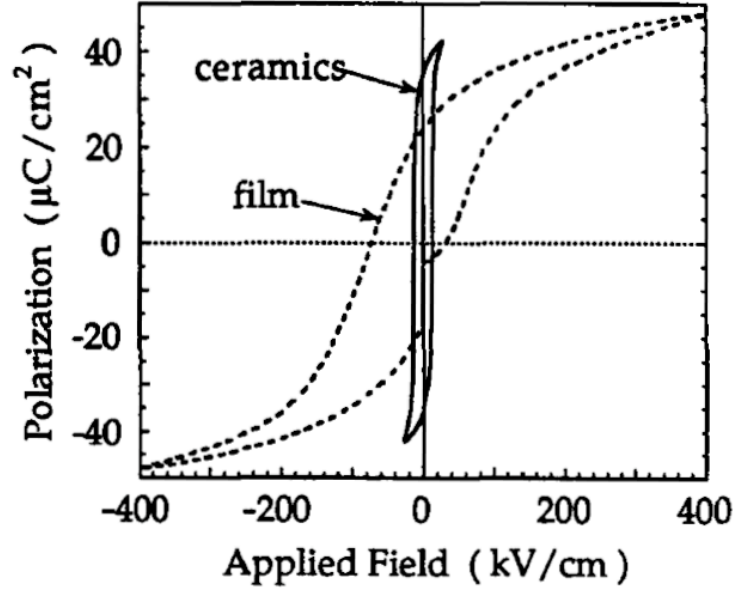


Figure 2.24: Example of loops for Nb-doped PZT for a 500 μm thick ceramics sample (2% Nb) and a 0.5 μm thick film (1% Nb) [Tagantsev, 1996].

What are the origins of this “size effects”?

Upon reduction of one dimension, the depolarisation field can be increased greatly when the polarisation is in the direction of the film thickness. Interface effects on the boundary of the ferroelectric become very important. Among them, one can mention passive non-ferroelectric layers, roughness effects, and electronic junction phenomena including depletion and barriers. Interface-related phenomena in ferroelectrics are known to be difficult to understand and to deal with [Murali, 2007]. Nevertheless, their understanding and control is crucial for high density storage devices based on ferroelectrics.

2.4.4 Polarisation Reversal in Thin Films

The polarisation reversal in thin films can be different from the reported scenario in the bulk with generally a sideways-growth limited polarisation reversal. In this context, experimental data on switching kinetics in ferroelectric thin films suggest that all three scenarios for a rate-limiting step may occur: domain nucleation [Tagantsev et al., 2002a], forward growth of elongated domains [Hong and Setter, 2002], [Hong and Setter, 2002], or sideways growth [Fu et al., 2002] may essentially control the switching rate. These conclusions were based on microscopic studies of thin PZT films.

Nucleation-Limited Switching Model

It has been reported experimentally [Lohse et al., 2001] that the polarisation reversal kinetics in polycrystalline thin films cannot be explained by the classical theories, namely by the Fatuzzo and the Kolmogorov-Avrami model.

In the case of polycrystalline thin films, the polarisation reversal can be expected to occur independently in different regions of the film. Such a scenario cannot be described in the classical Kolmogorov-Avrami and Fatuzzo model (see section 2.4.2). They consider only the geometrical overlapping of neighbouring domains in a homogeneous medium.

For the polycrystalline thin films, we consider a model of individual regions with a broad distribution of nucleation times. Under the assumption that the *waiting time for nucleation* is longer than the time needed for the sideways or forward growth of the nuclei through the individual regions, the polarisation reversal kinetics are determined by the waiting time statistics of the ensemble of independently switching regions. Consequently, each region needs its own nucleation centre.

Tagantsev et al. have developed such a nucleation-limited switching (NLS) model, which takes into account a broad distribution of nucleation times [Tagantsev et al., 2002a]. The fraction of the reverse polarisation $c(t)$ can then be expressed as in equation (2.31):

$$c(t) = \begin{cases} \Gamma h \left\{ \frac{\pi}{2} - \arctan \left[\frac{1}{\Gamma} \log \left(\frac{t_1}{t} \right) \right] \right\} & \text{for } t < t_1 \\ \Gamma h \left\{ \frac{\pi}{2} + \frac{1}{\Gamma} \log \left(\frac{t}{t_1} \right) \right\} & \text{for } t_1 < t < t_2 \\ \Gamma h \left\{ \frac{\pi}{2} + \frac{1}{\Gamma} \log \left(\frac{t_2}{t_1} \right) + \arctan \left[\frac{1}{\Gamma} \log \left(\frac{t}{t_2} \right) \right] \right\} & \text{for } t_2 < t. \end{cases} \quad (2.31)$$

The parameters Γ , t_1 , and t_2 define the distribution function of the waiting times, which is constant between the times t_1 and t_2 and has tails characterised by a quadratic decay controlled by Γ below t_1 and above t_2 . The parameter $h = [\log(t_2/t_1) + \Gamma\pi]^{-1}$ is used to normalise the distribution function.

Switching curves from the KA model (a) are compared to those of the NLS model for a variable parameter t_1 (b) and t_2 (c) in figure 2.25.

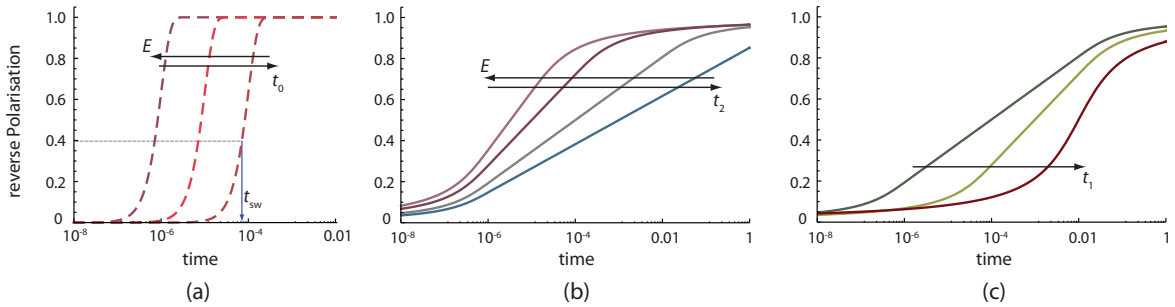


Figure 2.25: Exemplary sets of switching curves from the Kolmogorov-Avrami (a) and the nucleation-limited switching (b,c) model. The parameters were varied as follows $t_0 = 10^{-6}, 10^{-5}, 10^{-4}$ and $n = 2$ in (a), $t_1 = 10^{-6}$ s and $t_2 = 10^{-5}, 10^{-4}, 10^{-2}, 1$ s in (b), and $t_1 = 10^{-6}, 10^{-4}, 10^{-2}$ s and $t_2 = 10^{-2}$ s in (c); cp. equations (2.28) and (2.31) with $\Gamma = 0.8$.

The figures 2.25(b,c) illustrate that the width of the nucleation waiting time distribution in the NLS model is directly related to the polarisation reversal duration. The polarisation reversal process can therefore stretch over several orders of magnitude in time

with a corresponding waiting time distribution. The limits t_1 and t_2 of the waiting time distribution mark approximately the range of an increased slope, in which most of the polarisation reverses.

The switching curves resulting from the KA model in figure 2.25(a) for $n = 2$ are in contrast very steep and the polarisation reversal stretches over approximately one order of magnitude in time only.

The switching time, t_{sw} , is commonly defined as the maximum of the derivative $\partial P_{\text{sw}}/\partial t$ of the switching curve, which corresponds to a maximum in the switching current and coincides approximately with half of the switchable polarisation in most of the cases. The exact solution for the switching time is $t_{\text{sw}} = t_0 \left(\frac{n-1}{n}\right)^{1/n}$ for the general KA model with exponent n and the parameter in the KA model t_0 according to equation (2.28). The switching time t_{sw} is indicated for the third curve in figure 2.25(a).

Upon an increase of the voltage, the parameter t_0 decreases and a simple shift of the curves towards shorter switching times in the KA model occurs. In the NLS model, however, it has been shown [Tagantsev et al., 2002a] that a voltage change mainly acts on the parameter t_2 according to an exponential law as shown in equation (2.32).

$$t_2 = \tau_0 \exp \left[\frac{E_0}{E} \right]^m \quad (2.32)$$

τ_0 represents the waiting time at an infinite applied field and can be related to the soft mode frequency (in PZT: $\tau_0 \approx 10^{-13}$ s), E_0 is an activation field ($< E_{\text{c,th}}$), and m an exponent, which was found to be close to 1.5. Due to the strong dependence of t_2 on the applied field, the slope changes in the NLS model upon a field variation as shown in figure 2.25(b).

Hence, we can state that the polarisation behaviour represented in the switching curves is fundamentally different for the KA model with a simple time shift and the NLS model with a significant slope change for applied field variations.

With more adjustable parameters in the NLS than in the KA model, it can be expected that the fit to experimental data is better. Assuming a waiting time distribution as described, the parameters Γ , t_1 , and t_2 are free parameters, one more than in the KA model (t_0 , and in a very limited range the exponent n).

Nevertheless, the NLS model provides a valid idea of the influence of a statistically distributed waiting time on the polarisation reversal in the stated context as could be shown experimentally. The NLS model was successfully applied to thin polycrystalline PZT films [Tagantsev et al., 2002a, Stolichnov et al., 2003, Song et al., 2005]. Microscopical studies of polycrystalline films by PFM further revealed a region-by-region switching process [Stolichnov et al., 2005, Gruverman et al., 2005]. This is a manifestation of the importance of individual regions for the polarisation reversal in polycrystalline films and is an indication that the kinetics may in fact be governed by the statistics of the waiting time for nucleation for the individual regions.

2.5 Polarisation Reversal in Ferroelectric Polymers

2.5.1 Rotation of the Molecular Chain

The characteristic feature of ferroelectrics, the polarisation reversal, can be understood as a molecular chain rotation in the PVDF polymers, in which the polarisation is normal

to the main axis of the macromolecules (cf. figures 2.8 and 2.9).

In a first theory of molecular rotations in PVDF [Aslaksen, 1972], rotational increments in a chain of 180° were proposed. Further theoretical studies disagreed with such steps [Dvey-Aharon et al., 1980]. A process involving a thermally activated kink formation at the surface of a crystalline lamellae, and subsequent motion through it, was suggested. Dvey-Aharon et al. calculated that the formation of kinks was the slow, limiting step for the molecular reorientation, whereas the kink motion was fast. In the case of 180° rotational increments, the required energy for the kink formation would result in unrealistically high waiting times. A mechanism was suggested, which involves 60° increments. The formation energy for kinks with such rotational increments calculated in their model was reduced and the resulting waiting time for a kink formation met the experimental observations for the polarisation reversal more accurately.

The potential energy of a molecule close to a 60° domain boundary — like the molecule 1 illustrated in figure 2.27 — was calculated as a function of the rotation angle θ around the chain axis.

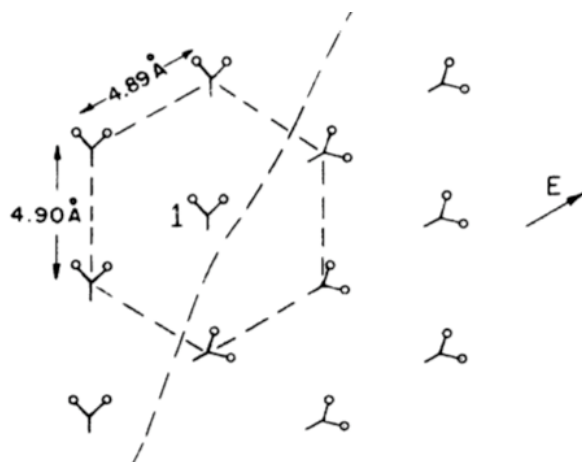


Figure 2.26: PVDF molecules shown across a 60° domain boundary (from [Dvey-Aharon et al., 1980])

The results according to Dvey-Aharon et al. [Dvey-Aharon et al., 1980] are shown in figure 2.26 with a global minimum at 60° and a local minimum at 30° . The energy minima can be related to the rotational steps happening during the polarisation reversal. The local minimum at 30° may help to form kinks. It allows sections of the chain to be trapped in a 30° position, which can then rotate independently to 60° .

Further reduction of the activation energy towards more realistic values was suggested. Reneker and Mazur proposed a model, in which several chains rotate synchronously [Reneker and Mazur, 1985]. This behaviour can be seen as a moving twist boundary across several polymer chains. They claimed that their model described the energetic and kinetic aspect of the polarisation reversal under realistic experimental conditions.

Chain rotations are however only one part of the complex polarisation reversal of polymers. The complex structure with crystalline lamellae in an amorphous matrix makes the process harder to understand and to investigate. Based on three structural levels of these polymers, namely the atom, chain and lamellae arrangement, Furukawa [Furukawa, 1989] described the polarisation reversal in ferroelectrics by three stages:

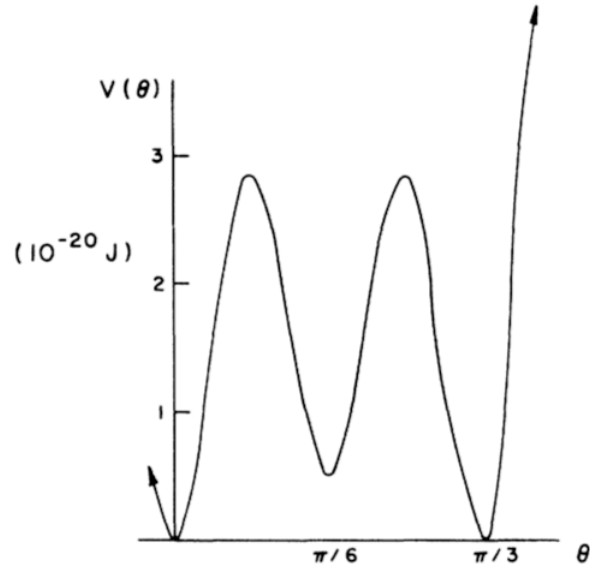


Figure 2.27: The potential energy plotted as a function of the rotation angle for the PVDF molecule 1 as shown in figure 2.26 (from [Dvey-Aharon et al., 1980]). Global and local minima are at 60° and 30° , respectively.

- (i) the first, intramolecular stage involves the reversal of a single molecular chain [figure 2.28(A)] as described by Dvey-Aharon et al.,
- (ii) the second stage deals with the expansion of the rotated chains in a lamella, and
- (iii) the third stage concerns the totality of the film with the interactions between the lamella and the matrix in between.

The first process (i) is very fast (a chain rotation propagates along the chain within 50 ps along 10 nm at room temperature [Dvey-Aharon et al., 1980]) and hence, is not the limiting stage for the polarisation reversal in ferroelectrics.

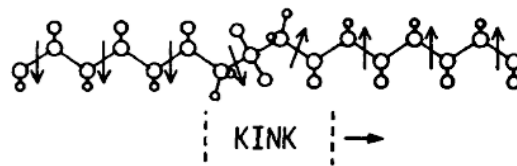
The second process (ii) agrees with a nucleation and growth scenario similar to the one described for perovskite ferroelectrics (cp. section 2.3.1) and is probably the rate-limiting step in the polarisation reversal of PVDF-type ferroelectric polymers because — as suggested by Reneker and Mazur — the reversal does not occur via the rotation of single chains, but several molecules.

Two cases exist for the third process (iii) depicted schematically in the left and right half of figure 2.28(C). The situation on the left with many nuclei and growing domains occurs if the domain expansion is slow compared to the waiting time for nucleation. If the domain growth is fast and the nucleation rate slow, a crystalline region reverses its polarisation as soon as a single nucleus appears. The waiting time for nucleation then dominates the polarisation reversal process in the film.

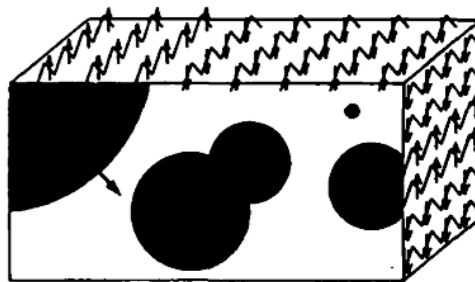
Furukawa observed that the switching current follows the Merz law and concluded therefore that it is probably process (ii) which dominated the polarisation reversal due to its similarity to the Merz nucleation and growth mechanism.

There are still many open questions about these processes and especially the role of the amorphous matrix. Does it play an important role in any of the described polarisation reversal processes? The difficulty to get experimental evidence on a microscopic level does

(A) MOLECULE



(B) LAMELLA



(C) FILM

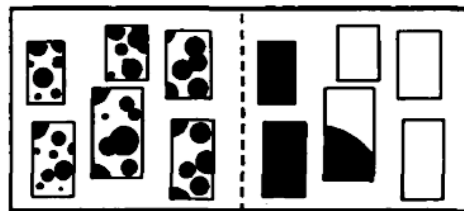


Figure 2.28: Polarisation reversal in PVDF comprises three stages according to Furukawa [Furukawa, 1989].

not allow us to answer this question yet. Microscopic techniques as PFM (cp. chapter 3 and 5) may, however, give some more insight into this problem.

The described mechanisms are closely related to the kinetics of the polarisation reversal. The kinetics is in general highly relevant for possible applications. The following section gives an overview over this field.

2.5.2 Kinetics of the Polarisation Reversal in PVDF

The polarisation reversal kinetics discussion is divided into three subsections. The division is done according to the thickness of the experimentally studied samples, because different aspects are important depending on the sample dimensions.

Bulk Polymers and Thick Films

In the beginning of intensive studies on ferroelectric polymers during the 1970s, the polarisation reversal was found to be rather slow, i.e. from tens of seconds up to days. Buchman studied the switching currents at a temperature above 110°C [Buchman, 1973]. He found, interestingly, current vs. time curves in the shape as reported by Merz on BaTiO₃ [Merz, 1956], which are characterised by a first peak and a subsequent maximum. Even an electric field and temperature dependence of the switching time according to an exponential law was found. Nevertheless, the switching times were of the order of tens of seconds and thus substantially higher than in BaTiO₃ (in the range of microseconds). Other experiments at room temperature also showed switching times of several seconds [Kepler, 1995].

A new impulse was brought by the theoretical paper on the polarisation reversal¹¹ that predicted orders of magnitude smaller switching times in PVDF [Dvey-Aharon et al., 1980]. With the calculated switching time of a single chain of 50 ps (at a temperature of 373 K), the switching time of a sample consisting of crystallites with about 10⁷ chains was estimated. Under the assumption that the polymer chains rotate sequentially, they predicted a switching time of the order of 1 ms. Compared to earlier expectations and experimental reports, this was much faster and seemed very unrealistic.

However, after the publication of the work of Dvey-Aharon et al., the experimental work caught up with the theoretical prediction and demonstrated that the polarisation reversal in PVDF could in fact occur on time scales as fast as those proposed by Dvey-Aharon.

Furukawa and Johnson were the first who demonstrated switching times of 4 μ s at 393 K. They used much higher fields of 2000 kV/cm compared to previous experiments in their 7 μ m thick, oriented films of PVDF [Furukawa and Johnson, 1981]. They investigated further the temperature and field dependence of the switching time and found an exponential dependence on the inverse electric field as illustrated in figure 2.29 and a significant deceleration of the polarisation reversal for a decreasing temperature $t_{sw} \propto 1/T$.

These results were a big step forward for experimentalists as well as theoreticians. The model suggested by Dvey-Aharon was thereafter revised by Clark and Taylor with a modified kink formation energy [Clark and Taylor, 1982] (see [Kepler, 1995], p. 199). Their model could describe the polarisation reversal time behaviour from Furukawa and Johnson, including the linear switching time variation with the inverse of the temperature.

¹¹The authors termed the polarisation reversal in that paper ‘poling’.

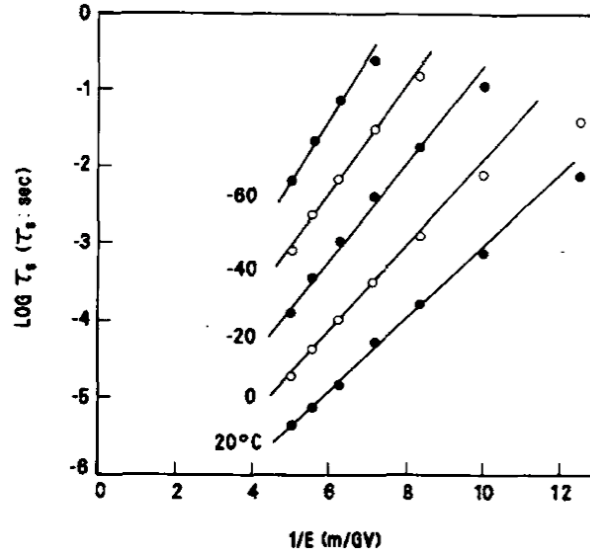


Figure 2.29: Switching time as a function of the inverse field and for various temperature in PVDF, taken from Furukawa and Johnson [Furukawa and Johnson, 1981].

The experimental data on the switching time as a function of field was described by the exponential law [equation (2.24) in section 2.3.2] that was found in the classical the perovskite ferroelectrics for the low-field regime. Furukawa and Johnson could however not exclude the power law — used for the high-field regime in BaTiO₃ [equation (2.25)] — as a good description of the polarisation reversal kinetics in PVDF due to the limited measurement range [Furukawa and Johnson, 1981].

Polarisation reversal in BaTiO₃ and PVDF are compared in terms of the switching parameters α and n in table 2.2. The parameter α in the exponential law can be associated with an activation field [equation (2.24)]. n is the exponent in the power law [equation (2.25)].

From the larger values in PVDF, it is clear that the polarisation reversal in PVDF requires much greater applied electric fields for comparable polarisation reversal times. The origin for the difference in the activation fields was, however, unclear. The coercive field differs also by at least three orders of magnitude between PVDF and BaTiO₃ (MV/cm compared to kV/cm).

Table 2.2: Comparison of the parameters for exponential and power law field behaviour [cf. equation (2.24)] of the switching time for PVDF and BaTiO₃ at room temperature [Furukawa and Johnson, 1981, Merz, 1954, Stadler and Zachmanidis, 1963].

Material	exponential law α [MV/m] (low field range)	power law n (high field range)
PVDF	$1.1 \cdot 10^3$	8
BaTiO ₃	1.6	1.4 – 1.5

Furukawa et al. extended the measurements done on PVDF thick films to similar

VDF/TrFE (65/35) copolymer samples with a thickness of $20\text{ }\mu\text{m}$ [Furukawa et al., 1984]. The results essentially agreed with the observed behaviour in the uniaxially drawn, highly crystalline PVDF samples. The switching time could be described by the Merz exponential law according to equation (2.24) with an activation field α ranging from 0.8 GV/m (at 80°C) to 1.8 GV/m (at -80°C) and $E_\alpha \propto 1/T$. The switching transient after a voltage pulse was modelled by the following equation (2.33):

$$D(t) = \varepsilon E + 2P_r \left[1 - e^{-(t/t_s)^\gamma} \right] + \sigma E t . \quad (2.33)$$

The permittivity is represented here by ε , t_s stands for the switching time, the exponent γ determines the shape, specifically the slope of the switching curve [cp. to figure 2.23(a)], and σ represents the dc conductivity. The last term accounts for dc leakage in the film and can be neglected for pulse widths below 100 s [Furukawa, 1989].

The measured switching times for the P(VDF-TrFE) copolymer thick films were very short, i.e. in the order of tens of μs at fields of about 100 MV/m . This proves that fast polarisation reversal in ferroelectric polymers was possible.

Further development of the polarisation reversal model for PVDF strove to integrate the kink propagation model in the theory of polarisation reversal mechanism with nucleation and growth. Such attempts resulted in the conclusion that the problem is too complex to be solved easily [Kepler, 1995], p. 202.

To conclude this section about thick film and bulk PVDF, we can state that the polarisation reversal is surprisingly similar to perovskite ferroelectrics. This concerns the model of nucleation and growth and kinetic models and descriptions. The details of the polarisation reversal are not completely understood in either oxide ferroelectrics or in the polymer ferroelectrics. The model of kink formation and propagation by Dvey-Aharon et al. is almost certainly relevant to the polarisation reversal and probably dominates the kinetics.

Considering the complexity of the polymer ferroelectrics with structural features on the intramolecular, intermolecular, crystallite lamellae, and film level, the predictions from the phenomenological models based on perovskite materials are in surprisingly good agreement with experiments.

Thin Films

Due to large electric fields needed to reverse the polarisation in ferroelectric polymers, there is a particular interest to reduce the film thickness in order to reduce the applied voltage. Along with the down-scaling of the film thickness from thick (several micrometres) to thin films (below about 200 nm) come the necessary change of the material. Films cannot easily be oriented by stretching on a rigid substrate. Since pure PVDF cannot be brought into the desired β -phase without stretching, the copolymer P(VDF-TrFE) is preferred. It crystallises directly in the ferroelectric β -phase from the melt or solution (see section 2.2.3).

Studies on the polarisation reversal in ferroelectric copolymer films can be categorised by their thickness into thin and ultrathin films. Ultrathin films are characterised by a thickness below 60 nm , but usually only several nanometres. They are typically deposited by the Langmuir-Blodgett (LB) technique. Thin films with a thickness of about 60 nm to several hundreds of nanometres are typically spin coated.

Studies on polarisation reversal kinetics of spin-coated thin films with thickness down to 50 nm were undertaken more than 20 years ago [Kimura and Ohigashi, 1986]. They fabricated large area capacitors (5 mm²) with Al electrodes by spin coating a 75/25 VDF/TrFE copolymer in a dimethylformamide solution. A change in the switching kinetics at a thickness of 100 nm was noted. Below this limit, the polarisation reversal was considerably slower than in 850 nm thick films. Kimura and Ohigashi claimed a transition of the polarisation reversal at the critical thickness. Below 100 nm, a linear relation between the inverse switching time and the applied field was observed and associated with a limited domain growth, whereas in thicker films the exponential behaviour between the switching time and the applied field was associated with a nucleation limited switching.

The size effect at about 100 nm was commonly observed with Al electrodes. Al electrodes react more easily with the polymer than Au electrodes [Naber et al., 2004, Furukawa et al., 1985, Nakajima et al., 2005] and may modify the electrode-ferroelectric interface. The observed transition around 100 nm may thus originate rather in interfacial than intrinsic ferroelectric effects. Details are discussed in combination with our own results in chapter 5.

A study of the polarisation reversal in thin copolymer films has recently been published by Furukawa et al. [Furukawa et al., 2006]. VDF/TrFE copolymers with a 75/25-composition were studied under variable thickness, temperature, and electrode materials. In these copolymer films with a thickness between 50 and 380 nm, the switching transient currents could be fitted to the same laws, according to equations (2.33) and (2.24), as for films thicker than 1 μ m in the above cited study [Furukawa, 1989]. The broadening of the switching curves was attributed to a higher relative roughness (compared to the film thickness) [Nakajima et al., 2005].

Annealing conditions and crystallinity, the effect of electrode metals and electrical factors such as pulse trains, and fatigue were further studied

Furukawa et al. found that the grain size (characterised by AFM topography) and the remnant polarisation increased with increasing annealing temperature up to about 140°C. This was explained by the increased crystallinity of the sample [Furukawa et al., 2006].

More experimental and theoretical details on polarisation reversal mechanisms, including kinetics, in thin VDF/TrFE copolymer films are presented and discussed in chapter 5.

Ultrathin Films

Switching studies are rather difficult in ultrathin films, because the films consisting of only a few polymer layers become very leaky. Hysteresis loops were therefore typically measured as pyroelectric hysteresis loops¹², where the problem of leakage through the film can be circumvented in contrast to normal polarisation hysteresis loops. If the charge is measured, a high leakage contribution can conceal the characteristic charge from the polarisation reversal (see section 2.6.1).

Sorokin et al. studied polarisation reversal in LB P(VDF-TrFE) film samples of an intermediate thickness between 36 and 62 nm, i.e. thicker than ultrathin samples, but thinner than typical spun films [Sorokin et al., 2005]. The polarisation state was measured via the pyroelectric effect. Typical switching curves were measured for various voltages and with increasing pulse width. The derivative of such switching curves was assumed to be

¹²In a pyroelectric loop, the charge is measured as a function of heating pulses and a slow driving field similar to piezoelectric loops (see section 2.6.2).

proportional to the distribution of the critical time to switch an independent ferroelectric unit. Following this logic, a very wide critical time distribution was found, which spreads over about three decades on the time scale. The reason for the observed dispersion was unclear. The authors suggested two possibilities:

- (i) The sample inhomogeneity due to grain boundaries and strain may affect the local transition temperature, coercive fields and switching dynamics.
- (ii) Thickness and density variations impact the electric field distribution and thus broadening of the observed switching times.

The most spectacular studies on ultrathin films of the copolymer of VDF and TrFE were concerned with the size limit of ferroelectricity as introduced briefly in section 2.1.8. This issue appeared, when the switching mechanism was investigated in ultrathin LB films of a P(VDF-TrFE) copolymer. Below a certain film thickness of about 30 monolayers (ML), a threshold coercive field was reported, which did not depend on the measurement frequency. Such a behaviour would suggest an intrinsic switching, which is not governed by an activation process, but involves a coherent switching of the dipoles, and consequently a thermodynamic coercive field predicted by the Landau-Ginzburg-Devonshire description (see in section 2.1.2). Such a polarisation reversal would be in contrast to the extrinsic polarisation reversal involving nucleation and growth, in which the coercive field showed in general a frequency dependence. Ducharme et al. released a paper on an intrinsic coercive field in ultrathin copolymers [Ducharme et al., 2000]. The agreement between the theoretical and the experimental value, and the temperature behaviour of the coercive field, was taken as evidence for an intrinsic switching. They reasoned with the thickness (1–100 nm) dependence of the coercive field, which increased with decreasing thickness down to 15 nm and saturated below. This behaviour was interpreted as a transition from extrinsic to intrinsic switching.

Such an interpretation of the results was questioned however, because the switching times are orders of magnitudes too high (1–10 s) and interface and electrode effects may control the observed behaviour [Bratkovsky and Levanyuk, 2001, Naber et al., 2006]. It has to be noted as well that the cited studies were based on samples with Al electrodes.

2.6 Macroscopic Characterisation Methods of the Polarisation Reversal

Standard macroscopic characterisation methods, which have been used to characterise ferroelectric materials for a long time, are introduced briefly in this section. Despite their importance, detailed descriptions in textbooks are limited, e.g. [Lines and Glass, 1977]. Some reviews are available, but they generally focus on results and less on the application and experimental details of the technique — e.g. [Dawber et al., 2005]. We give here an overview over these techniques; more details are specified in the chapters in which the techniques are employed.

2.6.1 Polarisation Hysteresis Loops

One of the simplest and most important characterisation techniques to illustrate ferroelectricity in a material is the hysteresis loop measurement [Lines and Glass, 1977, Rabe et al., 2007]. It shows the polarisation as a function of the electric field for a complete voltage cycle from zero to a maximal positive, then a maximal negative voltage, and back to zero.

The coercive field, $E_c = E(P = 0)$, and remnant polarisation, $P_r = P(E = 0)$, can be extracted from a polarisation loop [Jaffe et al., 1971], p. 35. These values depend on the driving frequency and, at least in some cases, on the poling prehistory of the sample.

The polarisation is determined by the measurement of the switching charge upon the application of a driving voltage. The driving signal is typically a triangular or sinusoidal waveform with frequency between 10 Hz to 1 kHz. We refer to a hysteresis loop as being either positive or negative depending on the initial polarity of the waveform (compare to figure 2.30).

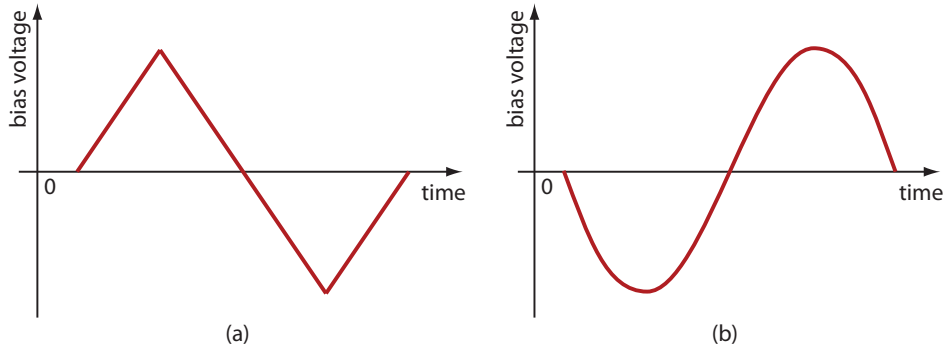


Figure 2.30: Waveforms commonly used as driving voltage for polarisation loop measurements: a triangular form starting with a positive polarity for a “positive” loop (a); and a sinusoidal form starting with a negative polarity for a “negative loop” (b).

The charge measurement was traditionally performed using a so-called Sawyer-Tower loop [Sawyer and Tower, 1930] with the ferroelectric sample and a reference capacitor in series. Nowadays, charge amplifiers are frequently used in the polarisation loop measurement instrumentation. They are advantageous in terms of a greater precision and a larger measurement range. In a Sawyer-Tower circuit, the reference capacitor has to be adjusted to the capacitance of the sample.

Polarisation loops are relatively simple to measure, but the simplicity conceals some dangers. It is possible to measure ferroelectric loop-like characteristics in (non-ferroelectric) leaky non-linear dielectrics. It is therefore crucial to verify that the hysteresis loops exhibit a typical behaviour. The polarisation saturates at high voltages and exhibits retention in ferroelectrics. The latter can be checked by consecutive positive and negative loop measurements.

The leakage contribution to the measured charge can be checked by measuring the polarisation hysteresis loops at different frequencies [Lines and Glass, 1977, Scott, 2008, Miller et al., 1990]. According to equation (2.34), the leakage term is time, and hence, frequency dependent:

$$Q_{\text{meas}} = 2P_{\text{sw}}(E)A_C + \int_0^t \sigma_l E_{\text{app}} d\tau; \quad (2.34)$$

with Q_{meas} , P_{sw} , A_C , σ_l , and E_{app} referring to the measured charge, the switching polarisation, the capacitor area, the leakage “conductivity” of the capacitor, and the applied electric field, respectively.

At low frequencies, the loops are expected to be of a more rounded shape under the influence of a significant non-linear leakage contribution. At high frequencies, the second term in equation (2.34) can be neglected.

Examples of real and deformed polarisation hysteresis loops are depicted in figure 2.31 for samples of PZT, a non-ferroelectric dielectric¹³, epitaxial PZT, and a leaky BaTiO₃ film.

Our measuring system for polarisation hysteresis loops is based on a LabView program, a data acquisition card (DAQ; *National Instruments*, former item name: PCI-MIO-16XE-10, actual name: NI PCI-6030E), and a charge amplifier (*Kistler AG*, type 5011B11). Usually, a voltage pulse of a triangular waveform was generated by the DAQ card. The maximum output of the DAQ card is ± 10 V and the highest sampling rate 100 kHz. The maximum frequency for a loop with 200 measured points was therefore $100'000 \text{ Hz}/200 = 500 \text{ Hz}$. The driving voltage signal was amplified by a wide bandwidth amplifier (*Krohn-Hite Corp.*, model 7602M) if this was needed.

2.6.2 Piezoelectric Loops

The piezoelectric effect was discussed in section 2.1.7. From equation (2.15) follows that a ferroelectric sample shows an expansion or contraction as a linear function of the applied field and with respect to the polarisation and crystallographic orientations.

Equation (2.19) shows further that the piezoelectric coefficient is proportional to the permittivity and the polarisation. A small driving ac field thus induces a periodic displacement of the sample surface due to the converse piezoelectric effect. This small ac response can be sensed by an interferometer or the piezoelectric force microscope (PFM). With an additional bias voltage of a triangular or sinusoidal waveform, as illustrated in figure 2.30, a piezoelectric loop can be measured. Equation (2.19) shows that at a change of sign of the polarisation induces a change of sign of the piezoelectric coefficient and thus the piezoelectric response. This is however only true at $E = 0$ or in a single domain case. In general the piezoelectric coefficient changes the sign already before the polarisation due to domain contributions [Tagantsev et al., 2004a]. More details on the shape of

¹³The sample characterised by the curve (b) in figure 2.31 was provided by T. Yamada.

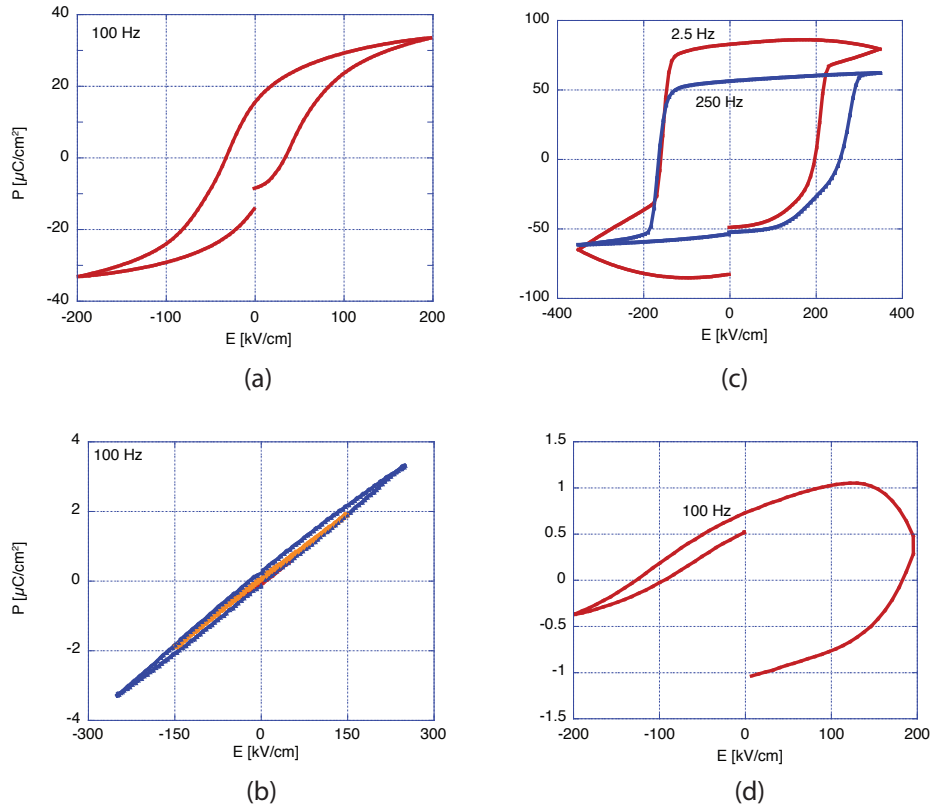


Figure 2.31: Examples of polarisation P – E loops of several materials: (a) a typical ferroelectric, (b) a non-ferroelectric dielectric (CeO-BaTiO₃ composite), (c) a ferroelectric epitaxial PZT 20:80 thin film, sputtered on Nb:STO, which is leaky at a low frequency (2.5 Hz), and a leaky epitaxial BaTiO₃ thin film measured at 100 Hz.

piezoelectric loops can be found in this reference.

Piezoelectric loops with PFM

During the application of a small driving ac field across the sample, the piezoelectric response is sensed microscopically in this technique (see also section 3.1). The piezoelectric response is recorded either under the applied bias voltage or between the bias steps at zero bias. The bias voltage waveforms, shown in figure 2.30, is therefore modified. It is applied in voltage steps, as illustrated in figure 2.32. The superimposed small ac driving field is continuously applied. The piezoelectric response can then be measured during or after each voltage step.

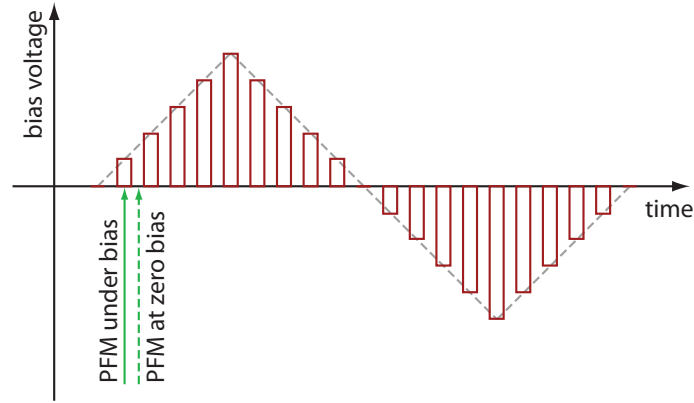


Figure 2.32: The scheme showing how the bias voltage is applied for a “positive” (initially positive voltages) piezoelectric loop, the number of steps is generally higher than shown here. The piezoelectric response is then detected *under bias* or *at zero bias* for each voltage step.

In the piezoelectric loop mode, the cantilever is scanning only one line instead of an area. In principle, a loop can be measured for each point of the scanned line. The resolution is determined by the number of points (typically 256 points per line) and the length of the scanned line. On one hand, piezoelectric loops can be recorded with a high spatial resolution (e.g. every about 4 nm in the given example) by scanning a very short line (e.g. of a length of 1 μm). On the other hand, choosing appropriate lock-in amplifier settings, i.e. a large time constant, the piezoelectric response signal can be averaged across several points on the scanned line. This corresponds then to a more “macroscopic” loop.

For quantitative measurements of the piezoelectric coefficients, the PFM has to be calibrated. This is typically done by comparing piezoelectric loops from PFM measurements to a piezoelectric loop measured by interferometry.

Piezoelectric Loops with Interferometry

The displacement of the surface of a ferroelectric thin film, which is of the order of 10^{-1} to 10^{-2} Å for driving fields below the coercive field, is most precisely detected by an interferometer. In this technique, the phase shift of a laser beam reflected from an oscillating surface — via the converse piezoelectric effect and an ac field — is measured using lock-in technique. It was found that a single beam interferometer is insufficient, because it does

not take into account sample bending. Since the bending effect may dominate the pure piezoelectric response in thin films, a dual beam, the so-called Mach-Zender interferometer was suggested [Zhang et al., 1989, Pan and Cross, 1989, Kholkin et al., 1996] for the quantification of the piezoelectric effect. With a laser beam reflected from the front and backside of the sample, the piezoelectric response can be distinguished clearly from the bending contribution.

Microscopic investigations of the piezoelectric response to a small ac perturbation is limited by the laser beam diameter to a lateral resolution of tens of micrometers. Interferometry can however be used to calibrate the PFM response. This allows quantitative analysis of PFM measurements.

This technique was used in this thesis for the characterisation of reference epitaxial PZT thin films and for PFM calibration. An example¹⁴ of a capacitor with a thickness of 650 nm and a top electrode with an area of $400 \times 800 \mu\text{m}^2$ is given in figure 2.33.

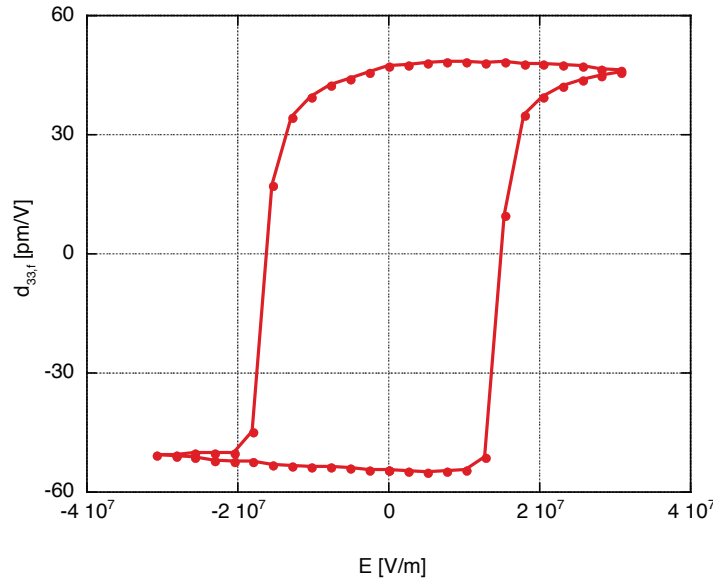


Figure 2.33: A piezoelectric loop of an epitaxial PZT sample (with a “tetragonal” Zr:Ti ratio of 20 : 80, sputter-deposited on a Nb-doped STO substrate) measured with a Mach-Zender interferometer.

2.6.3 Pulse Switching Technique

Polarisation loops provide only limited information about the polarisation reversal kinetics. The shape of the loop depends of the driving voltage frequency, but it is affected by leakage and passive layers as well, as demonstrated in a couple of publications [Tagantsev et al., 1995].

Hence, the switching time, i.e. the time required to reverse the polarisation, cannot be determined unambiguously from polarisation loops. Already Merz realised that the characterisation of transient currents after the application of voltage pulses provided more clarity and insight into the polarisation reversal kinetics [Merz, 1954].

¹⁴The sample was measured by Janine Conde.

A more sophisticated technique using voltage pulses was described by Lohse, Grossmann et al. [Lohse et al., 2001, Grossmann et al., 2000]. They suggested applying a series of three switching pulses of alternating polarity, with a first pulse to pole the sample, a second to reverse the polarisation as a function of the pulse width or voltage, and a third to measure the switching effect of the second pulse.

Switching curve refers to the switching polarisation measured as a function of the pulse width of pulse voltage. A more detailed discussion of the technique can be found in chapter 5, in which ferroelectric polymer samples were studied using this technique.

2.6.4 Dielectric Characterisation

An important characteristic of dielectric samples is the dielectric constant or permittivity (see section 2.1.5). The capacitance is experimentally measured as a function of frequency, temperature, or bias voltage. The dielectric constant ε can be calculated with the relation for parallel plate capacitors, $C = \varepsilon_0 \varepsilon A / t$, where A and t are the area of an electrode and the thickness of the film between the two electrodes for the given dimensions of the capacitor.

The capacitance is probed by a small ac electric field applied to the sample. An *LCR* meter analyses the impedance and gives the capacitive response. In our work, we used a precision *LCR* meter (*Hewlett Packard*, 4284A) for the characterisation.

If the small ac field is superposed to a bias voltage of a triangular waveform as given in figure 2.30, a dielectric polarisation loop can be measured. An example of such a so-called “butterfly” loop is shown in figure 2.34.

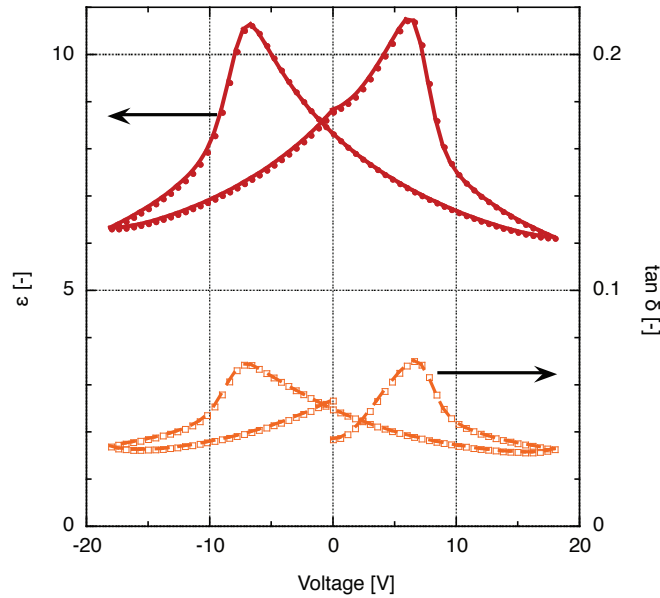


Figure 2.34: Examples of an dielectric constant vs. bias voltage loop of a ferroelectric P(VDF-TrFE) copolymer. The dielectric constant was probed at a frequency of 10 kHz and with a small ac amplitude of 1 V at room temperature. The loss tangent is shown on the second y -axis.

By the application of a bias field opposite to the polarisation direction, the thermodynamic potential gets shallower, which is associated with an increase of the dielectric

response to the small driving field. At a high enough (coercive) field, the polarisation reverses and a further increase of the field, now in the direction of the polarisation, has a “hardening” effect. The potential well gets steeper and the dielectric constant decreases.

Additional effects from extrinsic contributions, as discussed in section 2.1.6, can be seen. At the coercive field, the ferroelectric is in a multidomain state and the maximum permittivity can be increased beyond its intrinsic value via reversible domain wall responses.

Dielectric constant measurements as a function of temperature in order to find phase transitions are of interest. Above the Curie point, Curie-Weiss behaviour [equation (2.12)] can typically be observed in such measurements.

2.7 Domain Imaging Methods

Since the discovery of ferroelectricity in 1921, the methods to detect domains have improved in terms of sensitivity and resolution. Kay and Rhodes were the first to study domains, in this case 90° domains, in BaTiO_3 with an optical microscope and x-ray diffraction [Kay and Rhodes, 1947]. Techniques were subsequently found to make 180° domains visible in BaTiO_3 [Matthias and von Hippel, 1948], and in Rochelle Salt [Forsbergh, 1949, Furuichi and Mitsui, 1950].

Further traditional methods mainly used the fact that the surfaces in ferroelectric materials are charged as a consequence of the spontaneous polarisation. The sign of the charge at the surface depends on the orientation of the polarisation. To visualise the charge and thus the domains, a multitude of techniques [Soergel, 2005] were developed.

2.7.1 Surface Decoration Methods

In the surface decoration methods, polar or charged particles (powders, liquid crystals, droplets) interact with the surface charges and arrange themselves in a way that reproduces the domain pattern. The handling of the powders and the limited resolution impeded popularity of these methods.

2.7.2 Selective Etching Methods

Etching methods to reveal the domain structure were more common, even though they are destructive. Selective or differential etching is based on the difference of the etching rate for positively and negatively charged faces. In BaTiO_3 , hydrofluoric acid etches the positive titanium side much faster than the negative oxygen side. However, it is not a general rule for any ferroelectric crystal that the positive side is etched faster. The etched patterns can be observed by different means:

- Optical microscope
- Scanning electron microscope, for higher resolution
- Imaging the topography with an atomic force microscope (AFM)

2.7.3 Optical Methods

Purely optical methods were used to directly study domain structures as well. A transparent crystal is placed between crossed polarisers. The different refractive index of a - and c -domains yields contrast in the image. Anti-parallel c -domains can only be seen if the crystal is strained, e.g. by an electric field. The lateral resolution is not better than several micrometres, as can be seen in the images of [Pang and Baba-Kishi, 1998]. Merz and Fatuzzo studied the switching mechanisms in ferroelectric crystals by optical techniques, which they combined with etching [Merz, 1954, Fatuzzo and Merz, 1959].

2.7.4 Electron Microscopy

Scanning electron microscopes (SEM) offer a higher resolution than provided by optical microscopes. Electrons that are sensitive to charged surfaces and due to the oppositely

charged surfaces between domains, a domain contrast in SEM images can be observed. Nevertheless, the dielectric nature of ferroelectric materials makes it difficult to avoid charging of the samples under the electron beam. It is thus a complex task to get stable SEM images of the domain structure. Some improvements were reported using environmental scanning electron microscopes (ESEM), which work at pressures 10'000 times higher than SEM [Zhu and Cao, 1997].

With the *transmission electron microscope* (TEM), a static domain structure can be imaged with a very high resolution. A number of different TEM modes are possible for domain imaging (high resolution, holographic imaging, etc.) [Soergel, 2005]. The preparation of a sample thin enough to allow the transmission of electrons is time-consuming and destructive for the sample. Dynamic observation of the switching process is not trivial, since switching of the sample by an applied electric field to the sample is perturbed by the electron beam.

2.7.5 Scanning Probe Microscopy

The invention of the scanning tunnelling microscope (STM) [Binnig and Rohrer, 1982] gave rise to the invention of a large variety of scanning probe microscopes (SPM). Although most of the techniques are well established, research and development of scanning probe methods to reach higher performance in terms of time, resolution, and functionality continues (e.g. [Kemiktarak et al., 2007]).

All scanning probe techniques have the same principle: A small probe is scanned over a sample surface. During scanning, a certain interaction between the sample surface and the tip is monitored. The signal from the interaction is processed and an image is produced, which maps the local properties. A requirement for this technique is the possibility of very precise displacements between the sample and the small probe. Piezoelectric elements enabled the operation with a sub-nanometre resolution.

One of the most widely used scanning probe techniques, *atomic force microscopy* (AFM), was developed [Binnig et al., 1986] soon after the STM. In contrast to the STM, in which the tunnelling current is a measure of the spacing between a conductive sample and a sharp tip, the forces between the probe and the sample are recorded via the bending of the cantilever in AFM. It is therefore more versatile — without being limited to conductive samples — and appropriate to characterise sample topographies.

Atomic Force Microscopy

There are various modes to characterise the surface of a sample using an AFM [Sarid, 1994]. We introduce them here in some more detail, because they are relevant for the methods (related to PFM) developed in this thesis.

Contact Mode In this mode, the tip is in contact with the sample surface. Two methods can be distinguished: a *constant force* and a *constant height* method.

In the *constant force mode*, the AFM probe is scanned across the surface and it is deflected as it moves over the surface ridges and grooves. The tip is kept at a constant deflection, i.e. with a constant force according to Hooke's law, and thus at a constant distance from the sample surface (on a chemically homogeneous surface). Small deflection changes of the cantilever due to ridges and grooves on the sample are corrected by height adjustments z of the sample stage. The z adjustment data is then displayed for each probed dot in the scanned (x,y) plane.

In the *constant height* or *variable deflection* mode, the height z is not adjusted and the topography is represented by the cantilever deflection. This method does not need a sophisticated feedback loop, but is only feasible on flat surfaces.

The contact mode involves a hard contact between the tip and the sample. Cantilevers with lower stiffness, i.e. spring constants of at most a couple of N/m, are therefore preferred.

The resolution of this technique can be improved in a vacuum chamber. In vacuum conditions no water layer covers the sample surface as in standard AFM.

The AFM is used in contact mode for the piezoelectric force microscopy technique.

Lateral Force Microscopy measures frictional forces. The tip has therefore to be in contact with the sample surface. By measuring the torsion of the cantilever, rather than its deflection, one can qualitatively determine regions of higher and lower friction in the scanned area. Topological features interfere with the friction information.

This mode is somewhat analogous to the lateral signal in PFM (cp. section 3.3.6).

Non-contact mode uses an cantilever that oscillates at its resonance frequency. The cantilever is close enough to the surface to feel the attractive forces without touching it (“non-contact”). The forces between the tip and the sample surface are quite low, i.e. of the order of pN. The detection scheme is based on the measurement of resonant frequency shifts of the oscillating cantilever due to changing tip-surface forces. In order to achieve fast and low-noise measurements, stiff cantilevers with high resonance frequencies are preferred.

Dynamic Force / Intermittent contact / “tapping mode” AFM is similar to the non-contact mode, with the difference that the cantilever is oscillated closer to the sample than in non-contact mode. Part of the oscillation extends into the repulsive regime (feeling repulsive forces of the sample), which means that the tip intermittently touches the surface. Very stiff cantilevers are typically used, as tips can get “stuck” in the water layer covering the sample surface in standard AFM.

The benefit of tapping the surface is an improved lateral resolution on soft samples. Lateral forces such as drag, common in contact mode, are virtually eliminated.

These normal AFM methods can only be used for domain imaging when combined with one of the decoration methods discussed before. Other scanning probe techniques are therefore more direct and more appropriate for ferroelectric domain imaging.

Scanning Probe Domain Imaging Techniques

Techniques to image the domain structure include, *piezoelectric force microscopy* (PFM), *electrostatic force microscopy* (EFM), *magnetic force microscopy* (MFM; for ferromagnetic materials), *scanning surface potential force microscopy* (SSPM), *scanning near-field optical microscopy* (SNOM), and *scanning non-linear dielectric microscopy* (SNDM).

In EFM, the electrostatic field is detected in the non-contact AFM mode, in which long-range forces dominate the tip-sample interaction [Stern et al., 1988]. EFM is however not widely used due to limitations concerning screening of the polarisation, sample surface conditions (e.g. water layer), and resolution.

In scanning surface potential microscopy (SSPM) [Kalinin and Bonnell, 2001], a voltage potential is applied to the AFM tip to nullify the potential difference between the tip and the sample. The applied potential is a measure of the surface potential and can be mapped over the scanned surface [Kalinin and Bonnell, 2001]. Screening effects and domain structures can be studied by this method down to a nanometre scale.

Scanning non-linear optical microscopy (SNOM) combines the scanning probe technique with electro-optical characterisation and even manipulation [Tikhomirov et al., 2000, Zayats and Smolyaninov, 2004]. SNOM is considered an interesting method, not only for domain imaging, but also for local property characterisation and optical manipulation of ferroelectric materials.

Scanning non-linear dielectric microscopy (SNDM) is able to detect the capacitance variation between a sharp conductive tip and the bottom electrode of a sample by means of an LC circuit with resonance at microwave frequency. The non-linear term of the dielectric constant, which is measured by the non-linear capacitance variation, changes its sign with the polarisation [Cho et al., 1996, Odagawa and Cho, 2002]. The method can be used to image domains. A nanometre resolution due to the electric field concentration below the sharp tip was demonstrated [Cho et al., 1999].

Piezoelectric Force Microscopy

The most common tool to characterise the domain structure of ferroelectric thin films on a nanometre scale is the piezoelectric response microscope (PFM). It allowed a huge step forward in the understanding of ferroelectrics by the microscopic insight into the polarisation reversal as well as degradation effects, such as fatigue, imprint and retention loss. This technique is discussed in more detail in chapter 3.

In the frame of this thesis, two scanning probe techniques were used: AFM in order to image the topography of the samples and PFM in order to characterise the piezoelectric response of samples and to image the domain pattern, i.e. to map the polarisation direction in ferroelectrics.

Chapter 3

Microscopic Characterisation of the Polarisation Reversal

Abstract The development of scanning probe techniques, and more specifically piezoelectric force microscopy (PFM), has provided a very important insight into the polarisation reversal on a microscopic level. In the context of the traditional polarisation reversal model with nucleation, forward and sideways growth, knowledge on the domain shape and details about its growth on a microscopic scale is of great interest, but could not be answered satisfactorily by the traditional PFM technique. The main shortcoming was that static observations of domain configurations and quasi-dynamical studies of domain growth were always performed on the surface of ferroelectric films.

Direct insight into the domain growth details is possible from observations of the domain structure and development during the switching process on the cross section — normal to the surface — of ferroelectric films.

The difficulties in the cross section preparation and in the characterisation are discussed in detail.

Our Contribution We demonstrated for the first time a PFM study on the cross section of ferroelectric films. In combination with switching pulses, this allowed us to directly image the polarisation reversal in ferroelectric films, quasi-dynamically.

3.1 Piezoelectric Force Microscopy

The most widely-accepted tool to characterise the domain pattern of ferroelectric thin films, among direct methods, is the piezoelectric response microscope, from the scanning probe microscope family (see section 2.7.5). It has allowed for a huge step forward in the understanding of ferroelectrics due to its ability to non-destructively image of domain patterns and the possibility to identify the polarisation orientation on a very small scale. In addition to static domain patterns, quasi-dynamical studies of ferroelectric thin films have offered further insight to phenomena such as fatigue and polarisation reversal, which are relevant for theoretical understanding as well as (memory) applications of ferroelectrics [Colla et al., 1998, Stolichnov et al., 2002, Gruverman et al., 2005].

3.1.1 Working Principle of PFM

The idea of domain pattern mapping with the piezoelectric force microscope (PFM) is rather simple. A weak electric field induces a deformation of the crystal lattice via the converse piezoelectric effect. The resulting microscopic deformation is sensed locally by an AFM cantilever.

The converse piezoelectric effect was described by equation (2.15), with the piezoelectric coefficient proportional to the polarisation as given in equation (2.19). Alternatively, we can describe the working principle by a small polarisation variation δP_3 . The polarisation variation in the direction of the polarisation can be written as proportional to the sinusoidal driving field $V^{\text{ac}} = V_0 \sin(\omega t)$, with the angular frequency ω , the time t , and the amplitude V_0 :

$$\delta P_3 \propto V_0 \sin(\omega t). \quad (3.1)$$

We assume that the polarisation in a ferroelectric with a tetragonal symmetry is in the direction perpendicular to the surface (index 3). The field is applied parallel to the polarisation. The strain in the polarisation direction can then be written as

$$x_{33} = Q_{11} P_3^2 = Q_{11} (P_{3,c} + \delta P_3)^2 = Q_{11} [P_{3,c}^2 + 2P_{3,c} \delta P_3 + (\delta P_3)^2], \quad (3.2)$$

where Q_{11} and $P_{3,c}$ are the electrostrictive coefficient and the constant polarisation part, respectively. We measure the strain response to a small driving field in PFM and thus the term $2P_{3,c}Q_{11}\delta P_3$. If we divide the strain also into a constant $x_{33,c}$ and variation part $\delta x_{33}(V^{\text{ac}})$ with $x_{33} = x_{33,c} + \delta x_{33}(V^{\text{ac}})$, we can then write with equation (3.1):

$$\delta x_{33}(V^{\text{ac}}) \propto 2P_{3,c}Q_{11}\delta P_3 \propto 2P_{3,c}V_0 \sin(\omega t). \quad (3.3)$$

The response is proportional to the spontaneous polarisation and changes its sign when the polarisation is reversed. This sign change can however be expressed in a phase shift ϕ of 180° in the detected sinusoidal strain variation:

$$\delta x_{33}(V^{\text{ac}}) = 2|P_{3,c}|Q_{11}V_0 \sin(\omega t - \phi). \quad (3.4)$$

In the PFM method, the AFM has to be operated in contact mode (section 2.7.5) to detect the fast strain response (typically in a frequency range of several kHz).

In pioneering work [Lüthi et al., 1993, Saurenbach and Terris, 1990] on direct domain or domain wall imaging, the domain information was superimposed on the topographic information. Whereas no piezoelectric information was involved in the above cited work, Birk et al. measured local hysteresis loops¹ [Birk et al., 1991]. Güthner and Dransfeld were the first to use the converse piezoelectric response to image the domain pattern of ferroelectric polymers [Güthner and Dransfeld, 1992]; studies on PZT followed soon thereafter [Franke et al., 1994, Gruverman et al., 1996].

More sophisticated methods have been developed involving techniques to determine arbitrary polarisation directions [Eng et al., 1998, Abplanalp et al., 1998, Okino et al., 2001, Rodriguez et al., 2004] or PFM in liquid media [Rodriguez et al., 2006]. Reviews of the various PFM techniques were published by different authors [Gruverman et al., 1998, Gruverman and Kholkin, 2006, Kalinin et al., 2006].

¹The local piezoelectric response of P(VDF-TrFE) without scanning a surface region, but with a static probe.

Many studies concerning the forces between the AFM probe and surface have been published for AFM, in general [Sarid, 1994]. For the specific situation in PFM, additional electrostatic forces have to be included in the considerations. Abplanalp analysed the relevant interactions in chapter 3 of his thesis [Abplanalp, 2001]. He distinguished the following forces:

Van der Waals forces The electrostatic interaction between globally neutral molecules or atoms results in an attractive force. In non-polar atoms, such a force is present due to fluctuating dipoles, which average over time to non-polarity. Considering the tip sample interaction in the geometrically simplified model of a sphere with radius R and a flat plane, the van der Waals forces F_{vdW} are

$$F_{\text{vdW}} \propto -\frac{R}{z^3} \quad (3.5)$$

for the separation between the tip and the surface $z \ll R$. More sophisticated models are available [Israelachvili, 1995, Saint Jean et al., 1999].

Repulsive forces As the AFM tip approaches to the sample surface, its penetration into the solid sample body is impeded by strong repulsive forces. These are due to covalent bonds between the atoms in the sample. The corresponding interaction energy was traditionally given by a potential function without much physical basis (but for mathematical convenience, compare to the proportionality for the attractive forces), which decays very fast with increasing distance following the potential law below:

$$F_{\text{repulsive}} \approx \frac{C}{z^n}, \quad (3.6)$$

with a constant C and an exponent n , typically larger than 8.

Capacitive forces are due to the interaction between a conductive tip and a counter electrode, in general the bottom electrode in the case of PFM. The capacitive force can be written as the derivative of the work in a capacitor:

$$F_C = \frac{dW}{dz} = \frac{1}{2} \frac{dC}{dz} U_{\text{tip-ce}}^2, \quad (3.7)$$

where C is the capacitance. $U_{\text{tip-ce}}$ is the potential difference between the tip and the counter electrode.

The potential difference depends not only on the applied field, but also on the work function² of the involved materials and the surface potential³. It does not depend on the material, but only on the charge carried by the surface. In ferroelectric samples, the polarisation and the compensating charges contribute to the surface potential.

²The work function is defined as “the minimum energy required to remove an electron from the interior of a solid to a position just outside.” [Ashcroft and Mermin, 1976], p. 354.

³The surface potential is the potential to move an electron from the surface (outside the crystal) to infinity

The capacitance [C in equation (3.7)] of the system depends on the geometry of the tip as well as the electrode and their separation. The tip geometry can be approximated by different models (sphere, half sphere and cone, etc.) and the capacitance calculated accordingly. Such models generally result in complicated expressions [Abplanalp, 2001].

Due to different dependencies of the above mentioned forces on the tip-surface separation distance, electrostatic and electromechanical imaging regimes can be distinguished [Kalinin and Bonnell, 2002]. At larger tip-surface separation distances, $z \gg R$, the long-range capacitive forces ($F \propto z$ in a first approximation for a parallel plate capacitor) are predominant. In the “contact” regime, $z \ll R$, the short-range electromechanical and repulsive forces govern the total interactions. This was also demonstrated experimentally [Hong et al., 2001]. Further modelling of interactions and cantilever deformations are available [Jesse et al., 2006].

The displacement of a sample surface under an AFM tip was calculated for a BaTiO₃ crystal [Felten et al., 2004]. This group took into account the mechanical properties of the sample and found a surface displacement between 50 and 500 pm depending on the distance from the centre of contact and the tip-sample separation.

The surface displacement can be estimated simply with equation (2.15) considering only field and strain in the direction (3) perpendicular to the sample surface. If clamping, field inhomogeneities, and polarisation directions out of the field directions are neglected, the strain x_{33} can be estimated for the application of a subswitching electric ac field.

When an ac field with an amplitude of 0.4 V is applied across a PZT film with thickness of 200 nm, the electric field $E_3 = 20 \text{ kV/cm} = 2 \text{ MV/m}$ induces a strain of $x_{33} = 2 \cdot 10^{-4}$, assuming a piezoelectric coefficient of $d_{33} = 100 \text{ pm/V}$ for a tetragonal composition at room temperature [Haun et al., 1989].

The absolute movement of the surface can be roughly estimated as $\delta l = x_{33} \cdot l = 40 \text{ pm}$, with the strain x_{33} and the sample thickness l .

This simple estimation shows that the displacement is very small, below the size of a unit cell of the crystal. Its detection in PFM is described in the following section.

3.1.2 Instrumentation for PFM

PFM System

The cantilever deflection signal is used as a feedback signal for the AFM control unit in the contact AFM mode. The high-frequency oscillations of the cantilever induced by the converse piezoelectric response are detected on the photodetector. These high-frequency (compared to the topographical response) oscillations are analysed using a lock-in technique with respect to the source ac signal. In our configuration, the piezoelectric oscillations are induced by the ac signal from the built-in voltage source of the lock-in amplifier. The amplitude and phase information from the lock-in amplifier is read via a data acquisition (DAQ) card to a computer, in which a LabView program writes the signal to an amplitude and phase image. The configuration is depicted schematically in figure 3.1.

The AFM system consists of a piezoelectric scanner unit, a detecting head with the AFM probe and a laser unit, a controller, an anti-vibration table, and a user interface. In our specific systems, the sample is mounted on the piezoelectric scanning tube equipped with a magnetic sample holder. The AFM tip is fixed in the detecting head. In order to

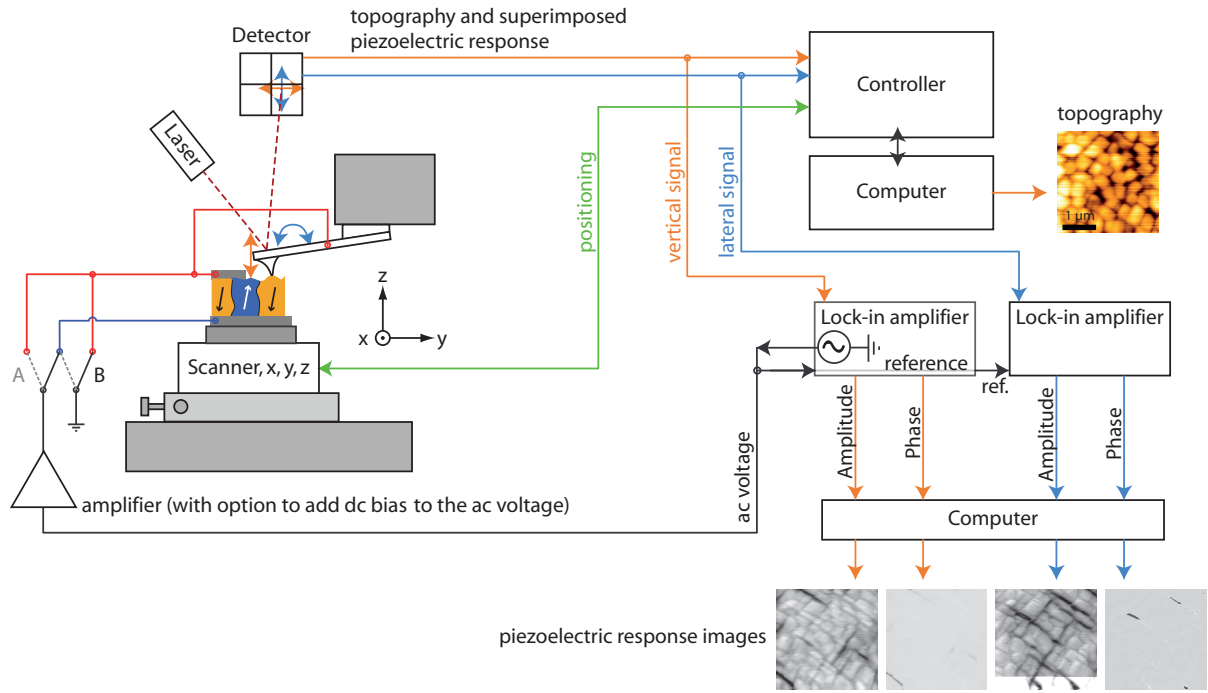


Figure 3.1: A schematic illustration of the PFM configuration with the AFM and its controlling unit, the lock-in amplifiers for vertical and lateral signal extraction, the computer unit to generate the topography image and another computer to produce the PFM images. A switch applies the voltage either to the tip used as a top electrode and grounds the bottom electrode (position A) or applies the voltage to the bottom electrodes and grounds the tip and the top electrode for scanning through a top electrode (position B).

take a topography image of the sample, the sample is moved under the fixed tip while the controller keeps the force between the sample surface and the AFM tip constant (*constant force mode*). To do so, the controlling unit drives the piezoelectric tube to bring the sample closer to the tip or to retract it depending on the topography of the sample. This movement, perpendicular to the sample in the z -direction, can be registered and used to reconstruct the image of the sampled surface.

The force between the sample and the AFM tip is assumed to be proportional to the cantilever deflection, according to the simple Hooke's law in equation (3.8):

$$F = kd, \quad (3.8)$$

where F is the force, k the spring constant, and d the deflection.

Typical AFM probes are shown in figure 3.2⁴, in which the microscopic tip can be seen at the end of the cantilever. The AFM cantilever suppliers provide information about the dimensions and the spring constant of the tip. The spring constant has to be written to the cantilever parameter file in the AFM system to allow for the calculation of the contact force.

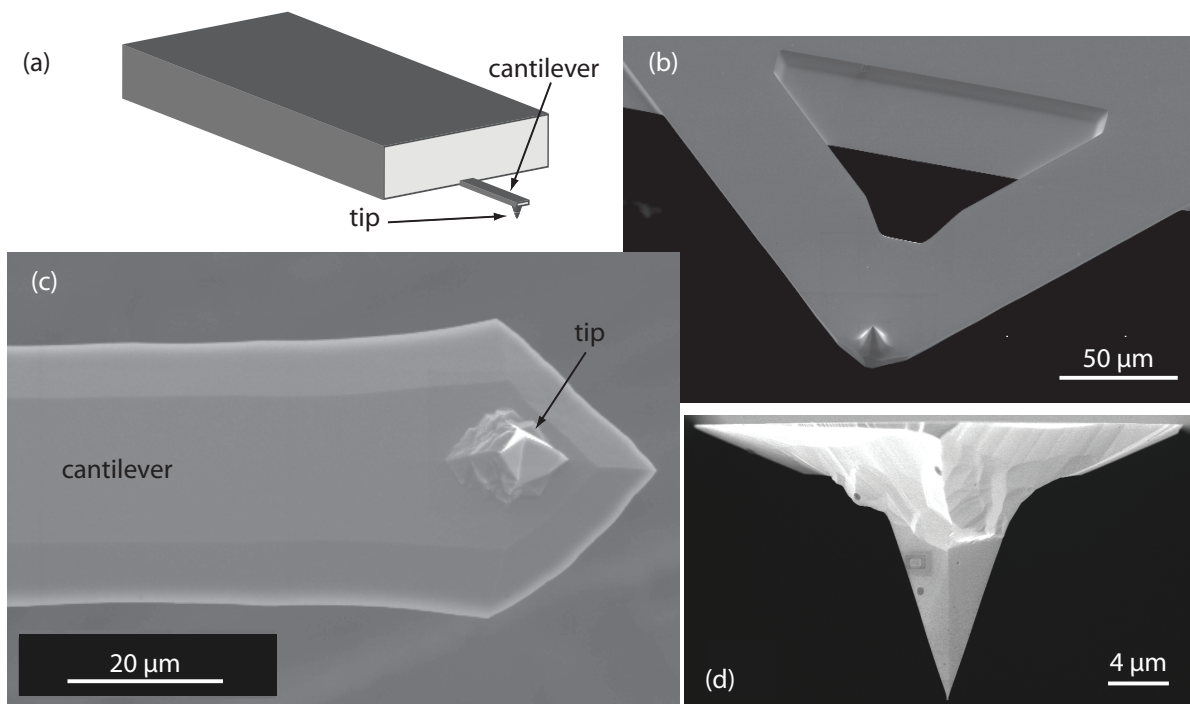


Figure 3.2: A schematic illustration of the whole structure with body, cantilever, and tip is given in figure (a). Typical cantilevers with a metal coated tip for PFM measurements are shown in the SEM images of: (b) a triangular shape cantilever (μ masch, Ultrasharp); beam-like cantilevers (*Nanoworld*) in bottom (c) and front view (d).

⁴SEM image (d) was taken by Jeroen Steen.

PFM Signal Detection

The tip deflection is measured by means of a laser beam that is reflected on the backside of the cantilever. The laser is mounted on the right hand side of the detecting head, the photodetector on the left hand side. The laser beam has to be directed onto the backside of the cantilever from where it is reflected (between several mirrors) to the photodetector. The photodetector is divided into four quadrants. A potential difference can be measured between the quadrants depending on the position of the reflected laser beam on the photodetector. The potential difference is thus a measure of the deviation of the laser beam from the central position.

A standard AFM can detect the vertical force between the sample surface and the tip, the lateral force, which gives rise to a torsion of the cantilever. Due to the bending of the cantilever around its axis, the beam is reflected differently compared to the vertical bending of the cantilever. The respective bending modes of the cantilever are detected by four quadrants. The deflection in either vertical or lateral direction is determined calculating the potential ratio of either $(A + B) : (C + D)$ or $(A + D) : (B + C)$, where A , B , C , and D are the respective electric potentials proportional to the beam intensity on each quadrant.

For piezoelectric force microscopy (PFM), the user would like to measure the vertical as well as the possible lateral vibrations of the piezoelectric material under investigation. This would allow the a - and c -domains to be distinguished, or the detection of vibrations due to the coefficients d_{33} , d_{15} , or d_{31} as was demonstrated [[Abplanalp, 2001](#), [Schlaphof, 2005](#)].

Lock-in amplifiers allow for the detection of very small oscillation amplitudes of the sample surface and thus the AFM probe. The magnitude of this oscillation is typically on the order of tens of picometers and one can imagine that thermal oscillations of the atoms have to be distinguished from the piezoelectric displacements. The optical system with the laser beam can amplify the small displacement. Lock-in techniques can filter the desired frequency signal and enable the detection of the small piezoelectric response.

PFM Images

Each pixel of an amplitude or phase image⁵ represents the locally measured piezoelectric response. The amplitude is divided into 255 levels with the largest for the maximum amplitude recorded by the lock-in amplifier. The phase angle range from 0 to 359° is also divided into 255 levels and 0 is defined by the chosen phase shift in the lock-in amplifier. The signal levels are represented by a grey colour scale from black to white for the values from 0 to 255.

Important parameters for PFM studies are listed below:

- Probe type:

Resonance frequency and force constant of the cantilever are important for the accuracy of the measurement, i.e. the noise level can be reduced by a faster measurement. We always worked with an ac frequency (1–30 kHz) below the resonance frequency of the tip, however, other methods have been reported as well [[Harnagea et al., 2006](#)].

⁵Our PFM images are of a resolution of typically 256×256 pixels

Tip radius indicates the sharpness of the AFM tip. The smaller the tip radius, the sharper the tip and the more local information can be collected. If conductive tips are needed and voltages are applied, a smaller tip radius is more critical to apply a field. Sharper tips are prone to faster wear of the conductive coating, leading to deterioration of the electric tip-sample contact and hence, a loss in the stability of the measurement.

Tip coating It should be resistant to wear and has to provide a high enough conductivity. Pt/Ir coatings proved to be better than gold in terms of wear resistance.

Reflectivity of the cantilever backside; it should be reflective in order to get enough signal for the laser detection system in the AFM.

Geometry Triangular and beam-like cantilever geometries are available. For studies involving lateral signal detection, cantilevers with the beamlike geometries are more suitable.

- Driving ac field:

Frequency The higher the frequency, the more oscillations can be included in the evaluation of the signal and the obtained statistics are better. However, resonance of the sample, the cantilever, and the system have to be avoided. Optimisation of the frequency in a range between 1 and 20 kHz was generally helpful⁶. Sophisticated analysis of the frequency dependence of the response are available [Jesse et al., 2006] as well as explanations based on PFM system inherent effects [Jungk et al., 2006].

Amplitude of the driving field has to be below the coercive field, since the driving field should not affect the polarisation state of the sample. Smallest possible values to avoid the movements of domain walls are in concurrence with the need for noiseless, clear signals, which are in general obtained at higher amplitudes.

- AFM scanning:

Scanning speed A trade-off has to be made between high resolution and a low-noise signal and the acquisition time, which may affect studies on sample with significant relaxation phenomena on time scales in the order or below the image acquisition time. This parameter is defined in our AFM system as a line frequency. For fast PFM measurements, the line frequency was 0.5 Hz, slow measurements were done at 0.05 Hz.

Size The scan size should be chosen accordingly to the expected feature size and the region of interest. The choice must also account for a good enough resolution. The images are generally measured in a matrix of 256×256 or 512×512 points (or pixels).

Contact force can impact the topography of the soft sample surface and may even have an impact on the recorded signal due to an increased bending of the cantilever.

- Lock-in amplifier(s):

⁶The values refer to our system and the frequency range, we used in in the measurements for this thesis.

Integration time gives the period for the signal integration. It has to be matched to the number of measured points and the scanning frequency (scanning speed). With a standard scanning frequency for a decent resolution of $\nu_{\text{scan}} = 0.15$ Hz and thus $t_L = 6\frac{2}{3}$ s/line, the integration time was generally chosen as $\tau_L = \frac{t_L}{N_{\text{points}}} = \frac{6.67}{256}$ s = 26.0 ms \approx 30 ms.

Phase shift A constant value should be chosen in order to generate easily interpretable images. The problem arises from the fact that the phase is described by values between 0 and 360° with a discontinuity between the maximum and minimal values of this interval, which in reality represent the same phase signal. If the recorded phase signal oscillates around this numerical discontinuity, there will be a large difference in contrast between phase values $> 0^\circ$ and $< 360^\circ$, even though they should be very similar.

- Sample:

Mounting The sample should be fixed on the ferromagnetic steel plate well before (in our experience about half an hour) the measurement in order to allow the fixing medium and the sample to relax.

Top electrodes may or may not be used. In the first case, the mechanical excitation are sensed through the top electrode. The achievable resolution is therefore dependent on the electrode thickness. In the second case, the field is applied between the tip and the bottom electrode. The advantages of the use of a top electrode are more homogeneous fields and good electrical contact between the tip and the sample.

- Measuring environment:

Humidity not only has an impact on certain ferroelectrics (e.g. KNbO₃), but is important in terms of polarisation screening and tip-surface interactions. The resolution is lower if a water layer is covering the sample surface and the tip. Therefore, high precision, atomic resolution measurements have to be done in vacuum (or as discussed next, completely in water).

Medium Most commonly, PFM measurements are done in air or in vacuum. However, demonstrations of PFM in liquids (water and water with NaCl) were reported in order to enhance the resolution by an improved control over environment [Rodriguez et al., 2006].

Temperature dependent measurements are a very interesting option, but not feasible in our system. Heating or cooling of the sample is not straightforward, because a temperature change has an impact on the piezoelectric scanning tube of the AFM. This is true for our AFM system, since the sample is mounted on the piezoelectric actuator tube directly⁷.

Quantitative PFM Measurements

In order to get quantitative measurements, i.e. the absolute value of the piezoelectric coefficient d_{33} , the PFM system has to be calibrated. This is ideally done with a flawless, preferably single-domain sample, which can be measured by a double-beam interferometer

⁷Other AFM systems exist in which the cantilever is moving and the sample is on immobile support.

system. The measured absolute value of the piezoelectric response can then be used to calibrate the PFM system. Quartz single crystals are typically used for this purpose.

For the quantification, piezoelectric hysteresis loops (see section 2.6.2) are usually recorded.

3.1.3 Possible Experimental Configurations

Four modifications of PFM for the characterisation of thin films can be distinguished:

- (i) scanning a free surface of the ferroelectric film deposited on a bottom electrode; the conductive AFM tip is used here as the top electrode to apply both the switching field and the driving ac field to monitor the converse piezoelectric response [Gruverman et al., 1996];
- (ii) use of top and bottom electrodes to apply both electric fields while sensing the piezoelectric response through the top electrode [Auciello et al., 1997, Colla et al., 1998, Birk et al., 1991];
- (iii) applying technique (i) to a ferroelectric film which is homogeneously thinned down to different thicknesses (step by step), in order to obtain information about the depth profile of the piezoelectric response in the film [Hong et al., 2004]; and
- (iv) applying technique (i) to a film obliquely thinned down [Lu et al., 2002].

Method (i) ensures a high resolution because the electric field is concentrated directly below the tip. This gives rise to a local piezoelectric response, which is beneficial for a high resolution. The direct mechanical contact is however a disadvantage for tips with a conductive layer. The conductive layer may be worn resulting in a main voltage drop not in the sample but in the sample-tip contact or the tip.

For the characterisation of the polarisation reversal in ferroelectric capacitors (as used for instance in ferroelectric memories, see chapter 6), the switching conditions are more easily reproduced with a top electrode, method (ii), than without, method (i).

For method (ii), the top electrode is kept thin enough (about 30–40 nm) to detect the vibration with a high lateral resolution through the top electrode. The advantage of this method is a homogeneous field distribution in the ferroelectric [Colla et al., 1998, Auciello et al., 1997] and no electrical contact problems due to tip wear.

However, the homogeneous electric field throughout the capacitor leads to an averaging of the piezoelectric response over the film thickness so that the information on the depth distribution of the polarisation is lost.

Information on the three-dimensional distribution of the polarisation can be obtained using techniques (iii) and (iv) but, because of the destructive character of these methods, the study of domain growth is problematic.

A natural alternative to these PFM methods is to monitor the cross section of a parallel-plate capacitor, in which the piezoelectric vibrations are driven by the field applied between the electrodes. Thereby, the advantages of methods (i) and (ii) are combined, i.e. the homogeneous driving field and the high resolution detection of the local piezoelectric response. Additionally, such a technique can provide information on the polarisation distribution across the film thickness.

3.2 Combination of PFM with Short Pulse Technique

PFM provides us with a direct static image of the domain pattern in a ferroelectric film. Our interest is however on the polarisation reversal mechanisms and the involved domain wall motion. With the integration of the macroscopic technique of pulse switching (described in section 2.6.3) in the static microscopic PFM analysis, domain patterns of a stepwise switched ferroelectric can be observed. Hence, we can follow the polarisation reversal quasi-dynamically in terms of domain wall motion.

There are, in principle, two ways to switch the ferroelectric stepwise. We can either use a gradually increasing switching pulse width or an increasing pulse amplitude.

The combination of PFM with pulse switching has been used before to study the polarisation reversal mechanism, including nucleation, and domain wall motion in PZT films. Gruverman et al. applied a pulse switching sequence with double pulses (including the optional pulses in the scheme in figure 3.3) with a gradually increasing pulse width of the (second) switching pulse [Gruverman et al., 2005]. They found an increase of the switched area following the Kolmogorow-Avrami-Ishibashi model (see section 2.4.2 for more details) in the beginning, but a deceleration of switching and hindrance of the polarisation reversal by the presence of domain walls.

Hong et al. [Hong et al., 1999, Hong and Setter, 2002] used a pulse sequence with increasing voltage to characterise the polarisation reversal of PZT in a capacitor structure directly. The sequence of the mapped domain patterns revealed a gradual amplitude change. This behaviour was associated with a domain growth that is limited in the polarisation direction.

If we want to characterise a full polarisation reversal process, i.e. from one fully poled state to the fully poled state in the opposite polarisation direction, the ferroelectric has first to be poled completely by a voltage pulse of a sufficient amplitude and width. The first pulse in figure 3.3(a) is poling the ferroelectric completely. Switching pulses of increasing width and opposite polarity (compared to the poling pulse) switch the ferroelectric stepwise. These switching pulses alternate with PFM domain mapping as illustrated schematically in figure 3.3 and the domain growth can thus be observed. As a modification of this pulse scheme, an additional poling pulse can be introduced before each switching pulse. This always brings the ferroelectric back to the fully poled reference state, before the switching pulse is applied (optional pulses in figure 3.3).

The use of a top electrode is preferred for the pulse switching method. This has two practical reasons. On one hand, the polarisation can be reversed over a large area by a single pulse. On the other hand, the use of a top electrode allows us to compare the microscopically observed domain growth to pulse switching curves. The use of a top electrode is associated with mainly field distribution advantages and resolution drawbacks as discussed briefly in the previous section. Nevertheless, interesting work combining short pulse technique with PFM with a conductive tip has been reported [Rodriguez et al., 2005, Tybell et al., 2002, Paruch et al., 2006].

The polarisation reversal of the copolymer of P(VDF-TrFE) was studied by the method described above with the use of thin top electrodes; results are presented in chapter 5.

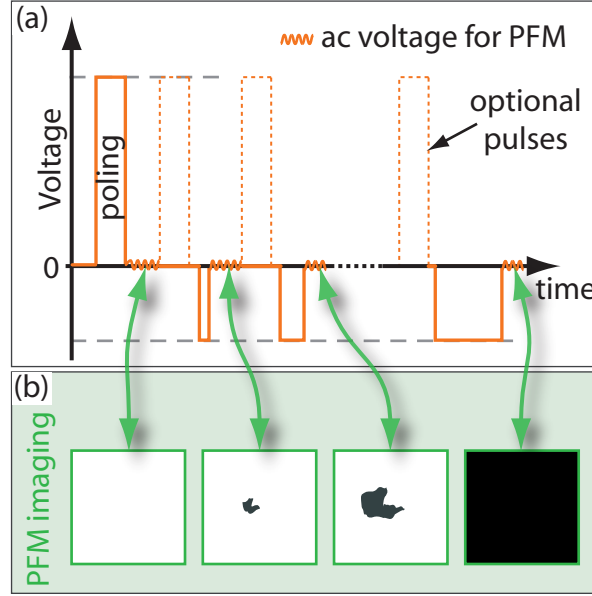


Figure 3.3: The pulse sequence (a) in alternation with PFM imaging (b) allows for more insight into the switching mechanism and domain wall motion. The switching pulses are shown here with a negative voltage and increase gradually in width. The optional poling pulses reset the sample to a reference domain state before each poling pulse.

3.3 Cross-sectional PFM

3.3.1 Statement of the Problem

Imaging of domains in a ferroelectric based on the use of their piezoelectric response has been described in section 3.1. The studies of the domain growth during the polarisation reversal is possible with the integration of the short pulse technique in PFM imaging.

Scanning of the film surface does however not allow conclusive statements on the growth mechanism, because it is not possible to access directly the three dimensional domain pattern.

This can be illustrated by studies on the domain growth mechanisms during the polarisation reversal. Hong et al. stated that they found evidence for a domain growth that was forward-growth limited [Hong et al., 1999, Hong and Setter, 2002]. Many others observed however that the domain growth was limited by the sideways expansion of the domains [Merz, 1954, Shur, 1996, Gopalan and Mitchell, 1998, Paruch et al., 2006]. The argument that a domain wall with a head-to-head configuration in the forward limited growth is very unfavourable from a thermodynamical point of view due to the charged domain wall and the electrostatic energy, can be countered with a zig-zag domain wall as illustrated in figure 3.4(c, d), but the correctness one or the other model has to be proven experimentally.

The difference between the sideways-limited growth and the forward-limited growth model is illustrated in figure 3.4. With a limited number of nucleation sites, the nuclei first grow through the film to the opposite electrode and expand subsequently sideways, as shown in figure 3.4(a). In this case, the sideways growth is the growth limiting step (together with the critical nucleation). In figure (b), there are a lot of nucleation sites and many domains slowly grow forward. In this case, the forward growth is the limiting

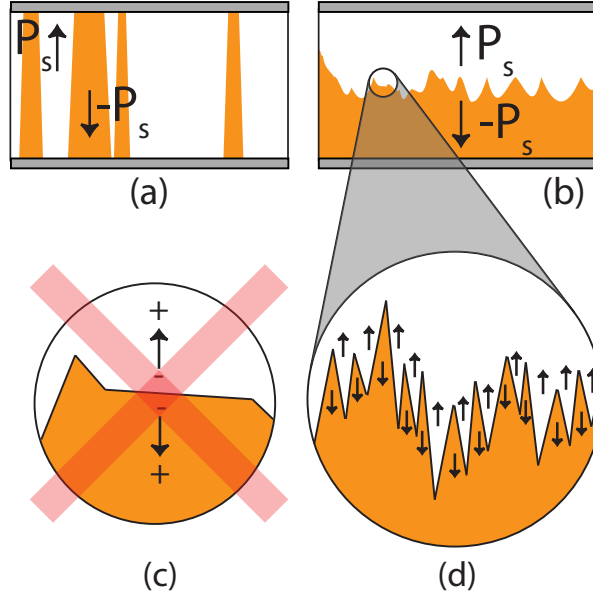


Figure 3.4: The illustration shows the sideways growth limited (a) and the forward growth limited (b) polarisation reversal model. Domains grow through the films from one electrode to the other. To avoid tail-to-tail (or head-to-head) configurations (c) in the second model, a zig-zag-shaped domain wall is formed as showed in the detail of (d).

step. The question is thus how to distinguish between these scenarios experimentally.

3.3.2 Idea for Our Approach

In order to understand the polarisation reversal mechanisms, we would like to get more information about the nucleation and domain growth. At what locations does the nucleation take place? Does it occur mainly on defect? And if so, on what kind of defects? Does nucleation happen randomly? Concerning the domain growth in ferroelectric thin film, we want to know whether it is limited by the sideways or forward growth.

If it was possible to access the domain pattern in three dimensions directly, one could determine the growth-limiting stage and answer questions about nucleation sites. Cross-sectional characterisation would allow for additional insight into the nucleation process and favourable nucleation sites and would be a step towards the three-dimensional domain pattern imaging.

In ferroelectric single crystals [Little, 1955], this was achieved more than fifty years ago, as shown in figure 2.17 of section 2.3.2. In thin films no thicker than about a micrometre, the resolution of optical microscopy is insufficient to resolve the domain pattern on the film's cross section. Modern techniques with a resolution on the order of tens of nanometres are thus needed and nowadays also available.

The PFM technique has proven to be suitable for domain imaging. Our idea was thus to map domain structures on the cross section of thin films by PFM.

The combination of PFM with the short voltage pulse technique (described in the above section 3.2) further allows a quasi-dynamical study of the evolution of the domain pattern and thus of the growth mechanism.

Such cross-sectional PFM studies have not been reported. The closest approach to

cross-sectional PFM has been realised by [Lu et al., 2002]. In this work, a sample was polished at a shallow angle in order to get the depth-sensitive piezoelectric signal. The piezoelectric response was then measured as a function of the position within the film in order to identify possible passive, non-ferroelectric layers. They could identify a reduced piezoelectric response in the layer close to the bottom electrode as is shown in figure 3.5.

It is not possible to study the polarisation reversal mechanism in a capacitor structure dynamically, using this experimental method.

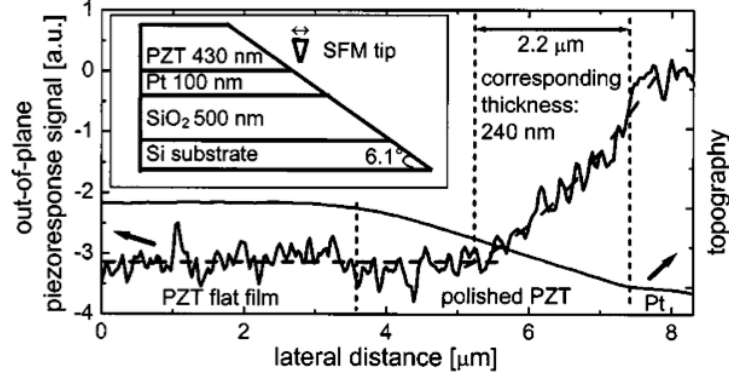


Figure 3.5: Approach of imaging the cross-section using a PZT sample polished under a shallow angle [Lu et al., 2002]. The original illustration from the reference shows the piezoelectric response and the topography signal as a function of the lateral distance. The inset depicts the used configuration.

A possible approach to cross-sectional PFM is related to work in which a small ferroelectric beam was micromachined by a focused ion beam (FIB) in a PZT thin film [Dunn, 2003]. The bottom electrode on the bottom of the beam was removed and a new electrode was deposited on the rear side of the beam. Subsequently, the piezoelectric response in the plane of the film was measured while applying the field between the rear electrode and the tip on the cross section. A depth dependent piezoelectric response (d_{33}) was observed, but the origin of this dependence was not clear⁸.

3.3.3 Sample Preparation

We considered two methods to prepare cross sections of ferroelectric thin films: mechanical polishing and polishing by a focused ion beam (FIB).

In both cases, silicon substrates with a PZT film were cleaved with a diamond scribe. Due to the need for a capacitor structure with bottom electrode (BE), ferroelectric film, and top electrode (TE), we made sure that the crack passed through a top electrode. Samples broken this way were used for either mechanical or ionic (FIB) polishing.

Mechanical Polishing

In order to protect the thin film from delamination during mechanical polishing, two samples were glued together with an epoxy glue with the thin films in the centre of this “sandwich” as shown in figure 3.6.

⁸From our experimental experience, the detrimental effect of a large ion dose on the piezoelectricity may be at the origin of this depth dependence (compare to section 3.3.3).

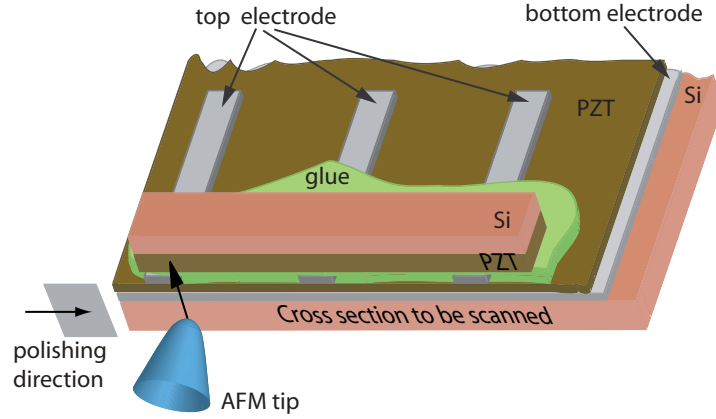


Figure 3.6: The sandwich structure with Si substrate, Pt electrodes, ferroelectric film, and top protection Si are shown. The cross section is polished in order to scan it afterwards with an AFM probe, symbolised by the cone and arrow, which indicates the scan direction.

The mechanical polishing was based on the transmission electron microscopy (TEM) sample preparation method and was done in the sample preparation facilities of CIME⁹ at EPFL. The polishing was done very carefully. The sample was manually moved over the diamond paper in the film direction only, in order to avoid delaminating the thin film from the substrate and smearing the relatively soft metal electrodes over the film surface. Diamond papers down to a grain size of $0.5\ \mu\text{m}$ were used.

A scanning electron microscope (SEM) image of a mechanically polished sample is shown in figure 3.7. Comparison to a sample polished without gluing it to a sandwich structure, as the example shown in figure 3.8, proved that the sandwich structure was required.

In the AFM characterisation of the sample with a ferroelectric PZT layer of 200–250 nm, the identification of the various layers is difficult due to the high polishing quality.

A possible solution for the layer identification is the use of a *potential measurements technique*, in which a voltage is applied to the bottom electrode. A conductive tip is then scanned over the cross section while the electric potential sensed directly by the tip. If the tip is touching the bottom electrode, the measured electric potential should correspond to the applied potential, whereas it is supposed to be close to zero in the non-contacted isolating layers.

The result of such a measurement using the sample depicted in the SEM figure 3.7 for a dc potential of 6 V (bottom part) and 2 V (top part) is depicted in figure 3.9. A high potential can be seen as a the bright colour in three lines. They correspond to the three electrodes of this sandwich sample. Since the potential was only applied to the bottom electrode, the image proves that there was an undesired electrical contact between the three electrodes.

The contact between the electrodes is related to the sample preparation method. When gluing two parts to a sandwich structure, the films generally break and since they are very thin, the electrodes contact each other. This problem is illustrated by the SEM image of the edge of the sandwich structure in figure 3.10.

⁹Centre interdisciplinaire de microscopie électronique, interdisciplinary centre for electron microscopy. I am grateful to Dong Su, who introduced me to the sample preparation.

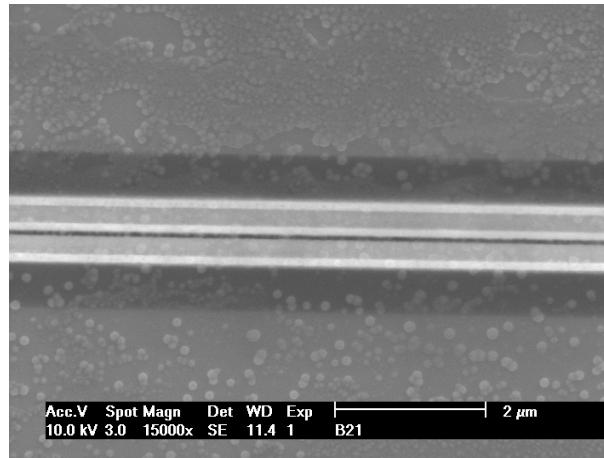


Figure 3.7: The cross section of a mechanically polished PZT sandwich sample. The sequence of layers from the bottom to the top: Si substrate; adhesion layer (slightly darker); Pt bottom electrode (110 nm, bright), PZT (200–250 nm), glue, Pt top electrode, PZT, Pt, bottom electrode, adhesion layer and Si.

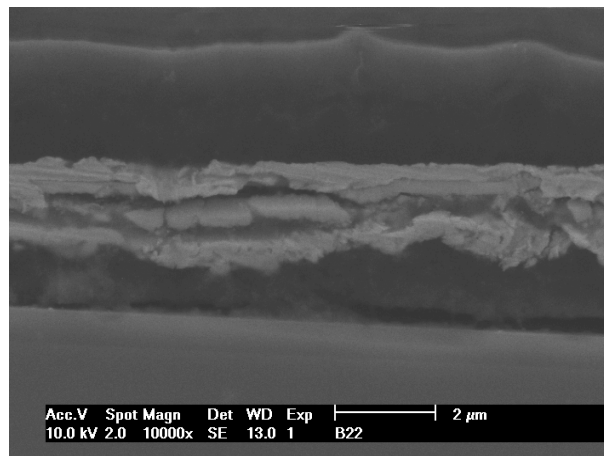


Figure 3.8: The cross section of a mechanically polished PZT sample, without a protective glued counter Si substrate (compare to figure 3.7). The film is delaminating and not useful.

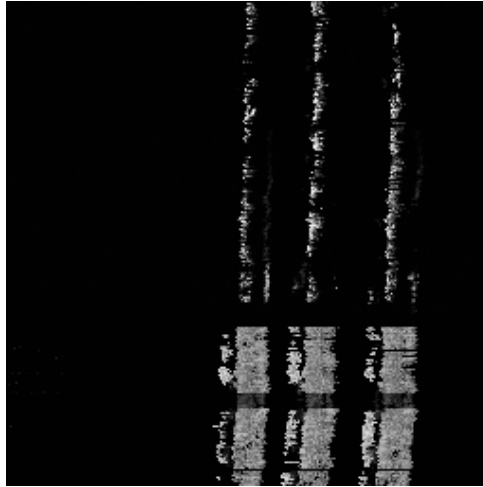


Figure 3.9: Scan over a polished cross section ($2.5 \times 2.5 \mu\text{m}^2$) as shown in figure 3.7 while probing the potential with a conductive tip. A voltage was applied between the bottom electrode and the ground potential of a voltmeter. The potential on the sample surface is represented by the contrast darkness (black for 0 V, white for the maximal measured potential). Not only the bottom electrode appears as white line, but also the other two electrodes. This indicates a short contact between all electrodes. In the lower third of the image, a voltage of 6 V was applied, while in the upper two thirds, the applied voltage was reduced to 2 V.

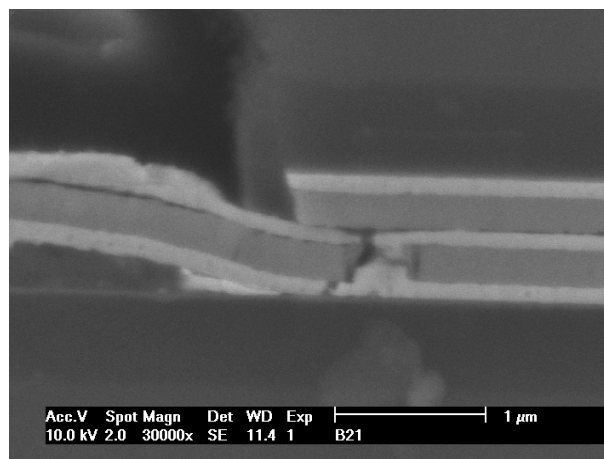


Figure 3.10: Mechanical polishing was problematic due to electrical short-circuiting between top and bottom electrodes.

With short-circuited electrodes, it is not possible to control the polarisation state and to apply an ac voltage between the top and bottom electrodes and thus to induce the necessary converse piezoelectric response.

There are two possibilities to circumvent the problem of electrically connected electrodes:

1. The first approach concerns the way the voltage is applied. Alternatively to the application of a voltage between top and bottom electrodes, the voltage can be applied between the electrodes and the conductive AFM tip. The top and bottom electrodes can then be shorted and a converse piezoelectric response can still be measured.

The difference between the two options to apply a field are illustrated in figure 3.11. If the voltage is applied between top and bottom electrode of the sample, the field is homogeneous as illustrated in figure (a). If a conductive AFM tip is used as an electrode, the field is non-uniform and field components normal and parallel to the electrodes are present.

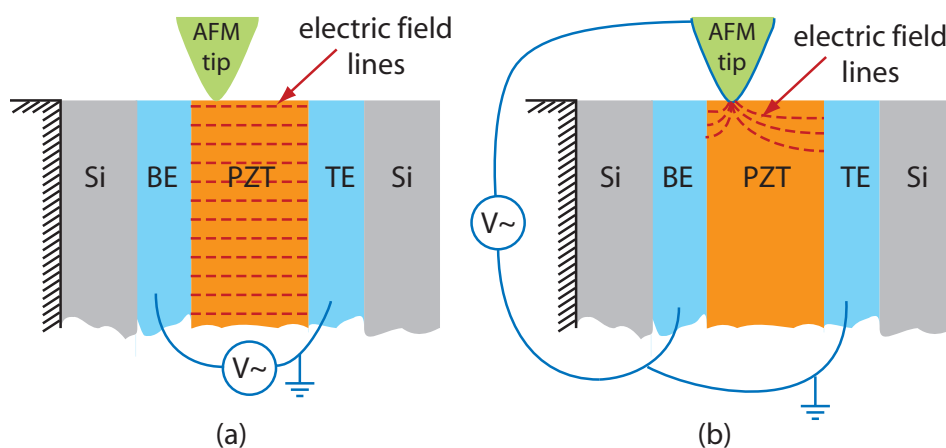


Figure 3.11: The electric field to induce the converse piezoelectric vibration for the PFM measurements can either be applied between the top and bottom electrodes (a) or between the conductive AFM tip and the electrodes (b). The measurement in (b) is feasible also for short-circuited top and bottom electrodes. The electric field lines are illustrative only.

Apart from the added difficulty in interpreting the piezoelectric response, the main disadvantage in this approach is the direct contact between the electrodes and the AFM tip. When the scan range is larger than the ferroelectric thickness, the AFM tip moves over the metal electrode. In this situation, the tip is in direct contact to the electrode, which results in high current densities through the very small contact area. The resulting detrimental impact on the conductive layer on the tip gives rise to unreliable measurement as is shown in section 3.3.4. It is possible to add a high resistance between the ground potential and the electrodes in order to limit the currents when they are shorted to the AFM probe. However, in such a circuitry the results were still not satisfying and the tip and its coating were still subject to wear and damage.

2. In the second approach thicker PZT films can be used to separate the electrodes more effectively and avoid the direct contact between top and bottom electrodes.

We used sol-gel fabricated films for the realisation of the second approach. Their fabrication was described elsewhere [Taylor et al., 1996]. We found that film thicknesses of at least 400 nm were necessary to solve the short-circuit problem.

With thicker ferroelectric films, another problem appeared. It became very difficult to resolve domains in PFM, as can be seen in figure 3.12, in which an 800 nm thick film is mapped. The piezoelectric response is high even outside the ferroelectric film, i.e. in the non-ferroelectric substrate, the glue, and the protective Si layer. The complete sample is vibrating here in phase, because the ferroelectric film induces a bending mode in the sample.

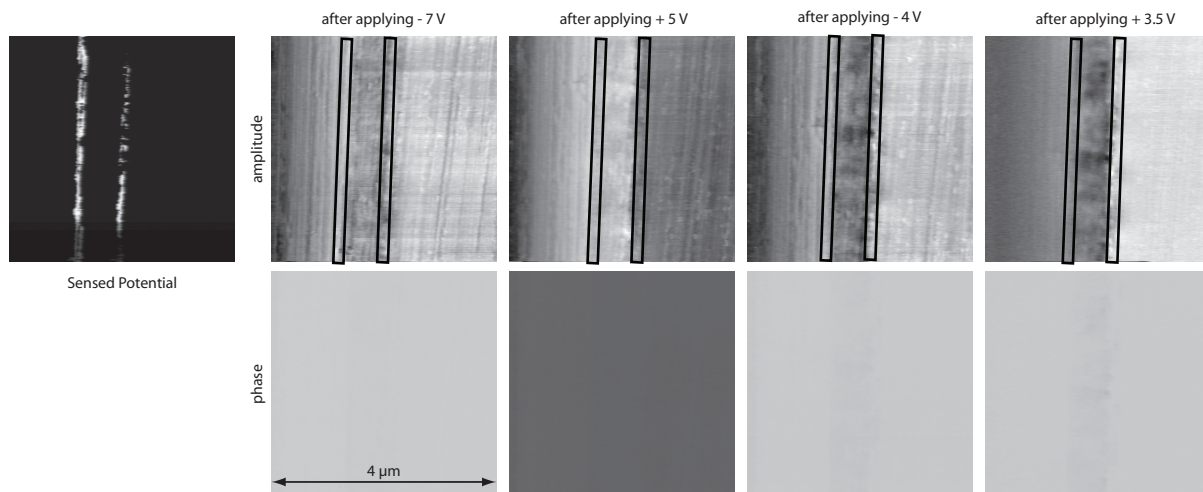


Figure 3.12: The phase of the piezoelectric response is changing with the polarisation direction throughout the whole sample. In the images from the left to the right, the switching pulse is reduced. In the last image, the voltage of +3.5 V is not sufficient to switch the polarisation of the film completely. In this case, the film can be hypothetically identified in the phase image. The sample vibrations due to the converse piezoelectric response in the ferroelectric film is also seen outside the film. Black rectangles indicate the 100 nm thick electrodes.

Better results using mechanically polished films were obtained on a sample with a 400 nm thick PZT layer. An example of the images is shown in figure 3.13. The amplitude image (a) reveals a high piezoelectric activity in the PZT film. At the bottom, the film is assumed to be in a multidomain state as indicated by the dark and bright patterns through the film cross section in the phase image (b). These images are however not good enough for our purpose of polarisation reversal mechanism studies.

Nevertheless, we learnt the following important points summarised below:

- Short circuits between top and bottom electrodes are a major problem when thin films (< 400 nm) are polished mechanically.
- Thick films and large top electrodes may induce bending modes in the sample, which are superimposed on the local converse piezoelectric response. This brings about difficulties for a reliable domain identification.
- Mechanical polishing is delicate and has to be done very carefully due to the small scales and the short-circuit problem between top and bottom electrodes.

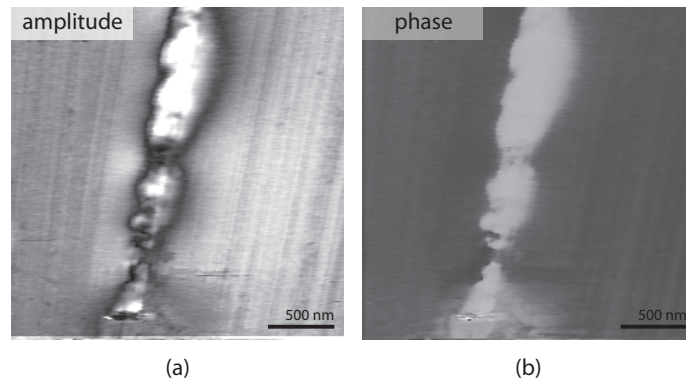


Figure 3.13: An example of a PFM image of a sol-gel prepared PZT film with a thickness of about 400 nm. The piezoelectric activity (a) is clearly at a maximum in the film, however, it is not homogeneous. There are areas of low activity (comparable to the neighbouring non-piezoelectric layers), which can either be domains or mechanical damage due to the mechanical polishing. The phase image (b) cannot reveal the domain structure very well.

- PFM in a scheme with the driving ac voltage applied between the conductive AFM probe and the top and bottom electrode does not work in a stable way. This is due to the direct contact between the conductive AFM tip and the electrodes during scanning.
- Different layers, which cannot be distinguished by topography, can be identified with the scanning potential method described above (best with a small ac field and lock-in technique in order to avoid damage to the tip, compare the point above)

Ionic Polishing

Micromachining has gained importance in the last thirty years with the rapid growth of semiconductor industry and the trend to miniaturisation. The need for a fast prototyping and correction of mistakes in very small circuits resulted in the development of a powerful tool to remove and deposit materials on a submicron scale, the focussed ion beam (FIB). This technique does not involve lithography, but can be used to manipulate the sample directly. However it is not well suited for mass production purposes, because it is slow and does not offer the upscaling and multiplication possibilities of lithography.

Apart from industrial production, it has proved to be very useful for fundamental studies of ferroelectricity on a very small scale [Birk et al., 1991, Tiedke et al., 2001]. A review on the FIB technique was written by Melngailis [Melngailis, 1987].

The FIB works on a similar principle to an electron microscope and the commercially available machines are usually called *dual beam*, because they have an electron and an ion beam. For imaging, the electron beam is used as in a standard scanning electron microscope (SEM). The accelerated and focussed ions are used for the machining. They carry more energy and momentum due to their larger mass. The impact of the ions on the material in the vacuum chamber of the instrument leads to either milling, doping, or deposition of material, depending on the ion dose, the acceleration voltage, and the precursor gas, (see figure 3.14). The ion-solid interactions may further lead to damage and electron emission, which can be used for imaging according to a SEM. Metal deposition,

figure 3.14(c), is achieved with precursor gases, which contain the desired species of insulator, semiconductor, or metal elements. The ion beam breaks the precursor molecules and induces the highly local deposition of the material.

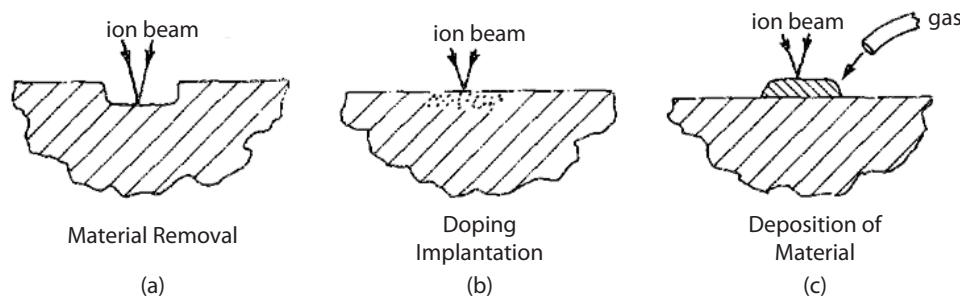


Figure 3.14: The principle possibilities of submicron manipulations offered by the focussed ion beam (FIB). Illustration from [Melngailis, 1987].

Different ion species are used in the ion beam: Ga^+ , H^+ , H_2^+ , He^+ , Ne^+ , Kr^+ , or Ar^+ . The most common ion is Ga^+ from a liquid metal source. The beam diameter depends on the focussing system and the beam current due to the repulsion between the ions. It is in general larger than 5 nm. For very precise, and thus slow, manipulations, the beam current is on the order of picoampères.

In ferroelectrics, the FIB technique has been applied successfully for investigations on size effects [Ganpule et al., 1999, Alexe et al., 2004, Nagarajan et al., 2003] (compare section 2.4.3), but special sample geometries have never been prepared for cross sectional PFM studies.

Radiation damage in ferroelectric PZT due to the Ga^+ -ion implantation has been reported [Stanishevsky et al., 2002]. It was claimed that the ion dose should be minimised when working with ferroelectric perovskites. The cited group reported on the loss of lead and oxygen, while gallium accumulated due to the irradiation with Ga^+ -ions in a 5–10 nm thick surface layer. Annealing did not heal it and recover the ferroelectric properties.

In our first attempt with a new FIB tool (Nova 600 Nanolab, produced by *FEI Company*) at the Center for Micro- and Nanotechnology (CMI) of EPFL, we tried to produce a sophisticated structure. Having a very small piezoelectrically active element (the produced structure is shown in figure 3.15), it was assumed that the bending mode motion of the complete structure (including the substrate and the electrodes as described in the mechanical polishing section 3.3.3) observed in thick films could be minimised. However, the complexity of the structure involved a large dose of Ga^+ ions, which suppressed the ferro- and piezoelectricity.

Annealing procedures in argon and oxygen (may lead to a Ga_2O_3 compound) atmospheres failed to recover the ferroelectric properties. The annealing procedures were also detrimental to the polished cross section due to the differences of the thermal expansion coefficients of the various layers.

In order to reduce the ion dose, the sample geometry was drastically simplified. A 1.2 μm thick sol-gel prepared PZT film [Taylor et al., 1996] with Pt electrodes was scribed on the substrate side, broken through a top electrode.

The sample was polished by FIB according to the following procedure: An additional Pt layer was first deposited on the top Pt electrode. This was an effective protection against the unavoidable milling due to scattered ions. The cross section was then milled

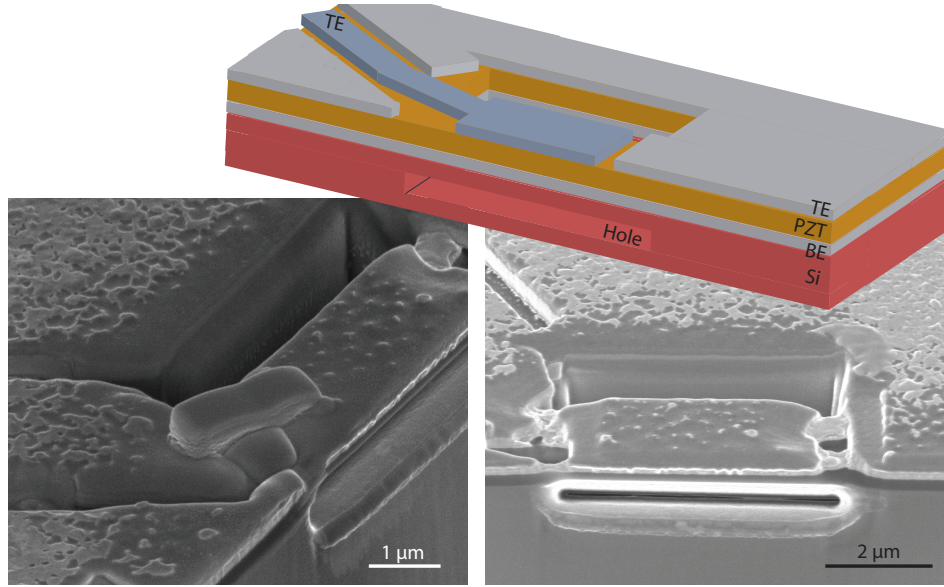


Figure 3.15: A scheme and two SEM images of the FIB-machined structures are shown. The ion dose to produce this was too high and the ferroelectric properties were suppressed.

on the broken face to level out the irregularities from the crack over a length between 5 and 10 μm . The final polishing step of the cross section produced a very smooth topography. This can be seen in the SEM image 3.16. The FIB preparation took between 0.5 and 2 hours depending on the charging problems with the sample.

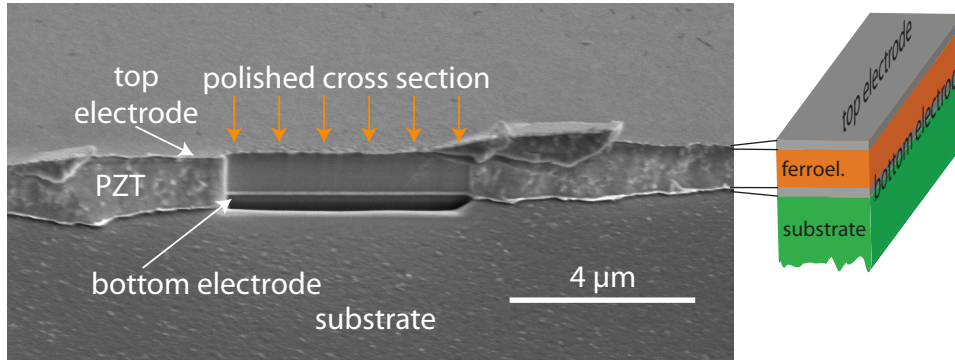


Figure 3.16: The polished cross section of PZT film between Pt electrodes and on a silicon substrate. On the right side, the structure is shown schematically.

Chemical analysis by energy dispersive x-ray analysis (EDX) of a polished cross section did not allow to identify a correlation between the Ga content and the distance from the polished cross section. The Ga content was always clearly below 1 %.

Measuring the polarisation hysteresis loop can reveal whether the ferroelectric properties were conserved during the FIB polishing. In the case of the minimised ion dose, the hysteresis changed little as shown in figure 3.17. The observable difference between the two loops is due to the difference in the maximal applied field. It is clear that the FIB processing had no significant detrimental impact on a large area (the top electrode size is about $1.8 \times 10^{-3} \text{ cm}^2$ or about 70 % of a circular top electrode with a diameter of 400 μm), since the polarisation in the loop after the treatment is about the same as before.

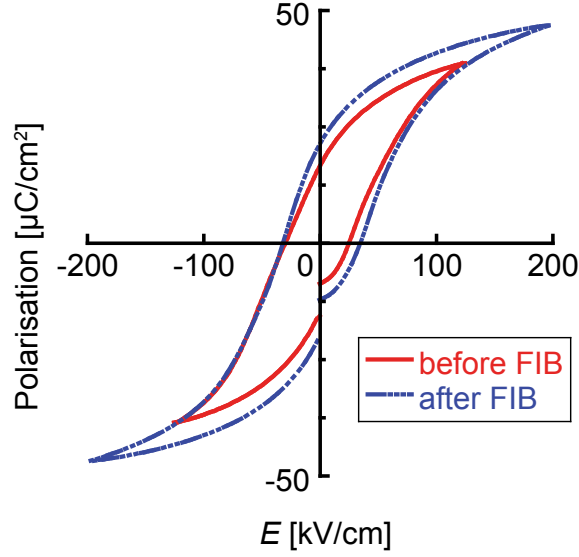


Figure 3.17: Polarisation hysteresis loops before and after FIB treatment. The loops are not influenced considerably, the difference seen between the loops is mainly due to the different maximal fields applied.

3.3.4 Probe-Sample Contact

The probe-sample contact is crucial for PFM studies on a sample without a top electrode. Si or Si₃N₄ cantilevers are used in most PFM studies. They are typically coated with either gold or Ir/Pt conductive layers. In order to keep the tip radii very small (typically about 25 nm), the metal coating has to be very thin. Alternatively, conductive doped diamond coating or highly doped Si tips can be used.

Due to mechanical wear, the thin conductive layer can be damaged easily at the very top of the probe. The electric field applied to the ferroelectric sample is therefore not only difficult to control, but also rather unstable during scanning. The converse piezoelectric response recorded in PFM is a function of the applied field and therefore also dependent on the tip quality.

Furthermore, we observed that the problem of the wear of the conductive layer is more critical with the application of a dc electric field. A dc field is more deleterious than an ac field.

The problem can be illustrated with the example of the potential measurement used to identify the ferroelectric film position between the electrodes on a sample. A small ac or dc voltage was therefore applied to bottom and top electrodes. The conductive AFM tip was scanned over the cross section sensing the electrical potential on the cross section (see the above section). This simple experiment resulted in images that changed with time (compare e.g. figure 3.9).

SEM images (a) and (b) in figure 3.18 confirm the origin of this instability: the AFM tip lost the conductive coating and thus, the contact between the tip and the electrodes degraded very rapidly during the experiment.

As the contact area of the tip with the electrodes is very small, the current density may attain very high values. Assuming a contact area A of the order of the square of the tip radius of $20 \times 20 \text{ nm}^2$ and a resistance of $1 \text{ M}\Omega$, the current density is $I/A = U/(RA) \approx$

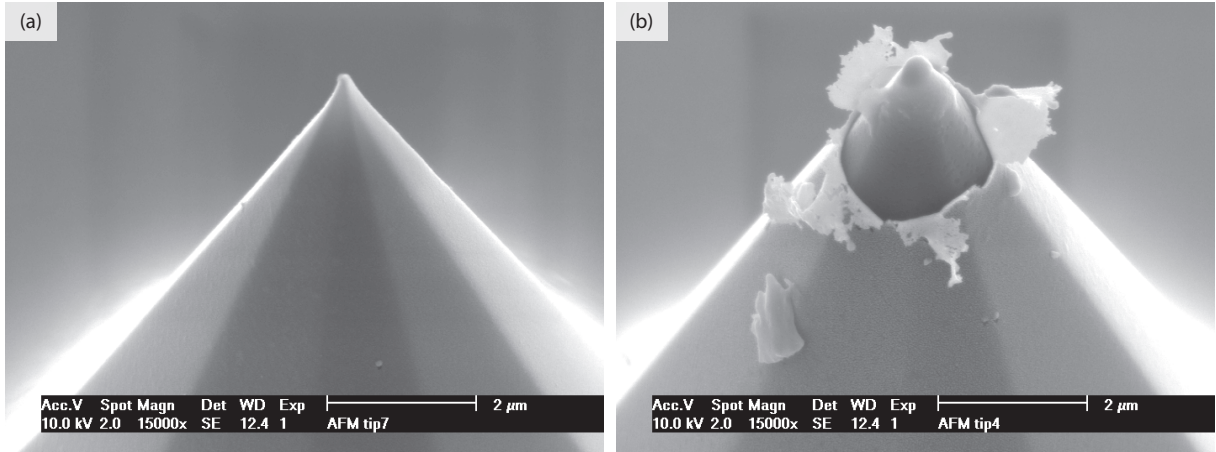


Figure 3.18: SEM image of the freshly gold sputtered AFM tip (a) and a used gold coated AFM tip after direct contact to the top and bottom electrodes in potential (dc) measurements (b).

10^5 A/cm^2 with an applied voltage of only $V = 0.1 \text{ V}$. Current densities can thus be very high and may destroy the thin conductive film on the AFM tip.

Cantilevers with a full metal body are expected to solve the wear problem inherent to conductive layers. They are under development [Steen, 2007, Steen et al., 2006], but are not yet commercially available. We could only do tests with such probes and measured a specially prepared sample, in which the potential on a metal conductor drops continuously. Figure 3.19 shows a scanned area of $10 \times 10 \mu\text{m}$. The z -axis depicts the sensed potential by the full metal tip provided by J. Steen.

For our experiments, we preferred the mode, in which the electric field was applied between the two thin-film electrodes. The advantage is not only that the field is more homogeneous, but also that the measurements do not depend on the conductive coating of the AFM probe.

3.3.5 Experimental Method and Technique

The standard PFM technique has been described in section 3.1. For cross-sectional observations of domains in thin films, the experimental technical configuration can be maintained. The changes concern mainly the sample, its mounting and preparation. Another difference is the fact that the scanning was performed at the edge of the sample, where the cross section was polished (we preferred the FIB prepared over the mechanically polished, “sandwiched” samples).

A polished sample was glued to a vertical face of a steel cuboid with the polished cross section showing up, i.e. towards the AFM tip, as shown in the photograph in figure 3.20. A thermal glue (or wax, which liquifies at about 60°C) was used to fix the sample on a the cuboid. Reheating enabled the nondestructive removal of the sample from the steel holder after the experiment. The cuboid was placed on the AFM piezoelectric scanning unit, which is equipped with a magnetic sample holder.

In order to map the domain pattern on the cross section, the polished part was scanned with an AFM tip while a driving ac voltage was applied between the top and bottom electrode of the sample, as illustrated in figure 3.21. The electric field was thus perpendicular

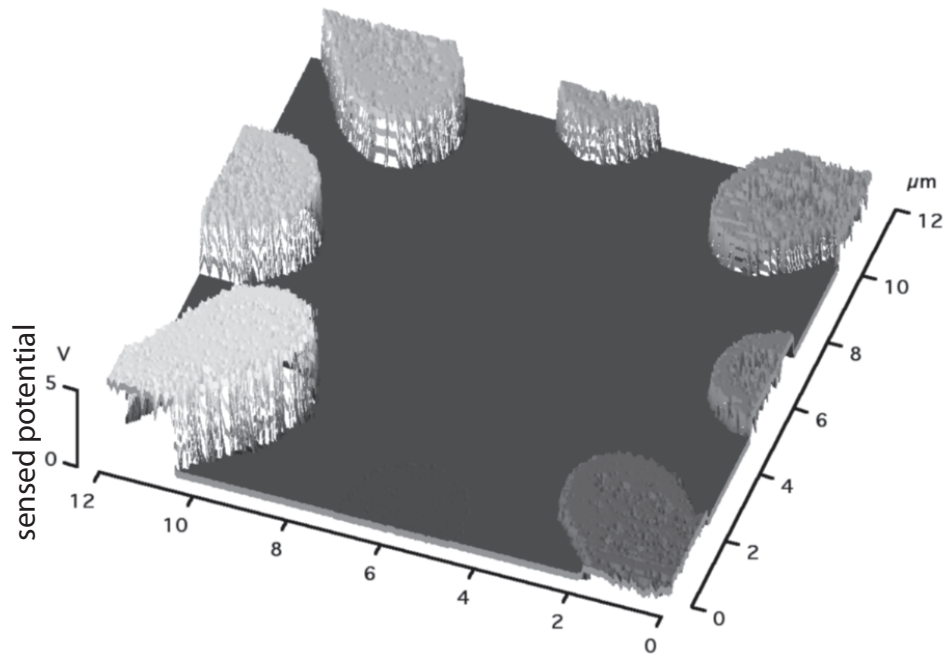


Figure 3.19: The potential drop from finger to finger on a continuous metal line on a silicon substrate is sensed by a full metal body cantilever provided by Jeroen Steen [Steen, 2007]. The potential levels decrease from 5 (brightest finger) to 0 V.

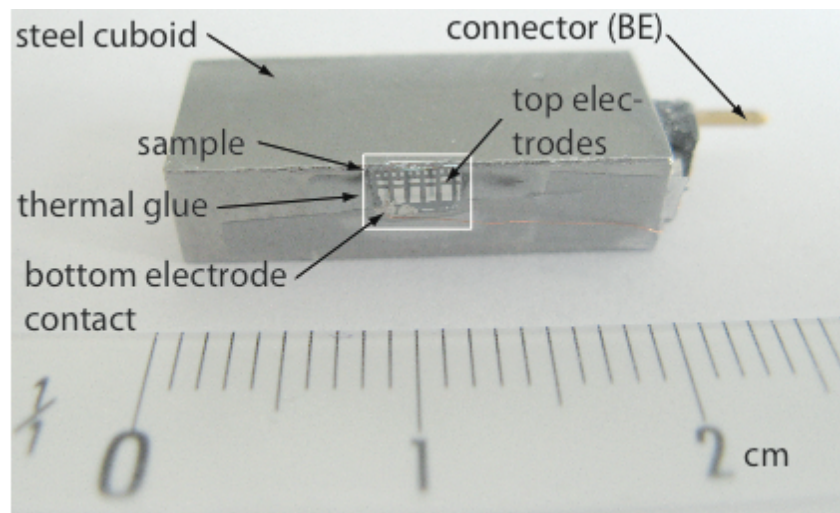


Figure 3.20: Photograph of the sample with bright Pt top electrodes glued to a steel cuboid and ready to be put into the AFM system. The electric connection from the connector via a thin copper wire to the bottom electrode (BE) can be seen. The length unit of the ruler in at the bottom are centimeters.

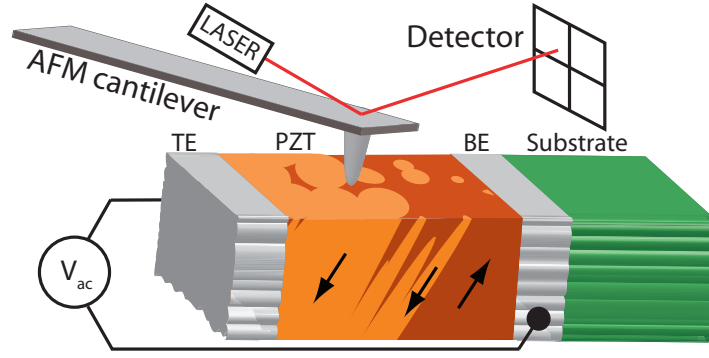


Figure 3.21: The AFM setup with the tip scanning over the cross section of the top (TE) and bottom electrode (BE), PZT film, and substrate.

to the axis of the sensing AFM tip as shown in figure 3.11(a). This is a main difference compared to standard PFM methods, where the electric field is in general normal to the scanned surface and in the direction of the tip axis.

The experimental difficulties are specified below:

- (i) Averaging of the response across the whole sample and bending modes
- (ii) Scanning the probe close to the edge of the sample
- (iii) Localisation of the polished cross section and scanning of the correct area
- (iv) Identification of the various layers
- (v) Contacting the top electrode

The first problem has already been addressed before. The use of small capacitors and multidomain states can reduce bending modes.

The last four points are technical problems. The identification of electrodes and testing of the electrode contact can be done by the potential-sensing technique described in section 3.3.3.

Scanning close to the edge of a sample can cause problems. When the AFM tip falls from the polished cross section, the scanning gets unstable due to the feedback unit that provokes an over-compensation. The feedback unit regulates the sample elevation in order to keep a constant force between the AFM tip and the surface (*constant force* mode, section 2.7.5). Activities to limit the feedback of the AFM control unit when working close to the edge of a sample existed, but were abandoned¹⁰. We found that the problem is less critical when the scanning range is carefully chosen. Besides that it is worth to mention that the tip falls not immediately into the free space next to the sample due to its geometry. The tip's half cone angle is 25° (given by the tip manufacturer¹¹) and allows therefore theoretically for an additional lateral scan of about $6\mu\text{m}$ for a tip height of $17\mu\text{m}$.

¹⁰Very sadly, our colleague Hirotake Okino, who was working among a lot of other things on this problem, passed away in a tragic traffic accident on July 27th 2006.

¹¹found on the web site: http://www.budgetsensors.com/force_modulation_afm_probes_electri.html

The third problem of finding the cross section arises due to the fact that it can hardly be seen in the optical microscope provided with the AFM system. SEM images of the sample were therefore taken and were used for sample positioning with respect to the tip. The optimal scanning regime with the tip on the cross section relative to the edge and the electrodes was found based on topographical scans.

The fifth problem of contacting only concerns the top electrode. The bottom electrode extends over the whole sample and can be easily contacted (can be seen in figure 3.20). The top electrode has to be as small as possible in order to avoid the averaging problem and bending modes. The small scale of only a couple of tens of micrometres makes it difficult to contact the top electrode. We used very small probes with thin tungsten wires of a diameter of $25\text{ }\mu\text{m}$ and a tip radius of $0.5\text{ }\mu\text{m}$ (*American Probe & Technologies*, model 72F-B4/05). These small probes were mounted to a triaxial micropositioner (*Quater Research & Development*, model XYZ 300ML). An additional binocular microscope was used to position the small tips on the top electrode of the sample.

A further advantage of the very small and soft probes is that only a small force is applied to the sample. Due to the scanning displacement of the sample relative to the contact probe, jerking can occur when the electrodes are contacted by a hard probe. With soft probes and the resulting small forces, the scanning of the sample relative to the contact probe is smoother.

3.3.6 Set of Acquired Data

Analogous to the standard PFM technique, sample topography and piezoelectric response are recorded simultaneously. Recording of the local vertical and lateral AFM tip response allows in principle the distinction of the longitudinal and transverse piezoelectric response. The longitudinal response is the response in the direction of the polarisation and the applied electric field. It can thus be related to the d_{33} coefficient (for more details, see section 2.1.7). The transverse vibration is perpendicular to the applied field, it corresponds to the d_{31} coefficient. Depending on the crystal symmetry of the investigated samples, other shear mode coefficients may contribute to the transverse or lateral response as well.

In the cross section configuration described here, the transverse mode is detected as the vertical movement of the tip, hence perpendicular to the applied electric field and the polished surface. The longitudinal piezoelectric response translates to a lateral motion of the tip, or more precisely, a torsion of the cantilever around its axis as illustrated in figure 3.22.

An example of a set of images with topography and piezoelectric response is shown in figure 3.23. The cross section of the PZT film was prepared by FIB as described.

The topography image in figure 3.23 reveals a very smooth polished cross section with a root-mean-square surface roughness of only about 1–2 nm. The roughness was determined from profile lines as shown in figure 3.24 over the indicated range. The inset in the graph shows the full topography image with the two profile lines. A coordinate system is given there with the scanning direction x , the edge direction y and the height direction z .

The color scale from black to yellow/white in topographical images is, as usual, plotted as a linear function of the local height (z direction). The sample is mounted on the right side of the image, which means that the top electrode and the ferroelectric layer are followed by the bottom Pt electrode and the substrate from the left to the right in the image. The black area on the left represents the free space in front of the edge of the

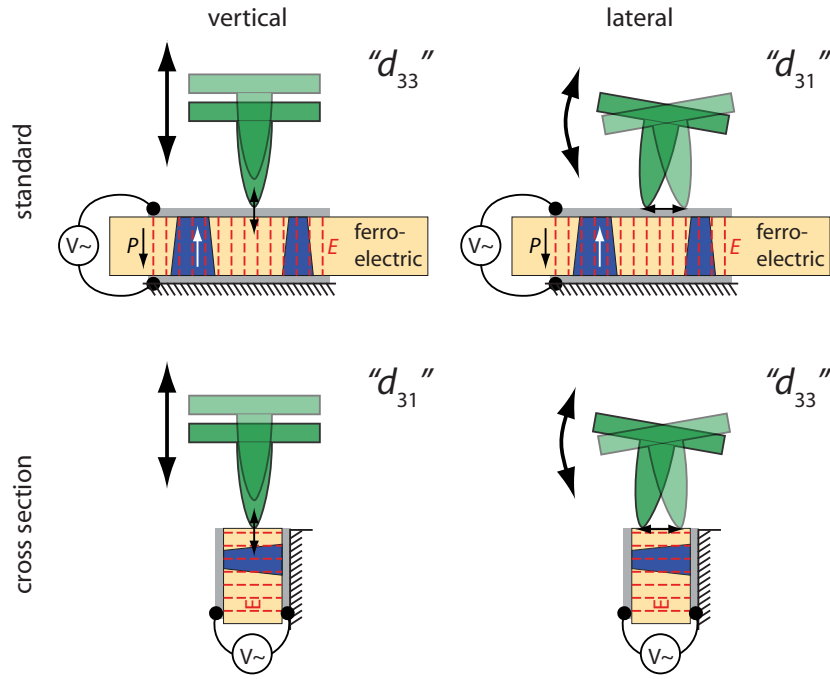


Figure 3.22: The vertical (z direction in the scanning system) and the lateral signal are detected by the AFM cantilever as a bending in the cantilever direction and a torsion around its axis, respectively. The vertical and lateral signals correspond to the transverse (" d_{31} ") and longitudinal (" d_{33} ", in field and polarisation direction) piezoelectric response, respectively, in the cross-sectional testing.

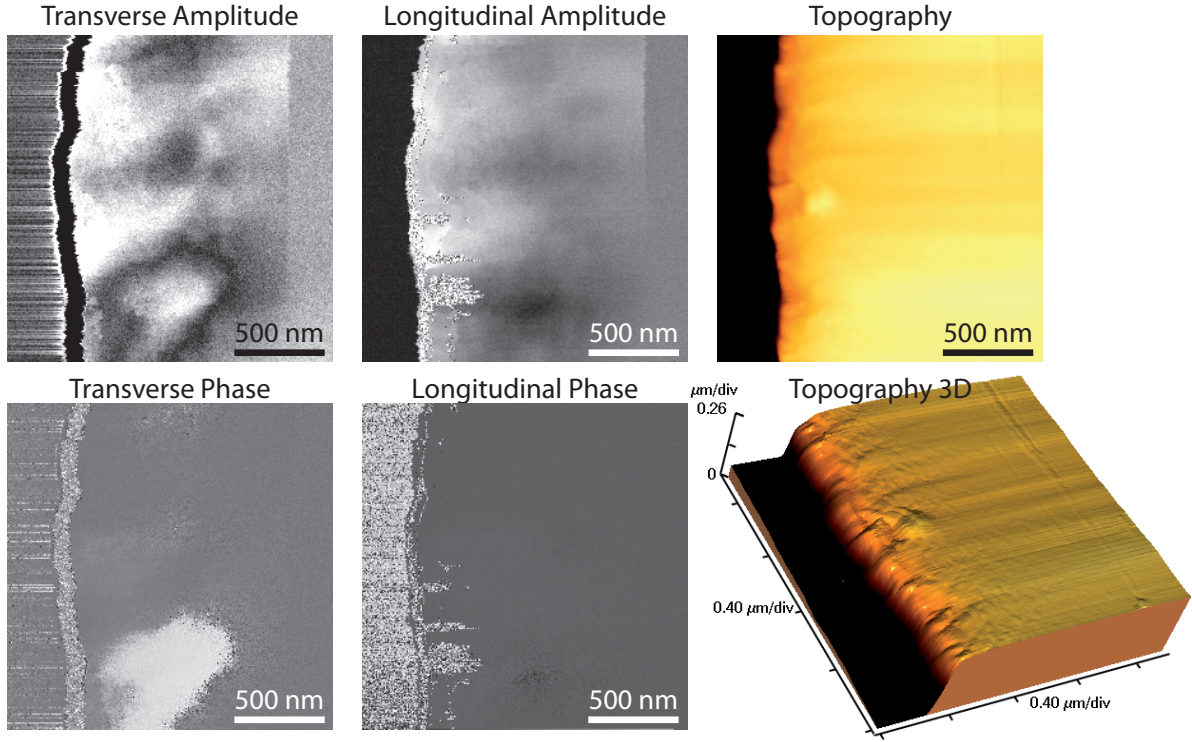


Figure 3.23: An example of a ferroelectric film cross section mapped by PFM, with topography, amplitude, and phase images as indicated and taken simultaneously.

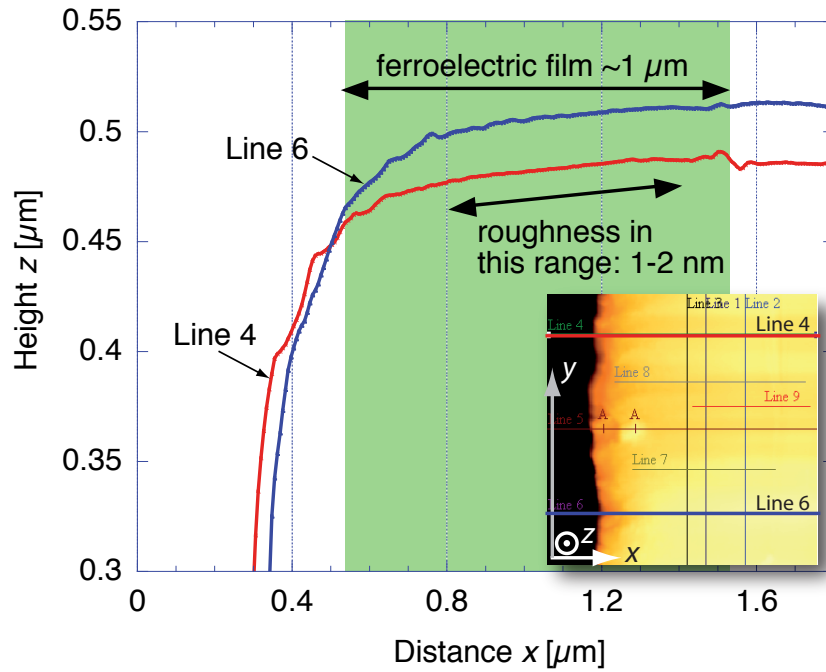


Figure 3.24: The polished cross section is illustrated here in two topographical profile lines taken at the positions indicated in the inset of the topography image.

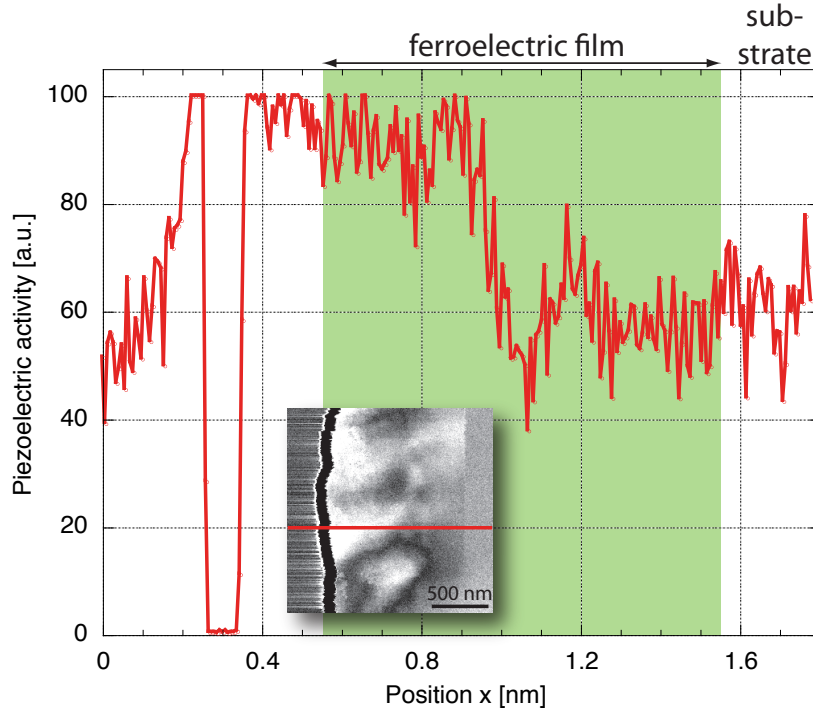


Figure 3.25: The transverse piezoelectric activity is shown as a function of the AFM tip position across the film section.

sample. The topography is illustrated in a convenient 3D representation, in which the edge can be seen clearly. The aspect ratio between the z direction and the x and y directions is usually not maintained. In the example shown in figure 3.23, the height is superelevated by about four times.

3.3.7 Discussion

The piezoelectric response signal is represented in an amplitude and a phase image for both, the vertical and the torsional cantilever deflections. The white colour in the amplitude images corresponds to the highest piezoelectric activity, the black for no piezoelectric response, and the states between the two extremes translate linearly to a grey scale. The brightest regions with the highest piezoelectric activity in the transverse amplitude image of figure 3.23 are at the free end of the ferroelectric film. There are dark spots in the centre of the film and noisy, darker regions at the left and right edge of the image. The difference in the contrast originates from the domain pattern, and also in the mechanical clamping of the film. Since the PZT film is attached to the bottom electrode, which is itself grown on the thick substrate, the film is fixed on the right hand side. The top electrode, on the left side in the images of figures 3.23–3.25, is about ten times thinner than the ferroelectric film and mechanically free. The mechanical constraints of the film are thus asymmetrical and the piezoelectric response increases towards the left edge as illustrated in figure 3.25.

The high piezoelectric activity on the left side of the image and outside the film is due to the fact that the AFM tip picks up the vibration even on a position $x \lesssim 0.55 \mu\text{m}$, which is out of the film already and on the top electrode. The piezoelectric film works as an

actuator on the “free” top electrode at that place and the sensed vibrations is therefore of an amplitude comparable to the one at the edge of the film. Even further away, the tip is in the free space next to the sample and a zero piezoelectric signal is measured, before a fast decaying signal is sensed again at positions $x \lesssim 0.25 \mu\text{m}$. This time, however, not with the apex of the tip but rather with a side wall of the AFM probe. The piezoelectric response profile in figure 3.25 can give misleading information due to the continued contact of the tip to the sample even when it is away the polished cross section and in the free space. It is therefore crucial to compare the piezoelectric profile to the topographical information.

On the right hand side of the transverse amplitude image, in the region of the bottom metal electrode and the substrate, the tip collects a piezoelectric response comparable to the response at this edge of the ferroelectric film. There are contributions due to the continuity of the medium and from a possible bending mode of the sample. The latter, macroscopic contribution also persists in the ferroelectric film and the top electrode. This contribution can however be reduced if the film is brought to a multidomain state. The macroscopic piezoelectric response is then effectively reduced compared to the local response, due to the averaging of the piezoelectric effect over all polarisation directions.

The bending effect of the sample composed of a thin ferroelectric film on a several hundreds of micrometres thick silicon substrate has been observed with interferometer measurements and gave rise to the development of the double-beam configuration [Kholkin et al., 1996]. Detailed measurements combining the interferometer technique with 2D sample scanning have shown that the sample bending can be observed even several millimetres away from the top electrode due to the piezoelectric effect of a PZT film on a Si substrate [Chao et al., 2005]. Further measurements in our group showed that a $1 \mu\text{m}$ thick PZT film in a capacitor structure with a diameter of $500 \mu\text{m}$ could induce resonance in the Si substrate with a frequency corresponding to the mechanical and geometrical properties of the substrate [Damjanovic, 2007].

The profile of the piezoelectric response across the cross section can therefore be explained qualitatively. We conclude, that it is more difficult to characterise ferroelectric films in a single domain state than in a multidomain state and that the quantitative analysis of the piezoelectric response is very difficult due to macroscopic bending contributions.

The PFM phase images are theoretically bicolour, because the phase has in principle only two states for up and down polarisation — even for arbitrary polarisation directions, which are not parallel or perpendicular to the sensing direction of the AFM tip. The transverse and longitudinal piezoelectric contribution of an arbitrary polarisation orientation would be in- or out-of-phase, depending on sign of the piezoelectric coefficient. Deviations from the two distinct theoretical values may occur due to mechanical and electronic limitations, e.g. concerning the bandwidth of the electronics or the inertia of the tip [Abplanalp, 2001].

In the transverse phase image of figure 3.23 only two states are present. They differ by almost exactly 180° as expected from the sign change due to opposite polarisation reversal as shown in figure 3.26 with the phase response of one scanned line. The phase outside the ferroelectric layer in the free space is rather blurred, probably due to the not well defined contact between the tip and the sample (on the side walls of the AFM probe).

There is another interesting issue we would like to address in figure 3.23. In the transverse amplitude image, black (i.e. zero piezoelectric response) domain walls are clearly observable. Together with the 180° phase change (bright-dark contrast), this is a strong indication for a domain. However, no domain can be observed in the longitudinal amplitude and phase image, representing the actual configuration of the piezoelectric

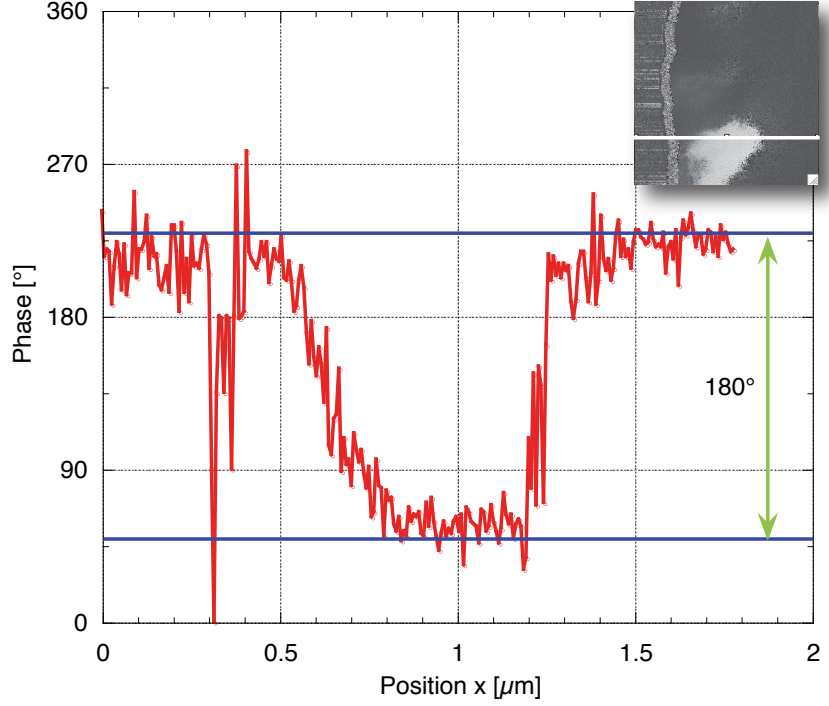


Figure 3.26: The phase values on one line of the transverse phase image in figure 3.23. The image inset identifies the line.

coefficient d_{33} .

One can wonder, why the domains in the longitudinal amplitude and phase images do not appear as expected, with domain walls and phase changes as in the transverse images. Two hypotheses are formulated below:

- (i) A special domain configuration is present with polarisation directions, which are not changing the sign in both, the lateral and vertical oscillations.
- (ii) The longitudinal and the transverse response are averaged over different probed volumes.

Reports on the polarisation reversal in several steps in perovskite materials suggest the first hypothesis [Rodriguez et al., 2004], in particular 180° polarisation reversal in several steps. This process is discussed in more detail in chapter 4.

The piezoelectric response parallel to the sample surface and out of the film plane originate from different sample volumes in general. Clamping is effective in all directions in the film surface whereas the ferroelectric film is not clamped in the out-of-plane direction. The difference in the mechanical constraints results in general in a different probed volume for the longitudinal and the transverse piezoelectric response. The vertical response can be expected to stem from a deeper volume while the lateral signal is expected to be probed in a more shallow surface region.

The cross-sectional PFM technique described was — to the best of our knowledge — first realised in our published work [Gysel et al., 2006]. The technique offers a more detailed insight into the switching mechanism of ferroelectric thin films. Careful sample preparation and solutions to avoid bending modes, which are superimposed on the local

piezoelectric signal and may conceal it, are essential for successful mapping. The potential for nucleation and polarisation reversal studies is very promising. Results of our studies as well as possible interpretations are discussed in chapter 4.

In a recent report, Liu et al. used the cross-sectional PFM technique to image the polarisation in a PZT (rhombohedral) capacitor with a thickness of 180 nm. They applied an electric field between the electrodes and a conductive AFM tip — claiming a higher resolution in this setup — and found that the nucleation is activated at lower fields than the forward (approximately at the coercive field) and sideways growth (approximately a field of three times the coercive field) [Liu et al., 2007].

3.4 Summary

Piezoelectric Force Microscopy is a powerful tool for microscopic investigation of the polarisation reversal. Our novel approach of a cross-sectional testing of ferroelectric films offers the crucial opportunity to study nucleation, interface effects, and the domain growth through the films. In the following chapter, an example of such a study is given.

Chapter 4

Experimental Results of Cross-Sectional PFM

Abstract Different stages of polarisation reversal in $\text{Pb}(\text{Zr},\text{Ti})\text{O}_3$ ferroelectric films have been directly observed using a technique of cross-sectional piezoelectric force imaging. Analysis of the local piezoelectric response measured across the cross-section strongly suggests that polarisation reversal occurs via oblique domain growth rather than by growth of domains perpendicular to the film plane. The proposed approach represents a valuable extension to the piezoelectric force microscopy (PFM) and contributes to a better understanding of results observed using more standard techniques. Particularly, oblique domain growth explains the gradual variation of piezoelectric response amplitude commonly observed in planar PFM images.

Our Contribution The experimental feasibility of cross-sectional PFM and its utility as a powerful tool for studying the polarisation reversal in ferroelectrics has been substantiated. We reported for the first time a successful cross-sectional mapping of domain patterns [Gysel et al., 2006]. The apparent contradiction between observations interpreted as a fast sideways growth and the classical scenario of a fast forward growth could be explained by an oblique polarisation direction with respect to the film plane. The domain growth in the studied films was sideways-limited. Surface-stimulated nucleation, preferentially on the electrode with a negative potential, was found and interpreted by a depletion layer at the interface.

4.1 Experimental Details

A tetragonal (film T) and a rhombohedral (film R) polycrystalline PZT film were used for the experiments. The composition of two the films was chosen on the Ti-rich and the Zr-rich side of the morphotropic phase boundary of the PZT phase diagram given in figure 2.7. The Zr/Ti ratio of the film T was 60/40 and of the film R 45/55. The film R was deposited by chemical solution deposition on a Pt coated silicon wafer in four steps (refer to the TEM image, which clearly shows the four layers corresponding to the four processing steps in figure 4.1). The tetragonal film was deposited by multi-target sputtering on a Si substrate with a Pt electrode and a TiO_2 seed layer. Their thicknesses of 1.2 (R) and 1.0 μm (T), respectively, were measured with the electron microscope and further confirmed by AFM.

Transmission electron microscope (TEM) images of the cross section confirmed the presence of a columnar film structure. It can clearly be seen in the bright field image in figure 4.1 that the columnar grains continue through the four layers, which are due to the sol-gel deposition in four steps.

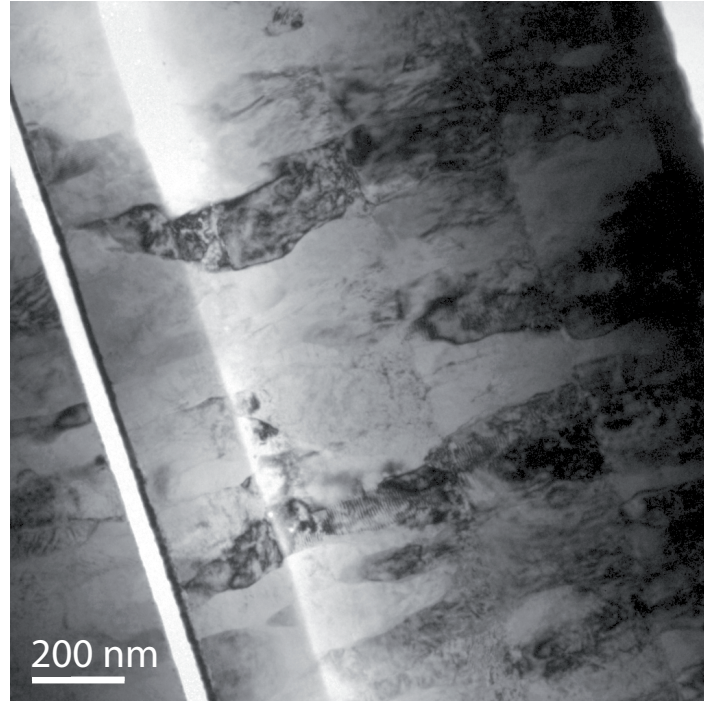


Figure 4.1: A TEM bright field micrograph of the rhombohedral PZT film prepared for the cross section PFM characterisation.

For the rhombohedral film R, a preferential (100) orientation of the grains was found in x-ray diffraction (XRD). For the tetragonal films, a preferential (111) orientation can be expected [Muralt et al., 1998].

Pt top electrodes were sputtered at room temperature and subsequently annealed at 550°C. The cross section needed for PFM experiments was prepared by wafer cleavage followed by polishing with a focused ion beam as described in section 3.3.3. The Ga⁺-ion dose was kept to a minimum in order to limit the damage of the ferroelectric material and the degradation of its switching properties. A spot where the cleavage line passes through a top electrode was used for preparation of the capacitor cross section.

The surface roughness was very low as was already discussed in section 3.3.6. SEM micrographs of the prepared cross sections of the film R and T are shown in figure 4.2.

4.2 Results

The nanoscale map of the polarisation distribution was obtained by PFM with ac and dc voltage applied between top and bottom electrodes, while the cantilever tip was used for detection of the mechanical displacement only. By scanning the capacitor cross section (figure 3.21), the piezoelectric vibration perpendicular to the capacitor surface associated with the longitudinal piezoelectric coefficient d_{33}^* was detected by lateral force microscopy,

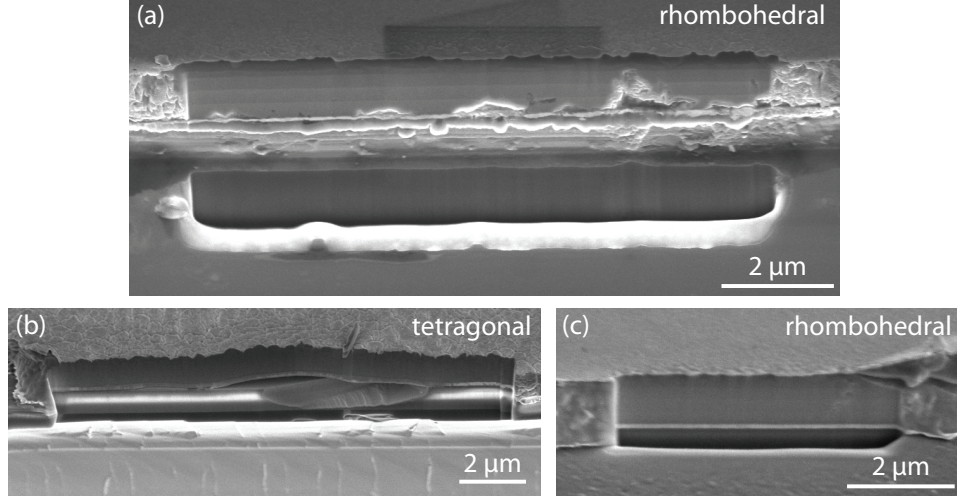


Figure 4.2: SEM images of the polished cross section of rhombohedral (a,c) and tetragonal (b) films. The four observable layers in image (a) are due to the sol-gel processing in four deposition and annealing steps.

whereas the vertical movement of the cantilever was related to the transverse piezoelectric coefficient d_{31}^* .

The capacitors were progressively switched by applying consecutive dc biases from -3.2 V to -6.0 V and from -12.0 V to 7.0 V respectively; the polarity was negative and positive with respect to the top electrode. After each bias step, PFM images of the amplitude and the phase of the local piezoelectric response were taken with an ac voltage of amplitude 0.9 V at zero bias field and a frequency of 19.3 kHz .

Figure 4.3 shows a polarisation hysteresis loop of film R. The triangular markers on the polarisation loop indicate the amplitudes of the applied voltage pulses, after which cross-sectional piezoelectric imaging was performed. Most of the images were taken around the coercive field. At this field, the up and down polarisation are balanced and bending modes of the sample are thus minimised. For the first measured triangle, at about zero polarisation (and a voltage of -3.2 V), one would expect a domain pattern with an equal amount of up and down domains, i.e. the two types of domains would be contained approximately the same volume.

The PFM images taken at voltages as indicated by the triangles in figure 4.3 are shown in figure 4.4 for film R. The images (a)–(f) show the amplitude (left) and phase maps of the lateral force associated with the d_{33}^* piezoelectric coefficient, measured on the capacitor cross section of the rhombohedral film R. The top and bottom electrodes are marked as TE and BE.

The first image (figure 4.4a) represents the mixed polarisation state, where different directions of polarisation are clearly seen in the phase image as bright and dark regions. As the amplitude of the poling voltage increases, the bright regions shrink down and finally disappear at a poling voltage of -6 V (figure 4.4f).

The presence of domain islands (R1, R2) can be observed in the PFM maps.

The images (a)–(p) in figure 4.5 represent the complete switching cycle in the tetragonal film T using the cross section technique, combined with a quasi-dynamic switching step technique with varying voltage, as for film R. In this example, the vertical response

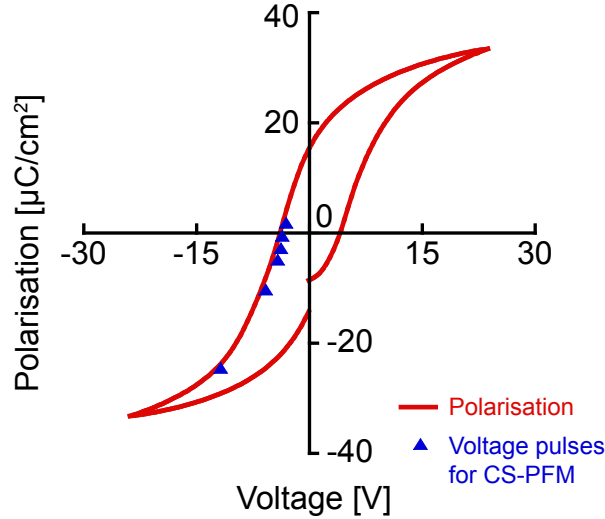


Figure 4.3: Polarisation hysteresis loop of the rhombohedral PZT sample with a thickness of about $1.2 \mu\text{m}$. The triangles indicate on the loop the amplitude of the switching voltage pulses, after which the cross section was mapped by PFM.

signal corresponding to the d_{31}^* piezoelectric coefficient is exploited.

The film in a single domain state after poling with a voltage pulse of 20 V is shown in figure 4.5(a). The application of negative pulses with increasing amplitude induces switching with the appearance of a small domain T0 in image (b) close to the top electrode. This domain grows to the counter electrode whereas other domains of opposite polarisation appear in parallel to finally complete the switching process as shown in image (g).

The cycle is then continued by a second change of the sign of the applied voltage, in order to reverse the polarisation back to the original state as mapped in figure 4.5(a). An island T1 of inverse polarisation appears in the image (i) after a dc pulse of 4.0 V. With increasing pulse height, it expands in all directions and grows through the film (figure 4.5j-l). A second (T2) and a third (T3) reverse domain island become visible in the centre of the film in image (l), they testify for a domain reversal process including nucleation and domain wall motion. The fully polarised film is shown in the image (p) with the polarisation direction opposite to the initial state.

Polarisation hysteresis loops with increasing maximal fields are depicted in figure 4.6 for the tetragonal film.

The loop with the largest maximum field was compared to the polarisation reversal as presented in the images of figure 4.5. By integration of the area with reverse polarisation and comparison to the total area, a switching ratio from -1 to 1 was calculated. The switched area was determined from images of the transverse phase response (bright and dark) for each applied voltage pulse. The areal switching ratio plotted versus the pulse amplitude in figure 4.7 the phase images that were the basis for the area ration calculation are inserted for some points. This PFM phase area loop is compared in the same graph to the polarisation hysteresis loop with the highest maximal field from figure 4.6.

The areal analysis of the switching domains in figure 4.7 is an illustration for the domain patterns that appear during the polarisation reversal, which happens at fields close to the coercive field.

Direct comparison of the polarisation and the areal ratio loops is however misleading.

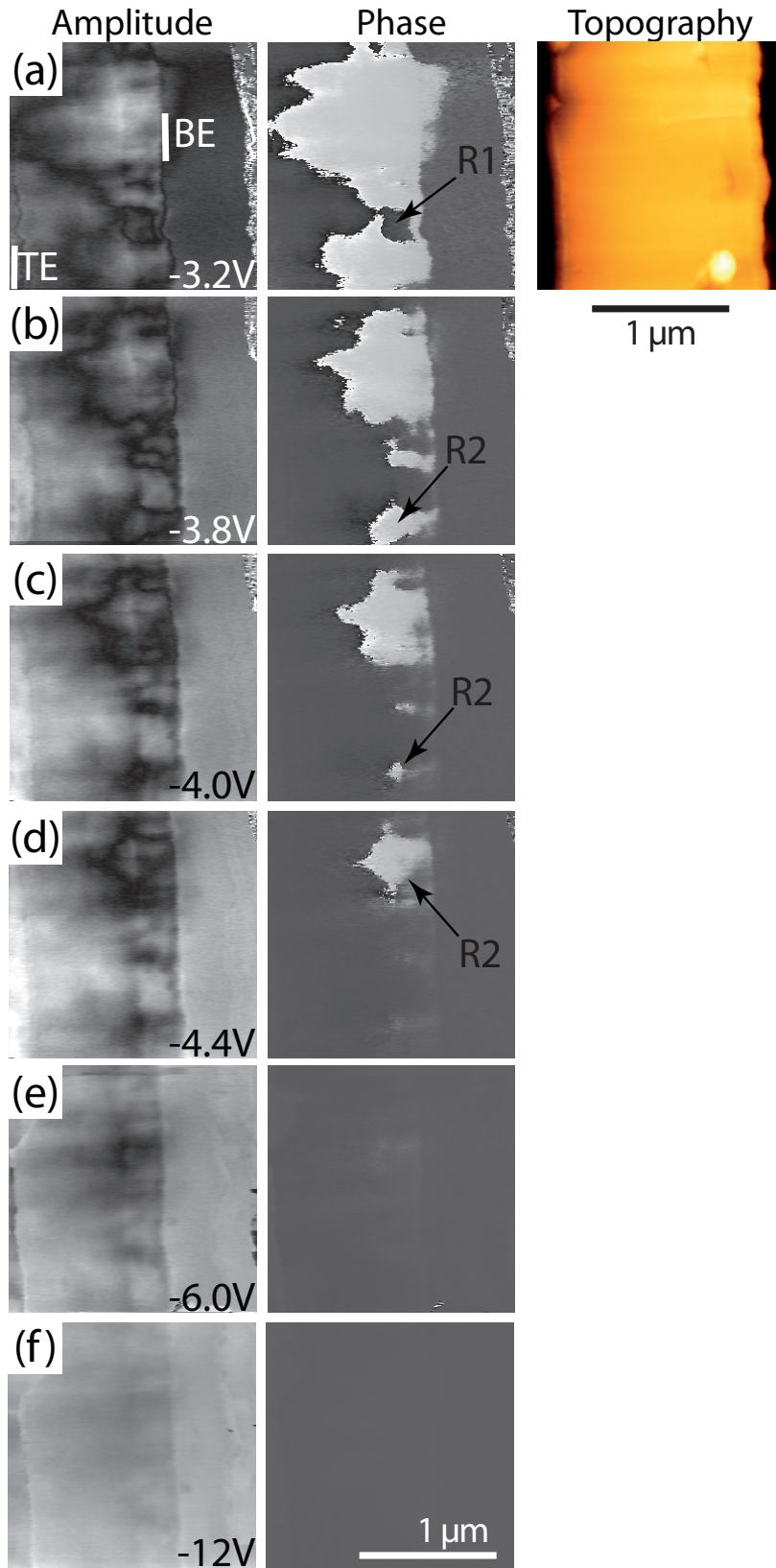


Figure 4.4: Quasi-dynamic switching observed on the cross section of a rhombohedral PZT film. Amplitude and phase signals collected from the longitudinal piezoelectric response. The voltage pulses are indicated with respect to the top electrode.

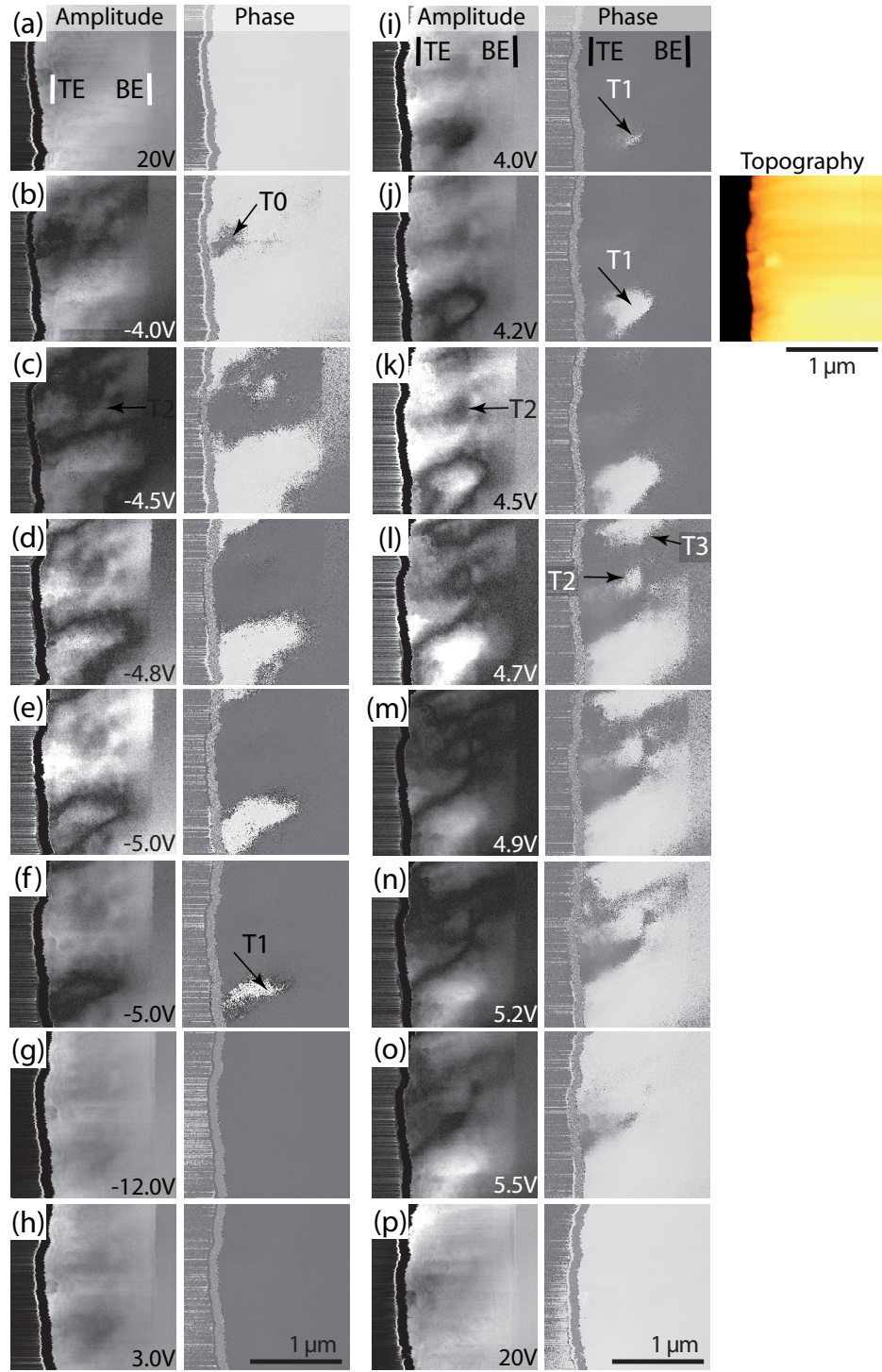


Figure 4.5: PFM images collected from the transverse (vertical in PFM) response of the tetragonal film T after consecutive dc pulses of given amplitude with respect to the top electrode.

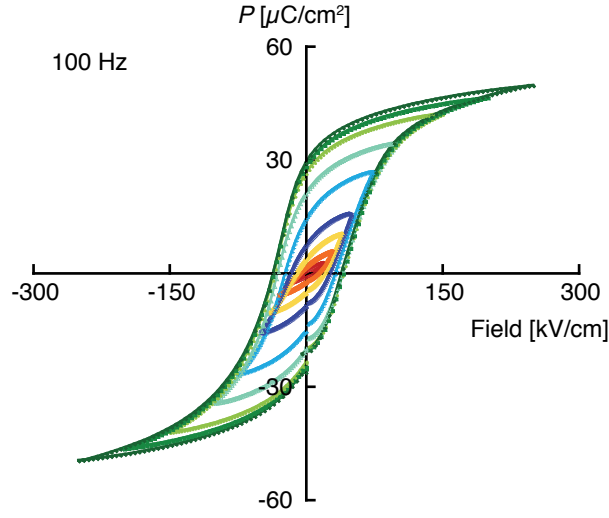


Figure 4.6: Polarisation hysteresis loop of the tetragonal PZT sample with a thickness of about $1.0\ \mu\text{m}$. Several loops with increasing maximal field were recorded at a frequency of 100 Hz.

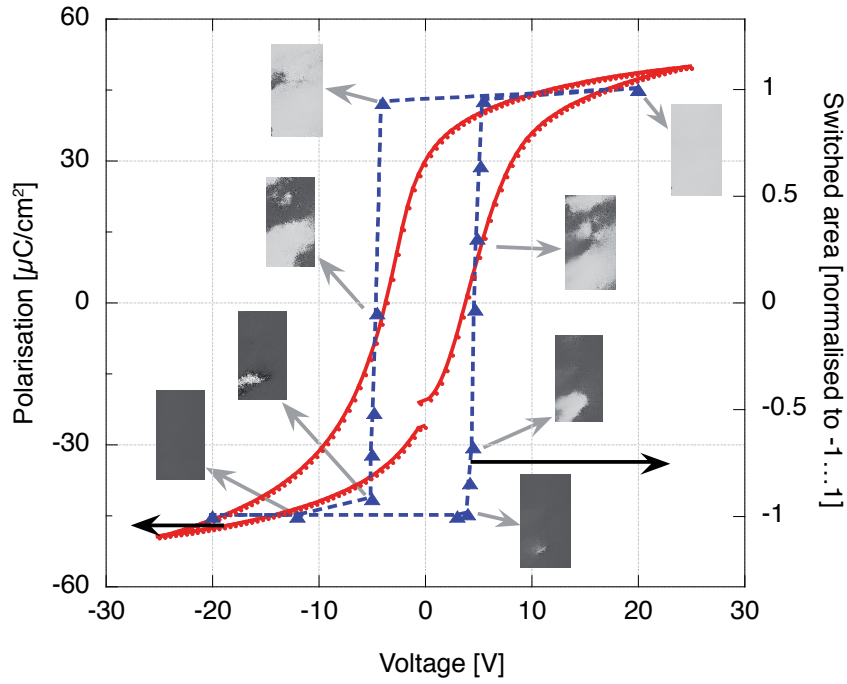


Figure 4.7: The hysteresis loop resulting from the polarisation reversal characterised by PFM is shown by the dashed line. The areal ratio of the black and white domains in the phase images (see figure 4.5) are plotted against the applied switching pulse amplitude. The continuous line shows the ordinary measured polarisation hysteresis loop.

The polarisation loop consists of the response of the whole capacitor, while for the PFM data, only a very small area and a few grains are taken into account.

4.3 Discussion

4.3.1 Polarisation Reversal Mechanism

The polarisation reversal of the ferroelectric films by consecutive pulses of increasing amplitude shown in figure 4.5 can be analysed in terms of nucleation, domain wall growth, and polarisation direction.

Considering possible domain growth mechanisms as discussed in section 2.3, the presence of isolated poled regions separated from the electrodes, i.e. regions T0-T3, R1-R3, is an intriguing feature of the images in figures 4.4 and 4.5. Interpretation of this finding, in terms of traditional switching concepts, is not straightforward. The scenario illustrated in figure 4.8(a), where the nucleation is followed by forward growth of needle-like domains perpendicular to the electrode, fails to explain the island-shaped structure of the images (a), (c), and (d) of figure 4.4 in film R as well as the images (b),(c),(f),(i) and (l) in the tetragonal film shown in figure 4.5. An alternative model involved zig-zag-shaped domains moving from one electrode to another as shown in figure 4.8(c) [Hong et al., 1999]. Obviously, it cannot explain the observed structure with the domain island in the film centre, either.

In principle, such a domain pattern with islands with reversed polarisation may be attributed to a separate grain, where the remnant polarisation is pinned by charged defects. However, analysis of the amplitude images does not support this scenario. Grain boundaries are normally observed in the amplitude image even in a completely poled state, while no signs of grain boundaries are observed in the amplitude images in figure 4.4(f) or 4.5(a),(h), and (p), where the film is fully switched.

The situation may be clarified if the switching process is considered assuming an oblique direction of the spontaneous polarisation with respect to the film plane. The justification of this assumption comes from the analysis of the capacitor structure studied. In the rhombohedral $(111)_c$ -oriented PZT film eight directions of spontaneous polarisation are possible, including the vertical direction and at 71° and 109° inclined directions (figure 4.9).

For the annealed PZT film grown on a Si substrate the lattice mismatch and difference in thermal expansion coefficients should result in a tensile strain. This kind of strain can favour oblique orientations of the polarisation [Tagantsev et al., 2002b, Cook et al., 1963, Spierings et al., 1995]. In that case, one may expect that polarisation reversal will occur via the growth of needle-like 180° domains inclined at about 19° with respect to the film plane. For the tetragonal film with an $(111)_c$ orientation and six possible polar directions, this inclination angle is approximately equal to 35° (figure 4.10).

In the context of these arguments, the island-like poled regions observed in the images in figure 4.4 and 4.5 can be interpreted as cross sections of inclined 180° domains that nucleated at the region adjacent to the electrode within the depth of the film (figure 4.8c). As soon as the needles reach the cross section of the thin film, a domain island appears in the PFM image. According to the literature (see section 2.3), the sideways growth is slower than the forward growth and leads to a domain island expansion subsequent to their appearance on the cross section.

It is important to note that due to such oblique domain orientation, the images in figure

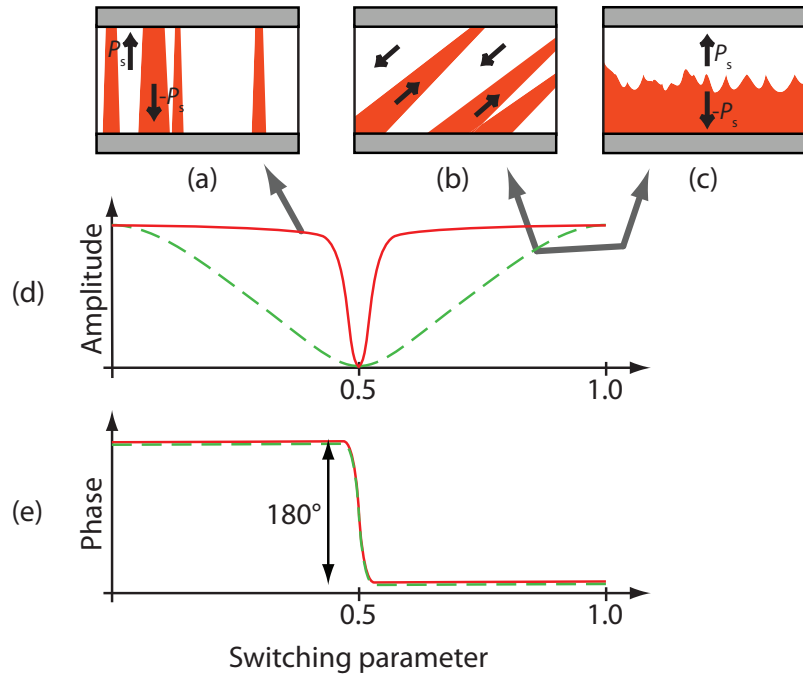


Figure 4.8: Three suggested scenarios for the growth of domains with anti-parallel polarisation (black arrows). Sideways growth (a), sideways growth of inclined needles (b), and “zig-zag-shaped” forward expansion (c). The expected amplitude (d) and phase (e) response during the polarisation reversal of a ferroelectric film for three different switching mechanisms. In the case of sideways-limited growth of perpendicular domains (a), the amplitude changes stepwise when a domain wall is crossing the local probed volume. In the case of sideways-limited growth of inclined domains (b) and forward-limited growth (c), the amplitude drops gradually to zero and increases back to the maximum when the sample has switched its polarisation through the whole thickness.

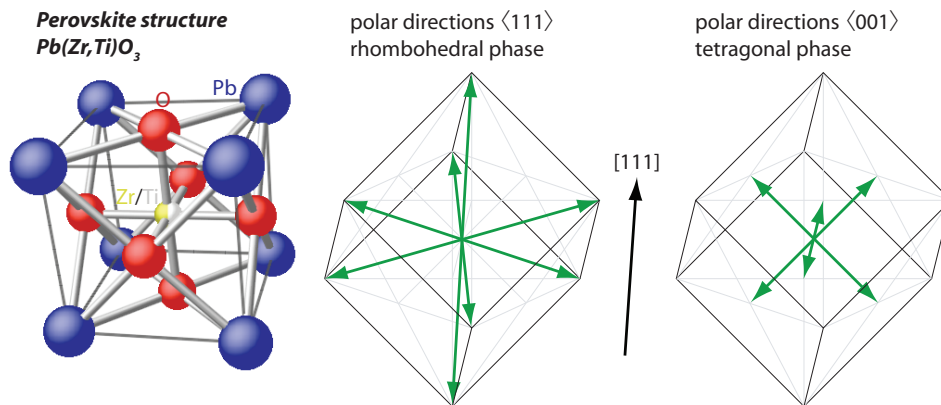


Figure 4.9: Polar directions of a perovskite structure in the rhombohedral phase are along $\langle 111 \rangle_c$ axes. The polar directions of a tetragonal crystals are along $\langle 001 \rangle_c$.

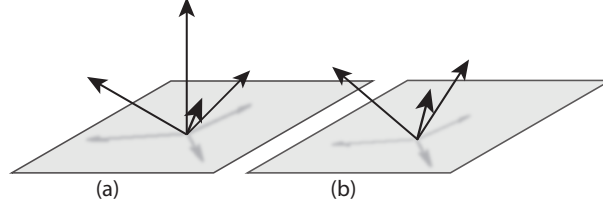


Figure 4.10: Possible orientations of the polar directions in a $(111)_c$ -oriented tetragonal (a) and rhombohedral (b) film.

4.4 and 4.5, which represent a local piezoelectric response averaged over a depth comparable to the film thickness, may include contributions from different domains. Hence, the borders between the poled areas might not be very sharp and a gradual variation of the piezoelectric response amplitude would be expected [figure 4.8(d)] .

This is also valid for standard PFM characterisation of ferroelectric capacitors, where the top electrode surface is scanned. If the domain orientation is oblique, the amplitude of the piezoelectric response may change continuously [figure 4.8(d)], with a diffuse border between regions of different polarisation. Such behaviour of the piezoreponse amplitude has previously been interpreted as the manifestation of a “tail-to-tail” domain configuration associated with a zig-zag-type domain growth [Hong et al., 1999, Hong and Setter, 2002]. However, in the context of the present results this may be interpreted in the framework of the traditional scenario of fast forward- and sideways-limited domain growth [figure 4.8(a)] , wherever it is permitted by an oblique orientation of the spontaneous polarisation [figure 4.8(c)].

4.3.2 Surface-Stimulated Nucleation

The cross-sectional studies discussed in this section allow for the identification of the nucleation sites across the film thickness. Even though the resolution of the instrument may not be sufficient to observe small nucleus of critical size, the first appearance of a reverse domain indicates the nucleation site. There are two indications of the nucleation sites:

- (i) a region of opposite polarisation appears,
- (ii) a reduced piezoelectric response (amplitude) over domain walls or within region with a phase change, due to averaging over reverse and original domains in the probed volume.

If both of the mentioned characteristics are present in PFM images after the application of a poling pulse and a reduced pulse of opposite polarisation (in order to induce the start of polarisation reversal), such a region can be associated with a nucleation site.

Such an analysis of the nucleation location in rhombohedral film, strongly suggests a nucleation at the electrode with the negative potential. An example is given in figure 4.11. In the fully poled film shown in image (a), the phase image looks completely homogeneous.

In figure 4.11(b), a pulse of -5.0 V applied to the bottom electrode (while the top electrode is at ground potential) induces nucleation of opposite domains at the ferroelectric-bottom electrode interface. This can be seen by the reduced amplitude in the regions

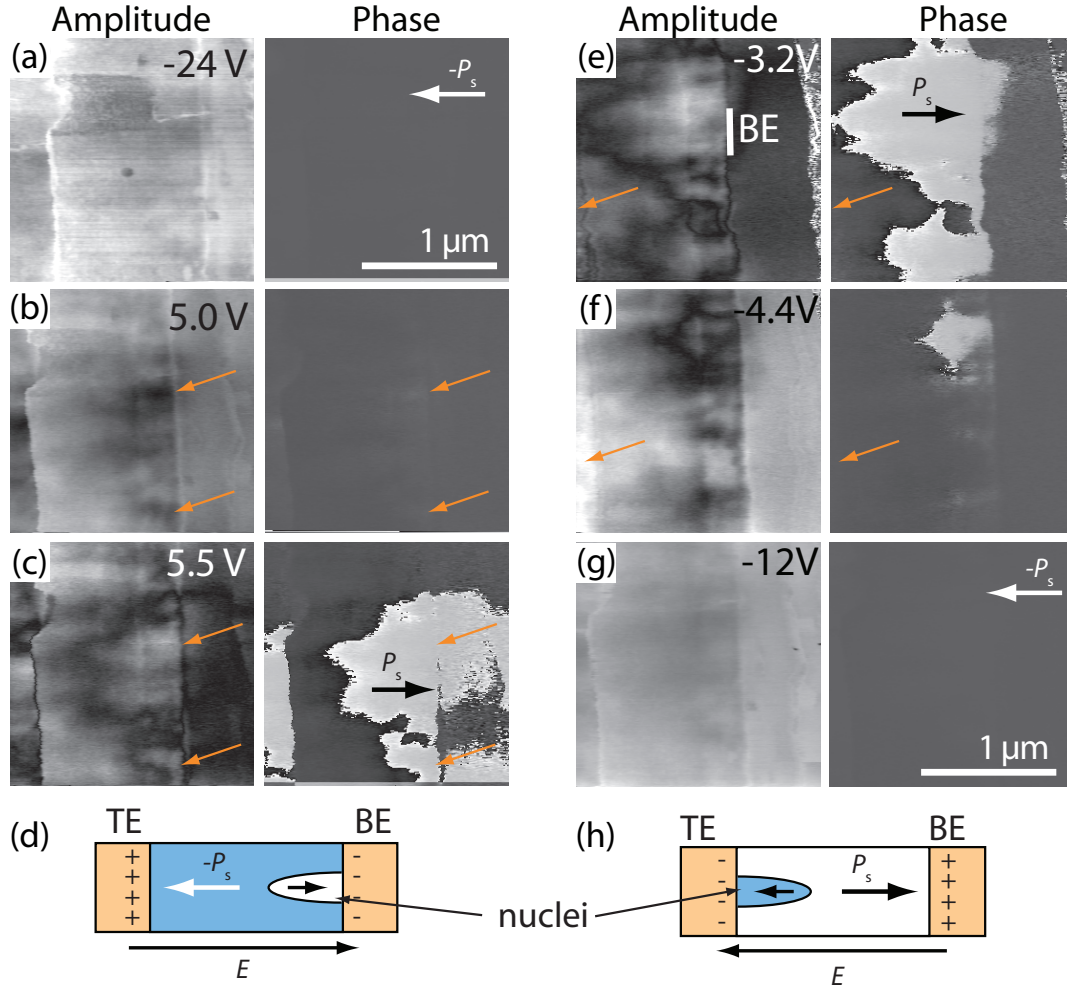


Figure 4.11: Amplitude and phase PFM images collected from the response of the rhombohedral film after consecutive dc pulses of a given amplitude with respect to the top electrode (TE). In images (a-c) a reverse domain appears at the bottom electrode when an electric field is applied as shown figure (d). For the antiparallel field (e-h), a reverse domain nucleates at the top electrode. Nucleation occurs preferentially on the electrode with the negative potential. The domains grow then to the counter top electrode through the film (c; e-g). Primary nucleation sites are indicated by inclined arrows.

indicated by the arrows. The nuclei are however too small to exceed the response of the surrounding domains for the given resolution of the instrument. Nevertheless, the opposite response of new born domains leads to a substantially lower average response as is illustrated by the dark colour (indicated by the arrows). Figure 4.11(c) shows that the domain in fact grew around the nucleated region and that a phase contrast appears as is expected for a polarisation reversal.

Another poling series is shown after poling the film with a positive voltage with respect to the top electrode in figures 4.11(e-g). Half of the film has already been switched by a pulse of -3.2 V in figure (e). The unswitched regions are clearly located at the bottom electrode to which a positive potential was applied. Upon the increase of the amplitude of the switching pulse, the (dark) domains grow to the counter electrode. We can therefore assume that the nucleation happened at the top electrode; a possible location in the centre of the largest domain is indicated by the arrows in figure 4.11(e) and (f).

We can summarise that the nucleation for the polarisation reversal in both directions occurs preferentially at the electrode with the negative potential. This is a strong indication for surface-stimulated nucleation.

Discussion

The preferential nucleation on the electrode to which a negative potential is applied can be explained with the *depletion-assisted nucleation* model [Tagantsev, 1997]. It is based on a Schottky barrier model with a depletion layer. In a semiconductor, a depletion layer builds up when a semiconductor is brought in contact with a metal. The work function difference between the electrode and the semiconductor or a high concentration of interface states induce a space charge region coupled with a built-in field.

In contrast to classical semiconductors, the depletion takes place at deep levels in most perovskite ferroelectrics. Even though this levels may reach thermodynamical equilibrium at annealing temperatures, the charges are frozen in deep levels at room temperature. The depletion layer is illustrated in figure 4.12(a,b).

The depletion width w depends on the concentration of deep levels N_d in the material as given in the relation:

$$w = \sqrt{\frac{2\varepsilon_0\varepsilon_l V_{bi}}{qN_d}}, \quad (4.1)$$

where ε_l , and q are the lattice dielectric constant and the charge, respectively.

It can be seen schematically in figure 4.12(c,d) that the built-in field E_{bi} is independent of the film thickness if the film thickness, h , is large enough to allow for a neutral layer between the depleted layers ($h > 2w$). However, if the thickness is smaller than double the depletion layer width $h < 2w$, the film is fully depleted and the built-in field depends on the film thickness h [Tagantsev et al., 1994]:

$$\begin{aligned} E_{bi} &= \frac{qN_d}{\varepsilon_0\varepsilon_f} w \text{ for } h > 2w, \text{ and} \\ E_{bi} &= \frac{qN_d}{\varepsilon_0\varepsilon_f} \frac{h}{2} \text{ for } h \leq 2w. \end{aligned} \quad (4.2)$$

Here, ε_f is the effective dielectric constant of the ferroelectric.

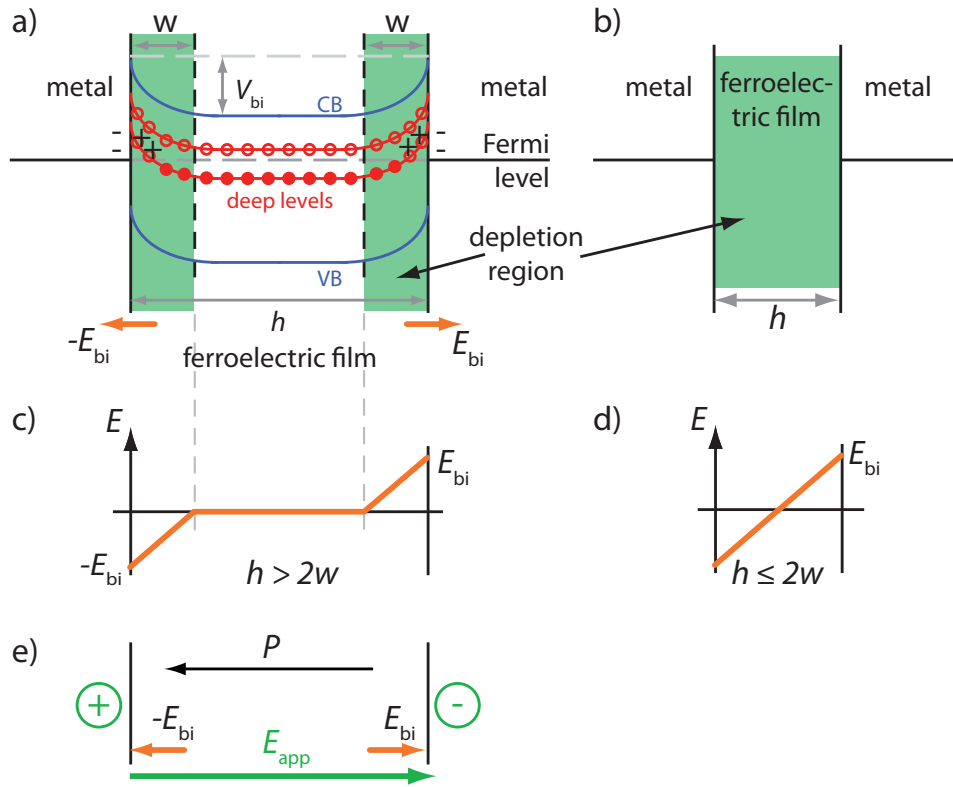


Figure 4.12: Metal-ferroelectric-metal junction with Schottky barriers and a partial depletion for (a) a ferroelectric layer thickness $h > 2w$ and (b) full depletion for $h \leq 2w$. CB and VB are conduction and valence band, respectively.

To switch the film, it can be assumed that a threshold field E_{cn} is needed to create the first nuclei. In the case of a film with a depletion layer, the field seen by the ferroelectric is the sum of the applied field and the built-in field. The condition for nucleation is thus:

$$E_{\text{cn}} = E + E_{\text{bi}}. \quad (4.3)$$

Based on this equation, the maximal field in the film is achieved at the electrode to which a negative potential is applied.

Preferential nucleation on the electrodes with a negative potential is illustrated schematically in figure 4.12(c), where the built-in field is parallel to the applied electric field. This involves an upward band bending towards the interfaces in the ferroelectric as depicted in figure 4.12(a). If the polarisation reversal occurred preferentially on the positively biased electrode, the band bending would be downwards.

In a study on leakage conduction in PZT capacitors with Pt electrodes, the field dependent leakage current could be interpreted in terms of a space-charge influenced injection model [Stolichnov and Tagantsev, 1998]. In order to explain the experimental data, a band structure in the ferroelectric identical to the one shown in figure 4.12 with upward banding towards the interfaces was used to model the leakage current dependence (fig. 11 in the cited reference) and agrees thus to our conclusion about the preferred electrode for nucleation.

In the tetragonal film, the first reverse domain T0 appears also on the top electrode with the negative potential in figure 4.5(b). Many reverse domains T1-T3 appear however as islands rather between the electrodes than close to one of the them. This makes it difficult to judge whether they were grown from a nucleus on the top or bottom electrode. Nevertheless, the region adjacent to the bottom electrode with the negative potential in the images 4.5(l-o) is reversed before the region close to the counter electrode. This is an indication for a nucleation at the electrode with the negative potential at the bottom as well.

4.4 Summary

A modified PFM technique of cross-sectional imaging has been applied for studying polarisation reversal in ferroelectric films. The observed patterns of amplitude and phase of the local piezoelectric response enable an insight into the switching mechanism of a rhombohedral and a tetragonal (111) PZT film suggesting that the polarisation reversal occurs via sideways growth of 180° domains, which are inclined with respect to the normal of the film plane normal. These results may influence the interpretation of PFM images widely used in ferroelectric film characterisation. In particular, they explain the gradual change of amplitude typically observed in piezoelectric response maps measured on ferroelectric capacitors used in nonvolatile memories. Surface-stimulated nucleation, preferentially at the electrode with a negative potential, was explained by depletion model at the interface.

Chapter 5

Polarisation Reversal in Ferroelectric Polymers

Abstract Ferroelectric polymers offer a unique combination of a decent remanent polarisation, low permittivity, and easy integration on semiconductors due to the low processing temperature. Ferroelectric polymers, including the copolymer of vinylidene fluoride and trifluoroethylene P(VDF-TrFE), have been investigated in bulk and thick film forms for many years. Recent progress in ultrathin film processing made these materials attractive for low voltage applications as well as for basic studies exploring the fundamental limits of ferroelectricity [Bune et al., 1998, Ducharme et al., 2000].

Our Contribution A combination of microscopic and macroscopic methods used for the first time in organic ferroelectrics enabled a better insight into polarisation reversal of the copolymer of vinylidene fluoride and trifluoroethylene P(VDF-TrFE). Piezoelectric force microscopy (PFM) and a fast pulse switching technique together with switching charge measurements suggested that the polarisation reversal is impeded by a restricted domain growth. This limits the applicability of the conventional Kolmogorov-Avrami model and the potentially better suited nucleation-limited switching model with a broad distribution of nucleation times for individual regions for the reversal kinetics.

We demonstrated that an interface-adjacent passive layer may impact on the switching properties and gives rise to a retardation of the polarisation reversal. Furthermore, an extraordinary dielectric constant increase was observed in the films with a passive layer due to an additional domain wall contribution. Capacitors with aluminium electrodes were more prone to passive layer effects than samples with gold electrodes.

5.1 Introduction

The structural, piezoelectric, pyroelectric, and ferroelectric properties of the “classical” family of ferroelectric polymers, vinylidene fluoride and its copolymers, were addressed in a number of publications [Nakamura and Wada, 1971, Lovinger et al., 1987, Furukawa, 1989, Legrand, 1989, Kepler and Anderson, 1992, Bauer, 1996, Zhang et al., 1998] as well as [Kochervinskii, 2005, Sorokin et al., 2005, Furukawa et al., 2006]. The physical nature of the polarisation reversal in P(VDF-TrFE) remains under debate and the role of the intrinsic ferroelectric switching and extrinsic interface effects is not completely clarified [Kliem and Tadros-Morgane, 2005, Naber et al., 2006]. The question arose especially

with the use of aluminium electrodes, where a pronounced thickness dependence of switching time was found [Kochervinskii, 2005, Furukawa et al., 2006]. Even though macroscopic characterisations such as dielectric measurements or pyroelectric and polarisation loops have been performed quite extensively, from thick to ultrathin films, studies of ferroelectric polymers on a submicron scale involving piezo-force scanning probe microscopy (PFM) are still limited [Chen et al., 1999, Rodriguez et al., 2007] compared to oxide ferroelectrics¹.

The focus of this chapter is on an understanding of the switching mechanisms in PVDF-based ferroelectrics, including the effect of electrodes, by combining microscopic and macroscopic experimental methods. The switching properties of the P(VDF-TrFE) films with reactive (Al) and noble (Au) electrodes, are directly compared over a wide temperature range. The comprehensive body of experimental data is analysed in terms of the classical polarisation reversal model.

5.2 Fabrication and Methods

5.2.1 Film Deposition

The 70:30 mol % copolymer of vinylidene fluoride and trifluoroethylene, purchased from *Solvay Solexis S.A.* in a granule form, was dissolved under stirring at 60°C for at least 4 h in cyclohexanone. The solution was spun onto metallised Si substrates at a rotation speed of 3000 rpm and subsequently annealed at temperatures above 100°C to evaporate the solvent and to increase crystallinity.

The thickness of the spun polymer films was controlled for the specific solvent by two parameters: the concentration of the polymer dissolved in the solvent and the rotation speed during the deposition. Their influence was investigated briefly for solutions of 1, 3, and 4 mass % of the copolymer in cyclohexane. The plot in figure 5.1 reveals a linear relation between the inverse rotation speed for the limited data points.

The AFM was used to measure the film thickness. The polymer film was removed with a small soft stick over an area smaller than the maximum scan size of the AFM. An AFM line scan over the trench allowed then for the determination of the film thickness from the measured profile. The stick used has to be soft enough to avoid scratching of the bottom metal electrode and to enable an accurate measurement of the film thickness as illustrated in figure 5.2.

5.2.2 Deposition and Structuring of Top Electrodes

In order to investigate the effect of different electrode materials on the switching behaviour, samples with aluminium and gold electrodes were prepared in all possible combinations for top and bottom electrodes. The diameter of the circular top electrodes of the capacitors under investigation was between 75 and 200 μm .

The capacitors were produced by a photolithographic process. After the deposition of the copolymer film, the annealing process, and the deposition of the top electrode by evaporation without sample heating, a positive photoresist (S1813, Shipley²) was spun (standard: 3000 rpm during 30 s) onto the top electrode metal and dried for 1 min at

¹Pioneering PFM work was — paradoxically — conducted on this copolymer [Güthner and Dransfeld, 1992]

²More information is available here: http://cmi.epfl.ch/materials/S1813/S1813_1.htm

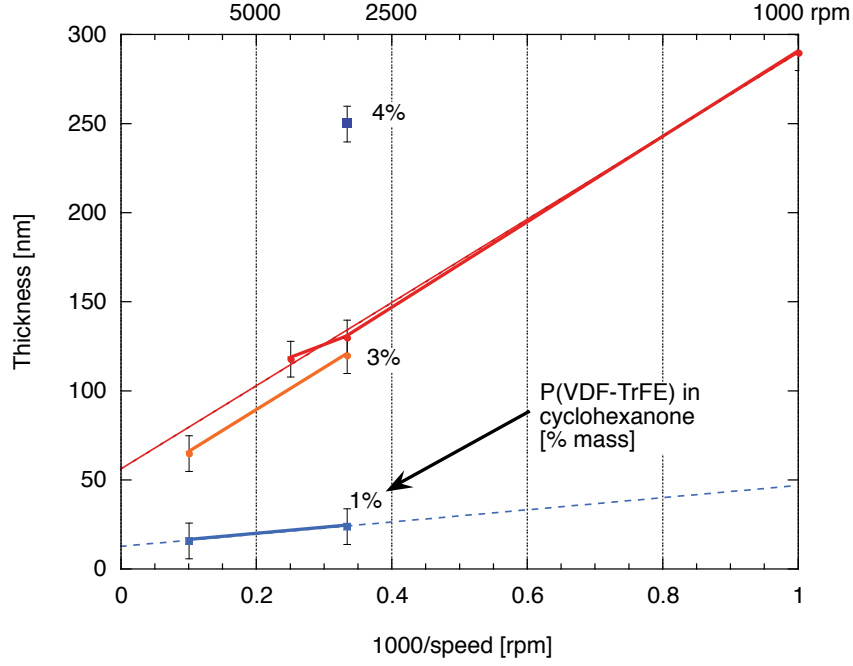


Figure 5.1: Thickness as a function of copolymer concentration in the solvent cyclohexanone and the rotational speed in the spinning process.

115°C. The photoresist was then exposed (the exposure time varied with the used electrode material: Au \sim 18 s, Al \sim 22 s) through a chromium mask with filled circles of various radii.

A developer (Microposit 351 from *Shipley*, diluted with water in a 1 : 5-ratio) removed in 45 s the portion of the photoresist, which was made soluble by the exposure. In the consecutive wet etching process with specific etchants, the unprotected portion of metals were etched. The etching agent for gold was a solution of potassium iodide (KI, 50 g; I₂, 12.5 g; H₂O, 500 ml) with a high etching rate: about 5 s were enough to etch the top electrodes of typically 100 nm. This etching solution was provided by the *Centre for Micro- and Nanotechnology* of EPFL³. The etchant for aluminium electrodes was a solution of acetic acid, nitric acid, phosphoric acid and some water [85 %-concentrated H₃PO₄, CH₃COOH (100 % conc.), and HNO₃ (70 % conc.) in a volume ratio of 75 : 5 : 3].

In order to finalise the samples, the remaining photoresist on the round metal electrodes was exposed to the light source and was removed by the developer as well. The use of acetone was excluded from the process due to the solubility of the copolymer in this solvent.

5.3 Annealing and Morphology

In our standard process, the samples were annealed at a temperature of 135°C for 10 min before the top electrode metal deposition. For our standard copolymer films (with a rotation of 3000 rpm and a concentration of 3 %mass in the solution), a layer thickness

³CMI, EPFL: <http://cmi.epfl.ch/organisation/materials.html>

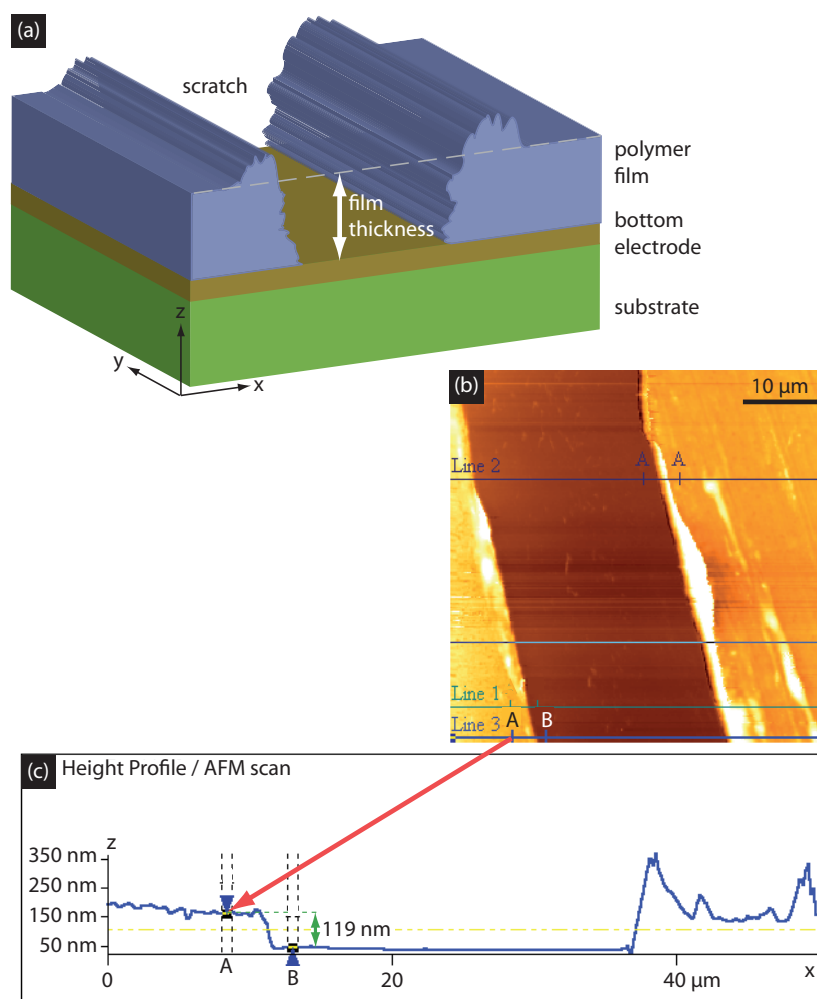


Figure 5.2: Illustration of the thickness measurements of thin polymer films. A scan across a scratch made by a soft stick reveals the height differences between the flat plateaus of the polymer film and the bottom electrode. The height difference was taken as the film thickness.

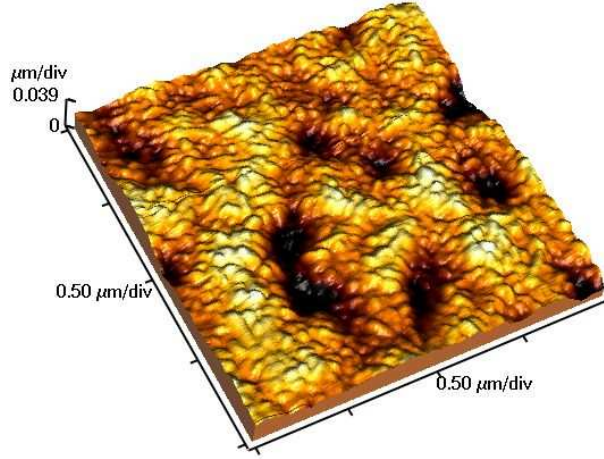


Figure 5.3: Topography scan ($2 \times 2 \mu\text{m}^2$) of the spun P(VDF-TrFE) thin film (thickness about 115 nm) on Au imaged by non-contact AFM.

of $115 \pm 5 \text{ nm}$ was measured by AFM. The AFM topography image in figure 5.3 reveals clearly a polycrystalline morphology of the copolymer film.

The impact of the annealing temperature was studied in P(VDF-TrFE) samples. Three films of about 120 nm were annealed at 100, 130, and 145°C for 10 min after spinning with identical conditions on gold coated substrates. A θ - 2θ xrd scan of the three films was measured over the interesting angular range around the peak at $2\theta \approx 20^\circ$, which was assigned to (110)(200) reflections. The three curves are presented in figure 5.4.

The surface topography was analysed with the AFM in non-contact mode (cantilevers used: *Ultrasarp*, NSC11/Pt, 3 and 45 N/m and *Nanoworld*, NCHR, 21–78 N/m). The obtained images of scan areas of $2 \times 2 \mu\text{m}^2$ [except for (c), 1×1 , and (f), $4 \times 4 \mu\text{m}^2$] are shown in figure 5.5 for the three films. Figure (a) shows very small grains with a size of about 50 nm when annealed at 100°C . Increasing the annealing temperature to 130°C and 145°C results in more elongated grains with lengths (measured parallel to film plane) of approximately 100 nm of several hundreds of nanometres, respectively. In the last sample, the morphology is not homogeneous across the sample. Figure (e) shows the topography in another region of the film with smaller, but ordered crystallites.

Image (f) illustrates that soft cantilevers were crucial for non-destructive and correct probing of these polymer films. Already small contact forces in combination with a fast tip-sample approach can deform and indent the film as can be seen by the pit marked by the dashed circle in the centre of the image. The non-contact AFM mode (see section 2.7.5) is thus very useful in order to get high resolution topographical information. For polarisation information with PFM, an intimate contact between the film and the conductive probe is required to apply the electric field. For such measurements, cantilevers with a stiffness below 1 N/m were used.

The XRD results showed an increasing intensity of the (110)(200) peak with increasing annealing temperature from 100 to 145°C . Apart from the annealing temperature, all other fabrication parameters remained identical for the three samples. The greater peak intensity is thus interpreted as an increase of the crystallinity with increasing annealing temperature. Such a behaviour has previously been reported [Tajitsu et al., 1987].

The higher crystallinity was confirmed by the increasing crystallite size and the formation of distinct, elongated shapes of the crystallites as found in the topography images

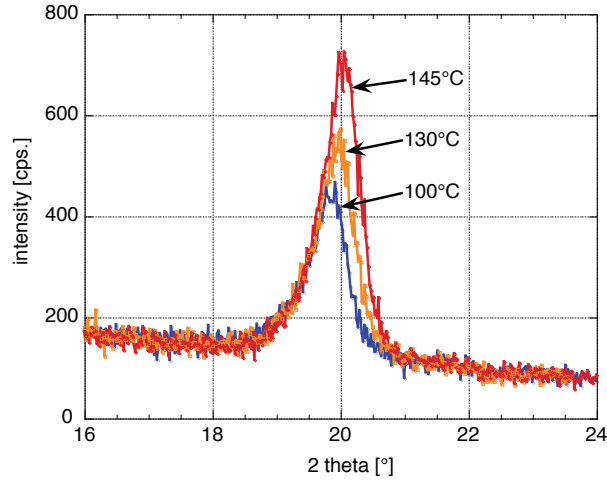


Figure 5.4: Influence of the annealing temperature on the structure characterised by XRD. The growing intensity of the peak, assigned to the (110)(200) reflection with annealing temperature indicates an increase of the structural order.

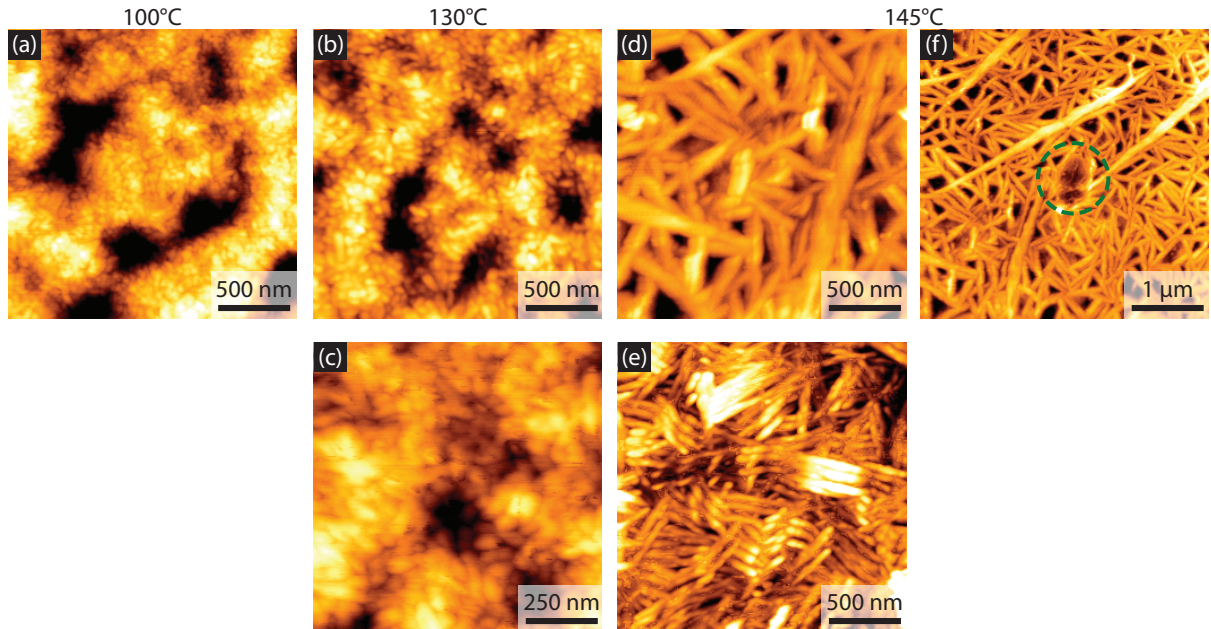


Figure 5.5: The topography taken in the non-contact AFM mode of spun P(VDF-TrFE) thin films annealed at 100 (a), 130 (b,c), and 145°C (d-f). (d) and (e) were taken in different regions, (f) shows the indentation of the AFM tip when it approached the sample too fast (for scanning in the contact mode).

(figure 5.5). The regional difference of the morphology in figures (e) and (f) may be due to temperature gradients during the short annealing procedure. These qualitative results suggest that the influence of the temperature profile, especially the high temperature duration and the cooling curve, should be studied in more detail.

Fukuma et al. investigated the influence of the annealing temperature on the morphology of spun P(VDF-TrFE) films (thickness 20–50 nm) on graphite [Fukuma et al., 2000]. This group observed a very similar behaviour of the crystallite growth with increasing temperature (25 to 140°C).

5.4 Polarisation Reversal

5.4.1 Methods

The switching behaviour of metal-polymer-metal ferroelectric capacitors was studied using microscopic and macroscopic techniques. Besides the standard macroscopic characterisations of ferroelectrics, i.e. hysteresis loop and capacitance measurements, a pulse switching technique was used to investigate the polarisation reversal as a function of pulse amplitude and duration.

Polarisation hysteresis loops were measured by applying a triangular voltage waveform with a frequency of 100 Hz between the bottom and the grounded top electrodes. Loops were measured in a cryostat, in which the temperature was varied between 130 and 360 K⁴. The permittivity was measured using an *LCR* meter (*Hewlett Packard*; 4284A) at an ac frequency of 1 kHz.

The employed pulse switching technique was previously described by Grossmann et al. [Grossmann et al., 2000] and Tagantsev et al. [Tagantsev et al., 2002a]. It delivers switching curves representing the reversed polarisation as a function of the switching pulse voltage and time; it excludes leakage current contributions and separates the switching clearly from the non-switching polarisation. A sequence of three pulses was used in order to measure the reversed polarisation. The first “poling” pulse (I) switched the ferroelectric completely. The second “switching” pulse (II) was of opposite polarity and reversed the ferroelectric to a degree, which depended on its amplitude and duration. The third “measuring” pulse (III) was identical to the first one (see figure 5.6).

The charge switched by the third pulse was monitored within a short delay, which was in our case 3 ms, after the pulse termination. Due to retention losses, a longer delay may result in a lower value of the measured charge. In the studied system, the effect of the retention loss was found to be rather weak; specifically, an additional delay of 100 ms resulted in a small relaxation of the measured spontaneous polarisation, which was less than $0.3 \mu\text{C}/\text{cm}^2$ (see figure 5.7).

For poling and measuring pulses (I and III), the duration was 1 ms and the voltage was set between 22 V and 44 V in order to guarantee a complete switching. The pulses were generated by a pulse generator (*Agilent, Inc.*; 33250A) and were amplified by a wideband amplifier (*Krohn-Hite Corp.*; 7602M). The charge was measured with a charge amplifier (*Kistler AG*; 5011).

Direct microscopic observation of the switching dynamics was performed with piezo-electric force microscopy (PFM), which is particularly useful for ferroelectric materials as described in chapter 3. In the configuration used in the present study, the electric field was

⁴The lower limit of the temperature range was given by the polymer; it broke down below 130 K before the polarisation could be reversed.

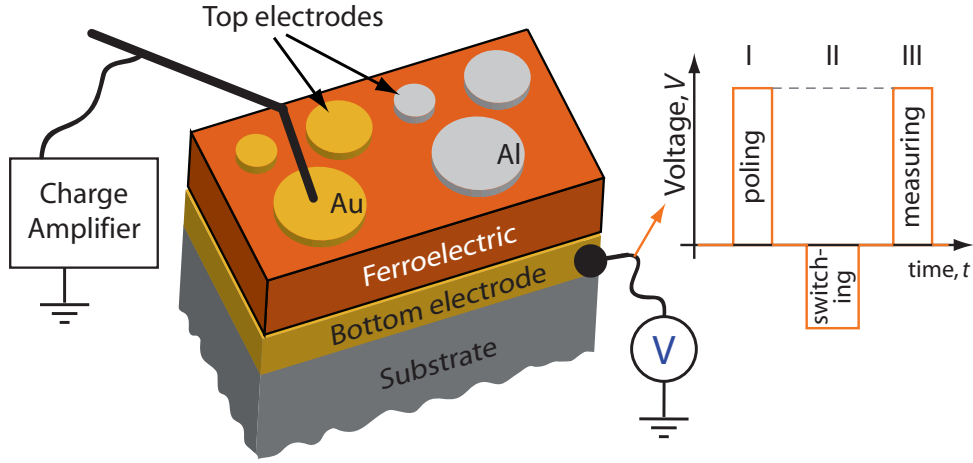


Figure 5.6: Three voltage pulses are applied to the bottom electrode. The charge is collected from the top electrodes after the third pulse in order to determine the switching charge. The meaning of the duration t and voltage V of the switching and the measuring pulses are shown in the diagram on the right side.

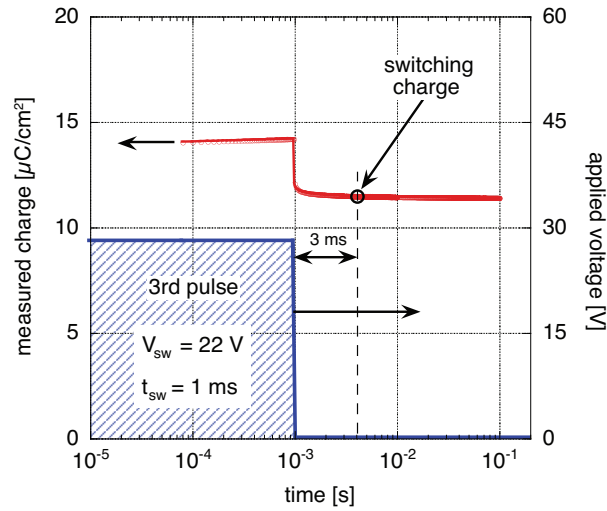


Figure 5.7: An example of the measured charge at the end of the third pulse as a function of time. The retention losses after a waiting time of 3 ms are negligible. The switching polarisation is taken as the charge measured 3 ms after the end of the third pulse.

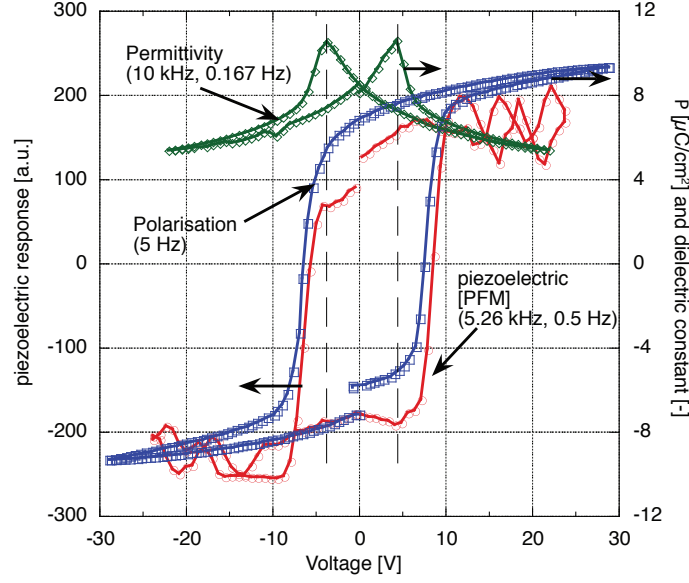


Figure 5.8: Three different electric field cycling measurements to illustrate the polarisation reversal: a piezoelectric loop, a polarisation loop by measuring the switching charges, and a dielectric butterfly loop.

applied between the bottom and the top electrode [Colla et al., 1998]. The top electrode was kept thin enough (about 30-40 nm) to allow the detection of the vibration with a high lateral resolution. The advantage of this method is a homogeneous field distribution in the ferroelectric [Auciello et al., 1997, Colla et al., 1998].

The AFM cantilevers were Pt coated and had a spring constant of 3 N/m. A lock-in amplifier (*Stanford Research Systems, Inc.*; SR830) was used to detect the amplitude and phase of the piezoelectric vibration.

This domain imaging technique was combined with the pulse switching technique in order to follow domain wall motions, similar to earlier studies on $\text{Pb}(\text{Zr,Ti})\text{O}_3$ (PZT) as described in chapter 4 [Hong et al., 1999, Gruverman, 1999, Gysel et al., 2006]. Here, a first polarisation pulse was followed by a sequence of switching pulses with constant amplitude but increasing width (see section 3.2). The domain pattern was recorded by PFM between consecutive pulses. The comparison of the domain patterns made it possible to follow the domain growth on a sub-micron scale and reveal microscopic details of the domain growth.

5.5 Results

5.5.1 Piezoelectric Properties

The piezoelectric response was characterised during polarisation reversal by PFM for samples with Au electrodes. Figure 5.8 shows a hysteresis loop. The loop is not characterised by a strong “hump and nose” feature [Tagantsev et al., 2004a]. The piezoelectric response has not been calibrated and the piezoelectric coefficient is thus unknown for our samples.

The piezoelectric response is compared in figure 5.8 to capacitive response (permittivity) and switching charge measured in the capacitor structure.

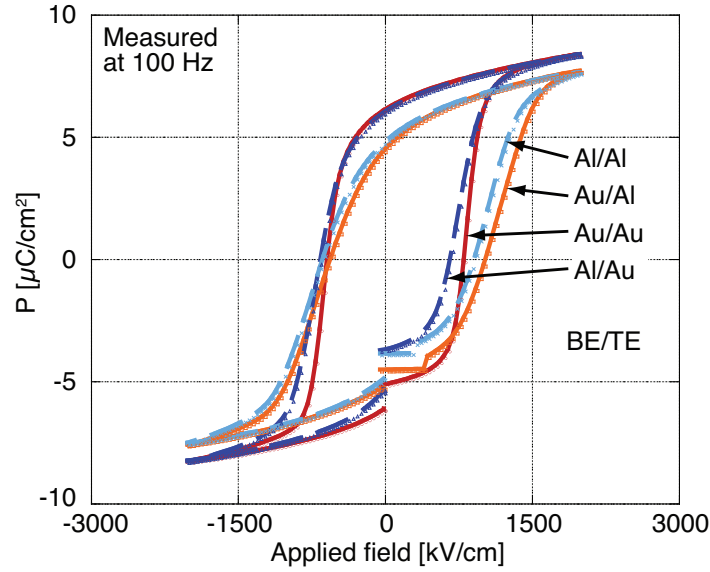


Figure 5.9: Effect of the electrode metals on the polarisation hysteresis loops measured at room temperature. The loops for all combinations of top (TE) and bottom electrodes (BE) with Au and Al are shown.

The coercive field of the two loop measurements are in good agreement, due to the comparably low frequencies. The maximum permittivity is at a bias voltage, which is substantially smaller than the coercive voltage of the loops. The permittivity measurement was performed under an even lower bias frequency than for the piezoelectric and the charge loop. The capacitance was measured with a high-frequency, small-signal ac voltage of 10 kHz. This involves contributions of reversible domain wall oscillations and can thus differ from the polarisation hysteresis loops characterised by reversible and irreversible domain wall movements.

5.5.2 Polarisation Reversal and Temperature

The polarisation hysteresis loops of the samples with Al and Au electrodes differ considerably as is illustrated in figure 5.9. The spontaneous polarisation for Au electrodes is $6.0 \mu\text{C}/\text{cm}^2$, whereas it is reduced in the sample with Al electrodes by about 20 % to only $4.7 \mu\text{C}/\text{cm}^2$. Furthermore, the loop tilts more with Al electrodes. From figure 5.9 it is clear that the top electrodes affect the tilt of the loop stronger than the bottom electrodes. Having the same top electrode material, the capacitors with Al and Au bottom electrodes manifest a similar polarisation loop.

The polarisation hysteresis loops measured from samples with Au and Al electrodes show a strong temperature dependence (figure 5.10). Upon sample cooling from room temperature to 173 K, the coercive field increases by almost four times. Furthermore, it could be observed that switching gets very difficult at temperatures below 130 K and the films tend to break down rather than to switch polarisation. Additionally, the steep part of the loops, in which the polarisation is reversed, becomes more tilted (out of the vertical position) at lower temperatures⁵. From the comparison of the loops with gold and

⁵A similar trend can be seen as well upon heating above room temperature in the sample with Al electrodes

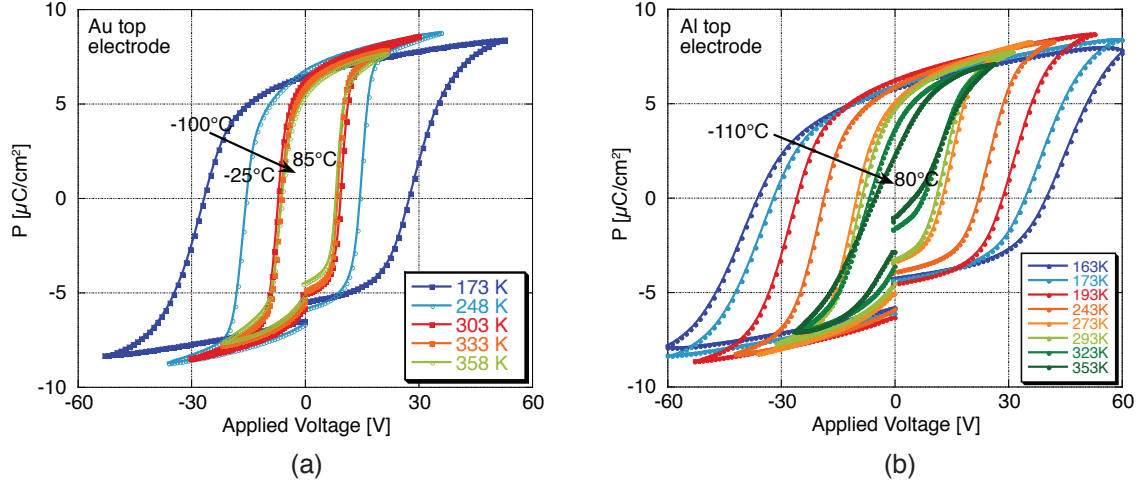


Figure 5.10: Polarisation hysteresis loops at various temperatures measured at a frequency of 100 Hz for samples with Au (a) and Al electrodes (b).

aluminium electrodes, it is clear that the loops are more inclined with Al electrodes. The samples were prepoled for 1 second before the loop measurement; hence the gap measured at zero electric field represents the polarisation retention loss after a 1 second delay. In the case of Al top electrodes this loss is stronger than in the case of Au electrodes.

The coercive field E_c determined from polarisation loops measured at a frequency of 100 Hz is shown in figure 5.11 as a function of temperature. To a good precision, the coercive field E_c is a linear function of the inverse temperature.

5.5.3 Permittivity and Temperature

The temperature dependence of the dielectric permittivity of the ferroelectric films in the sandwich structure, with electrodes of gold and aluminium is shown in figure 5.12. The initial permittivity at -150°C is 3.3 ± 0.3 . For both kinds of electrodes upon heating to a temperature of about -25°C , the permittivity increases slowly, independently of the electrode material. Above 25°C , the permittivity increases rapidly. The permittivity of the sample with Al electrodes shows a maximum value of 34 ± 3 at 65°C , whereas there is no obvious local maximum for the sample with Au electrodes up to 90°C . The largest permittivity measured with Au electrodes is 15 ± 1 , and is less than half of the value measured on the identically processed sample with Al electrodes.

5.5.4 Polarisation Reversal Kinetics

More comprehensive information about the switching kinetics can be obtained from switching curves representing the reverse polarisation as a function of the pulse duration for a constant voltage of the switching pulse (figure 5.13). The switching time t_{sw} , defined as the time required to reverse half of the switchable polarisation, resides below $1 \mu\text{s}$ (about 300 ns) at a field of $2.4 \text{ MV}/\text{cm}$ (corresponding to a voltage of 28 V) for the film with Au electrodes at room temperature. The use of Al electrodes results in a switching time which is at least one order of magnitude smaller compared to Au electrodes at the same switching voltage. Furthermore, the polarisation reversal happens over a wide

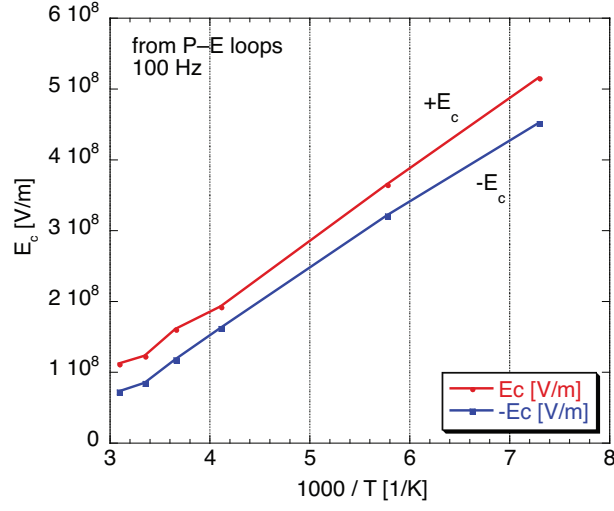


Figure 5.11: Coercive field, E_c , vs. inverse temperature $1/T$. E_c is determined from the polarisation loops of a sample with Au electrodes; $-E_c$ and $+E_c$ are the coercive fields with reference to the top and bottom electrode, respectively.

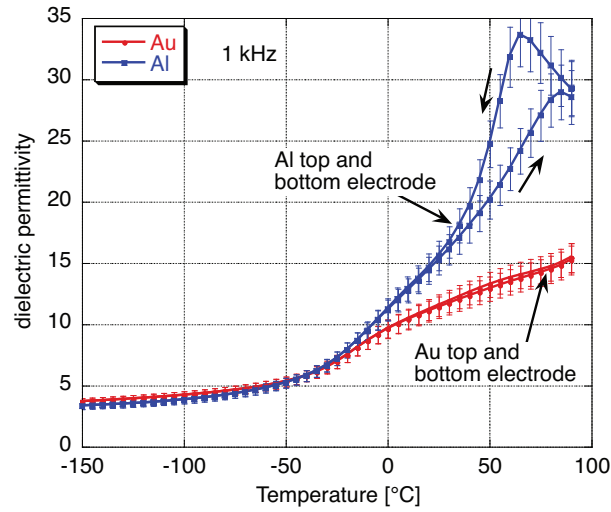


Figure 5.12: Temperature dependence of the relative permittivity of capacitors with Au and Al top and bottom electrodes.

time scale corresponding to the smaller slope of the curves.

The copolymer film shows a retarded polarisation reversal for long switching pulse widths. This effect is most remarkable with Al electrodes, but it can also be observed with Au electrodes, especially at elevated temperatures.

The polarisation reversal rate slows down rapidly as the switching voltage decreases. The switching time is plotted versus the inverse of the electric field in figure 5.14. The linearity in this plot agrees well with the exponential law found for low fields by Merz in BaTiO₃ as presented in equation (2.24) on page 27.

The temperature dependence of the activation field α is shown in figure 5.15. The value of α for gold electrodes is close to 1.2 GV/m at room temperature and decreases to about 0.8 GV/m at 60°C. The room temperature value is close to the number given by Furukawa et al. [Furukawa et al., 2006] of 1 GV/m for the same copolymer with a slightly different composition (75:25 mol %), film thicknesses between 50 and 330 nm, and with Au electrodes, but rather far away from BaTiO₃ (see table 2.2 on page 45).

The incomplete set of data for the Al electrodes does not allow for the determination of the activation field α , however, the two points obtained from the film with Al electrodes follow the trend observed with Au electrodes rather well.

In the temperature range considered, the activation energy is a linear function of the inverse temperature in a first approximation.

In order to link the macroscopic dynamics of the polarisation reversal with the kinetics of the domain growth at sub-micron scale, the pulse switching measurements were combined with PFM imaging as described in section 3.2. Such studies are very helpful in order to get a better understanding of the polarisation reversal on the microscopic scale and allow us to draw conclusions on the polarisation reversal mechanism, e.g. concerning the homogeneity of the domain expansion, a prerequisite for the ideal KA model.

Furthermore, the dependence of the growth mechanism on the electric field is of interest. It was seen from the switching curves in figure 5.13 that the polarisation reversal is not only orders of magnitudes faster, but the curves are also steeper, i.e. the first derivative peak (this would correspond physically to the switching current) is more distinct, at higher fields.

Figure 5.16 shows an example of PFM phase images of the local piezoelectric response taken after 12 V switching pulses with widths between 30 μ s and 14 ms. In these $1 \times 1 \mu\text{m}^2$ scans taken across a 40 nm thick Au top electrode, the non-switched areas are shown in black, whereas the grey areas that grow progressively from image (a) to (h) correspond to the reverse polarisation. The ferroelectric copolymer capacitor was first poled with a voltage of 23 V for a few seconds.

For easier comparison between the consequent images, different stages of the polarisation reversal are shown with two gradations of grey, dark (in colour: red) and bright. The bright colour marks newly grown switched areas, which were not observed in the previous image. Comparing the images in figure 5.16, one observes an irregular domain growth under the influence of the voltage pulses of increased width. This growth is characterised by a restricted geometry, where both static (**s**) and mobile (**m**) domain walls can be seen as marked in the images (e) to (g).

The domains are growing in a particular, non-homogeneous way. Some domains, e.g. on the right upper corner of image (f) expand in all directions, whereas others grow in preferred directions, e.g. the domain in the centre of image (f).

There seem to be “hard” regions, which do not reverse their polarisation even after long pulses of 14 ms, at which over 90 % of the polarisation is reversed [see figure 5.13(a)].

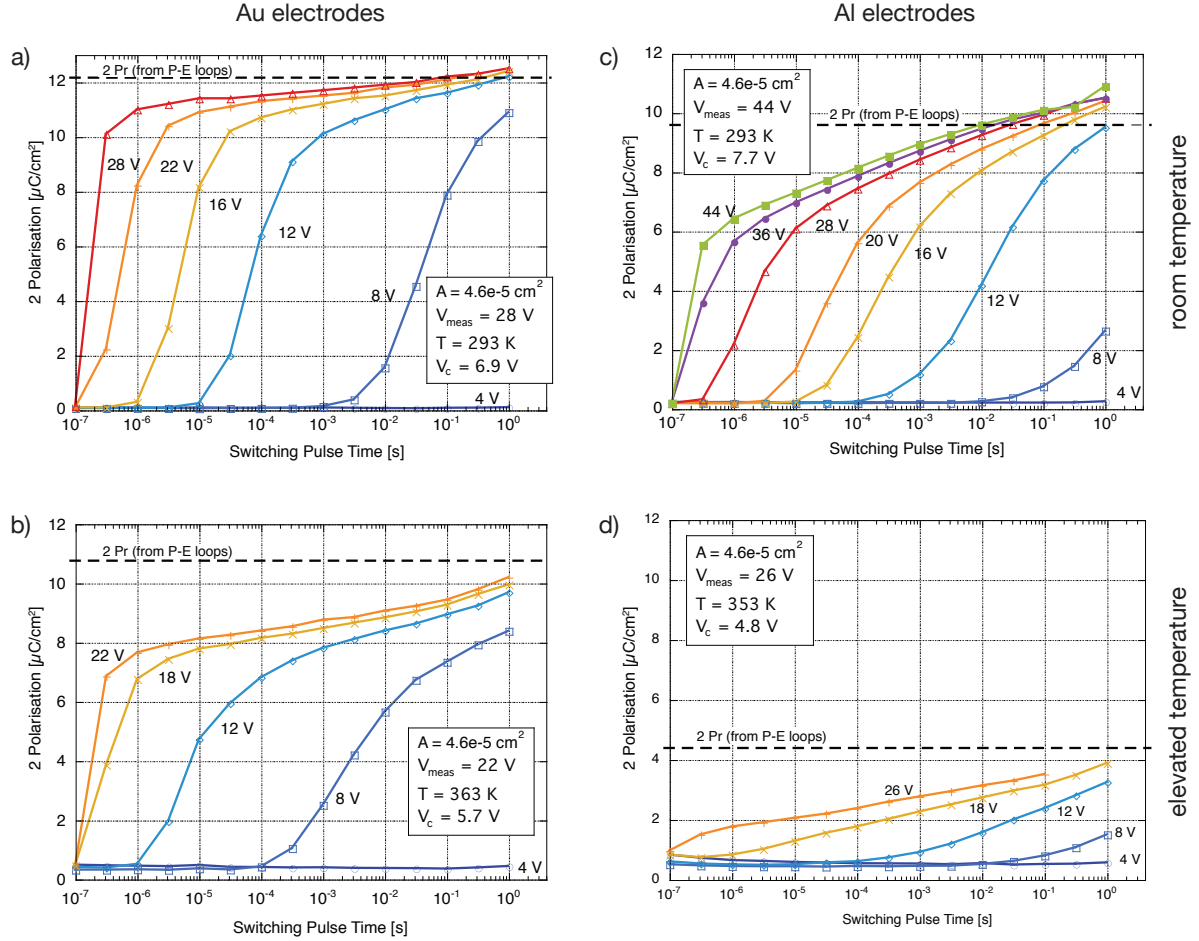


Figure 5.13: Pulse switching curves as a function of the switching pulse duration and voltage for Au (a, b) and Al (c, d) electrodes. The measurements were performed at room (a,c) and at elevated temperature of 90°C (c) and 80°C (d), respectively. The remanent polarisation, P_r , measured from hysteresis loops as in figure 5.10, is indicated with a dashed horizontal line. Details of the capacitors and the measurements are given in the inserts: the top electrode area, A , the measuring pulse amplitude, V_{meas} , and the coercive voltage, V_c , determined from polarisation loops taken at a frequency of 100 Hz .

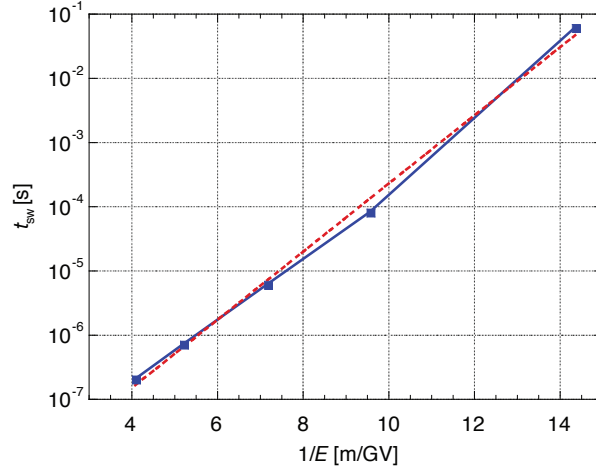


Figure 5.14: The switching time t_{sw} depends exponentially on the reciprocal switching field. The dotted line represents a fit based on equation (2.24) for low fields with an activation field $\alpha = 1.2$ GV/m at room temperature. Each dot is extracted from a switching curve at a constant voltage from figure 5.13(a).

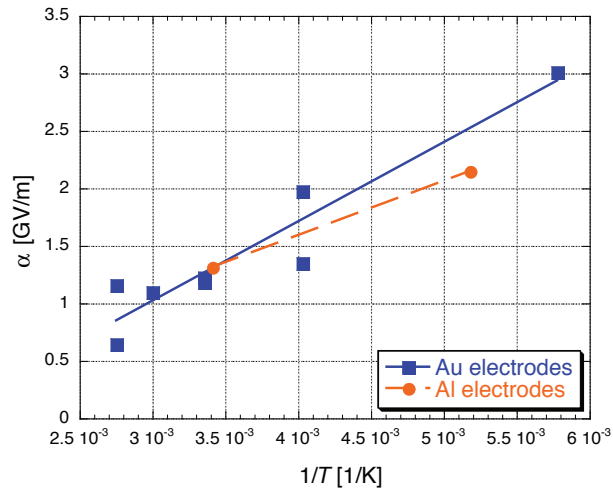


Figure 5.15: The activation field, α , is a linear function of the inverse temperature $1/T$.

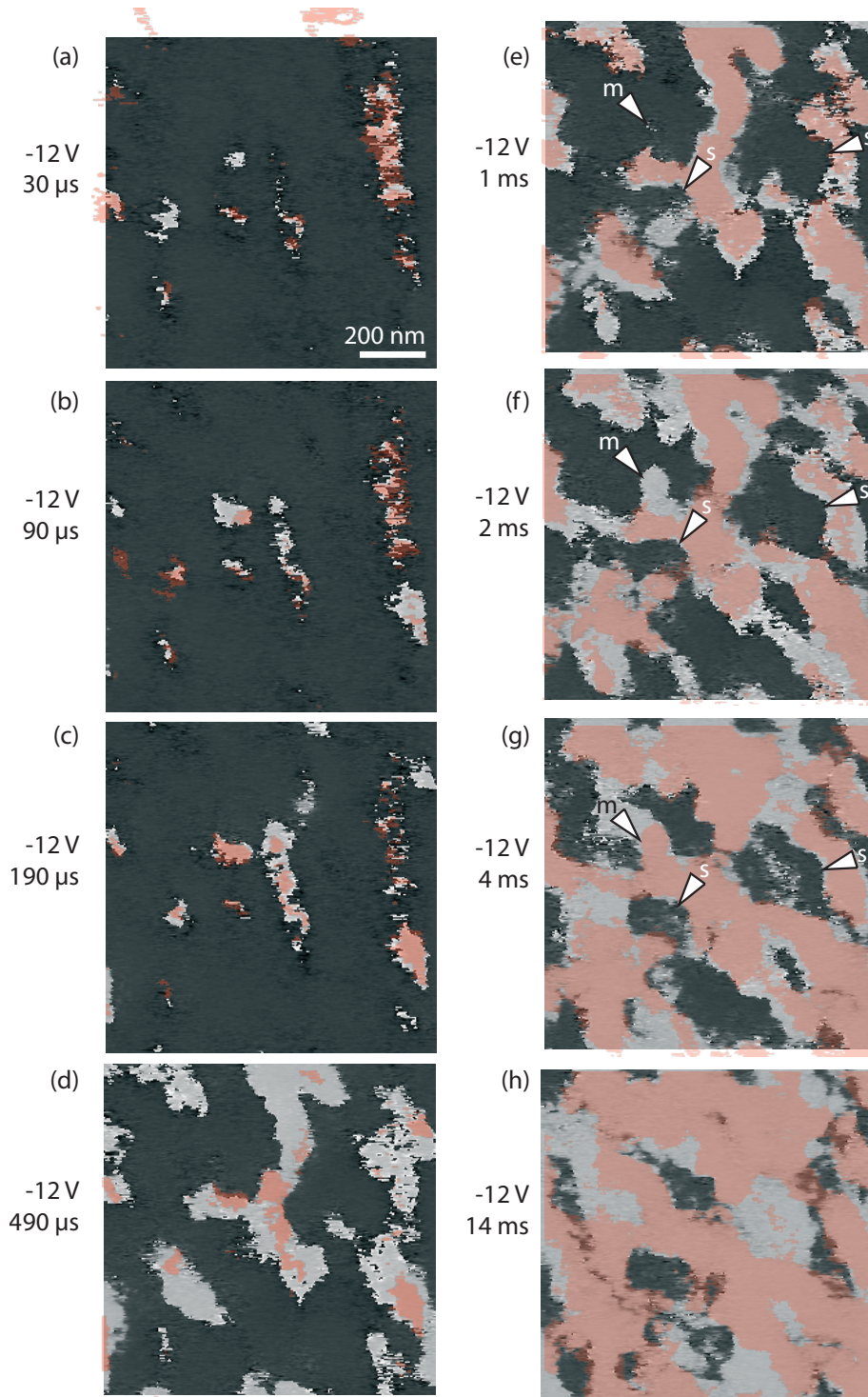


Figure 5.16: Microscopic PFM phase images of an area of $1 \times 1 \mu\text{m}^2$ after pulses with an amplitude of -12 V and a width as indicated next to each image. The red shaded regions indicate the domain pattern in the previous image. Static domain walls at places, marked with (s), and mobile regions, marked with (m), are both observable.

Additionally, this is in agreement with the statement in the previous section that the gain in polarisation, up to this stage, is associated with a regional growth of the domains and not to a polarisation enhancement in the reverse domains (compare to figure 5.18).

A corresponding series of PFM images was taken at higher electric field pulses and is shown in figure 5.17.

Compared to the series at a voltage level of 12 V, no fundamentally different growth scenario can be found. Of interest are image pairs (a) and (b) as well as (c) and (d), which were taken after identical pulses of $0.2\ \mu\text{s}$ and $0.3\ \mu\text{s}$, respectively. For both pairs, it is clearly demonstrated that the repetition of the same pulse (after a waiting time of about 30 min, the acquisition time of the PFM images) does not induce any change in the domain pattern.

Furthermore, hard regions are also present in this film. Even after a relatively long pulse of $500\ \mu\text{s}$, at which the reversal seems to be almost completed as found in figure 5.13(a), some dark, unswitched regions are still present.

For a representative scan covering a sufficient number of domains, the area of the switched domains normalised to the total scan area is expected to be close to the normalised reverse polarisation measured using the pulse switching technique (figure 5.13). To verify this approach, the ratio between the switched and total scan area is calculated for several pulse widths and a constant pulse amplitude of $-24\ \text{V}$. The measured switching charge curve and normalised switched area calculated from phase images as shown in figures 5.17(a-l) plotted as a function of the pulse width (figure 5.18d) follow each other well, suggesting that the studied $1 \times 1\ \mu\text{m}^2$ images are representative of the integral switching characteristics of the studied capacitor.

The phase images (a-c) in figure 5.18 of the $1 \times 1\ \mu\text{m}^2$ -area illustrate exemplarily the evolution of the switched areas under a certain applied voltage. After a short pulse of $24\ \text{V}$ ($E = 2\ \text{MV}/\text{cm}$) and a width of $200\ \text{ns}$, some regions with the reverse polarisation are detectable. The size of the reverse domains is variable; some domains are rather large, with diameters up to about $300\ \text{nm}$, whereas others are small, being less than $80\ \text{nm}$ in diameter (figure 5.18a). Increasing the pulse duration to $2\ \mu\text{s}$ (b) provokes the growth of the reverse areas in some directions, whereas in some other directions the growth is hindered. There are domain wall tracts that remain immobile after applying additional voltage pulses as was seen already for a smaller switching pulse amplitude in figure 5.16. A pulse duration of $500\ \mu\text{s}$ is long enough to allow the growth of the domains to reverse the polarisation almost completely in the capacitor (c). However, there are still some remnants of non-reversed domains detectable.

The observations described in this section can be summarised as follows:

- (i) The polarisation loops with Al electrodes are more tilted than with Au electrodes.
- (ii) The loop tilt correlates with the material of the top electrodes.
- (iii) A large gap was observed between the starting and end point in a polarisation loop for Al electrodes.
- (iv) The coercive field is a linear function of the inverse temperature.
- (v) The dielectric permittivity increases rapidly from -25°C upon heating and the increase is more pronounced with Al than with Au electrodes.
- (vi) Switching is faster with Au electrodes than with Al electrodes and may occur on the order of nanoseconds for high enough fields.

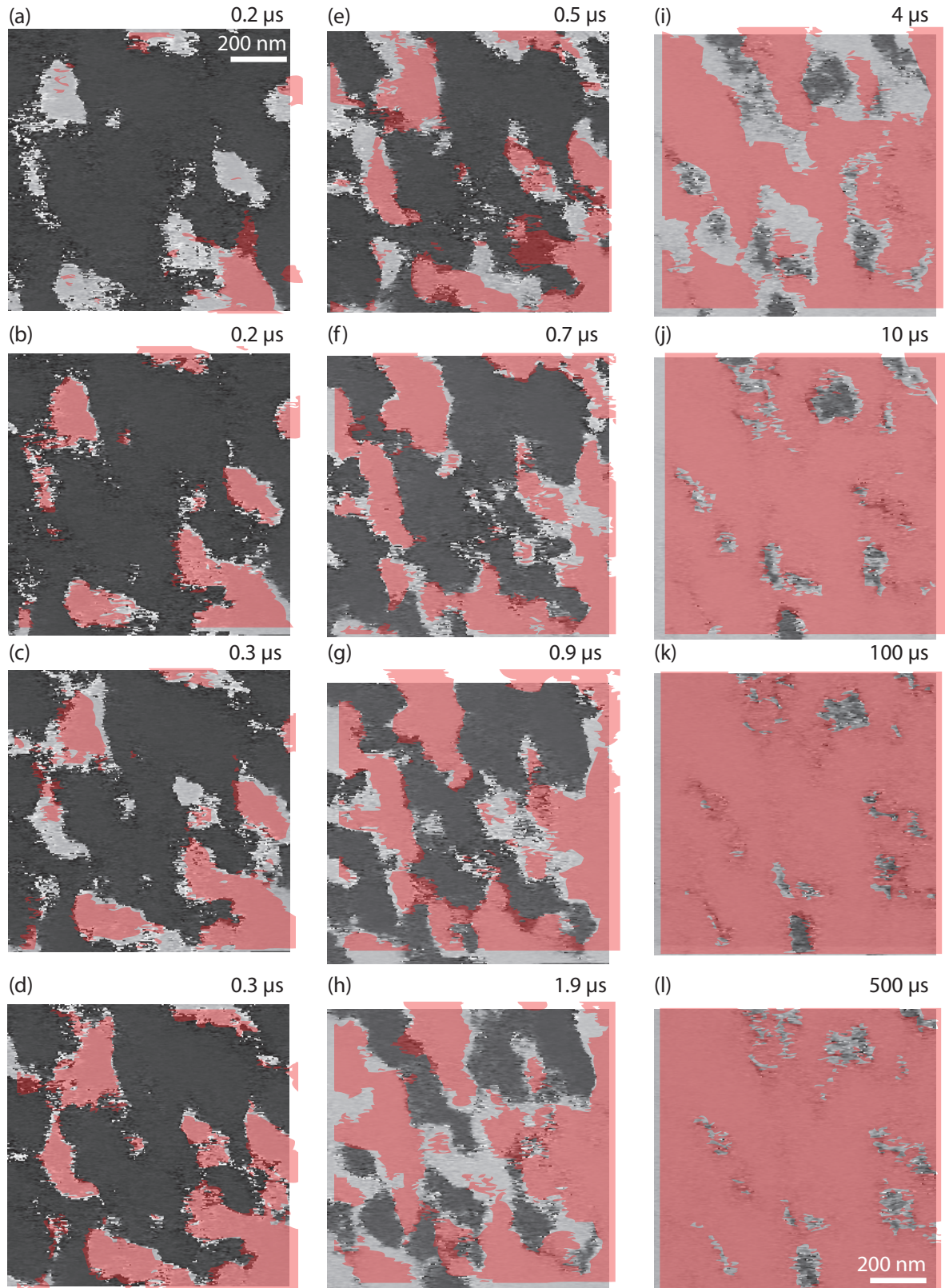


Figure 5.17: Microscopic observation of the domain growth with PFM through electrode technique on an area of $1 \times 1 \mu\text{m}^2$. The film was first poled with a voltage of 23 V with respect to the bottom electrode before voltage pulses of -24 V and a duration, indicated for each image, were applied. The darker (red) shaded regions indicate the domain pattern in the previous image.

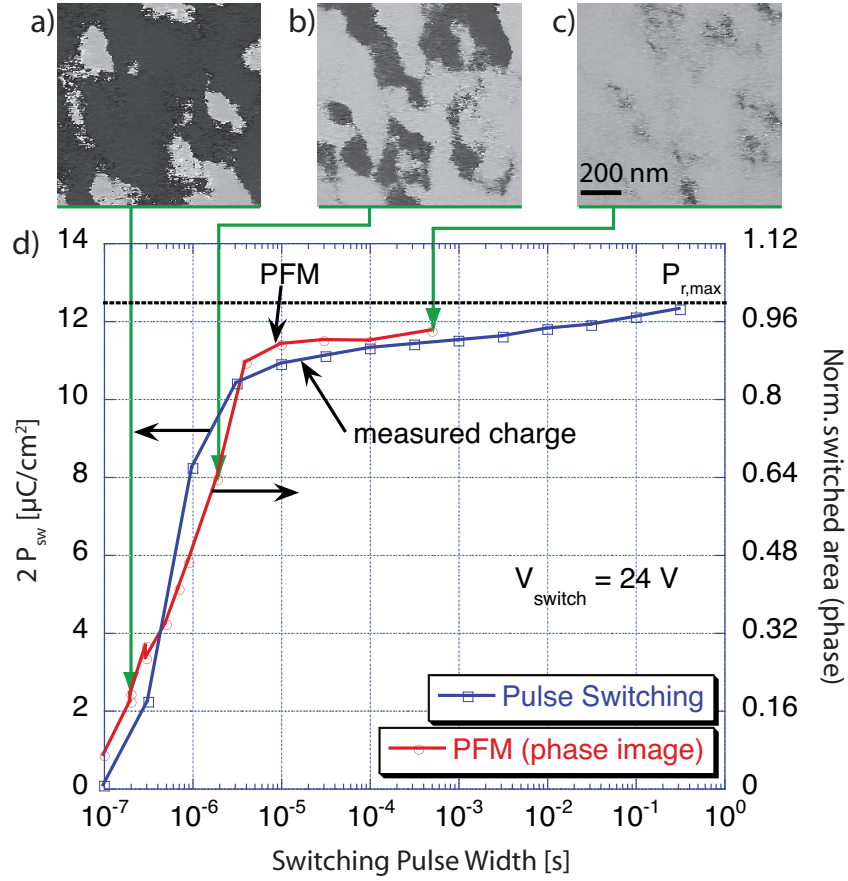


Figure 5.18: Comparison of the switching polarisation curve (d) of the sample with Au electrodes obtained by measuring the charge response and the switched area in a series of phase images from PFM including (a-c).

- (vii) The polarisation reversal is retarded at the end of switching, especially with Al electrodes.
- (viii) The PFM study reveals a restricted geometry of the domain growth and inhomogeneous expansion of the switched areas.

5.6 Discussion

5.6.1 Dielectric Properties vs. P – E hysteresis

In our experiments it is clearly seen that there is a correlation between the shape of P – E hysteresis loops and the small signal dielectric permittivity of P(VDF-TrFE) films with Au and Al electrodes. Specifically, at temperatures above -20°C , the films with Al electrodes exhibit:

- (i) higher values of the permittivity (figure 5.12) and
- (ii) more tilted loops than Au electroded films (figures. 5.9 and 5.10).

Such behaviour of the loop can be readily rationalised. As indicated by several authors [Xia and Zhang, 2003, Takahashi et al., 2004, Naber et al., 2004, Furukawa et al., 2006], the electric properties of P(VDF-TrFE) films with Al electrodes suggest the presence of a dead layer between the ferroelectric and metal (some more fundamental studies showed a different reactivity of the fluoropolymers with various metals [Wu et al., 1994, Chen and Mukhopadhyay, 1995]). At the same time, the dead layer in a ferroelectric capacitor should result in a tilt of the P – E hysteresis loop [Tagantsev et al., 1995] and a smaller remanent polarisation.

This explains the observed lower remanent polarisation and the loop tilt in the case of Al electrodes. Additionally, the large gaps in the P – E loops corroborate the presence of a dead layer.

As for the small signal permittivity, one expects that the presence of a dead layer in a ferroelectric capacitor will result in a reduction of its effective permittivity. In many situations, this is the case. Indeed, if the permittivity is controlled by the lattice contribution, the impact of the dead layer can be described by the well-known in-series capacitor formula

$$\frac{h + d}{\varepsilon_{\text{eff}}} = \frac{h}{\varepsilon_f} + \frac{d}{\varepsilon_d} \quad (5.1)$$

where ε_{eff} is the effective relative permittivity of the sandwich, ε_f and h are the relative permittivity and thickness of the ferroelectric, and ε_d and d are the relative permittivity and thickness of the dead layer, respectively. In the typical situation for ferroelectrics, where $\varepsilon_f \gg \varepsilon_d$, even a thin dead layer, $d \ll h$, can essentially suppress the sandwich permittivity [it follows from equation (5.1)]. If the domain contribution is appreciable, the dead layer has a smaller impact on the effective permittivity of the sandwich. In this case, the dead layer behaves as that with an effective value of the relative permittivity ε_d^* that is larger than ε_d [Mokry et al., 2004].

Assuming the relative permittivity of the ferroelectric ε_f be independent of the parameters of the dead layer, we conclude that the dead layer should not lead to any increase of

ε_{eff} , which contradicts our experimental observations. However, in the case of an appreciable domain contribution, ε_f can readily be dependent on the parameters of the dead layer. For example, the dead layer in a ferroelectric capacitor can lead to the ferroelectric spontaneously breaking into domains [Kopal et al., 1997] thus affecting its measured relative permittivity. Hence, when treating the impact of the dead layer on the effective relative permittivity of the system one should take into account two competing effects:

- (i) the “direct” one acting through the last term in equation (5.1) and
- (ii) the “indirect” one acting through the dependence of ε_f on the parameters of the dead layer.

In the case of the studied PVDF-based capacitors the direct effect is negligible due to the small value of the lattice permittivity, whereas the indirect effect leads to an increase of the effective permittivity in the presence of the dead layer. This is demonstrated in the foregoing discussion.

In the further discussion and for reasons of clarity, we will use the schematic images of the P – E loops shown in figures 5.19(a-d). These images correspond to the loops taken from the films with Au and Al electrodes at temperatures in the intervals 200–250 K and 270–320 K (cf. figure 5.10). These temperature intervals are remarkable not only for the difference in the features of the loops, but also for the difference in the behaviour of the dielectric permittivity. Specifically, in the 200–250 K interval, the measured permittivity of the films is independent of the electrode material whereas, in the other interval, the permittivity measured with Al electrodes is larger (cf. figure 5.12).

The features seen in figure 5.19(a-d) can be summarised as follows:

- (i) only the loops taken from capacitors with Al electrodes exhibit an appreciable tilt, which is virtually temperature independent;
- (ii) the coercive field, in both cases, increases with decreasing temperature;
- (iii) the schematics of the loops contain four elements: nearly horizontal “top” and “bottom” and two inclined “side parts”. Bearing in mind that the large field-driven variation of the polarisation is possible only in multidomain state, we attribute the states corresponding to the “top” and “bottom” to single-domain states, whereas the “side parts” are attributed to multi-domain states.

The difference between the loops shown in figures 5.19(a-d) can be related to the values of the small signal permittivity measured at $E = 0$. This can be done using the slope of the loop at $E = 0$ as an indicative value of the small signal permittivity measured at $E = 0$ ⁶.

In capacitors with Au electrodes, the ferroelectric at $E = 0$ is in the single-domain state at all temperatures. This corresponds to the position of the shoulder (marked with a circle) at negative E in figures 5.19(a) and (c). At the same time, in capacitors with Al electrodes, the state of the ferroelectric at $E = 0$ depends on the temperature. In this system, the presence of a dead layer leads to the depolarising field, which destabilises

⁶If at $E = 0$ the state of the ferroelectric is single-domain, the slope of the loop just gives the value of the small signal permittivity. If it is a multi-domain state, then the permittivity is controlled by the contribution of reversible wall motion whereas the slope of the loop reflects this contribution plus that of irreversible wall motion.

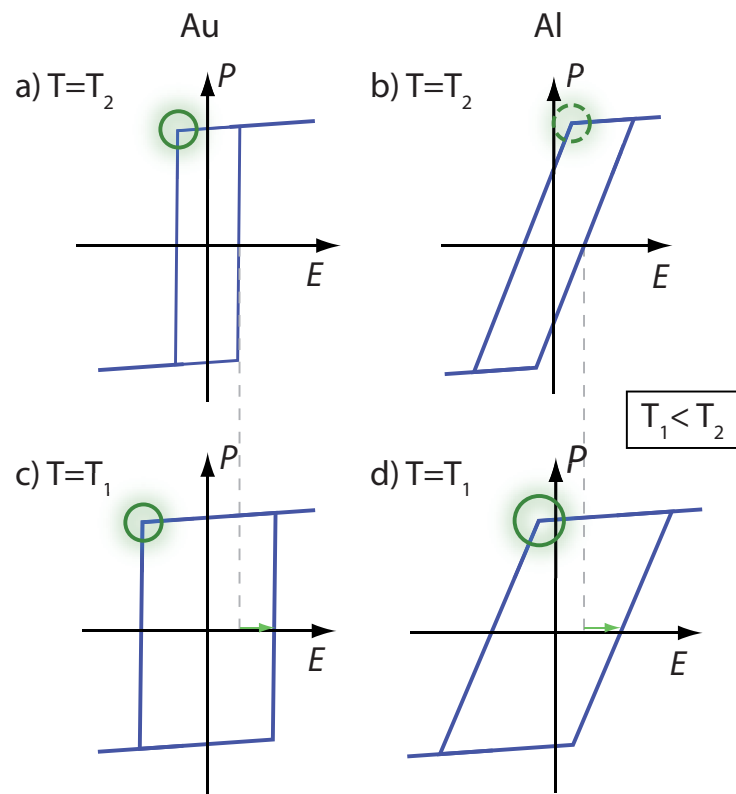


Figure 5.19: Schematic of the polarisation hysteresis loops of a ferroelectric with and without a passive layer at different temperatures and thus different coercive fields.

the single-domain state of the ferroelectric. However, at low temperatures, where the coercivity is relatively high, this field is not strong enough to induce the multi-domain state. This corresponds to the position of the shoulder (marked with a circle) at negative E in figure 5.19(d). For higher temperatures with lower coercivity, the depolarising field brings about the multi-domain state at $E = 0$. This corresponds to the position of the shoulder (marked with a circle) at positive E in figure 5.19(b).

Now using the above breakdown, we can establish a relation between the behaviour of the permittivity and the presence of the dead layer.

At low temperatures and $E = 0$ for both types of capacitors, the ferroelectric is in the single-domain state. Here, despite the presence of the dead layer in the case of Al electrodes, one expects the relative permittivity obtained from both types of capacitors to be the same. The point is that the relative permittivity of the ferroelectric (controlled here by the lattice contribution) is relatively small (≈ 5). Since the relative permittivity of the *thin* dead layer is expected to be of the same order of magnitude, it should not affect the effective relative permittivity of the system. Thus, the presence of the dead layer at Al electrodes is not in conflict with the fact that the same effective relative permittivity is measured with both types of electrodes.

At high temperatures and $E = 0$, the ferroelectric with Au electrodes is still in the single-domain state exhibiting relatively low effective relative permittivity controlled by the lattice contribution. At the same conditions, the ferroelectric with Al electrodes is in the multi-domain state and hence shows a higher effective permittivity because of the additional domain contribution. Thus, we have come across an unexpected situation, where the addition of a dead layer can lead to an increase of the effective permittivity of a ferroelectric system.

5.6.2 Switching Mechanism and Polarisation Reversal Dynamics

Our experimental data on the polarisation reversal in P(VDF-TrFE) films (switching charge and PFM measurements) enables us to draw some conclusions concerning the physical mechanisms that control this phenomenon. It strongly suggests that switching in these films occurs according to a scenario, which is far from, both the classical Kolmogorov-Avrami (KA) [Ishibashi and Takagi, 1971] and the nucleation limited switching model (NLS) recently proposed for granular films [Tagantsev et al., 2002a] as discussed in section 2.4. However, the granular structure of our films (figure 5.3) might favour the latter.

As a test for the KA scenario, we checked the compatibility of the switching rates at the early stage of switching (where the overlapping of the growing domains is negligible) with those for the intermediate stage (where the domains essentially overlap). As customarily done for the description of switching in ferroelectric films with KA theory, it is assumed that the switching starts with the formation of isolated cylindrical domains via fast forward growth from electrode-adjacent nuclei (stimulated by applied field and/or thermal fluctuations) or from preexisting remnants of reverse domains. The further evolution of the domain pattern occurs via expansion of the initial cylindrical domains with their subsequent overlapping.

If the time of the forward growth and the area of the initial domains are neglected, the KA theory leads to the well known expression in equation (2.28) on page 35 for the fraction of polarisation, $c_{KA}(t)$ (see e.g. references [Ishibashi and Takagi, 1971, Shur et al., 1998]).

Using equation (2.28) we tried to fit our data by checking the possibility to describe with a single relationship, both the initial stage of the domain growth, where

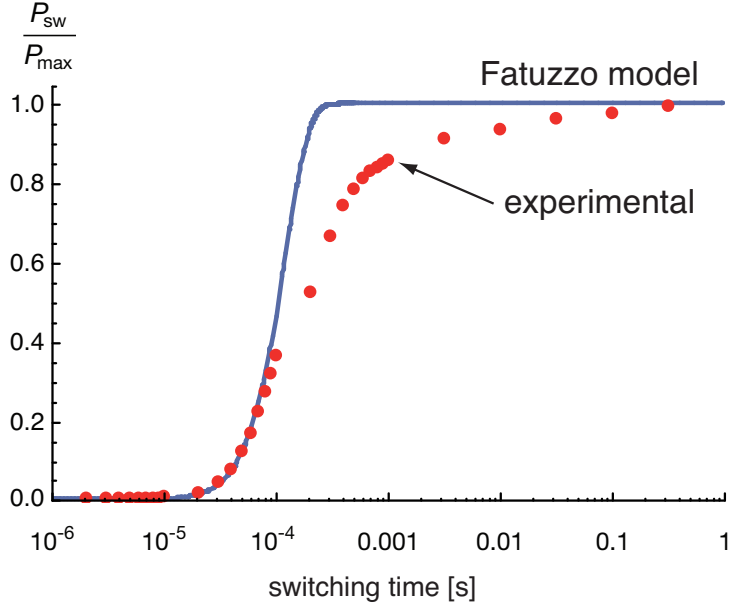


Figure 5.20: Analysis of a switching curve from figure 5.13 according to the Fatuzzo model [equation (2.30)].

$$c_{KA}(t) \approx \left(\frac{t}{t_0} \right)^n \quad (5.2)$$

and the intermediate stage, where the switching rate slows down due to the overlapping of growing domains. In our analysis, first, the beginning of a switching curve (as shown in figure 5.13) was fit to equation (5.2) with $n = 2$ to determine parameter t_0 and, second, we compared the rest of the experimental points to the plot of equation (2.28) with the already determined value of t_0 .

We found that at a normalised switched polarisation $c \approx 0.3$, where the difference between the plots of equations (2.28) and (5.2) becomes appreciable, the experimental points deviate from both plots towards smaller values. Similar behaviour was found when using equation (5.2) with $n = 3$. This discrepancy could be taken as an indication to the incompatibility of our data with the KA scenario. However, it may also be attributed to the oversimplification of the description of the overlapping domains in terms of the α and β models.

In the model of Fatuzzo presented in section 2.4.2 and described by the equations (2.29) and (2.30), the switching starts like in the α model but, at large times, tends to the β model behaviour. Thus, being properly treated, the KA model may exhibit an additional (compared to the α and β models) slowing down at intermediate times. This qualitatively resembles the situation we have come across in our analysis. Bearing this in mind, we repeated our analysis using the relation derived by Fatuzzo for the fraction of switched polarisation, equation (2.30).

The result of this analysis, presented in figure 5.20, clearly indicated that slowing down of the polarisation reversal at the intermediate times cannot be described even with the corrected KA scenario. We also tried to fit our experimental switching curves in terms of the NLS model, equation (2.31), but failed to do this with physically reasonable values for the parameters of the model.

To get a better insight into this problem, we invoked the PFM data. This data reveals that the character of the domain pattern evolution (figures 5.16, 5.17, and 5.18) is incompatible with the principle assumption of the KA theory on the homogeneity of the wall mobility throughout the system. Indeed, inspecting the time evolution of the PFM images, it is seen that some wall segments change their positions from image to image, whereas others stay immobile for a long time (cf. figure 5.16).

The observed switching behaviour can be rationalised as follows. The wall mobility is strongly inhomogeneous through the sample. At the beginning of the switching, a motion of wall segments through areas with relatively high mobility (“easy regions”) occurs. Actually, this motion does not seem to be continuous, it looks rather like a region-by-region reversal with jumps of wall segments, so that one can only speak about wall mobility “on average”. Along with the progress in switching, further polarisation reversal requires involvement of the regions with lower wall mobility.

The inhomogeneity of the wall mobility may be related to the morphology of the copolymer, which was described in terms of crystalline lamellae that are embedded in amorphous regions [Lovinger, 1983, Furukawa et al., 2006].

The presence of the low-mobility regions leads to deceleration of the switching, in addition to that originating from domain coalescence. We believe that this effect is responsible for the reduction of switching rates at the intermediate times below those predicted by the KA theory, which we experimentally documented.

We observed the above phenomenon in films, both with Au and with Al electrodes. This is compatible with the “bulk nature” of the mechanism, which we put forward for its explanation. Further analysis of our data shows that there is at least one more effect that makes the switching behaviour different from the classical KA scenario and that this effect is interface related. Specifically, the inspection of the curves “switching charge vs. time” in figure 5.13 reveals a clear retardation at the final stage of switching, where the switching charge evolves logarithmically with time. In this regime the switching is stretched by many decades in time. Such behaviour is clearly incompatible with any version of the KA scenario, where the switching of the second half of the available polarisation takes less than a couple of decades in time, as was illustrated in figure 2.25(a).

This effect is electrode-dependent and eminently pronounced in the films with Al electrodes. For P(VDF-TrFE) capacitors with Al electrodes, such retarded switching was reported, but the authors commented mainly on the slowing effect of Al electrodes in the beginning of switching [Tajitsu, 1995, Nakajima et al., 2005, Naber et al., 2004]. The retardation at the final polarisation reversal step was hardly commented and was briefly explained by the contribution of the leakage current to the switching charge. Such an explanation might pass for the measuring technique used in [Nakajima et al., 2005, Furukawa et al., 2006], where the leakage current does contribute to the switching charge. However, our measuring techniques (pulse switching technique and PFM) enable the elimination of this contribution. Thus, the leakage-related interpretation can be discarded.

We believe that the retardation in the end of the polarisation reversal is controlled by the depolarising effect caused by the dead layer at the Al/ferroelectric interface. We have already traced some manifestations of this effect in the dielectric response and the shape of the polarisation loops. The average depolarising field, being proportional to the average polarisation of the sample, is directed along the applied field during the first half of the switching (from a poled state) and against the field during its second half. Thus, in the presence of a dead layer, the first half of the switching should be accelerated, whereas the second decelerated. This effect provides a qualitative explanation for our observations.

However, the question arises as to whether the depolarising field can be strong enough to explain the remarkable retardation of switching that we observed. In attempting to answer this question we performed preliminary modelling of the phenomenon in terms of the standard KA model⁷.

The basic equations of the KA model for the normalised switched polarisation can be written as

$$c(t) = \frac{P_{\text{sw}}(t)}{\Delta P} = 1 - \exp \left[-\frac{S_{\text{tot}}(t)}{S_0} \right], \quad (5.3)$$

$$S_{\text{tot}}(t) = N\pi [r_0 + \Delta r(t)]^2, \text{ and} \quad (5.4)$$

$$\Delta r(t) = \int_0^t v[c(\tau)] d\tau, \quad (5.5)$$

with the total switchable polarisation ΔP , the reverse polarisation $P_{\text{sw}}(t)$ after time t , the switched area $S_{\text{tot}}(t)$ on the capacitor surface S_0 , the number of domains N with a radius r_0 at $t = 0$ and the increment $\Delta r(t)$ after time t , and the domain wall velocity $v(c)$ as a function of the polarisation state $c(t)$. Using equations (5.3)–(5.5), one can find the integral equation for the normalised switched polarisation

$$c(t) = 1 - \exp \left\{ -\frac{N\pi}{S_0} \left[r_0 + \int_0^t v[c(\tau)] d\tau \right]^2 \right\}. \quad (5.6)$$

The radial growth distance $\Delta r(t)$ can be expressed from equation (5.3) and (5.4) and compared to equation (5.5) to get

$$R \sqrt{\ln \frac{1}{1 - c(t)}} - r_0 = \int_0^t v[c(\tau)] d\tau, \quad (5.7)$$

where $R^2 = S_0/(N\pi)$, hence, R represents the average nucleation distance. Differentiation of equation (5.7) by the time yields

$$\dot{c}(t) = \frac{2}{R} \sqrt{\ln \frac{1}{1 - c(t)}} [1 - c(t)] v[c(t)], \quad (5.8)$$

with the initial condition

$$c(t) = 1 - \exp \left[-\frac{r_0^2}{R^2} \right]. \quad (5.9)$$

The generalised approach with equations (5.8) and (5.9) can be used to describe the polarisation reversal in thin films for varying domain wall velocities. If an exponential domain wall velocity according to Miller and Savage, equation (2.27), is taken, which is compatible with the exponential field dependence of the switching time observed in our films [equation (2.24)], one has to solve the differential equation (5.10):

⁷This modelling was mainly done with the help of Pavel Mokřý, working at the Technical University of Liberec, Czech Republic.

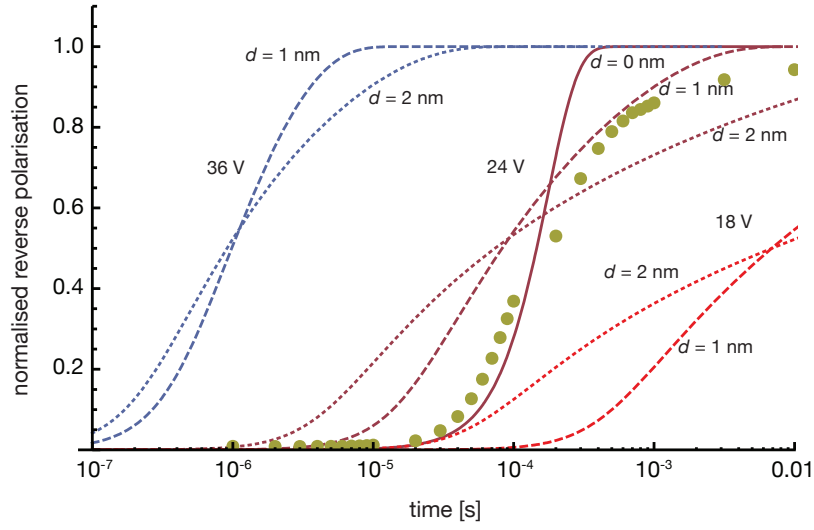


Figure 5.21: The retardation effect due to the depolarisation field of dielectric layer according to equation (5.10) is illustrated here for a passive layer of a thickness $d = 1$ (dashed) and 2 nm (dotted) and three voltages $V = 36, 24$, and 18 V. Experimental points of the 115 nm thick film with Au are shown as dots with a pulse amplitude of 12 V.

$$\dot{c}(t) = \frac{2}{t_\infty} \sqrt{\ln \frac{1}{1 - c(t)}} [1 - c(t)] \exp \left\{ -\frac{\delta}{E[c(t), V]} \right\}, \quad (5.10)$$

with the time constant t_∞ from the Miller–Savage wall velocity for infinitely large fields and the average electric field in the ferroelectric $E[c(t), V]$:

$$E = \frac{\frac{V}{h} - \frac{d}{\varepsilon_0 \varepsilon_d h} P_f}{1 + \frac{d \varepsilon_b}{h \varepsilon_d}} = \frac{\frac{V}{h} - \frac{d P_s}{\varepsilon_0 \varepsilon_d h} [2c(t) - 1]}{1 + \frac{d \varepsilon_b}{h \varepsilon_d}}, \quad (5.11)$$

with the ferroelectric polarisation P_f , h and d standing for the thickness of the ferroelectric and the dielectric layer, respectively, and ε_b , respectively ε_d for the relative background dielectric constant of the ferroelectric and the dielectric constant of the dielectric layer.

An example of the model described above with the thickness $h = 115$ nm, the relative permittivity of the ferroelectric layer $\varepsilon_f = 9$, the relative permittivity of the dielectric layer $\varepsilon_d = 2$, the spontaneous polarisation $P_s = 7 \mu\text{C}/\text{cm}^2$, the time constant $t_\infty = 10^{-10}$ s, and the activation field from the Miller–Savage wall velocity law $\delta = 3 \cdot 10^9$ V/m is shown in figure 5.21.

In the beginning of the polarisation reversal, when the depolarisation field is directed parallel to the applied electric field, the polarisation reversal is accelerated. When half the polarisation is reversed, a depolarisation field emerges that reduces the field in the ferroelectric. The field reduction leads to a deceleration of the polarisation reversal in the second half of the polarisation reversal as can be seen in figure 5.21.

This shows that the depolarising effect in the KA model with the exponential wall mobility law can lead to an appreciable retardation at the final stage of the polarisation reversal. The results of this model cannot be applied directly to the quantitative descrip-

tion of our data, since these results are based on the KA model, which is not valid for our system. However, we believe that they indicate that the depolarising effect can lead to a substantial retardation of switching in the ferroelectric capacitors with a dead layer.

5.7 Summary

Characteristic features of dielectric and hysteresis loop measurements of thin P(VDF-TrFE) films have shown a strong temperature and electrode material dependence. The increase in the permittivity upon heating and the tilt of the loop could be related to the presence of a passive layer. The unusual effect of an increase of the permittivity due to the passive layer was explained by a multidomain state at zero field favoured by the passive layer and low coercitivity. With the strong temperature dependence of the coercive field, the higher permittivity in the sample with Al compared to Au electrodes could be explained.

It was further shown that the polarisation reversal mechanism does not follow the simple Kolmogorov-Avrami (KA) model with nucleation and expansion of cylindrical domains. Nevertheless, the switching onset follows this model in a first step, but decelerates considerably when almost half of the polarisation is switched. Based on switching charge and AFM results, we suggest that this deceleration is controlled (in addition to domain overlapping) by two more effects: (i) the effect of inhomogeneity of the wall mobility and (ii) the impact of the depolarising effect induced by a dead layer in the sample.

Chapter 6

Switching Properties in Applications — Ferroelectric Transistors

Abstract A simple concept, high integration potential, and a non-destructive read-out process make non-volatile transistors very attractive for memory applications. Such devices with a ferroelectric gate could not be realised on large industrial scales due to material processing and property-related problems with the traditional perovskite oxide ferroelectrics. Organic ferroelectrics as a gate material offer a promising alternative due to their interesting combination of a low permittivity, a reasonably high spontaneous polarisation, and a low-temperature deposition process. Capacitors with organic ferroelectrics integrated in silicon-based devices have been investigated experimentally, but very little data is available on single transistor (1T) memory structures with organic ferroelectrics. Important questions of switching performance of these ferroelectrics and retention properties have therefore not been addressed.

Our Contribution In collaboration with the group of Prof. A. Ionescu from the *Laboratory of Micro/Nanoelectronic Devices* at EPFL, we demonstrated for the first time a hybrid silicon/P(VDF-TrFE) transistor with non-volatile operation. The polarisation reversal kinetics was measured and compared in the transistor and the simple capacitor structures. Direct PFM studies on the ferroelectric films integrated in the transistor structure demonstrated the stability of the polarisation and enables a better understanding of retention loss mechanism. A possibility to explain the observed exponential decay of the drain current was given in terms of a semi-quantitative retention model with charge injection in a linear, low field regime.

6.1 Working Principle

6.1.1 Ferroelectric Memories

The ideal memory for general purposes would have the following characteristics:

- non-volatile,
- electrically erased and programmed in-system,
- random access,

- high bit density,
- short read and write times,
- excellent reliability, and
- low costs per bit.

Ferroelectric field effect transistors make for an ideal memory in view of these criteria. The idea of information storage with ferroelectric materials has thus existed for decades [Anderson, 1952]. Its realisation has however involved serious complications and the number of commercial products based on ferroelectric memories is still very limited. The main issue concerns the reliability requirements of such devices with a functionality for at least 10 years. Costs, processing, and integration problems were additionally hindering their development.

In the charge based design of ferroelectric devices (ferroelectric random access memory, FeRAM), a ferroelectric capacitor needs to be supported by a transistor. The transistor is required for the addressability of the capacitor. It guarantees that a voltage signal is only written to the capacitor, when both the word and the bit line are at the high voltage level as shown schematically in figure 6.1(a).

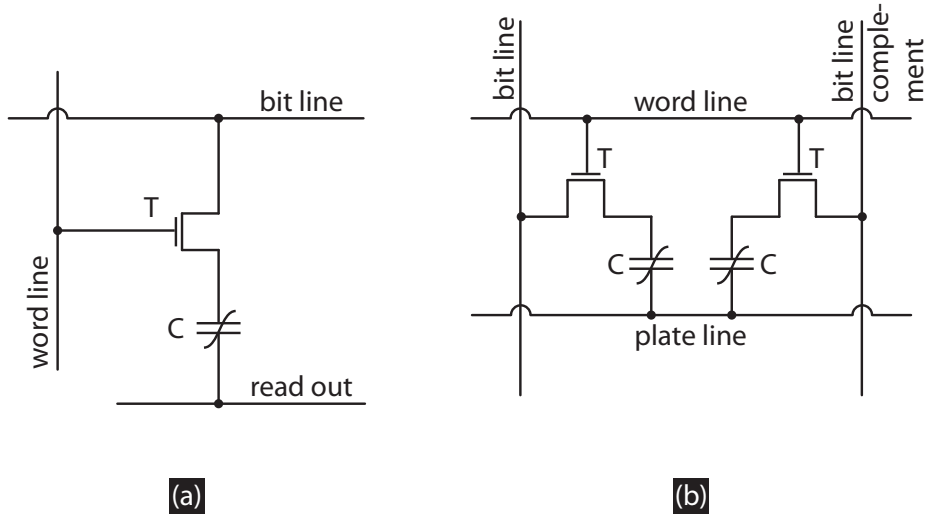


Figure 6.1: Typical design for a cell of a 1C-1T (a) and a 2C-2T (b) non-volatile ferroelectric memory. T denotes a transistor, C a ferroelectric capacitor.

To read the information of such a cell, the capacitor is re-written and the output current is measured and compared to a reference capacitor. If the polarisation of the ferroelectric capacitor is reversed, the current is higher than in the non-switching case and can be interpreted as a “1” information [Dawber et al., 2005].

In the 1C-1T design, there is a single reference capacitor for all the cells in a memory block. This causes a lifetime problem for the reference transistor, since it fatigues much faster than a single memory cell due to the increased number of writing steps. This problem was solved by a change in the design. In the 2C-2T layout shown in figure 6.1(b), each cell consists of a memory capacitor and a reference capacitor. The reference capacitor is written always together with the memory capacitor and is therefore not more

prone to fatigue. Even though the problem of different fatigue rates can be solved in this design, it is not very advantageous in terms of bit density. Texas Instruments are now about to develop 4 and even 8 Mbit devices [ISAF, 2008]. A survey of studied ferroelectric cell designs and architectures is available [Sheikholeslami et al., 2000].

The preferred ferroelectric materials in the above mentioned memory cells are PZT and strontium bismuth tantalate (SBT). The latter is less prone to fatigue, whereas the first can be processed at lower temperatures [Dawber et al., 2005]. Such memory cells cannot be found in a large number of applications, but they were realised in niche products, like game's consoles, radio frequency tags (RF tags), or ticket systems¹ with somewhat lower memory storage densities.

In addition to high temperature processing difficulties, a disadvantage of the FeRAM design is the *destructive read-out* process that is characteristic for charge based memories. Due to required writing after each reading process, the devices are more susceptible to fatigue and have a higher power consumption.

A valid alternative to the above discussed ferroelectric memory cells are field effect transistors with a ferroelectric gate (FeFET), a resistive base device. FeFET are very attractive due to the non-destructive read-out and the single transistor design, which has a higher potential in terms of bit density.

Before we discuss ferroelectric field effect transistors (in section 6.1.3), standard field effect transistors are briefly introduced.

6.1.2 Field Effect Transistors

Field effect transistors (FET) are unipolar² devices, in which a current flow between two electrodes, called *source* and *drain* is controlled by the potential on a third electrode, the *gate*. The electric current in the channel between source and drain is determined by the conductance of the channel, i.e. the concentration and mobility of free charge carriers. The concentration of carriers in the channel is controlled by an electric field in FET, which penetrates into the semiconductor material.

There are two types of field effect transistors, the junction field effect transistor (JFET) and the metal-oxide-semiconductor field effect transistor (MOSFET)³. The physics of such semiconductor devices is discussed in many textbooks [Kasap, 2002, Sze, 1985]. We consider here only MOSFET, which were used in this work. Its name refers to the material structure with the metallic gate, the insulator, typically an oxide, but also other dielectrics, e.g. Si_3N_4 , and the semiconductor channel.

A schema of the MOSFET is shown in figure 6.2. A *p*-type semiconductor is heavily doped with donor elements by ion implantation forming the source and drain n^+ -regions. At the pn^+ contact, space charge layer including a depletion region builds up due to the electron and hole concentration gradients and the consequent diffusion and recombination.

Without a biased gate, the n^+pn^+ region between source and drain blocks the conductance through the channel as shown in figure 6.2(a) and (c).

The situation changes, when a (high enough) voltage is applied between the gate electrode and the source. Due to the electric field penetrating into the semiconductor,

¹So-called smart cards based on FeRAM memory are used in the ticketing system of the *Japan Railways Group*.

²“Unipolar devices are devices, in which only one type of carrier predominantly participates in the conduction process.”[Sze, 1985]

³This name is for the most common case with an oxide used as dielectric layer. For the more general case, the structure is called metal-insulator-semiconductor field effect transistor (MISFET).

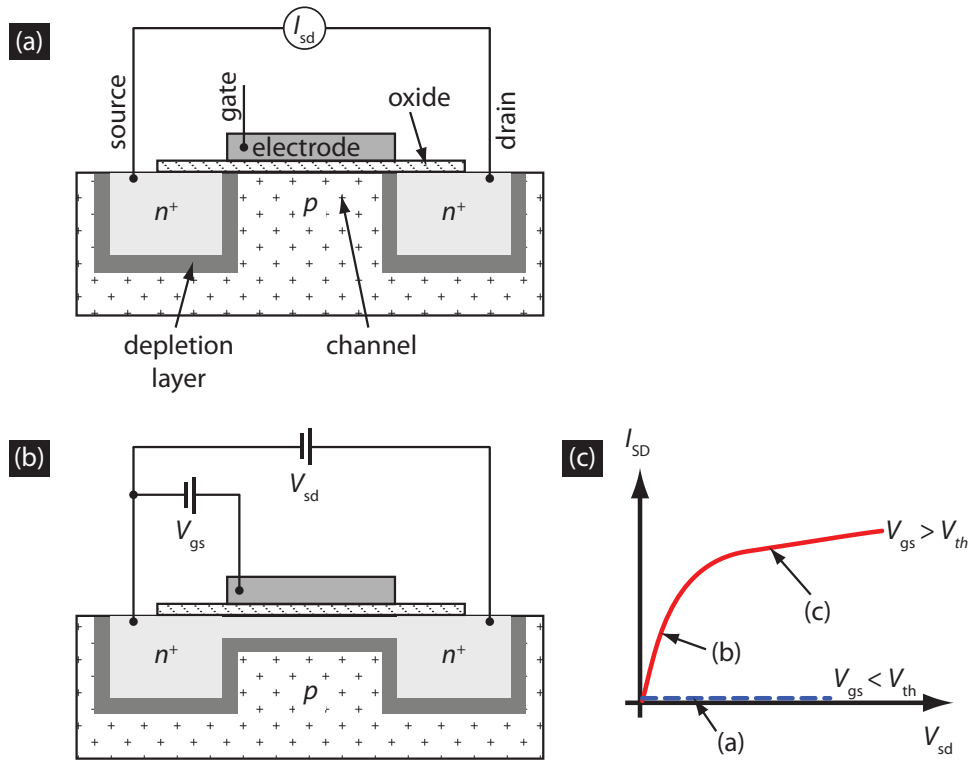


Figure 6.2: The schematic structure of a metal-oxide-semiconductor field effect transistor (MOSFET) without any applied voltage (or $V_{gs} < V_{th}$), in the “off” state (a); in the “on” state with an applied voltage between the gate and the source $V_{gs} > V_{th}$ to open the channel for electrons to drift from source to drain (b). The drain current I_{sd} is shown as a function of the source-drain voltage V_{sd} in figure (c).

holes drift away and the region below the dielectric layer becomes *depleted* of holes with respect to the equilibrium concentration of holes. Above a threshold gate voltage, V_{th} , the concentration of holes becomes much smaller than the concentration of electrons according to the mass-action law $np = \text{const.}$ within a layer of a certain width adjacent to the dielectric, as shown in figure 6.2(b). The formation of the n channel layer in the p -type semiconductor, the so-called *inversion layer*, brings about a continuous n -type layer between source and drain with mobile electrons as charge carriers. This allows for the electrical conduction between the source and drain regions in the co-called “on” state.

The MOSFET is a volatile device. With a zero gate-source voltage, the device is in the “off” state independent of the previously applied voltage. A non-volatile FET integrating a ferroelectric material is described below.

6.1.3 Ferroelectric Field Effect Transistors

The idea to replace the electric gate by a ferroelectric material in a field effect transistor has existed for a long time; Ross patented it in the 1950s [Ross, 1957]. The structure of such a device is depicted in figure 6.3(a).

Compared to an ordinary field effect transistor (figure 6.2), an electric field in the source-drain channel is maintained even after the removal of the electric field applied to the gate electrode due to the ferroelectric polarisation. If the polarisation of the ferroelectric gate is reversed by a positive voltage pulse, an inversion state in the p -doped region is induced, electrons accumulate in the channel, and a current can pass from the source through the channel to the drain [“on” state, figure 6.3(c)].

In the case of the “off” state, the drain current is small due to the Schottky barriers at the np and pn interfaces that represent two oppositely oriented diodes that block the charge carrier transport. Consequently, only a small leakage current can pass from the source to the drain contact [“off” state, figure 6.3(b)].

A ferroelectric field effect transistor (FeFET) can be used to store information. Compared to the memory cells presented in the previous section, there are four main advantages:

- a non-destructive read-out,
- a better fatigue resistance,
- a lower power consumption, and
- a higher bit density.

A non-destructive read-out of the stored information is possible by testing the source-drain current of the FeFET. Such a check does not change the polarisation state of the ferroelectric and thus the information is maintained. Re-writing of the information to the ferroelectric capacitor is therefore redundant after a read-out step and entails advantages of read/write endurance as well as a reduced power consumption. The integration of the ferroelectric directly in the gate of the transistor structure is supposed to increase the bit density compared to the 1C-1T and even more compared to the 2C-2T memory cell design.

The realisation of a FeFET using triglycine sulfate (TGS) as a ferroelectric and CdS semiconductor was first reported in 1963 by Moll and Tarui [Moll and Tarui, 1963]. The

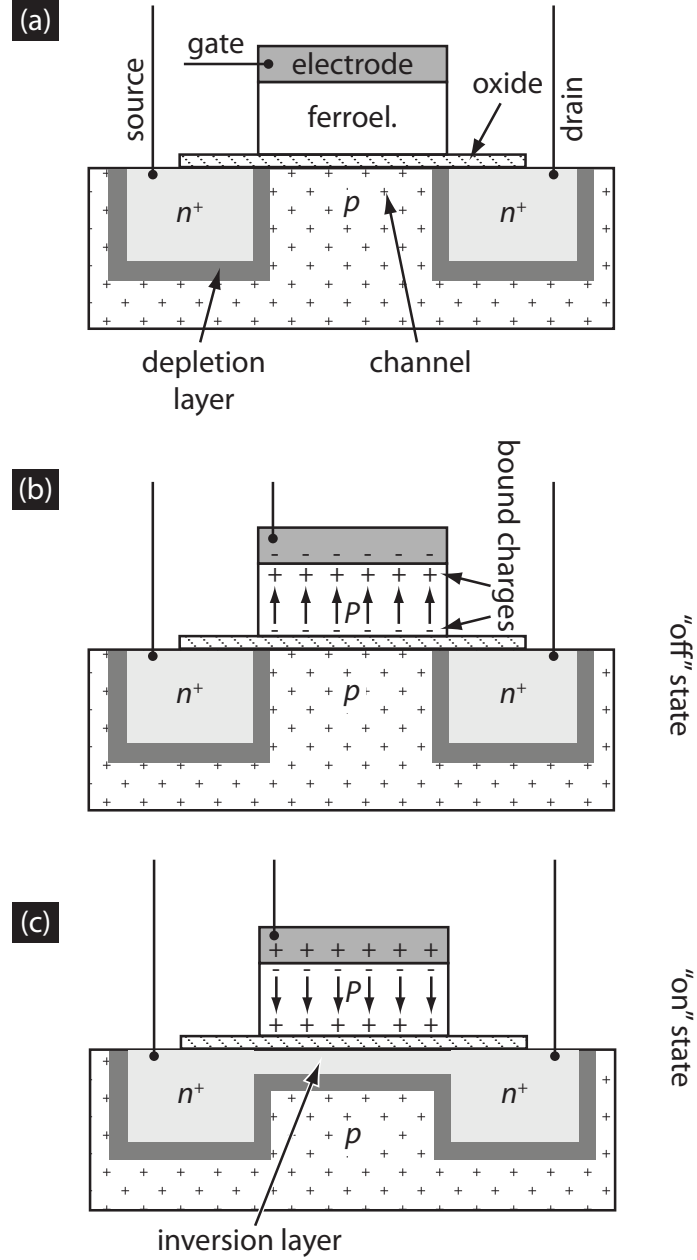


Figure 6.3: The schematic structure of a ferroelectric field effect transistor (a). Only a leakage current can flow between source and drain in a nnp -structure without mobile negative charge carriers in the channel (b). Polarisation reversal of the ferroelectric and the resulting mobile negative charge carriers in the channel “opens” the transistor and a relatively large source-drain current I_{SD} can flow (c).

first transistor with Si was realised about ten years later with a $\text{Bi}_4\text{Ti}_3\text{O}_{12}$ ferroelectric gate [Wu, 1974]. In more recent works, perovskite ferroelectrics like PZT were used [Mathews et al., 1997]. The performance of these devices in terms of modulation efficiency of the ferroelectric gate and retention were however not satisfactory. As such, commercial realisation of these devices has not yet been achieved, despite the mentioned advantages of FeFET.

The properties of current state of the art FeFETs are shown in table 6.1. The reported values of retention time, drain current ratio, and programming time are the best values of different devices. The impressive results could however not be reproduced by other groups. Furthermore, the fabrication for these devices is complex and expensive.

Table 6.1: Current state of the art of inorganic ferroelectric field effect transistors (measured in different devices) [Aizawa et al., 2004, Li et al., 2002].

Property	value	unit
retention time	16	days
drain current on/off ratio	10^9	-
programming time	10^{-8}	s

6.1.4 Difficulties in the Realisation of Ferroelectric FET

Several difficulties for the realisation of FeFET were reported. They are listed below.

- (i) The polarisation in some ferroelectric materials might not be high enough [Wu, 1974]
- (ii) Injection of charges and screening of the polarisation [Wu, 1974]
- (iii) Reduction of the ferroelectric polarisation due to the high depolarisation field
- (iv) Polarisation reversal complications due to the low permittivity oxide layer
- (v) Direct (or via a buffer layer) contact between the gate ferroelectric and the channel makes the interfacial properties crucial for the working of the device
- (vi) Processing limitations, especially in terms of heat treatments

These difficulties can be divided into two categories of physical (i-iv) and fabrication (v, vi) issues.

Fabrication Problems

Processing (vi) is indeed a problem of FeFETs, because normal oxide ferroelectrics have to be annealed at relatively high temperatures of at least 500°C in oxygen atmosphere. Such conditions are not compatible with the Si transistor structure, which requires processing typically below 400°C .

Physical Problems

The first and second points turned out not to be a problem contrary to the expectations in the pioneering cited papers. The required polarisation can be estimated with the required gate voltage V_g^{on} for the “on” state and the oxide layer thickness d . The field in the dielectric is given by the relation:

$$E_d^{\text{on}} = V_g^{\text{on}}/d. \quad (6.1)$$

The same field can be induced at zero field by a ferroelectric polarisation, which is equal to the dielectric displacement in the oxide layer:

$$P_r \approx D = \varepsilon_0 \varepsilon_d E_d. \quad (6.2)$$

Entering realistic parameters for our transistors (see section 6.4) with $d = 10$ nm, $\varepsilon_d = 3.9$ for SiO_2 , and $V_g^{\text{on}} \approx 3$ V (compare to figure 6.15), we get a required polarisation to achieve the saturation region of $P_s = 1 \mu\text{C}/\text{cm}^2$. This value corresponds to $\approx 20\%$ of the remnant polarisation of P(VDF-TrFE) and of course even less in the case of typical high-performance perovskite ferroelectrics, which have polarisation values ten times greater than PVDF.

The minimal polarisation requirements are thus much lower than in the 1T-1C and 2C-2T memory cells, in which the remnant polarisation has to be at least $10 \mu\text{C}/\text{cm}^2$ in order to permit the detection of the switching charge [Dawber et al., 2005].

It is true that the device is sensitive to surface traps and charge injection (v). In order to reduce charge injection, an insulating oxide layer between the ferroelectric gate and the semiconductor is indispensable (figure 6.3).

The introduction of a low-permittivity dielectric layer (v) complicates the polarisation reversal in the ferroelectric (iv). In a structure with a high-permittivity ferroelectric and a low-permittivity dielectric, an applied voltage drops mainly in the dielectric layer.

However, the primary physical issue is the short retention (compared to the required retention of several years) and drain current control by the ferroelectric gate with a high “on”/“off” ratio.

The short retention time for information in FeFET was attributed to two major causes [Ma and Han, 2002]: the *depolarisation field* (iii) and the *gate leakage current* (ii).

Depolarisation Field

In the following, we give an estimate of the depolarisation field as a function of the insulating layer. To discuss the problem of the depolarisation field, we consider the gate structure as a ferroelectric and a dielectric capacitor that are connected in series, as illustrated in figure 6.4.

We write for the dielectric displacement in the ferroelectric:

$$D_f = \varepsilon_0 \varepsilon_b E_f + P_f, \quad (6.3)$$

with the ferroelectric contribution to the polarisation P_f , the background dielectric constant ε_b of the ferroelectric, and the electric field in the ferroelectric layer E_f .

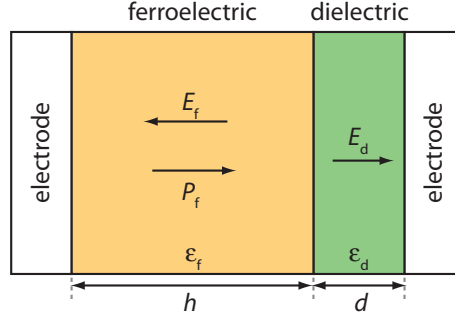


Figure 6.4: An electrode-ferroelectric-dielectric-electrode structure.

For an equal dielectric displacement $D_{f,\perp} = D_{d,\perp}$ in the dielectric and the ferroelectric perpendicular to the film surface, we can write:

$$\varepsilon_0 \varepsilon_d E_d = \varepsilon_0 \varepsilon_b E_f + P_f, \quad (6.4)$$

where ε_d and E_d are the dielectric constant and the electric field in the dielectric layer, respectively.

The total potential V drop in the ferroelectric and the dielectric with thicknesses h and d , respectively, is given by:

$$V = E_f h + E_d d, \quad (6.5)$$

Combining equation (6.5) with $V = 0$ for shorted electrodes and (6.4), we find for the electric field in the ferroelectric:

$$E_f = -\frac{P_f}{\varepsilon_0 \varepsilon_d \frac{h}{d} + \varepsilon_0 \varepsilon_b}. \quad (6.6)$$

E_f opposes the polarisation and thus called the depolarisation field.

There are two effects, which can reduce the polarisation due to the depolarisation field. The *first effect* is the reduction of the polarisation *in a single domain state* due to the field opposite to the polarisation. We can see from the equation of states (2.5) that the polarisation is reduced under the influence of the depolarisation field. Together with the electric field $E = E_f$ from equation (6.6), we get:

$$E_f = -\frac{P_f}{\varepsilon_0 \varepsilon_d \frac{h}{d} + \varepsilon_0 \varepsilon_b} = \alpha_1 P_f + \alpha_2 P_f^3. \quad (6.7)$$

The polarisation P from equation (2.5) was replaced here by P_f , which is needed for a more accurate description of depolarisation effects. Equation (6.7) can be rewritten as

$$0 = \left(\alpha_1 + \frac{1}{\varepsilon_0 \varepsilon_d \frac{h}{d} + \varepsilon_0 \varepsilon_b} \right) P_f + \alpha_2 P_f^3. \quad (6.8)$$

With equation (2.6), we can see that the effect from the depolarisation field corresponds to a shift of the Curie temperature to $T_0^* = T_0 - \frac{1}{\varepsilon_0 \varepsilon_d \frac{h}{d} + \varepsilon_0 \varepsilon_b} \frac{1}{\beta}$. T_0^* is lower than the Curie temperature T_0 of the ferroelectric at zero field.

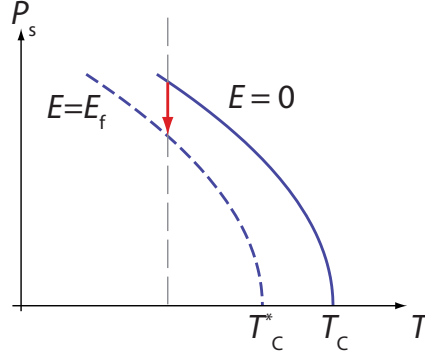


Figure 6.5: Illustration of the polarisation reduction in the single domain state due to the Curie temperature shift induced by the depolarisation field.

This leads to a reduction of the polarisation at a given temperature, as illustrated in figure 6.5.

The relative reduction of the polarisation due to the depolarisation field can then be found. Using $|\alpha_1|\varepsilon_0 = \frac{1}{2\varepsilon_f} = \frac{1}{2(\varepsilon - \varepsilon_b)}$ with the dielectric constant $\varepsilon = \varepsilon_f + \varepsilon_b$ as the sum of the ferroelectric and the background dielectric constants, it follows from equation (6.8)

$$\begin{aligned} P_f^2 &= -\frac{1}{\varepsilon_0\alpha_2} \left[\varepsilon_0\alpha_1 + \frac{1}{\varepsilon_d \frac{h}{d} + \varepsilon_b} \right] \\ &= -\frac{1}{\varepsilon_0\alpha_2} \left[\frac{1}{2(\varepsilon - \varepsilon_b)} + \frac{1}{\varepsilon_d \frac{h}{d} + \varepsilon_b} \right] \\ &\approx -\frac{1}{\varepsilon_0\alpha_2} \left[\frac{1}{2(\varepsilon - \varepsilon_b)} + \frac{d}{\varepsilon_d h} \right]. \end{aligned} \quad (6.9)$$

The second term in the last row can be seen as the variation ΔP_f of the polarisation P_f due to the depolarisation field. It follows then

$$2P_f\Delta P_f \approx \frac{d}{h} \frac{1}{\varepsilon_d \varepsilon_0 \alpha_2}; \quad (6.10)$$

and the relative change of the polarisation due to the depolarisation field can be written as:

$$\frac{\Delta P_f}{P_f} = -\frac{d}{h} \frac{2(\varepsilon - \varepsilon_b)}{\varepsilon_d}. \quad (6.11)$$

Thus it is seen that a small dielectric constant of the ferroelectric leads to a less pronounced impact of the passive layer on P_f .

In the *second effect*, a high depolarisation field causes the ferroelectric to break into domains. Domain formation leads to a reduction in the macroscopic polarisation of the ferroelectric and, consequently in the in the FeFET, to a possible loss of the inversion state in the source-drain channel.

Depolarisation can occur due to an insulating layer even without an intentionally deposited dielectric layer. A low-permittivity transition layer can form by the interdiffusion of the constituent elements at the ferroelectric-silicon interface, typically in high temperature processes.

Low remnant polarisation ferroelectrics, different device designs, high-permittivity dielectric layers were proposed to solve the problem of poor retention behaviour. The best retention results, according to [Setter et al., 2006], were achieved with high permittivity HfO_2 and HfAlO layers in a $\text{Pt}/\text{SrBi}_2\text{Ta}_2\text{O}_9$ (SBT)/ HfO_2/Si structure with a retention time of 30 days.

With a special 1T2C design incorporating the ferroelectric SBT in two oppositely poled capacitors on Pt and a silicon transistor, the retention time could be improved due to the reduction of the depolarisation field [Yoon and Ishiwara, 2001]. The simplicity of the single transistor FeFET was however lost in this design.

Leakage Current and Trapping

The other main cause for a reduction of the retention is gate leakage and trapping of carriers at the gate ferroelectric/dielectric interface. With a high field in the dielectric layer $E_d \approx -\frac{P_s}{\epsilon_0 \epsilon_d}$ and a thin dielectric layer [equations (6.5) and (6.6)], charge carriers can be injected through the insulating layer. Trapping of these charge carriers in interface states leads to a local compensation of the polarisation. Hence, the inversion layer of the source-drain channel is gradually lost.

Solution to the Problem

A thicker insulating layer could reduce the charge injection efficiently. Nevertheless, we can see from the equation (6.6) that increasing d also increases the depolarisation field. It is not possible to simultaneously eliminate the two major detrimental effects on retention time by modifying the insulating layer alone. A trade-off between the two effects has to be found concerning the insulating layer. Alternatively, a more suitable ferroelectric material, with an appropriate combination of spontaneous polarisation and of low dielectric constant would be beneficial.

Furthermore, one has to take into account low programming voltage requirements [problem (iv) in the above list of issues]. With the introduction of a dielectric layer of low permittivity, the voltage drops mainly there. In the case of a high permittivity ferroelectric, the applied voltage drops in the dielectric layer and the small electric field felt by the ferroelectric may not be sufficient for fast polarisation reversal. Ferroelectric materials with a low permittivity are therefore preferable.

6.2 Integration of Organic Ferroelectrics into Transistors

6.2.1 Advantages of the Organic Ferroelectrics in Transistors

Polymer ferroelectrics with the ferroelectric characteristics, discussed in the previous chapters, differ however from perovskite ferroelectrics in the dielectric constant, the spontaneous polarisation, and the magnitude of the electric field for small switching times.

The main advantages of the integration of organic ferroelectrics in the gate of FET are given below.

- Low dielectric constant
- Low temperature and relatively simple processability

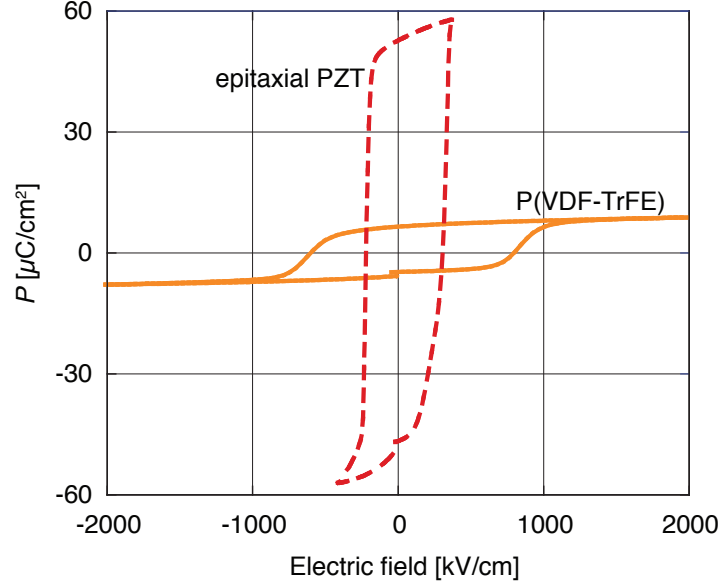


Figure 6.6: Comparison of an epitaxial PZT thin film sample with a P(VDF-TrFE) ferroelectric. The differences in the remnant polarisation and the coercive field are considerable.

- Good ferroelectric properties in terms of polarisation reversal times
- Non-toxic

The low dielectric constant in comparison to oxide ferroelectrics makes organic ferroelectrics very attractive for applications, in which a polarisation reversal has to be achieved within a structure with low-permittivity layers as discussed before.

Processing of P(VDF-TrFE) below 140°C is a crucial advantage over oxide perovskites⁴ that generally have to be annealed at temperatures higher than the critical limit of 400°C for silicon technology.

The polarisation reversal was shown to be fast with switching times below 1 μs at high enough fields. Studies on the polarisation reversal of P(VDF-TrFE) and especially its kinetics in transistor structures are however missing.

A smaller spontaneous polarisation of P(VDF-TrFE) compared to PZT or other ferroelectric oxides is considered an advantage, since the depolarisation field [equation (6.6)] is reduced and charge injection therefore suppressed, while the remnant polarisation is still well above the minimal polarisation required to achieve the saturation region in the silicon transistor (as discussed in section 6.1.4 above). A direct comparison of the hysteresis loops in figure 6.6 of a P(VDF-TrFE) film (thickness: 115 nm) with gold electrodes with an epitaxial PZT film (thickness: 650 nm) illustrates the main difference of a smaller remnant polarisation and a higher coercive field in the organic ferroelectric.

6.2.2 Drawbacks of the Organic Ferroelectrics in Transistors

Possible disadvantages of organic ferroelectrics are listed below:

⁴PZT requires an annealing temperature of at least 450°C for the transition from the pyrochlore to the perovskite phase; SBT requires even higher temperatures above 600°C

- Limited temperature stability
- Uncertainty of the fatigue properties and long term endurance
- Low melting temperature imposes limits on the thermal budget of the device
- High fields for fast polarisation reversal

Low temperature stability is due to a Curie point, which is just around 100°C (for the 65/35 weight% composition), and a melting point at about 155°C (according to the manufacturer *Solexis*). As well as the low Curie point, the rather strong temperature dependence of the coercive field (see chapter 5) limits the use of this material for fast and stable devices over a wide temperature range. For everyday, room temperature operation, the temperature stability is however sufficient.

Uncertainty of the properties of the P(VDF-TrFE) thin films integrated in transistor structures can be considered as a risk. In particular, the fatigue behaviour, the polarisation reversal, and the long term stability of such devices are not well studied.

Concerning processing, the most important problem is related to the fact that interlevel dielectric and protective coating of silicon devices is usually achieved using spin-on glass (SOG). It is best suited to fill voids between metal vias (connections). The SOG technique requires curing temperatures between 200 and 400°C [Madayag et al., 2001], which is above the thermal stability of P(VDF-TrFE). This problem is specific to CMOS technique and can be circumvented by a different choice of materials.

6.3 Literature Review on FET with Organic Gate Electrodes

The first study of a FeFET with an organic ferroelectric gate was presented by Yamauchi in the mid 1980s [Yamauchi, 1986]. The advantages of the organic ferroelectric were recognized in this work, but no retention properties were presented. In the fabricated Al/SiO₂/P(VDF-TrFE)/SiO₂/Si structure, the two oxide layers were used to improve breakdown resistance and to reduce charge injection into the ferroelectric. The P(VDF-TrFE) layer with a thickness of 80 nm was spun onto the silicon oxide. This FeFET was characterised by an excellent “on”/“off” drain current ratio of 10⁶. The required programming pulses, > 180 V for 10 s, were very high, presumably due to the thick SiO₂ layers (50 and 71 nm).

A more recent study of hybrid devices with organic ferroelectrics integrated in inorganic semiconductor devices were limited to capacitor — and not transistor — structures. Several groups measured the typical capacitance hysteresis of a metal-ferroelectric-insulator-semiconductor structure with P(VDF-TrFE) in thin Langmuir-Blodgett films [Gerber et al., 2006, Reece et al., 2003] and spun layers [Lim et al., 2004]. Gerber et al. reported that upon the application of a voltage between the *p*-type silicon and the metal electrode, the capacitance showed a hysteresis behaviour, which disappeared above the Curie point of the 36 nm thick ferroelectric film. Hence, the capacitance shift was ascribed to the ferroelectric properties of the copolymer. The voltage required for the hysteresis behaviour was only ±3 V, a value compatible with the required operation voltage in silicon devices.

Other hybrid concepts, such as the modulation of the electric transport properties of a two dimensional electron gas (2DEG), exist. In an Al_{0.3}Ga_{0.7}N/GaN heterostructure,

the conductance of the 2DEG could be modulated by a factor 3 due to a P(VDF-TrFE) ferroelectric gate [Malin et al., 2007]. The device costs are however a disadvantage for their application in commercial products.

Fully organic electronics are expected to emerge as an alternative besides silicon technology due to their advantages in terms of costs and processibility. In such fully organic systems, organic ferroelectrics might play an important role in memory applications. Therefore, most of the research on organic ferroelectric gates is directed at fully organic FeFETs and the hybrid approach with an organic ferroelectric gate on a silicon technology transistor is studied to a minor extent.

In fully organic FeFETs, the conductance increase in the semiconductor channel originates in the accumulation of charge carriers, which is not an inversion layer as in inorganic devices. Such devices were fabricated successfully by several groups. FETs with pentacene as the semiconductor and an organic ferroelectrics were studied. The ferroelectric was either a nylon⁵ or a P(VDF-TrFE) polymer. “On/off” drain current ratios of 200 and 30 at a gate voltages of 2.5 V and 0 V at programming times of more than 200 ms were achieved [Schroeder et al., 2004, Unni et al., 2004]. The ferroelectric nature of the observed effect was however questioned due to the low switching voltage compared to the coercive field of the used material [Naber et al., 2005].

Probably the most successful realisation of an entirely organic FeFET was based on a poly[2-methoxy, 5-(2'-ethyl-hexyloxy)-*p*-phenylene-vinylene] (MEH-PPV) *p*-type semiconductor and a ferroelectric P(VDF-TrFE) gate. These devices yielded an “on”/“off” drain current ratio of 10^3 to 10^5 [Naber et al., 2005]. Compared to inorganic transistors, the high drain current “on”/“off” ratio was achieved by a considerable increase of the surface charge accumulation ($1.8 \mu\text{C}/\text{cm}^2$) in the “on” state in the semiconducting polymer and, compared to organic transistors, by a low mobility of the charge carriers in MEH-PPV (only 1% of pentacene) in the “off” state. The absence of a gate oxide allows for higher charge densities on the gate, which are limited in inorganic FeFET by the insulator breakdown field. A “coercive” voltage of ± 35 V was measured for the $0.85 \mu\text{m}$ -thick P(VDF-TrFE) layer in drain current versus gate voltage measurements. The excellent results were explained by a good, well-defined interface due to the use of dissimilar solvents. Retention with an “on”/“off” ratio of 10^4 after one week was demonstrated and endurance after 1000 programming cycles is still good with a ratio of 10^3 [Naber et al., 2005].

A reduction of the coercive voltage below 5 V for organic ferroelectrics by a decrease of the film thickness (< 60 nm) seems to be possible. Nevertheless, one should keep in mind that the reduction of the film thickness leads to an increase in the depolarisation field, which destabilises the polarisation.

For a comparison of properties of PVDF and of materials used in commercial FeRAM cells (by Ramtron and Celis), table II in the work of [Ducharme et al., 2005] can be consulted.

6.4 Ferroelectric Field Effect Transistor Fabrication

We chose a hybrid approach with the integration of an organic ferroelectric as a gate in silicon technology transistor structures for studying polarisation reversal of the ferroelectric copolymer in transistor structures and its ability to control drain current.

The silicon semiconductor transistor element with the source and drain region, the

⁵The commercially available poly(*m*-xylylene adipamide) was used in the work of Schroeder et al.

channel and the gate structuring were produced by Giovanni A. Salvatore and Didier Bouvet affiliated to the group of Prof. A. Ionescu (*Laboratory of Micro/Nanoelectronic Devices* at EPFL).

6.4.1 Device Design

The transistor structure was fabricated using standard silicon technology with highly doped n^+ regions as illustrated in figure 6.3. The ferroelectric gate was deposited on top of the oxide layer and not directly above the source-drain channel, because the high SiO_2 band gap reduces charge injection into the ferroelectric.

In a single 4-inch silicon wafer, many transistors with different gate dimensions were fabricated. All possible combinations of length and width between 2 and $50\text{ }\mu\text{m}$ can be found on the wafer. A photo with field of transistors of various gate dimensions is given in figure 6.7(a). An example of a transistor with quadratic source and drain regions and the gold gate electrode on top of the ferroelectric is shown in figure 6.7(b); the whole structure is shown in the schematic (c). The respective thickness of each layer can be found in the overview of table 6.2.

6.4.2 Fabrication Details

The transistor regions in the $525\text{ }\mu\text{m}$ thick, p -type silicon $\langle 100 \rangle$ wafer with a resistivity of $0.1\text{--}100\text{ }\Omega\text{ cm}$ were separated by plasma etching of the wafer and the subsequent deposition of a low temperature oxide (LTO) in the resulting trenches. The wafer was chemical-mechanically polished. An LTO mask was built with lithography to define the source and drain regions for n^+ phosphorous doping. The silicon oxide mask was removed by a wet etching process and the gate oxide was then deposited to a thickness of 10 nm over the whole wafer surface.

The ferroelectric copolymer was then spun onto the oxide layer to form the ferroelectric gate and was annealed at $138\text{--}140^\circ\text{C}$ for 10 min . The gold electrode was then evaporated and was structured by photo lithography and wet etching as already described for the capacitors in section 5.2.2.

In the characterised structures, the source and drain regions were still covered by the thin oxide layer and the copolymer. With hard probes, a good contact could however be established (see 6.5.1) by scratching through the oxide.

6.5 Experimental Results

6.5.1 Polarisation Reversal in Transistor Structure

The fabricated and characterised samples are listed in table 6.2. The first sample, CapAu, is a normal capacitor with gold electrodes and a P(VDF-TrFE) thin film as already discussed in chapter 5; CapAl is identical but with aluminium electrodes. The third sample, Tr0, is a reference transistor structure without a ferroelectric gate. The transistor Tr1 consists of a ferroelectric film deposited directly on the source-drain channel without an intermediate oxide layer. The sample Tr2 is identical to Tr1, but includes an insulating oxide layer between the ferroelectric gate layer and the source-drain channel.

This set of samples allows for the investigation of the differences of the polarisation reversal properties between the simple capacitor structures as discussed in chapter 5 and

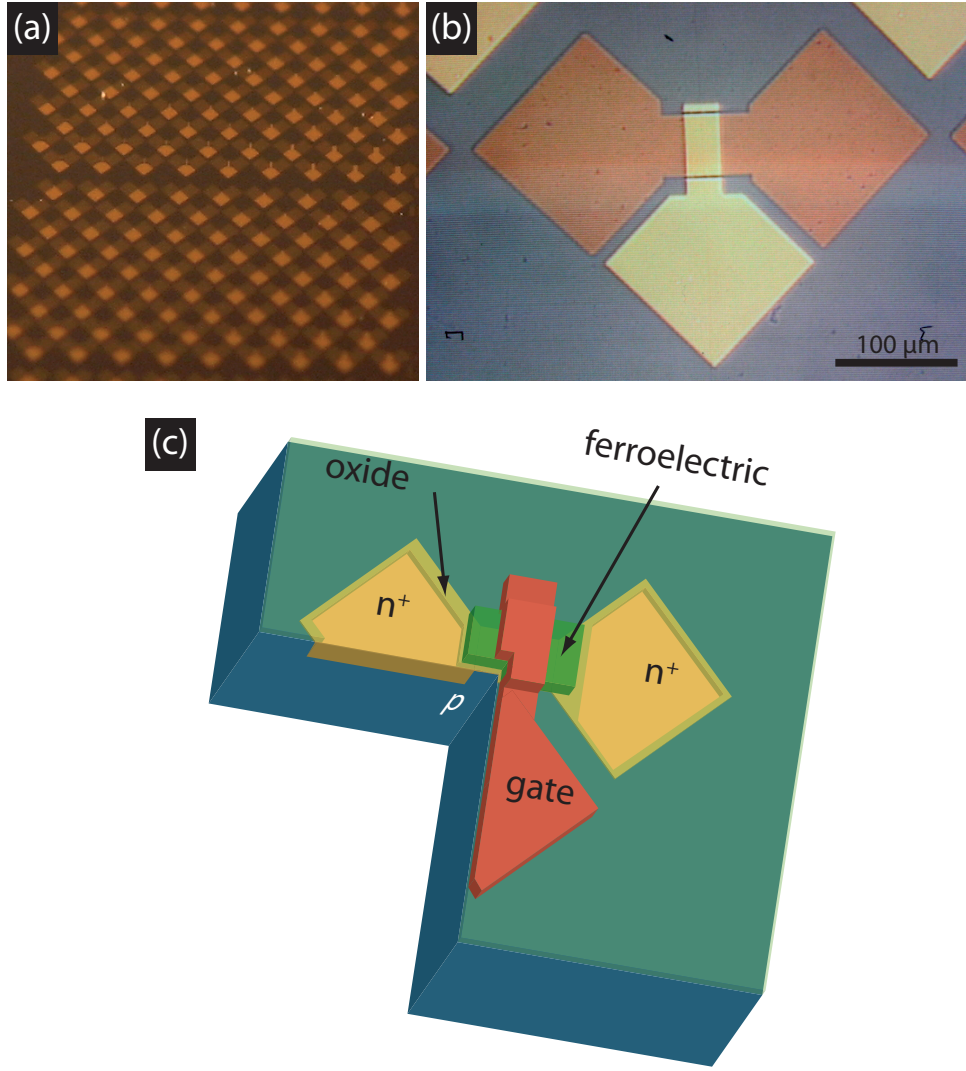


Figure 6.7: A small part of a wafer, about 4 mm wide, with an array of transistors with varying width and length of the gate is shown in (a). An example of a transistor with a channel length of $50\text{ }\mu\text{m}$ and a width of $30\text{ }\mu\text{m}$ (b) as well as a schema of the structure (c) are given.

Table 6.2: Fabricated samples used for the transistor characterisation (Tr X) and capacitor samples for comparison (Cap XX). The polymer was spun and annealed at T_{anneal} during 10 min.

Name	electrode		insulating layer [nm]	ferroel. thick-ness [nm]	T_{anneal} [°C]
	bottom	top			
CapAu	Au	Au	n.a.	118 ± 8	135
CapAl	Al	Al	n.a.	118 ± 8	135
Tr0	source-drain	gate, Au	SiO ₂ , 10	non	n.a.
Tr1	source-drain	gate, Au	non	150 ± 8	138–140
Tr2	source-drain	gate, Au	SiO ₂ , 10	210 ± 19	138–140

the three types of transistors.

Polarisation Hysteresis Loops

Polarisation loops of P(VDF-TrFE) in transistor structures with and without the channel oxide (Tr2 and Tr1) are presented in figure 6.8(a). The loops were measured under illumination with the voltage applied to the source and the charge collected from the gate electrode.

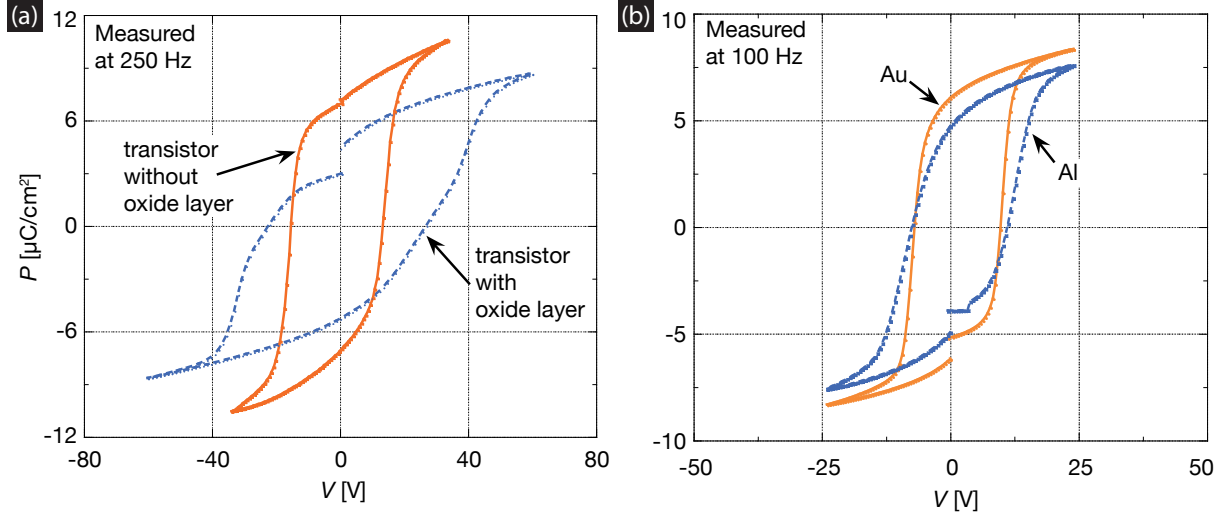


Figure 6.8: Comparison of polarisation hysteresis loops of P(VDF-TrFE) integrated in a transistor structure with (dashed) and without (continuous line) an insulating oxide between the ferroelectric and the channel (a) and in sandwiched between gold (continuous line) and aluminium (dashed) electrodes (b). The frequency of the triangular voltage pulse is indicated in the top left corner; the measurements were done under illumination.

The 10 nm thick oxide layer has three main effects on the loop:

- (i) a tilt out of the vertical position,
- (ii) a reduction of the remnant polarisation, and
- (iii) a decreased retention seen from the discrepancy between the remnant polarisation ($V = 0$) at the beginning — relaxed from the previously measured loop (a few seconds before) — and the end of the loop.

The capacitor sample with gold electrodes (CapAu) is shown in comparison to the identical sample with aluminium electrodes (CapAl) in figure 6.8(b). The three mentioned effects could also be observed in the sample sandwiched between aluminium electrodes. The passive layer, brought about by aluminium electrodes, compares well to the oxide layer in the transistor structure. From the viewpoint of the capacitor structures, it is interesting to see here that the artificially included low-permittivity oxide layer has the expected effects and confirms the conclusion of chapter 5 about the passive layer associated with aluminium electrodes.

The coercive voltage in the transistor structures are $V_c^{\text{Tr1}} = -15, 13 \text{ V}$ for the 150 nm thick P(VDF-TrFE) layer without gate oxide and $V_c^{\text{Tr2}} = -22, 27 \text{ V}$ for the 210 nm thick film with a gate oxide layer.

In figure 6.9(a), polarisation loops of the ferroelectric in a transistor structure with a gate oxide (Tr2) were measured in the dark and under illumination. A significant asymmetry of the loop measured in the dark could be observed. Under illumination, the asymmetry was suppressed.

Related to this asymmetry, we can notice a flat ramp of an almost constant polarisation. The ramp with an only slightly changing polarisation value from 0 V up to about +30 V (with respect to the source, at grounded gate condition) appears only for loop measurement in the dark as shown in figure 6.9(a). Interestingly, this feature of the voltage ramp also appeared in the capacitor samples with aluminium electrodes as shown in figure 5.9.

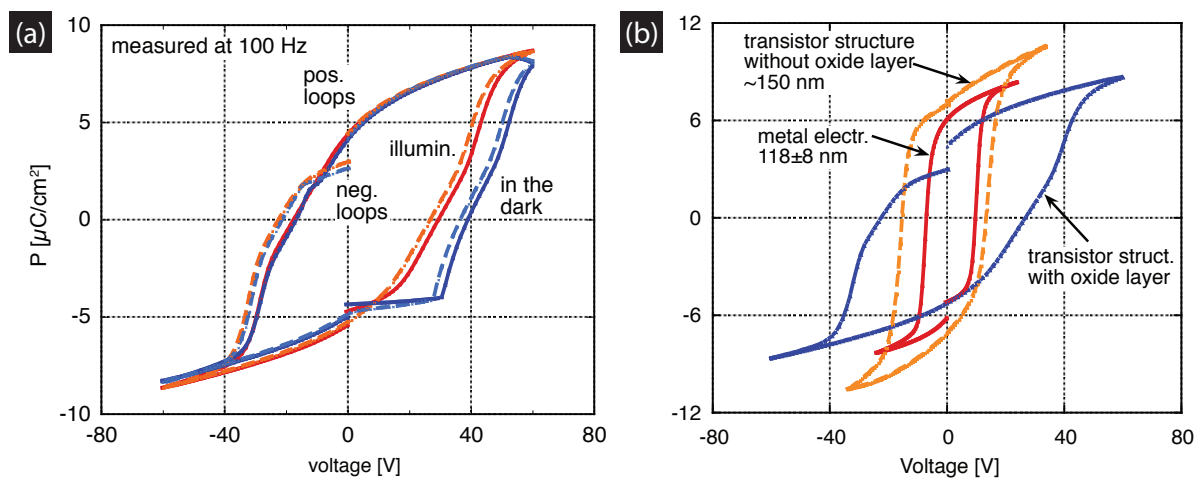


Figure 6.9: Polarisation hysteresis loops of P(VDF-TrFE) in a transistor structure with oxide layer (Tr2) under illumination and in darkness (a); the voltage is applied to the source while the gate is grounded. A polarisation loop of each of the three structures, with gold electrodes (CapAu), in a transistor without (Tr1) and with oxide (Tr2) is plotted in (b).

The direct comparison of the polarisation loops of the samples capacitor (CapAu) and transistor samples with (Tr2) and without oxide (Tr1) illustrates the similarities between the capacitor structure with gold electrodes and the transistor without an oxide layer, the copolymer film in the capacitor is about 30 % thinner and the coercive voltage thus smaller. The introduction of a gate oxide tilts the loop and reduces the remnant polarisation considerably.

Contacting the samples was not straightforward, since the oxide layer had to be scratched by very hard tips to get access to the source and drain regions. Other contacting techniques such as bonding and attaching small gold wires by a two component, conductive epoxy glue (*épotecny*, E212, with silver particles) after scratching the oxide were tested. The properties of the glued contacts were inferior to the direct contact with metal probes and micropositioners as shown in figure 6.10. An additional ohmic contact resistance or passive layer with conductance reduced the voltage felt by the structure and stretches the loop along the field direction. The probes usually used in this work (tungsten

probes with a tip radius of $2.4\text{ }\mu\text{m}$ from *Cascade Microtech, Inc.*) were not hard enough to get a good contact. Tungsten carbide probes were used instead (0.7 mm diameter, $7\text{ }\mu\text{m}$ tip radius, type T-07-10 provided by *Hilpert electronics AG*).

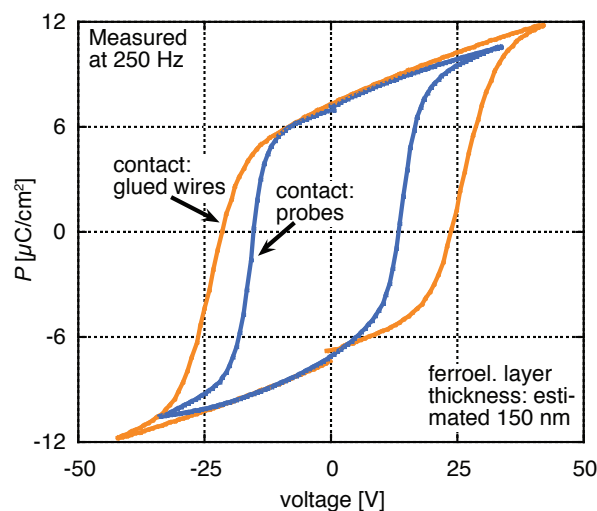


Figure 6.10: Polarisation hysteresis loops of P(VDF-TrFE) in a transistor structure without oxide layer (Tr1) contacted with hard probes and with glued gold wires. The samples were illuminated during the measurements.

Polarisation Reversal Kinetics

The polarisation reversal kinetics in transistor structures were characterised using a fast pulse technique and measuring the switching charges — as described in section 5.4.1.

The switching curves for several samples are presented in figure 6.11. The transistor with the gate oxide, Tr2, was measured under illumination (a) and in darkness (b). It is compared in this figure to the switching curves of the transistor, Tr1, without oxide layer (c) and the simple capacitor sample, CapAu, with gold electrodes in figure (d), both measured under illumination.

The apparent⁶ electric fields are given for each curve and were calculated dividing the switching pulse amplitude by the sample thickness according to table 6.2. The voltage of the switching pulse for the transistor sample with an oxide, Tr2, varied from $\pm 10\text{ V}$ to $\pm 90\text{ V}$ (a,b), for the similar sample without oxide, Tr1, from 5 V to 35 V (c), and for CapAu from 4 V to 28 V (d). The amplitudes of the first and third poling pulses were $\pm 90\text{ V}$ (a,b), 36 V (c), and 28 V (d), respectively. The numbers in the graphs indicate the electric fields and are given with respect to the switching pulse (the poling pulses are of opposite polarity) and the gate electrode. The voltages were applied to the source, while the gate was grounded via the charge amplifier that was connected to the gold gate electrode.

The switching time of the copolymer was fastest for the capacitor with metal electrodes. Comparing the two transistor structures, the type with a gate oxide (Tr2) switched

⁶The applied voltage is divided by ferroelectric layer thickness without taking into account the presence of a potential low permittivity layer.

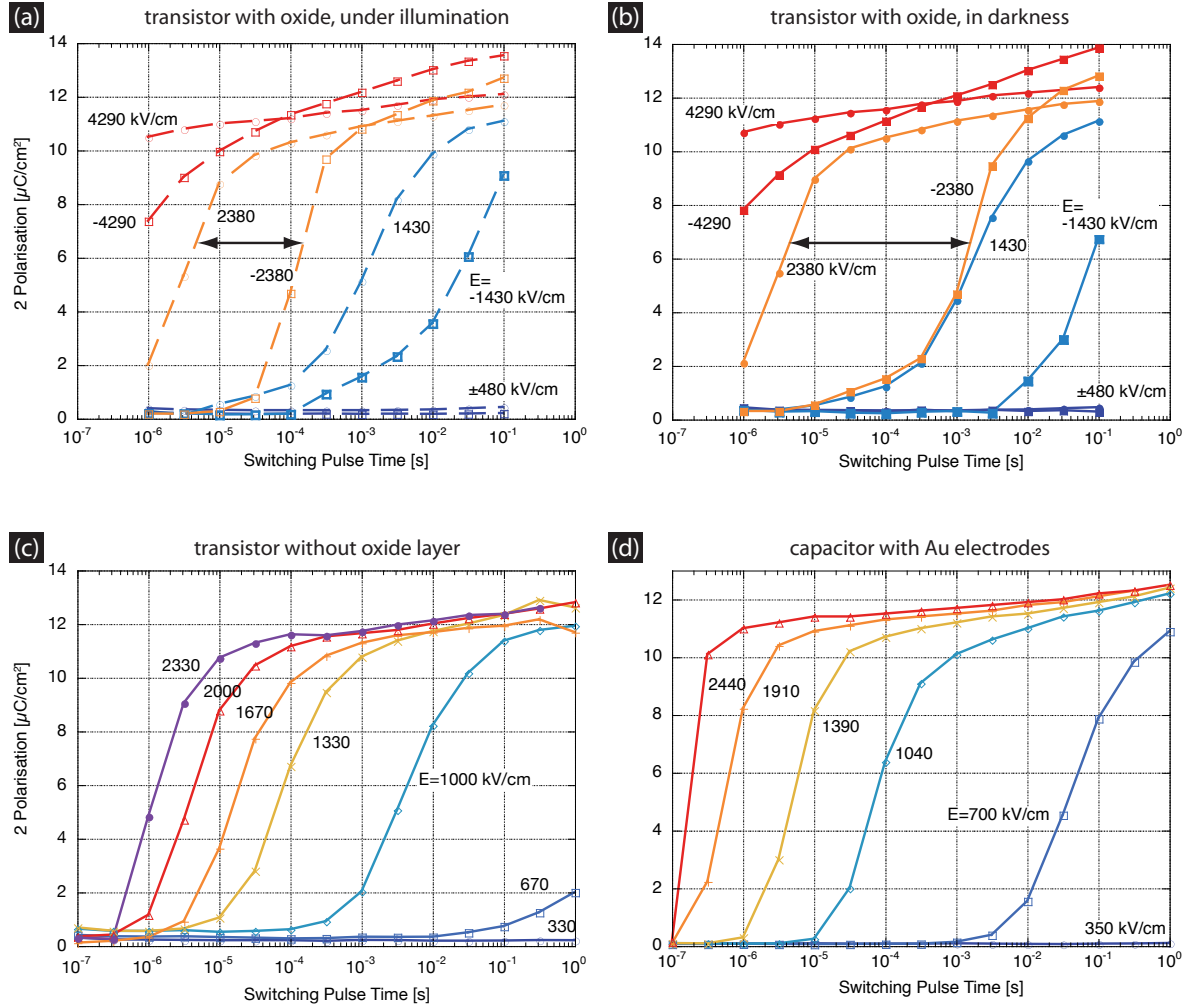


Figure 6.11: Switching curves of the P(VDF-TrFE) copolymer in the transistor structure with a gate oxide [Tr2] under illumination (a), in darkness (b), in a transistor structure without a gate oxide [Tr1] characterised under illumination (c), and in an illuminated capacitor [CapAu] structure with gold electrodes (d) were measured at room temperature. The numbers in the graph indicated the electric fields applied by the switching pulses and with respect to the gate electrode.

slower than the type without (Tr1). This is also illustrated in figure 6.12, in which the switching time is taken at a polarisation of $6 \mu\text{C}/\text{cm}^2$ ⁷.

Furthermore, the switching curves are less steep in the transistor structure. The polarisation reversal takes place within three time decades, whereas in gold coated films it happens within about two decades (figure 6.11). The decelerating effect on the polarisation reversal of a non-metallic or an insulating layer, respectively, is confirmed here again, after the observations in chapter 5 and the observations of the loop tilt.

The main features in the transistor structure with gate oxide presented in figures 6.11(a) and (b) is the deceleration of the reversal at negative applied voltages. The difference is larger in darkness than under illumination. The switching time for positive voltages (of the variable second pulse) with respect to the gate electrodes are almost invariable under illumination and in the dark. For negative voltages however, the difference between switching time under illumination and in darkness is considerable as shown in figure 6.12.

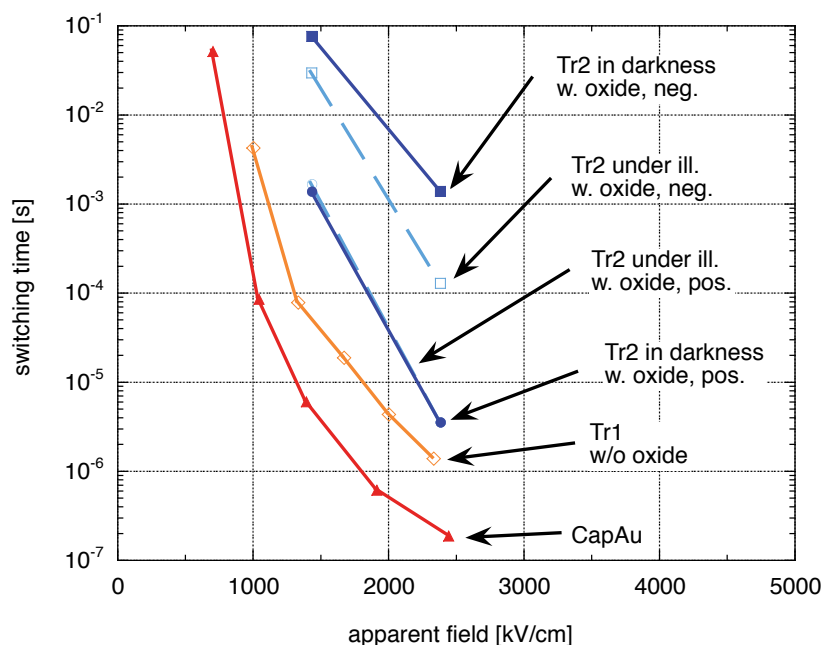


Figure 6.12: The switching times taken from the data in figure 6.11 at a polarisation of $6 \mu\text{C}/\text{cm}^2$.

In absolute numbers, complete polarisation reversal of the P(VDF-TrFE) integrated into the transistor gate can be achieved within less than $10 \mu\text{s}$. Nevertheless, such a fast reversal can only be achieved at voltages higher than 50 V in the 210 nm thick film.

6.5.2 “On”/“Off” Drain Current Ratio and Retention

The requirement of good drain current “on”/“off” ratios, as well as excellent data retention, is crucial in non-volatile memories. Retention in FeFET can be translated to a stable “on”, respectively “off”, state drain currents in FeFET over a long time.

⁷This value corresponds almost exactly to half of the switchable polarisation and therefore the resulting switching time corresponds approximately to the definition in section 5.5.4

“On” and “off” drain current states and retention curves showing the time-dependent behaviour of the drain current were measured with an electrometer (*Keithley*, 6517A) after the application of programming (poling) pulses. The rectangular programming pulses (from a function generator, *Agilent Inc.*, 33250A, and amplified by an amplifier, *Krohn-Hite Corp.*, 7602M) were of an amplitude of ± 30 V to ± 40 V and a duration of about 1 to 2 s. Such pulses are largely sufficient to completely reverse the polarisation in the ferroelectric as was shown in figure 6.11. The source and drain pads were contacted with the very hard tungsten-carbide probes, which contacted the n^+ regions through the 10 nm thick oxide layer. The drain current measurements were all done in the dark and at room temperature.

Figure 6.13 shows the measurement of “on” and “off” drain currents after the application of programming voltage pulses between the gate and the grounded source-drain channel. With a pulse of an amplitude of +30 V and a duration of 2 s, an “on” state with a drain current of $I_d^{\text{on}} \approx 10^{-4}$ A was programmed in a $50 \times 50 \mu\text{m}^2$ -sized source-drain channel of the transistor with a gate oxide layer (Tr2). The drain current was measured at a source-drain voltage of $V_{\text{sd}} = 0.5$ V. It can be seen from figure 6.13(a) that the “on” state remains when voltage goes back to 0 V.

Starting from the “on” state a pulse of opposite polarity with an amplitude of -30 V and a duration of 2 s reversed the of the polarisation of the ferroelectric and brought the transistor back to the “off” state with a drain current $I_d^{\text{off}} \approx 2 \cdot 10^{-7}$ A. The application of the +30 V pulse reproduced the “on” state with good retention as shown in figure 6.13(b).

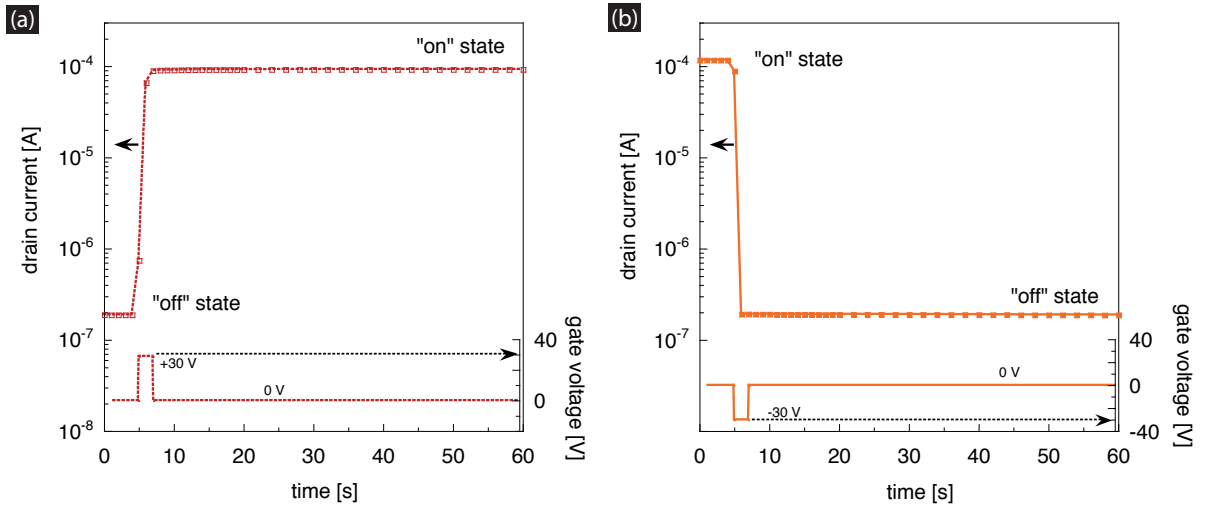


Figure 6.13: “On” and “off” states of the drain current measured at a source-drain voltage of $V_g = 0.5$ V after poling the ferroelectric gate with voltage pulses of width of 2 s and an amplitude of +30 V (a) and -30 V (b). The “on”/“off” ratio is about 500.

From these observations, we find thus a drain current “on”/“off” ratio $I_d^{\text{on}}/I_d^{\text{off}} \approx 500$ and a retention of at least minutes.

Drain current retention curves in figure 6.14 were measured on various transistors with sizes from 30×30 to $50 \times 50 \mu\text{m}^2$. The source-drain voltage was $V_{\text{sd}} = 0.5$ V as a standard, but two samples were measured at $V_{\text{sd}} = 2$ V. In these long term measurements, the gate was kept at floating conditions. A drain current value was recorded from the electrometer in 1 s-steps for the first 500 points. To reduce the number of points in long-term retention

measurements, the time interval was then increased to 30 s.

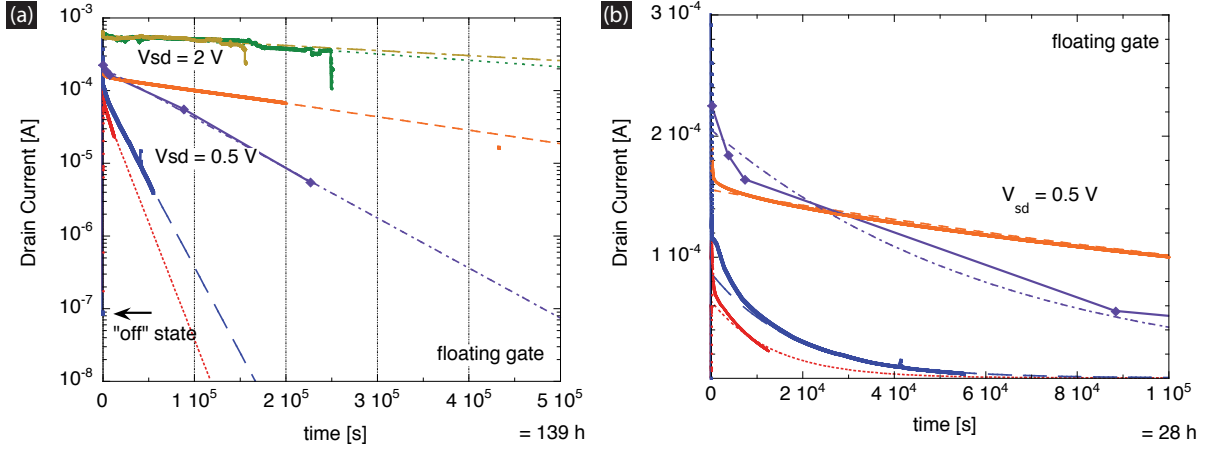


Figure 6.14: Retention of the drain current in a logarithmic-linear (a) and a linear-linear scale (b). The drain current was measured after poling pulses of an amplitude of either $V_g = 35$ V or 40 V for source-drain voltages of $V_{sd} = 0.5$ V or 2 V for different samples. The dashed lines represent fits for an exponential decay. The slopes of the curves vary considerably for different samples.

The leakage current in the “off” state varied typically between 10^{-9} and 10^{-7} A for different transistors. Programming the transistor to the “on” yielded a drain current typically between 10^{-6} and 10^{-3} A a few seconds after the programming pulse.

Apart from the behaviour as shown in figure 6.13, a less ideal behaviour was observed in numerous samples. The drain current decreases in a first step rapidly and reached then a second stage with a slower decay as illustrated in figure 6.14(a). The second stage follows in good approximation an exponential decay law for all devices. The fitting curves following an exponential decay law are given in the figures 6.14(a) and (b) as dashed lines. The slope of the lines, which represent a time constants of the exponential decay vary considerably and could not be correlated to a controllable parameter such as the transistor size, source-drain, or programming voltage. The time for the current to decrease by a factor of 10 is between 150 and 8.6 h for the slowest and the fastest decays shown at a source-drain voltage $V_{sd} = 0.5$ V.

6.5.3 Properties of the Transistor without a Ferroelectric Gate

Reference transistors of exactly the same dimensions and structure, but without a ferroelectric gate and with aluminium electrodes, were fabricated and characterised by the usual procedures. The fabrication and the measurement of the I_{sd} - V_{sd} -curve was undertaken by G. A. Salvatore and D. Bouvet at the *Laboratory of Micro/Nanoelectronic Devices* at EPFL.

Figure 6.15(a) shows the typical drain current vs. source-drain voltage curve of a transistor with a gate size of $50 \times 50 \mu\text{m}^2$ for three gate voltages $V_g = 2, 3, 4$ V. The saturation voltages are at about $V_{d,sat} = 0.75, 1.5$, and 2 V, respectively.

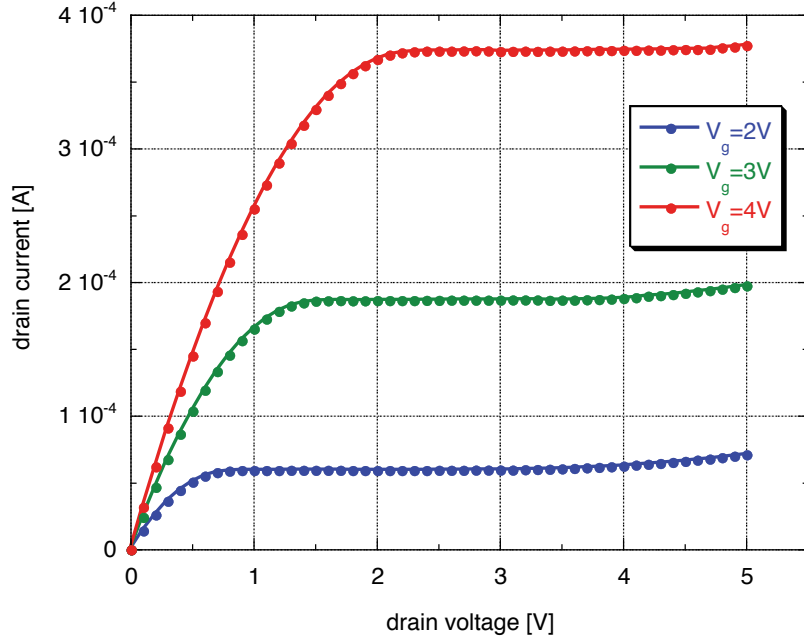


Figure 6.15: The drain current I_{sd} is shown as a function of the source-drain voltage V_{sd} in a reference transistor without a ferroelectric gate ($50 \times 50 \mu\text{m}^2$). Data courtesy of G. A. Salvatore and D. Bouvet at the *Laboratory of Micro/Nanoelectronic Devices*.

6.6 Discussion

6.6.1 Polarisation Loops and Switching Curves

The main observations from the switching curves and the polarisation loops in the previous section were slower switching curves in the transistor than in the capacitor structures and more inclined polarisation loops with the introduction of an oxide layer.

The slower switching times in the transistor structure with a metal and a semiconducting electrode can be explained by the slower polarisation screening process due to the limited conductivity of the semiconductor. Stabilisation of the polarisation does therefore take more time and the observed switching curves shift to longer times.

With the introduction of an insulating layer in the transistor structure (difference between the sample with and without an oxide layer, Tr1 and Tr2), the inclination of the polarisation loops increases strongly [figure 6.9(b)]. A low-permittivity interface layer can induce an inclination of the polarisation loop as discussed in chapter 5.

The described ramp of only moderately changing polarisation from zero bias in the direction of positive voltages observed in the hysteresis loops measured in the dark in figure 6.9(a) are remarkable. Considering the voltage given with respect to the source, this phenomena occurs only when the transistor is switched from the “on” to the “off” state.

On the other hand, a significant difference in switching times for the negative and positive switching pulses was observed in the transistor structure in figures 6.11(a,b) and 6.12. The fact that the switching curves for positive switching pulses (given here with respect to the gate electrode) are not affected by the illumination conditions, while the

switching curves with negative pulses show a considerable difference under illumination and in the dark, suggests that the observed ramp phenomena in the loop in figure 6.8(a) and the illumination effect in the switching curves originate from the same physical mechanism. Our hypothesis is that the electric field felt by the ferroelectric is reduced below a threshold field. This has a decelerating effect in the switching curve measurements and a retardation consequence in the loops.

The loop asymmetry with respect to the voltage observed in a transistor structure with an oxide layer (Tr2) and the shift of the switching curves may be linked by the asymmetry of the structure. The film is contacted on one side by a gold electrode, whereas on the other side, it is in direct contact with the gate oxide and the source-drain channel.

In unipolar devices, such an asymmetry can in general be expected. However, our explanation in terms of the depletion and inversion layer fails due to a sign incompatibility. It is puzzling that the polarisation reversal is impeded from the “on” [for negative measured polarisations in the loop of figure 6.9(a)] to the “off” state, where an inversion layer can be expected in the channel, and not for the opposite case of switching from the “off” to the “on” state with a depleted channel.

6.6.2 Required Polarisation for the “On” State of the Transistor

We know from the data of a reference transistor without ferroelectric given in figure 6.15 that the gate voltage required for an “on”-state drain current of $I_{d,on} = 10^{-4}$ A is $V_g \approx 3$ V at a source-drain voltage $V_{sd} = 0.5$ V. Based on equation (6.2), we concluded that a polarisation of about $1 \mu\text{C}/\text{cm}^2$ is required to achieve an “on” state in our transistor (Tr2) with a gate size of $50 \times 50 \mu\text{m}^2$.

This means that only about 20 % of the non-compensated remnant polarisation (5 to $6 \mu\text{C}/\text{cm}^2$) influences the drain current in our transistor. We assume therefore that the remaining 80 % is compensated for by charges very rapidly.

Hence the polarisation produced by the gate exceeds the value required for opening the transistor. A higher value of the reversible polarisation in the ferroelectric yields a higher field in the gate oxide layer. Considering statistically distributed breakdown fields around 9 MV/cm for SiO_2 films, breakdown failure of the oxide layer can be achieved with a ferroelectric polarisation of about $P_s = 3.1 \mu\text{C}/\text{cm}^2$ already according to equation (6.2). The spontaneous polarisation of our P(VDF-TrFE) copolymer films is above this breakdown limit. This might be a reason for the observed failure of the transistor devices. Failures were generally observed in the electrically as well as optically. Dark spots could typically be seen in the optical microscope on the gate electrode or in its vicinity as illustrated in figure 6.16.

6.6.3 Mechanism of Drain Current Relaxation

Two alternative scenarios of retention loss resulting in a drain current relaxation are considered:

- (i) a polarisation loss of the ferroelectric induced by depolarisation effects, or
- (ii) charge carriers that gradually compensate the ferroelectric polarisation and reduce the field in the semiconductor.

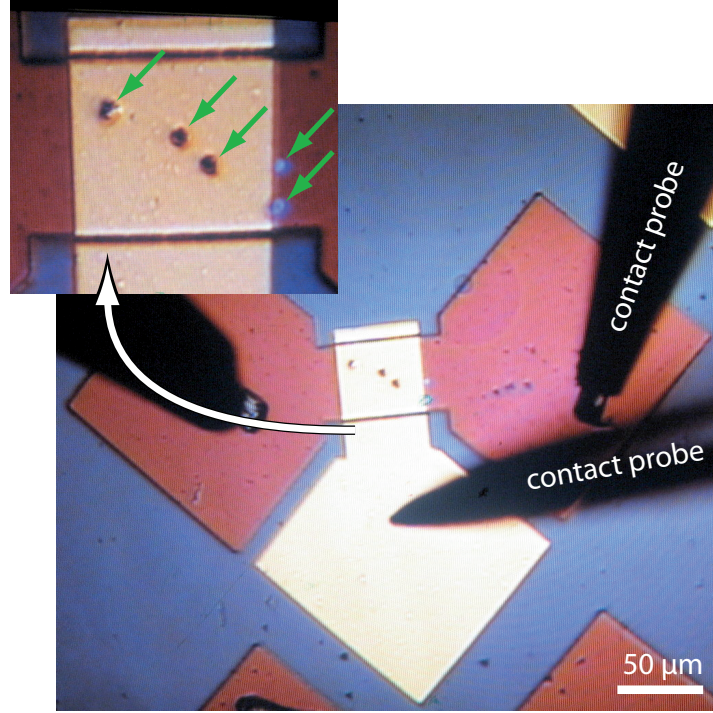


Figure 6.16: After programming the gate, some transistors broke down. Such failure was generally observable in the microscope by black dots as indicated here by the arrows.

The PFM technique with its ability to check the polarisation state is a valuable method to distinguish between the above mentioned scenarios. In the case of scenario (i) the polarisation partially switches back under the influence of the depolarisation field as discussed above. In scenario (ii), the polarisation, and thus the piezoelectric response, remains unchanged.

A demonstration of the polarisation retention, by measuring the piezoelectric response (PFM) of the ferroelectric integrated in the gate of the transistor gate, is given in figure 6.17(a) and (c). A piezoelectric loop was measured as described in section 2.6.2 with a small ac driving voltage of 3 V applied between the source and the grounded gate electrode. Piezoelectric vibrations originating in the ferroelectric gate were sensed through the gate electrode with a grounded conductive PFM probe at zero bias (compare to figure 2.32). The AFM probe scanned a single line during the loop measurement.

The direction of the loop (first positive or negative bias) was chosen in a way that the polarisation was reversed only in the second half loop⁸. This allows us to characterise the polarisation state at the beginning of the loop and to compare it to the value when it is freshly programmed. The difference between the piezoelectric response $R_{0,E=0}$ at the starting point of the loop ($E = 0$) and the piezoelectric response $R_{1,E=0}$ after going to minimum and back to $E = 0$ [figure 6.17(a)] is a measure of the relaxation of the polarisation.

When the piezoelectric hysteresis loop is completed, a third piezoelectric response $R_{2,E=0}$ value at $E = 0$ is recorded. This value can be used as a criteria of whether the

⁸Since the programming pulse was applied to the gate at grounded source, whereas the bias voltage for the loop measurement was applied to the source at grounded gate, the polarity of the first half-loop was opposite to the voltage pulse to the gate.

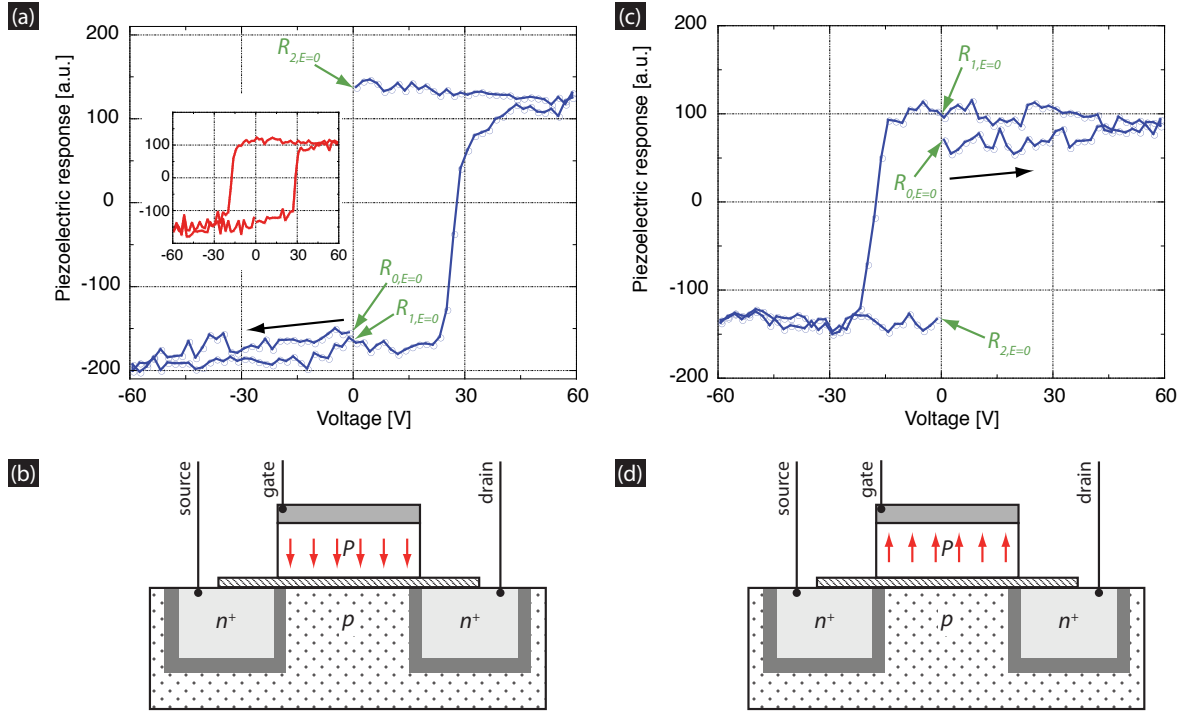


Figure 6.17: The piezoelectric loops in figure (a) was measured 10 hours after programming the “on” state to the transistor. The polarisation loop starting with a negative bias voltage applied to the source-drain channel shows that the polarisation remains stable. If an “off” state is programmed with a pulse of -35 V, the polarisation is reversed (c) as can be seen from the opposite sign of the piezoelectric response compared to (a). This is an indication that the polarisation remains stable even if the drain current decreases to the “off” state of the channel (b). Figure (d) shows ferroelectric transistor state if the “off” state is programmed.

polarisation could really be reversed; the sign of $R_{2,E=0}$ should be opposite to the sign of $R_{2,E=0}$ and $R_{1,E=0}$.

The inset in figure 6.17(a) shows a full loop when the bias field in the ferroelectric for the first half loop is in the same direction as the precedent programming pulse field.

Furthermore, applying an “off”-state programming pulse and changing the polarity of the applied bias voltages should result in a loop as shown in figure 6.17(c). The piezoelectric response was now positive ($R_{0,E=0} > 0$) and is reversed by the bias signal when measuring the loop to negative values ($R_{2,E=0} < 0$).

The polarisation loop in figure 6.17(a) shows that the polarisation in the ferroelectric remained constant within at least 10 h while the drain current decreased continuously.

In the case of an additional programming pulse of -35 V to the gate electrode, the polarisation can be effectively reversed 6.17(c).

These findings strongly support scenario (ii), which involves a gradual polarisation compensation and do not support scenario (i), which necessitates a polarisation relaxation that was not observed. One can therefore imagine a situation as shown schematically in figure 6.17(b). The polarisation is in the direction to induce an “on” state, but the channel is not in inversion state. We hypothesis that such a situation may occur due to charge injection and trapping in the ferroelectric or oxide layer.

6.6.4 Retention Loss — Semi-Quantitative Description

Due to the broad distribution of slopes of the exponential decays as shown in figure 6.14(a), we expect that failure mechanisms, such as the discussed breakdown problem, play an important role. Furthermore, we observed ferroelectric transistors, which were programmable only with a floating gate (in analogy to EPROM⁹ devices). Hence, there is some uncertainty about the involved mechanisms. We demonstrate in the following a possibility to explain the observed exponential decay of the drain current.

The decay cannot be associated with a scenario involving the relaxation of the polarisation under the influence of the depolarisation field (figure 6.17). A scenario with polarisation compensation by charge injection, as briefly described in section 6.6.3, therefore appears reasonable.

We would like to describe the injection of charges into the ferroelectric through a thin oxide layer. We write the electrostatic equation for the dielectric displacement in the ferroelectric D_f and the charge density (per unit area) of the trapped charge σ [Tagantsev et al., 2004b] for the ferroelectric-dielectric structure (as illustrated in figure 6.4):

$$D_f - \sigma = \varepsilon_0 \varepsilon_d E_d. \quad (6.12)$$

The transport equation for the density of the injection current J through the passive layer is expressed as a function of the electric field in the oxide layer E_d :

$$\frac{d\sigma}{dt} = J(E_d). \quad (6.13)$$

After the application of a voltage pulse to reverse the polarisation in the ferroelectric, the uncompensated polarisation results in a strong depolarisation field and a strong field

⁹EPROM stands for Erasable Programmable Read-Only Memory

across the oxide layer. The latter causes charge injection into the ferroelectric through the oxide layer, which accumulates at the interface described as the charge density $\sigma(t)$.

We have shown in figure 6.17 that the polarisation can be assumed to stay unchanged on the time scale of the observed drain current decays. Hence D_f is constant in this approximation at any time t .

From equations (6.12) and (6.13), we can thus write

$$\varepsilon_0 \varepsilon_d \frac{dE_d}{dt} = -J(E_d). \quad (6.14)$$

Charge transport in dielectrics have in general a linear regime [O'Dwyer, 1964] at low fields. The injection current density can then be written as $J(E_d) = \alpha E_d$ with a constant α .

In this linear regime, the differential equation (6.14) can be solved with an electric field in the oxide layer that decays exponentially with time:

$$E_d(t) = C \exp \left[-\frac{\alpha t}{\varepsilon_0 \varepsilon_d} \right], \quad (6.15)$$

with a constant C .

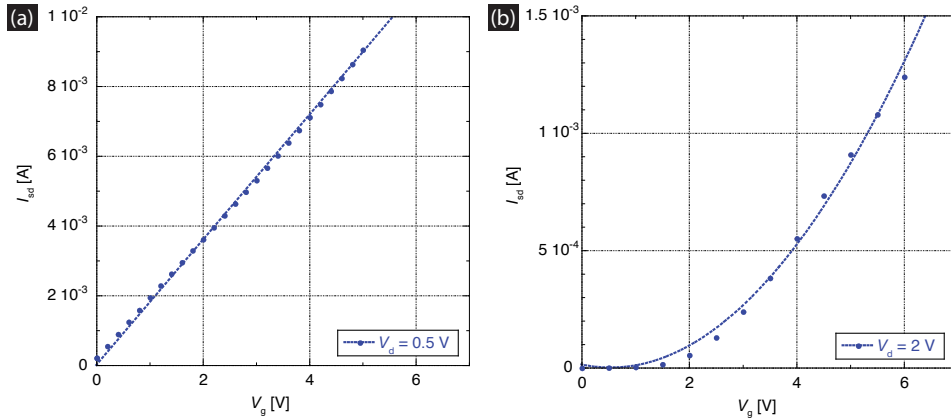


Figure 6.18: The drain current is measured as a function of the gate voltage in a transistor structure without the ferroelectric for a source-drain voltage $V_{sd} = 0.5$ (a) and 2 V (b). The transistor is in the saturation region for a source-drain voltage of 2 V, in which a quadratic dependence is expected and observed.

From the linear relation found from the I_{sd} vs V_g measurement in the reference capacitor without ferroelectric, shown in figure 6.18 (for the a source-drain voltage $V_{sd} = 0.5$) follows that the drain current decays exponentially:

$$I_{sd}(t) \propto V_g(t)/d = E_d = C \exp \left[-\frac{\alpha t}{\varepsilon_0 \varepsilon_d} \right]. \quad (6.16)$$

The exponential decay of the drain current with time in figure 6.14 may thus be explained by a charge injection process through the oxide layer into the ferroelectric in a small field regime.

We assume that the decay occurs in two steps. In a first, fast and high-field regime step, a large part of the remnant polarisation of the ferroelectric is screened. Consequently,

the field in the oxide drops considerably and the linear injection current regime is reached. This results in the observed exponential decay of the drain current.

The large variation of the time constant in the exponentially decaying drain current may be due to variations of the oxide thickness or local breakdown occurrence.

A large time constant variation in an exponentially decaying drain current was already reported 20 years ago [Langlois et al., 1987]. In the *p*-type silicon device with an 1.2 nm thick oxide layer, and a 40 μm thick P(VDF-TrFE) copolymer, Langlois et al. studied the induced inversion layer after coronal poling. After poling, they observed a broad distribution of time constants of the decay, which occurred in two steps after coronal poling of the polymer film. The authors suggested that the first fast step was associated with a transfer of positive charges through the polymer to the interface whereas the slow decay was attributed to the injection of electrons across the interface into the copolymer.

6.7 Summary

From the experiments and interpretations of the results in this chapter, we can thus draw the following conclusions.

- (i) A ferroelectric field effect transistor with high “on”/“off” drain current ratio and a strong retention performance was fabricated.
- (ii) The ferroelectric polarisation can be reversed rapidly in the transistor structure and remains stable for at least several days.
- (iii) Retention of the “on” state at a floating gate device is possible due to the ferroelectric.
- (iv) A large portion (80 %) of the ferroelectric polarisation is screened immediately after the polarisation reversal.
- (v) The drain current retention in the “on” state shows broad distribution of exponential decays.
- (vi) The exponential decay may be explained by high-field and low-field regime charge transport, in which the second low-field step was shown to result in an exponential decay.
- (vii) The general reliability of the devices has to be improved, e.g. leakage in the transistor from the gate to the channel has to be reduced in order to improve the drain current stability.
- (viii) Strong asymmetry with respect to the polarity of the external applied field of polarisation loops and switching curves was observed. This effect was enhanced in the dark.

Conclusions and Outlook

Conclusions

Important aspects of the use of ferroelectric materials as storage medium for non-volatile memories were investigated in this thesis.

The mechanism of polarisation reversal was studied in detail in thin films of the classical ferroelectric lead zirconate titanate, PZT. The crucial role of the electrode-ferroelectric interface for the polarisation reversal was confirmed. It was found that reverse domain nucleation occurs preferentially on the electrode with the negative potential. We demonstrated that the polarisation reversal mechanism in thin-films can be described in the traditional sideways-limited domain growth model based on observations in single crystals.

Oxide ferroelectrics are inferior to ferroelectric polymers in terms of fabrication simplicity and costs. Standard silicon processing dictates strict temperature limits, especially in oxygen atmosphere, which is in conflict to the relatively high annealing temperatures required for perovskite structures. Ferroelectric polymers do not involve high-temperature deposition in their solution-based deposition processes ($< 150^{\circ}\text{C}$).

We demonstrated that the processing conditions and the ferroelectric properties make the copolymer of polyvinylidene fluoride and trifluoroethylene, P(VDF-TrFE), a promising candidate for memory applications. This is particularly true in single transistor memory cells with a ferroelectric gate. We fabricated a first hybrid P(VDF-TrFE)/silicon with good retention properties. Due to a smaller spontaneous polarisation and better controlled interfaces, the potentially detrimental depolarisation field as well as charge injection and trapping are reduced compared to oxide ferroelectrics. Retention loss was explained in a model involving charge injection while the polarisation relaxation was shown to be insignificant.

Non-reactive metal electrodes are shown to be advantages for fast polarisation reversal. Fast switching below 1 microsecond at relatively high external electric fields were measured. The temperature dependence of the ferroelectric properties, including the coercive field and switching time, limit the applicability of the ferroelectric copolymer over a broad temperature range.

The developed characterisation methods, particularly the combination of macro- and microscopic techniques, are relevant for the investigation of the polarisation reversal mechanism of ferroelectrics in capacitor as well as transistor structures and are promising for the understanding of fundamental physics of ferroelectric materials, device characterisation and modelling.

Outlook

The developed cross-sectional piezoresponse technique is an excellent tool to study the polarisation reversal and especially the nucleation and domain growth in ferroelectric films. The investigation of epitaxial films is very promising for fundamental studies of domain nucleation. With the introduction of artificial defects (structured surfaces, chemical inhomogeneities, etc.) that act as potential nucleation centres, the nucleation process could be governed artificially potentially for enhancing the switching process.

Concerning the ferroelectric polymer, the relation between the morphology of the copolymer films (deposited by the LB technique or by solution deposition) and its ferroelectric properties is worth studying in more detail. The crystallisation conditions, including the used solvents and the heating and cooling profile, may have a strong influence on the polymer morphology. Structural studies and investigation of the role of the amorphous phase and interface effects on the polarisation reversal properties are crucial for a better understanding and improvement of this material for the use in memory application in terms of faster switching times and low-voltage operation.

The hybrid organic-inorganic non-volatile transistors are expected to improve considerably by an optimisation of the transistor design, especially the ferroelectric as well as the insulating layer between the gate and the channel. The demonstrated characterisation methods for transistors are applicable further in fully organic non-volatile transistors. Such devices may allow for new applications due to their flexibility and transparency.

Bibliography

- [Abe, 1959] Abe, R. (1959). Theoretical treatment of the movement of 180-degrees domain in BaTiO₃ single crystal. *Journal of the Physical Society of Japan*, 14(5):633–642.
- [Abplanalp, 2001] Abplanalp, M. (2001). *Piezoresponse scanning force microscopy of ferroelectric domains*. PhD thesis, Swiss Federal Institute of Technology, ETH Zürich.
- [Abplanalp et al., 1998] Abplanalp, M., Eng, L. M., and Günter, P. (1998). Mapping the domain distribution at ferroelectric surfaces by scanning force microscopy. *Applied Physics A*, 66(0):S231.
- [Aizawa et al., 2004] Aizawa, K., Park, B.-E., Kawashima, Y., Takahashi, K., and Ishiwara, H. (2004). Impact of HfO₂ buffer layers on data retention characteristics of ferroelectric-gate field-effect transistors. *Applied Physics Letters*, 85(15):3199–3201.
- [Alexe et al., 2004] Alexe, M., Harnagea, C., and Hesse, D. (2004). Non-conventional micro- and nanopatterning techniques for electroceramics. *Journal of Electroceramics*, 12(1-2):69–88.
- [Anderson, 1952] Anderson, J. R. (1952). Ferroelectric storage elements for digital computers and switching systems. *Electrical Engineering*, 71(10):916–922.
- [Ashcroft and Mermin, 1976] Ashcroft, N. W. and Mermin, N. D. (1976). *Solid State Physics*. Harcourt College Publishers, Orlando, FL.
- [Aslaksen, 1972] Aslaksen, E. W. (1972). Theory of the spontaneous polarization and the pyroelectric coefficient of linear chain polymers. *The Journal of Chemical Physics*, 57(6):2358–2363.
- [Astafiev et al., 2003] Astafiev, K. F., Sherman, V. O., Cantoni, M., Tagantsev, A. K., Setter, N., Petrov, P. K., Kaydanova, T., and Ginley, D. S. (2003). In-plane ferroelectricity in strontium titanate thin films. In *Materials Research Society Symposium - Proceedings*, volume 783, pages 109–114.
- [Auciello et al., 1997] Auciello, O., Gruverman, A., and Tokumoto, H. (1997). Scanning force microscopy study of domain structure in Pb(Zr_xTi_{1-x})O₃ thin films and Pt/PZT/Pt and RuO₂/PZT/RuO₂ capacitors. *Integrated Ferroelectrics*, 15(1-4):107–114.
- [Avrami, 1939] Avrami, M. (1939). Kinetics of phase change. I General theory. *Journal of Chemical Physics*, 7:1103–1112.
- [Avrami, 1940] Avrami, M. (1940). Kinetics of phase change. II Transformation-time relations for random distribution of nuclei. *Journal of Chemical Physics*, 8:212–224.

- [Avrami, 1941] Avrami, M. (1941). Kinetics of phase change. III Granulation, phase change, and microstructure. *Journal of Chemical Physics*, 9:177–184.
- [Bauer, 1996] Bauer, S. (1996). Poled polymers for sensors and photonic applications. *Journal of Applied Physics*, 80(10):5531–5558.
- [Binnig et al., 1986] Binnig, G., Quate, C. F., and Gerber, C. (1986). Atomic force microscope. *Physical Review Letters*, 56(9):930.
- [Binnig and Rohrer, 1982] Binnig, G. and Rohrer, H. (1982). Scanning tunneling microscopy. *Helvetica Physica Acta*, 55(6):726–735.
- [Birk et al., 1991] Birk, H., Glatz-Reichenbach, J., Jie, L., Schreck, E., and Dransfeld, K. (1991). The local piezoelectric activity of thin polymer films observed by scanning tunneling microscopy. *Journal of Vacuum Science & Technology B*, 9:1162.
- [Bratkovsky and Levanyuk, 2001] Bratkovsky, A. M. and Levanyuk, A. P. (2001). Comment on: “Intrinsic ferroelectric coercive field”. *Physical Review Letters*, 87(1):019701.
- [Buchman, 1973] Buchman, P. (1973). Pyroelectric and switching properties of polyvinylidene fluoride film. *Ferroelectrics*, 5(1):39–43.
- [Bune et al., 1998] Bune, A. V., Fridkin, V. M., Ducharme, S., Blinov, L. M., Palto, S. P., Sorokin, A. V., Yudin, S. G., and Zlatkin, A. (1998). Two-dimensional ferroelectric films. *Nature*, 391(6670):874–877.
- [Burtsev and Chervonobrodov, 1982] Burtsev, E. V. and Chervonobrodov, S. P. (1982). Some problems of 180°-switching in ferroelectrics. *Ferroelectrics*, 45:97–106.
- [Chao et al., 2005] Chao, C., Wang, Z., and Zhu, W. (2005). Measurement of longitudinal piezoelectric coefficient of lead zirconate titanate thin/thick films using a novel scanning mach-zehnder interferometer. *Thin Solid Films*, 493(1-2):313–318.
- [Chen and Mukhopadhyay, 1995] Chen, T. C. S. and Mukhopadhyay, S. M. (1995). Metallization of electronic polymers: A comparative study of polyvinylidene fluoride, polytetrafluoroethylene, and polyethylene. *Journal of Applied Physics*, 78(9):5422–5426.
- [Chen et al., 1999] Chen, X. Q., Yamada, H., Terai, Y., Horiuchi, T., Matsushige, K., and Weiss, P. S. (1999). Strong substrate effect in local poling of ultrathin ferroelectric polymer films. *Thin Solid Films*, 353(1-2):259–263.
- [Chew et al., 2003] Chew, K. H., Osman, J., Stamps, R. L., Tilley, D. R., Shin, F. G., and Chan, H. L. W. (2003). Surface aided polarization reversal in small ferroelectric particles. *Journal of Applied Physics*, 93(7):4215–4218.
- [Cho et al., 1999] Cho, Y., Kazuta, S., and Matsuura, K. (1999). Scanning nonlinear dielectric microscopy with nanometer resolution. *Applied Physics Letters*, 75(18):2833–2835.
- [Cho et al., 1996] Cho, Y., Kirihaara, A., and Saeki, T. (1996). Scanning nonlinear dielectric microscope. *Review of Scientific Instruments*, 67(6):2297–2303.

- [Clark and Taylor, 1982] Clark, J. D. and Taylor, P. L. (1982). Effect of lamellar structure on ferroelectric switching in poly(vinylidene fluoride). *Physical Review Letters*, 49(20):1532.
- [Cohen, 1992] Cohen, R. E. (1992). Origin of ferroelectricity in perovskite oxides. *Nature*, 358(6382):136–138.
- [Colla et al., 1998] Colla, E. L., Hong, S., Taylor, D. V., Tagantsev, A. K., Setter, N., and Kwangsoo, N. (1998). Direct observation of region by region suppression of the switchable polarization (fatigue) in $\text{Pb}(\text{Zr,Ti})\text{O}_3$ / thin film capacitors with Pt electrodes. *Applied Physics Letters*, 72(21):2763–5.
- [Cook et al., 1963] Cook, J. W. R., Berlincourt, D. A., and Scholz, F. J. (1963). Thermal expansion and pyroelectricity in lead titanate zirconate and barium titanate. *Journal of Applied Physics*, 34(5):1392.
- [Curie and Curie, 1880] Curie, J. and Curie, P. (1880). *Comptes Rendus de l' Academie des Sciences, Paris*, 91:924.
- [Damjanovic, 1998] Damjanovic, D. (1998). Ferroelectric, dielectric and piezoelectric properties of ferroelectric thin films and ceramics. *Reports on Progress in Physics*, 61:1267–1324.
- [Damjanovic, 2007] Damjanovic, D. (2007). personal communication, unpublished work.
- [Dawber et al., 2005] Dawber, M., Rabe, K. M., and Scott, J. F. (2005). Physics of thin-film ferroelectric oxides. *Reviews of Modern Physics*, 77(4):1083–48.
- [Devonshire, 1949] Devonshire, A. F. (1949). *Philosophical Magazine*, 40:1040.
- [Devonshire, 1954] Devonshire, A. F. (1954). Theory of ferroelectrics. *Advances in Physics*, 3(10):85–130.
- [Ducharme et al., 2000] Ducharme, S., Fridkin, V. M., Bune, A. V., Palto, S. P., Blinov, L. M., Petukhova, N. N., and Yudin, S. G. (2000). Intrinsic ferroelectric coercive field. *Physical Review Letters*, 84(1):175.
- [Ducharme et al., 2005] Ducharme, S., Reece, T. J., Othon, C. M., and Rannow, R. K. (2005). Ferroelectric polymer Langmuir-Blodgett films for nonvolatile memory applications. *IEEE Transactions on Device and Materials Reliability*, 5(4):720–735.
- [Dunn, 2003] Dunn, S. (2003). Determination of cross sectional variation of ferroelectric properties for thin film (ca. 500 nm) PZT (30/70) via PFM. *Integrated Ferroelectrics*, 59:1505–1512.
- [Dvey-Aharon et al., 1980] Dvey-Aharon, H., Sluckin, T. J., Taylor, P. L., and Hopfinger, A. J. (1980). Kink propagation as a model for poling in poly(vinylidene fluoride). *Physical Review B*, 21(8):3700.
- [El-Hami et al., 2003] El-Hami, K., Ribbe, A., Isoda, S., and Matsushige, K. (2003). Structural analysis of the P(VDF/TrFE) copolymer film. *Chemical Engineering Science*, 58(2):397–400.

- [Eng et al., 1998] Eng, L. M., Abplanalp, M., and Günter, P. (1998). Ferroelectric domain switching in tri-glycine sulphate and barium-titanate bulk single crystals by scanning force microscopy. *Applied Physics A*, 66(0):S679–S683.
- [Fatuzzo, 1962] Fatuzzo, E. (1962). Theoretical considerations on the switching transient in ferroelectrics. *Physical Review*, 127(6):1999.
- [Fatuzzo and Merz, 1959] Fatuzzo, E. and Merz, W. J. (1959). Switching mechanism in triglycine sulfate and other ferroelectrics. *Physical Review*, 116(1):61.
- [Felten et al., 2004] Felten, F., Schneider, G. A., Saldana, J. M., and Kalinin, S. V. (2004). Modeling and measurement of surface displacements in BaTiO₃ bulk material in piezoresponse force microscopy. *Journal of Applied Physics*, 96(1):563–568.
- [Fong et al., 2004] Fong, D. D., Stephenson, G. B., Streiffer, S. K., Eastman, J. A., Auciello, O., Fuoss, P. H., and Thompson, C. (2004). Ferroelectricity in ultrathin perovskite films. *Science*, 304(5677):1650–1653.
- [Forsbergh, 1949] Forsbergh, P. W. (1949). Domain structures and phase transitions in barium titanate. *Physical Review*, 76(8):1187.
- [Franke et al., 1994] Franke, K., Besold, J., Haessler, W., and Seegebarth, C. (1994). Modification and detection of domains on ferroelectric PZT films by scanning force microscopy. *Surface Science*, 302(1-2):L283–L288.
- [Fu et al., 2002] Fu, D., Suzuki, K., Kato, K., Minakata, M., and Suzuki, H. (2002). Investigation of domain switching and retention in oriented PbZr_{0.3}Ti_{0.7}O₃ thin film by scanning force microscopy. *Japanese Journal of Applied Physics*, 41(11B):6724–6729.
- [Fukuma et al., 2000] Fukuma, T., Kobayashi, K., Horiuchi, T., Yamada, H., and Matsushige, K. (2000). Nanometer-scale characterization of ferroelectric polymer thin films by variable-temperature atomic force microscopy. *Japanese Journal of Applied Physics*, 39(6B):3830–3833.
- [Furuichi and Mitsui, 1950] Furuichi, J. and Mitsui, T. (1950). Domain structure of rochelle salt. *Physical Review*, 80(1):93.
- [Furukawa, 1989] Furukawa, T. (1989). Ferroelectric properties of vinylidene fluoride copolymers. *Phase Transitions*, 18(3):143 – 211.
- [Furukawa et al., 1984] Furukawa, T., Date, M., Ohuchi, M., and Chiba, A. (1984). Ferroelectric switching characteristics in a copolymer of vinylidene fluoride and trifluoroethylene. *Journal of Applied Physics*, 56(5):1481–1486.
- [Furukawa and Johnson, 1981] Furukawa, T. and Johnson, G. E. (1981). Measurements of ferroelectric switching characteristics in polyvinylidene fluoride. *Applied Physics Letters*, 38(12):1027–1029.
- [Furukawa et al., 1985] Furukawa, T., Matsuzaki, H., Shiina, M., and Tajitsu, Y. (1985). Nanosecond switching in thin films of vinylidene fluoride trifluoroethylene copolymers. *Japanese Journal of Applied Physics*, 24(8):L661–L662.

- [Furukawa et al., 2006] Furukawa, T., Nakajima, T., and Takahashi, Y. (2006). Factors governing ferroelectric switching characteristics of thin VDF/TrFE copolymer films. *Dielectrics and Electrical Insulation, IEEE Transactions on* [see also *Electrical Insulation, IEEE Transactions on*], 13(5):1120–1131.
- [Ganpule et al., 1999] Ganpule, C. S., Stanishevsky, A., Su, Q., Aggarwal, S., Melngailis, J., Williams, E., and Ramesh, R. (1999). Scaling of ferroelectric properties in thin films. *Applied Physics Letters*, 75(3):409–411.
- [Gerber et al., 2006] Gerber, A., Kohlstedt, H., Fitsilis, M., Waser, R., Reece, T. J., Ducharme, S., and Rije, E. (2006). Low-voltage operation of metal-ferroelectric-insulator-semiconductor diodes incorporating a ferroelectric polyvinylidene fluoride copolymer Langmuir-Blodgett film. *Journal of Applied Physics*, 100(2):024110–5.
- [Gerra et al., 2005] Gerra, G., Tagantsev, A. K., and Setter, N. (2005). Surface-stimulated nucleation of reverse domains in ferroelectrics. *Physical Review Letters*, 94(10):107602.
- [Gerra et al., 2006] Gerra, G., Tagantsev, A. K., Setter, N., and Parlinski, K. (2006). Ionic polarizability of conductive metal oxides and critical thickness for ferroelectricity in BaTiO₃. *Physical Review Letters*, 96(10):107603–4.
- [Gopalan and Mitchell, 1998] Gopalan, V. and Mitchell, T. E. (1998). Wall velocities, switching times, and the stabilization mechanism of 180° domains in congruent LiTaO₃ crystals. *Journal of Applied Physics*, 83(2):941–954.
- [Grossmann et al., 2000] Grossmann, M., Bolten, D., Lohse, O., Boettger, U., Waser, R., and Tiedke, S. (2000). Correlation between switching and fatigue in PbZr_{0.3}Ti_{0.7}O₃ thin films. *Applied Physics Letters*, 77(12):1894–1896.
- [Gruverman, 1999] Gruverman, A. (1999). Scaling effect on statistical behavior of switching parameters of ferroelectric capacitors. *Applied Physics Letters*, 75(10):1452–1454.
- [Gruverman et al., 1996] Gruverman, A., Auciello, O., and Tokumoto, H. (1996). Scanning force microscopy for the study of domain structure in ferroelectric thin films. *Journal of Vacuum Science & Technology B*, 14(2):602.
- [Gruverman et al., 1998] Gruverman, A., Auciello, O., and Tokumoto, H. (1998). Imaging and control of domain structures in ferroelectric thin films via scanning force microscopy. *Annual Review of Materials Science*, 28(1):101–123.
- [Gruverman and Kholkin, 2006] Gruverman, A. and Kholkin, A. (2006). Nanoscale ferroelectrics: processing, characterization and future trends. *Reports on Progress in Physics*, 69(8):2443–2474.
- [Gruverman et al., 2005] Gruverman, A., Rodriguez, B. J., Dehoff, C., Waldrep, J. D., Kingon, A. I., Nemanich, R. J., and Cross, J. S. (2005). Direct studies of domain switching dynamics in thin film ferroelectric capacitors. *Applied Physics Letters*, 87(8):082902.
- [Gysel et al., 2006] Gysel, R., Tagantsev, A. K., Stolichnov, I., Setter, N., and Pavius, M. (2006). Ferroelectric film switching via oblique domain growth observed by cross-sectional nanoscale imaging. *Applied Physics Letters*, 89(8):082906–3.

- [Güthner and Dransfeld, 1992] Güthner, P. and Dransfeld, K. (1992). Local poling of ferroelectric polymers by scanning force microscopy. *Applied Physics Letters*, 61(9):1137.
- [Harnagea et al., 2006] Harnagea, C., Pignolet, A., Alexe, M., and Hesse, D. (2006). Higher-order electromechanical response of thin films by contact resonance piezoresponse force microscopy. *IEEE Transactions on Ultrasonics Ferroelectrics and Frequency Control*, 53(12):2309–2322.
- [Hasegawa et al., 1972] Hasegawa, R., Takahashi, Y., Tadokoro, H., and Chatani, Y. (1972). Crystal-structures of 3 crystalline forms of poly(vinylidene fluoride). *Polymer Journal*, 3(5):600.
- [Haun et al., 1989] Haun, M. J., Furman, E., Jang, S. J., and Cross, L. E. (1989). Thermodynamic theory of the lead zirconate-titanate solid-solution system, part V: Theoretical calculations. *Ferroelectrics*, 99:63–86.
- [Haun et al., 1987] Haun, M. J., Furman, E., Jang, S. J., McKinstry, H. A., and Cross, L. E. (1987). Thermodynamic theory of PbTiO_3 . *Journal of Applied Physics*, 62(8):3331–3338.
- [Hong et al., 1999] Hong, S., Colla, E., Kim, E., Taylor, D., Tagantsev, A., Murali, P., No, K., and Setter, N. (1999). High resolution study of domain nucleation and growth during polarization switching in $\text{Pb}(\text{Zr,Ti})\text{O}_3$ ferroelectric thin film capacitors. *Journal of Applied Physics*, 86(1):607–613.
- [Hong et al., 2004] Hong, S., Ecabart, B., Colla, E. L., and Setter, N. (2004). Three-dimensional ferroelectric domain imaging of bulk $\text{Pb}(\text{Zr,Ti})\text{O}_3$ by atomic force microscopy. *Applied Physics Letters*, 84(13):2382–2384.
- [Hong and Setter, 2002] Hong, S. and Setter, N. (2002). Evidence for forward domain growth being rate-limiting step in polarization switching in $\langle 111 \rangle$ -oriented- $\text{Pb}(\text{Zr}_{0.45}\text{Ti}_{0.55})\text{O}_3$ thin-film capacitors. *Applied Physics Letters*, 81(18):3437–3439.
- [Hong et al., 2001] Hong, S., Woo, J., Shin, H., Jeon, J. U., Pak, Y. E., Colla, E. L., Setter, N., Kim, E., and No, K. (2001). Principle of ferroelectric domain imaging using atomic force microscope. *Journal of Applied Physics*, 89(2):1377–1386.
- [Humphrey and Gyorgy, 1959] Humphrey, F. B. and Gyorgy, E. M. (1959). Flux reversal in soft ferromagnetics. *Journal of Applied Physics*, 30(6):935–939.
- [ISAF, 2008] ISAF (2008). Invited presentation of Texas Instruments, at the International Symposium on the Application of Ferroelectrics, Santa Fe, New Mexico, USA.
- [Ishibashi, 1996] Ishibashi, Y. (1996). Polarization reversal in ferroelectrics. In Araujo, C. P. d., Scott, J. F., and Taylor, G. W., editors, *Ferroelectric Thin Films: Synthesis and Basic Properties*, volume vol. 10 of *Ferroelectricity and related phenomena*, pages 135–151. Gordon and Breach Publishers, Amsterdam.
- [Ishibashi and Iwata, 2005] Ishibashi, Y. and Iwata, M. (2005). Landau theory of phase transition in ferroelectric vinylidene fluoride/trifluoroethylene copolymer single crystals. *Japanese Journal of Applied Physics*, 44(9 A):6624–6628.

- [Ishibashi and Takagi, 1971] Ishibashi, Y. and Takagi, Y. (1971). Ferroelectric domain switching. *Journal of the Physical Society of Japan*, 31(2):506.
- [Israelachvili, 1995] Israelachvili, J. N. (1995). *Intermolecular and surface forces*. Academic Press, London, second edition.
- [Jaffe et al., 1971] Jaffe, Cook, W., and Jaffe (1971). *Piezoelectric Ceramics*. Academic Press, London.
- [Jesse et al., 2006] Jesse, S., Baddorf, A. P., and Kalinin, S. V. (2006). Dynamic behaviour in piezoresponse force microscopy. *Nanotechnology*, 17(6):1615–1628.
- [Jona and Shirane, 1962] Jona, F. and Shirane, G. (1962). *Ferroelectric crystals*. Pergamon Press, Oxford.
- [Jungk et al., 2006] Jungk, T., Hoffmann, A., and Soergel, E. (2006). Quantitative analysis of ferroelectric domain imaging with piezoresponse force microscopy. *Applied Physics Letters*, 89(16):163507–3.
- [Junquera and Ghosez, 2003] Junquera, J. and Ghosez, P. (2003). Critical thickness for ferroelectricity in perovskite ultrathin films. *Nature*, 422(6931):506.
- [Kalinin and Bonnell, 2001] Kalinin, S. V. and Bonnell, D. A. (2001). Local potential and polarization screening on ferroelectric surfaces. *Physical Review B*, 63(12):125411/1–13.
- [Kalinin and Bonnell, 2002] Kalinin, S. V. and Bonnell, D. A. (2002). Imaging mechanism of piezoresponse force microscopy of ferroelectric surfaces. *Physical Review B*, 65(12):125408–11.
- [Kalinin et al., 2006] Kalinin, S. V., Rar, A., and Jesse, S. (2006). A decade of piezoresponse force microscopy: progress, challenges, and opportunities. *Ultrasonics, Ferroelectrics and Frequency Control, IEEE Transactions on*, 53(12):2226–2252.
- [Karasawa and Goddard III, 1992] Karasawa, N. and Goddard III, W. (1992). Force fields, structures, and properties of poly(vinylidene fluoride) crystals. *Macromolecules*, 25(26):7268–7281.
- [Kasap, 2002] Kasap, S. O. (2002). *Principles of electronic materials and devices*. McGraw-Hill, New York, second edition.
- [Kawai, 1969] Kawai, H. (1969). Piezoelectricity of poly(vinylidene fluoride). *Japanese Journal of Applied Physics*, 8(7):975.
- [Kay and Rhodes, 1947] Kay, H. F. and Rhodes, R. G. (1947). Barium titanate crystals. *Nature*, 160(4056):126–127.
- [Kemiktarak et al., 2007] Kemiktarak, U., Ndukum, T., Schwab, K. C., and Ekinici, K. L. (2007). Radio-frequency scanning tunnelling microscopy. *Nature*, 450(7166):85–88.
- [Kepler, 1995] Kepler, R. G. (1995). Ferroelectric, pyroelectric, and piezoelectric properties of poly(vinylidene fluoride). In Nalwa, H. S., editor, *Ferroelectric polymers: chemistry, physics, and applications*, *Plastics Engineering*, pages 183–232. Marcel Dekker Inc., New York.

- [Kepler and Anderson, 1992] Kepler, R. G. and Anderson, R. A. (1992). Ferroelectric polymers. *Advances in Physics*, 41(1):1–57.
- [Kholkin et al., 1996] Kholkin, A. L., Wutchrich, C., Taylor, D. V., and Setter, N. (1996). Interferometric measurements of electric field-induced displacements in piezoelectric thin films. *Review of Scientific Instruments*, 67(5):1935.
- [Kimura and Ohigashi, 1986] Kimura, K. and Ohigashi, H. (1986). Polarization behavior in vinylidene fluoride-trifluoroethylene copolymer thin-films. *Japanese Journal of Applied Physics*, 25(3):383–387.
- [Kliem and Tadros-Morgane, 2005] Kliem, H. and Tadros-Morgane, R. (2005). Extrinsic versus intrinsic ferroelectric switching: experimental investigations using ultra-thin PVDF Langmuir-Blodgett films. *Journal of Physics D*, 38:1860–1868.
- [Kochervinskii, 2005] Kochervinskii, V. V. (2005). Electrophysical properties of ultrathin films of ferroelectric polymers. *Polymer Science Series B*, 47(3-4):75–103.
- [Koga and Ohigashi, 1986] Koga, K. and Ohigashi, H. (1986). Piezoelectricity and related properties of vinylidene fluoride and trifluoroethylene copolymers. *Journal of Applied Physics*, 59(6):2142–2150.
- [Kolmogorov, 1937] Kolmogorov, A. (1937). *Izv. Akad. Nauk, Ser. math.*, 3:355.
- [Kopal et al., 1997] Kopal, A., Bahník, T., and Fousek, J. (1997). Domain formation in thin ferroelectric films: The role of depolarization energy. *Ferroelectrics*, 202(1):267–274.
- [Landauer, 1957] Landauer, R. (1957). Electrostatic considerations in BaTiO_3 domain formation during polarization reversal. *Journal of Applied Physics*, 28(2):227–234.
- [Lando and Doll, 1968] Lando, J. B. and Doll, W. W. (1968). The polymorphism of poly(vinylidene fluoride). I. The effect of head-to-head structure. *Journal of Macromolecular Science, Part B*, 2(2):205–218.
- [Langlois et al., 1987] Langlois, J. M., Noirhomme, B., Filion, A., Rambo, A., and Caron, L. G. (1987). Induced inversion at a silicon ferroelectric copolymer interface. *Journal of Applied Physics*, 61(12):5360–5365.
- [Larsen et al., 1991] Larsen, P. K., Kampschoer, G. L. M., Ulenaers, M. J. E., Spierings, G. A. C. M., and Cuppens, R. (1991). Nanosecond switching of thin ferroelectric films. *Applied Physics Letters*, 59(5):611–613.
- [Legrand, 1989] Legrand, J. F. (1989). Structure and ferroelectric properties of P(VDF-TrFE) copolymers. *Ferroelectrics*, 91(1):303–317.
- [Li et al., 2004] Li, J., Nagaraj, B., Liang, H., Cao, W., Lee, C. H., and Ramesh, R. (2004). Ultrafast polarization switching in thin-film ferroelectrics. *Applied Physics Letters*, 84(7):1174.
- [Li et al., 2002] Li, T. K., Hsu, S. T., Ulrich, B., Stecker, L., and Evans, D. (2002). One transistor ferroelectric memory devices with improved retention characteristics. *Japanese Journal of Applied Physics*, 41(11B):6890–6894.

- [Lim et al., 2004] Lim, S. H., Rastogi, A. C., and Desu, S. B. (2004). Electrical properties of metal-ferroelectric-insulator-semiconductor structures based on ferroelectric polyvinylidene fluoride copolymer film gate for nonvolatile random access memory application. *Journal of Applied Physics*, 96(10):5673–5682.
- [Lines and Glass, 1977] Lines, M. and Glass, A. (1977). *Principles and applications of ferroelectrics and related materials*. International series of monographs on physics. Clarendon Press, Oxford.
- [Little, 1955] Little, E. A. (1955). Dynamic behavior of domain walls in barium titanate. *Physical Review*, 98(4):978–984.
- [Liu et al., 2007] Liu, J. S., Zeng, H. Z., and Kholkin, A. L. (2007). Cross-sectional analysis of ferroelectric domains in PZT capacitors via piezoresponse force microscopy. *Journal of Physics D-Applied Physics*, 40(22):7053–7056.
- [Lohse et al., 2001] Lohse, O., Grossmann, M., Boettger, U., Bolten, D., and Waser, R. (2001). Relaxation mechanism of ferroelectric switching in $\text{Pb}(\text{Zr,Ti})\text{O}_3$ thin films. *Journal of Applied Physics*, 89(4):2332–2336.
- [Lovinger, 1983] Lovinger, A. J. (1983). Ferroelectric polymers. *Science*, 220(4602):1115–1121.
- [Lovinger et al., 1987] Lovinger, A. J., Davis, D. D., Cais, R. E., and Kometani, J. M. (1987). The role of molecular defects on the structure and phase transitions of poly(vinylidene fluoride). *Polymer*, 28(4):617–626.
- [Lovinger et al., 1983] Lovinger, A. J., Furukawa, T., Davis, G. T., and Broadhurst, M. G. (1983). Crystallographic changes characterizing the curie transition in three ferroelectric copolymers of vinylidene fluoride and trifluoroethylene: 1. as-crystallized samples. *Polymer*, 24(10):1225–1232.
- [Lu et al., 2002] Lu, X., Schlaphof, F., Grafstrom, S., Loppacher, C., Eng, L., Suchanek, G., and Gerlach, G. (2002). Scanning force microscopy investigation of the $\text{Pb}(\text{Zr}_{0.25}\text{Ti}_{0.75})\text{O}_3/\text{Pt}$ interface. *Applied Physics Letters*, 81(17):3215–3217.
- [Lüthi et al., 1993] Lüthi, R., Haefke, H., Grütter, P., Güntherodt, H. J., Szczesniak, L., and Meyer, K. P. (1993). Surface and domain structures of ferroelectric gash crystals studied by scanning force microscopy. *Surface Science*, 285(1-2):L498.
- [Ma and Han, 2002] Ma, T. P. and Han, J.-P. (2002). Why is nonvolatile ferroelectric memory field-effect transistor still elusive? *Electron Device Letters, IEEE*, 23(7):386–388.
- [Madayag et al., 2001] Madayag, A. C., Madayag, A. C., and Zhiping, Z. (2001). Optimization of spin-on-glass process for multilevel metal interconnects optimization of spin-on-glass process for multilevel metal interconnects. In Zhiping, Z., editor, *University/Government/Industry Microelectronics Symposium, 2001. Proceedings of the Fourteenth Biennial*, pages 136–139.
- [Malin et al., 2007] Malin, L., Stolichnov, I., and Setter, N. (2007). Ferroelectric polymer gate on $\text{AlGaIn}/\text{GaIn}$ heterostructures. *Journal of Applied Physics*, 102(11):114101–4.

- [Mathews et al., 1997] Mathews, S., Ramesh, R., Venkatesan, T., and Benedetto, J. (1997). Ferroelectric field effect transistor based on epitaxial perovskite heterostructures. *Science*, 276(5310):238–240.
- [Matthias and von Hippel, 1948] Matthias, B. and von Hippel, A. (1948). Domain structure and dielectric response of barium titanate single crystals. *Physical Review*, 73(11):1378.
- [Melngailis, 1987] Melngailis, J. (1987). Focused ion beam technology and applications. *Journal of Vacuum Science & Technology B*, 5(2):469.
- [Merz, 1954] Merz, W. J. (1954). Domain formation and domain wall motions in ferroelectric BaTiO₃ single crystals. *Physical Review*, 95:690–698.
- [Merz, 1956] Merz, W. J. (1956). Switching time in ferroelectric BaTiO₃ and its dependence on crystal thickness. *Journal of Applied Physics*, 27(8):938.
- [Meyer et al., 1975] Meyer, R. B., Liebert, L., Strzelecki, L., and Keller, P. (1975). Ferroelectric liquid-crystals. *Journal De Physique Lettres*, 36(3):L69–L71.
- [Miller and Savage, 1958] Miller, R. C. and Savage, A. (1958). Velocity of sidewise 180° domain-wall motion in BaTiO₃ as a function of the applied electric field. *Physical Review*, 112(3):755.
- [Miller and Savage, 1959] Miller, R. C. and Savage, A. (1959). Further experiments on the sidewise motion of 180° domain walls in BaTiO₃. *Physical Review*, 115(5):1176.
- [Miller and Savage, 1960] Miller, R. C. and Savage, A. (1960). Motion of 180° domain walls in metal electroded barium titanate crystals as a function of electric field and sample thickness. *Journal of Applied Physics*, 31(4):662–669.
- [Miller and Weinreich, 1960] Miller, R. C. and Weinreich, G. (1960). Mechanism for the sidewise motion of 180° domain walls in barium titanate. *Physical Review*, 117(6):1460–1466.
- [Miller et al., 1990] Miller, S. L., Nasby, R. D., Schwank, J. R., Rodgers, M. S., and Dressendorfer, P. V. (1990). Device modeling of ferroelectric capacitors. *Journal of Applied Physics*, 68(12):6463–6471.
- [Mitsui et al., 1976] Mitsui, T., Tatsuzaki, I., and Nakamura, E. (1976). *An introduction to the physics of ferroelectrics*, volume 1 of *Ferroelectricity and related phenomena*. Gordon and Breach Science Publishers, New York, London, Paris.
- [Mokry et al., 2004] Mokry, P., Tagantsev, A. K., and Setter, N. (2004). Size effect on permittivity in ferroelectric polydomain thin films. *Physical Review B*, 70(17):172107–4.
- [Moll and Tarui, 1963] Moll, J. L. and Tarui, Y. (1963). A new solid state memory resistor. *Electron Devices, IEEE Transactions on*, 10(5):338–338.
- [Molotskii, 2003] Molotskii, M. (2003). Forward motion of ferroelectric domain walls. *Philosophical Magazine Letters*, 83(12):763–767.
- [Mueller, 1935] Mueller, H. (1935). Properties of rochelle salt. *Physical Review*, 47(2):175.

- [Muralt, 2007] Muralt, P. (2007). Ferroelectric thin-films: The emancipation of ferroelectricity. *Nature Materials*, 6(1):8–9.
- [Muralt et al., 1998] Muralt, P., Maeder, T., Sagalowicz, L., Hiboux, S., Scalese, S., Naumovic, D., Agostino, R. G., Xanthopoulos, N., Mathieu, H. J., Patthey, L., and Bullock, E. L. (1998). Texture control of PbTiO_3 and $\text{Pb}(\text{Zr,Ti})\text{O}_3$ thin films with TiO_2 seeding. *Journal of Applied Physics*, 83(7):3835–3841.
- [Naber et al., 2006] Naber, R. C. G., Blom, P. W. M., and Leeuw, D. M. d. (2006). Comment on ‘Extrinsic versus intrinsic ferroelectric switching: experimental investigations using ultra-thin PVDF Langmuir-Blodgett films’. *Journal of Physics D*, 39(9):1984–1986.
- [Naber et al., 2004] Naber, R. C. G., Blom, P. W. M., Marsman, A. W., and de Leeuw, D. M. (2004). Low voltage switching of a spin cast ferroelectric polymer. *Applied Physics Letters*, 85(11):2032–2034.
- [Naber et al., 2005] Naber, R. C. G., Tanase, C., Blom, P. W. M., Gelinck, G. H., Marsman, A. W., Touwslager, F. J., Setayesh, S., and de Leeuw, D. M. (2005). High-performance solution-processed polymer ferroelectric field-effect transistors. *Nature Materials*, 4(3):243–248.
- [Nagarajan et al., 2003] Nagarajan, V., Roytburd, A., A. Stanishevsky, S. Prasertchoung, T. Zhao, L. Chen, J. Melngailis, O. Auciello, and R. Ramesh (2003). Dynamics of ferroelastic domains in ferroelectric thin films. *Nature Materials*, 2:43–47.
- [Nakajima et al., 2005] Nakajima, T., Abe, R., Takahashi, Y., and Furukawa, T. (2005). Intrinsic switching characteristics of ferroelectric ultrathin vinylidene fluoride/trifluoroethylene copolymer films revealed using au electrode. *Japanese Journal of Applied Physics*, 44(42-45):L1385–L1388.
- [Nakamura and Wada, 1971] Nakamura, K. and Wada, Y. (1971). Piezoelectricity, pyroelectricity, and the electrostriction constant of poly(vinylidene fluoride). *Journal of Polymer Science Part A-2: Polymer Physics*, 9(1):161–173.
- [Nakamura, 1954] Nakamura, T. (1954). Possible mechanism of ferroelectric domain boundary movement. *Journal of the Physical Society of Japan*, 9(3):425B–426.
- [Odagawa and Cho, 2002] Odagawa, H. and Cho, Y. (2002). Measuring ferroelectric polarization component parallel to the surface by scanning nonlinear microscopy. *Applied Physics Letters*, 80(12):2159–2161.
- [Ohigashi et al., 1992] Ohigashi, H., Kagami, N., and Li, G. R. (1992). Formation of ferroelectric domains in a copolymer P(VDF–TrFE). *Journal of Applied Physics*, 71(1):506–508.
- [Okino et al., 2001] Okino, H., Ida, T., Ebihara, H., Yamada, H., Matsushige, K., and Yamamoto, T. (2001). Domain orientation imaging of PbTiO_3 single crystals by vertical and lateral piezoresponse force microscopy. *Japanese Journal of Applied Physics*, 40(9B):5828–5832.
- [O’Dwyer, 1964] O’Dwyer, J. (1964). *The Theory of Dielectric Breakdown in Solids*. Clarendon, Oxford.

- [Pan and Cross, 1989] Pan, W. Y. and Cross, L. E. (1989). A sensitive double beam laser interferometer for studying high-frequency piezoelectric and electrostrictive strains. *Review of Scientific Instruments*, 60(8):2701–2705.
- [Pang and Baba-Kishi, 1998] Pang, G. K. H. and Baba-Kishi, K. Z. (1998). Characterization of butterfly single crystals of BaTiO_3 by atomic force, optical and scanning electron microscopy techniques. *Journal of Physics D*, 31(20):2846–2853.
- [Park et al., 2006] Park, Y. J., Kang, S. J., Park, C., Kim, K. J., Lee, H. S., Lee, M. S., Chung, U. I., and Park, I. J. (2006). Irreversible extinction of ferroelectric polarization in P(VDF-TrFE) thin films upon melting and recrystallization. *Applied Physics Letters*, 88(24):242908–3.
- [Paruch et al., 2006] Paruch, P., Giamarchi, T., Tybell, T., and Triscone, J.-M. (2006). Nanoscale studies of domain wall motion in epitaxial ferroelectric thin films. *Journal of Applied Physics*, 100(5):051608–10.
- [Prutton, 1958] Prutton, M. (1958). The polarization reversal process in ferroelectric single crystals. *Proceedings of the Physical Society of London*, 72(464):307–308.
- [Rabe et al., 2007] Rabe, K., Dawber, M., Lichtensteiger, C., Ahn, C., and Triscone, J.-M. (2007). Modern physics of ferroelectrics: Essential background. In *Physics of Ferroelectrics*, pages 1–30.
- [Rabe, 2002] Rabe, K. M. (2002). Computational materials science: Think locally, act globally. *Nature Materials*, 1(3):147–148.
- [Reece et al., 2003] Reece, T. J., Ducharme, S., Sorokin, A. V., and Poulsen, M. (2003). Nonvolatile memory element based on a ferroelectric polymer Langmuir-Blodgett film. *Applied Physics Letters*, 82(1):142–144.
- [Remeika and Jackson, 1954] Remeika, J. P. and Jackson, W. M. (1954). A method for growing barium titanate single crystals. *Journal of the American Chemical Society*, 76(3):940–941.
- [Reneker and Mazur, 1985] Reneker, D. H. and Mazur, J. (1985). Modelling of chain twist boundaries in poly(vinylidene fluoride) as a mechanism for ferroelectric polarization. *Polymer*, 26(6):821–826.
- [Rodriguez et al., 2004] Rodriguez, B., Gruverman, A., Kingon, A., Nemanich, R., and Cross, J. (2004). Investigation of the mechanism of polarization switching in ferroelectric capacitors by three-dimensional piezoresponse force microscopy. *Applied Physics A*, 80(1):99–103.
- [Rodriguez et al., 2006] Rodriguez, B. J., Jesse, S., Baddorf, A. P., and Kalinin, S. V. (2006). High resolution electromechanical imaging of ferroelectric materials in a liquid environment by piezoresponse force microscopy. *Physical Review Letters*, 96(23):237602–4.
- [Rodriguez et al., 2007] Rodriguez, B. J., Jesse, S., Kalinin, S. V., Kim, J., Ducharme, S., and Fridkin, V. M. (2007). Nanoscale polarization manipulation and imaging of ferroelectric Langmuir-Blodgett polymer films. *Applied Physics Letters*, 90(12):122904–3.

- [Rodriguez et al., 2005] Rodriguez, B. J., Nemanich, R. J., Kingon, A., Gruverman, A., Kalinin, S. V., Terabe, K., Liu, X. Y., and Kitamura, K. (2005). Domain growth kinetics in lithium niobate single crystals studied by piezoresponse force microscopy. *Applied Physics Letters*, 86(1):012906.
- [Ross, 1957] Ross, I. M. (1957). U.S. patent #2,791,760: Semiconductive translating device.
- [Saint Jean et al., 1999] Saint Jean, M., Hudlet, S., Guthmann, C., and Berger, J. (1999). Van der waals and capacitive forces in atomic force microscopies. *Journal of Applied Physics*, 86(9):5245–5248.
- [Sarid, 1994] Sarid, D. (1994). *Scanning force microscopy : with applications to electric, magnetic, and atomic forces*. Oxford series in optical and imaging sciences. Oxford University Press, New York.
- [Saurenbach and Terris, 1990] Saurenbach, F. and Terris, B. D. (1990). Imaging of ferroelectric domain walls by force microscopy. *Applied Physics Letters*, 56(17):1703–1705.
- [Sawyer and Tower, 1930] Sawyer, C. B. and Tower, C. H. (1930). Rochelle salt as a dielectric. *Physical Review*, 35(3):269.
- [Schlaphof, 2005] Schlaphof, F. (2005). *Kraftmikroskopische Untersuchungen dünner ferroelektrischer Filme*. PhD thesis, TU Dresden.
- [Schroeder et al., 2004] Schroeder, R., Majewski, L., and Grell, M. (2004). All-organic permanent memory transistor using an amorphous, spin-cast ferroelectric-like gate insulator. *Advanced Materials*, 16(7):633–636.
- [Scott, 2008] Scott, J. F. (2008). Ferroelectrics go bananas. *Journal of Physics*, 20(2):021001–2.
- [Scott et al., 1989] Scott, J. F., Araujo, C. A., Meadows, H. B., McMillan, L. D., and Shawabkeh, A. (1989). Radiation effects on ferroelectric thin-film memories: Retention failure mechanisms. *Journal of Applied Physics*, 66(3):1444–1453.
- [Setter et al., 2006] Setter, N., Damjanovic, D., Eng, L., Fox, G., Gevorgian, S., Hong, S., Kingon, A., Kohlstedt, H., Park, N. Y., Stephenson, G. B., Stolitchnov, I., Taganstev, A. K., Taylor, D. V., Yamada, T., and Streiffer, S. (2006). Ferroelectric thin films: Review of materials, properties, and applications. *Journal of Applied Physics*, 100(5):051606–46.
- [Shaw et al., 2000] Shaw, T. M., Trolier-McKinstry, S., and McIntyre, P. C. (2000). The properties of ferroelectric films at small dimensions. *Annual Review of Materials Science*, 30(1):263–298.
- [Sheikholeslami et al., 2000] Sheikholeslami, A., Sheikholeslami, A., and Gulak, P. G. (2000). A survey of circuit innovations in ferroelectric random-access memories a survey of circuit innovations in ferroelectric random-access memories. *Proceedings of the IEEE*, 88(5):667–689.

- [Shin et al., 2007] Shin, Y.-H., Grinberg, I., Chen, I. W., and Rappe, A. M. (2007). Nucleation and growth mechanism of ferroelectric domain-wall motion. *Nature*, 449(7164):881–884.
- [Shirane et al., 1956] Shirane, G., Pepinsky, R., and Frazer, B. C. (1956). X-ray and neutron diffraction study of ferroelectric PbTiO_3 . *Acta Crystallographica*, 9(2):131–140.
- [Shur et al., 1998] Shur, V., Rumyantsev, E., and Makarov, S. (1998). Kinetics of phase transformations in real finite systems: Application to switching in ferroelectrics. *Journal of Applied Physics*, 84(1):445–451.
- [Shur, 1996] Shur, V. Y. (1996). Fast polarization reversal process: Evolution of ferroelectric domain structure in thin films. In Araujo, C. P. d., Scott, J. F., and Taylor, G. W., editors, *Ferroelectric Thin Films: Synthesis and Basic Properties*, volume vol. 10 of *Ferroelectricity and related phenomena*, pages 153–192. Gordon and Breach Publishers, Amsterdam.
- [So et al., 2005] So, Y. W., Kim, D. J., Noh, T. W., Yoon, J.-G., and Song, T. K. (2005). Polarization switching kinetics of epitaxial $\text{Pb}(\text{Zr}_{0.4}\text{Ti}_{0.6})\text{O}_3$ thin films. *Applied Physics Letters*, 86(9):092905–3.
- [Soergel, 2005] Soergel, E. (2005). Visualization of ferroelectric domains in bulk single crystals. *Applied Physics B*, 81(6):729–751.
- [Song et al., 2005] Song, T. K., So, Y. W., Kim, D. J., Jo, J. Y., and Noh, T. W. (2005). Ferroelectric switching dynamics and pulse-switching polarization measurements. *Integrated Ferroelectrics*, 73:115–121.
- [Sorokin et al., 2005] Sorokin, A. V., Fridkin, V. M., and Ducharme, S. (2005). Pyroelectric study of polarization switching in Langmuir-Blodgett films of poly(vinylidene fluoride trifluoroethylene). *Journal of Applied Physics*, 98(4):044107–10.
- [Spaldin, 2004] Spaldin, N. A. (2004). Fundamental size limits in ferroelectricity. *Science*, 304(5677):1606–1607.
- [Spierings et al., 1995] Spierings, G. A. C. M., Dormans, G. J. M., Moors, W. G. J., Ulenaers, M. J. E., and Larsen, P. K. (1995). Stresses in $\text{Pt}/\text{Pb}(\text{Zr},\text{Ti})\text{O}_3/\text{Pt}$ thin-film stacks for integrated ferroelectric capacitors. *Journal of Applied Physics*, 78(3):1926.
- [Stadler, 1992] Stadler, H. L. (1992). Ferroelectric polarization reversal in single crystals. *Ferroelectrics*, 137(1):373 – 387.
- [Stadler and Zachmanidis, 1963] Stadler, H. L. and Zachmanidis, P. J. (1963). Nucleation and growth of ferroelectric domains in BaTiO_3 at fields from 2 to 450 kV/cm. *Journal of Applied Physics*, 34(11):3255–3260.
- [Stanishevsky et al., 2002] Stanishevsky, A., Nagaraj, B., Melngailis, J., Ramesh, R., Khriachtchev, L., and McDaniel, E. (2002). Radiation damage and its recovery in focused ion beam fabricated ferroelectric capacitors. *Journal of Applied Physics*, 92(6):3275–3278.

- [Steen, 2007] Steen, J. (2007). *Microfabricated electrically conducting and wear-resistant nanoprobe for scanning probe applications (EPFL Nr 3889)*. PhD thesis, Ecole Polytechnique Fédérale de Lausanne.
- [Steen et al., 2006] Steen, J. A. J., Hayakawa, J., Harada, T., Lee, K., Calame, F., Boero, G., Kulik, A. J., and Brugger, J. (2006). Electrically conducting probes with full tungsten cantilever and tip for scanning probe applications. *Nanotechnology*, 17(5):1464–1469.
- [Stern et al., 1988] Stern, J. E., Terris, B. D., Mamin, H. J., and Rugar, D. (1988). Deposition and imaging of localized charge on insulator surfaces using a force microscope. *Applied Physics Letters*, 53(26):2717–2719.
- [Stolichnov et al., 2002] Stolichnov, I., Colla, E., Tagantsev, A., Bharadwaja, S. S. N., Hong, S., Setter, N., Cross, J. S., and Tsukada, M. (2002). Unusual size effect on the polarization patterns in micron-size $\text{Pb}(\text{Zr,Ti})\text{O}_3$ film capacitors. *Applied Physics Letters*, 80(25):4804–4806.
- [Stolichnov et al., 2005] Stolichnov, I., Malin, L., Colla, E., Tagantsev, A. K., and Setter, N. (2005). Microscopic aspects of the region-by-region polarization reversal kinetics of polycrystalline ferroelectric $\text{Pb}(\text{Zr,Ti})\text{O}_3$ films. *Applied Physics Letters*, 86(1):012902–3.
- [Stolichnov and Tagantsev, 1998] Stolichnov, I. and Tagantsev, A. (1998). Space-charge influenced-injection model for conduction in $\text{pb}(\text{zr}_x\text{ti}_{1-x})\text{o}_3$ thin films. *Journal of Applied Physics*, 84(6):3216–3225.
- [Stolichnov et al., 2003] Stolichnov, I., Tagantsev, A., Setter, N., Cross, J. S., and Tsukada, M. (2003). Crossover between nucleation-controlled kinetics and domain wall motion kinetics of polarization reversal in ferroelectric films. *Applied Physics Letters*, 83(16):3362–3364.
- [Strukov and Levanyuk, 1998] Strukov, B. A. and Levanyuk, A. P. (1998). *Ferroelectric Phenomena in Crystals: Physical Foundations*. Springer-Verlag, Berlin Heidelberg.
- [Sze, 1985] Sze, S. (1985). *Semiconductor devices, physics and technology*. John Wiley & sons, New York.
- [Tagantsev et al., 2002a] Tagantsev, A., Stolichnov, I., Setter, N., Cross, J., and Tsukada, M. (2002a). Non-Kolmogorov-Avrami switching kinetics in ferroelectric thin films. *Physical Review B*, 66(214109):1–6.
- [Tagantsev, 1996] Tagantsev, A. K. (1996). Mechanisms of polarization switching in ferroelectric thin films. *Ferroelectrics*, 184(1-4):79–88.
- [Tagantsev, 1997] Tagantsev, A. K. (1997). Size effects in polarization switching in ferroelectric thin films. *Integrated Ferroelectrics*, 16(1):237–244.
- [Tagantsev et al., 1995] Tagantsev, A. K., Landivar, M., Colla, E., and Setter, N. (1995). Identification of passive layer in ferroelectric thin films from their switching parameters. *Journal of Applied Physics*, 78(4):2623–2630.

- [Tagantsev et al., 2004a] Tagantsev, A. K., Muralt, P., and Fousek, J. (2004a). Shape of piezoelectric hysteresis loop for non-ferroelastic switching. In *Mat. Res. Soc. Symp.*, volume 784, pages C10.6.1–6, Boston. Materials Research Society.
- [Tagantsev et al., 1994] Tagantsev, A. K., Pawlaczyk, C., Brooks, K., and Setter, N. (1994). Built-in electric field assisted nucleation and coercive fields in ferroelectric thin films. *Integrated Ferroelectrics*, 4(1):1–12.
- [Tagantsev et al., 2002b] Tagantsev, A. K., Pertsev, N. A., Muralt, P., and Setter, N. (2002b). Strain-induced diffuse dielectric anomaly and critical point in perovskite ferroelectric thin films. *Physical Review B*, 65(1):012104–4.
- [Tagantsev et al., 2003] Tagantsev, A. K., Sherman, V. O., Astafiev, K. F., Venkatesh, J., and Setter, N. (2003). Ferroelectric materials for microwave tunable applications. *Journal of Electroceramics*, 11(1 - 2):5–66.
- [Tagantsev et al., 2004b] Tagantsev, A. K., Stolichnov, I., Setter, N., and Cross, J. S. (2004b). Nature of nonlinear imprint in ferroelectric films and long-term prediction of polarization loss in ferroelectric memories. *Journal of Applied Physics*, 96(11):6616–6623.
- [Tajitsu, 1995] Tajitsu, Y. (1995). Effects of thickness on ferroelectricity in vinylidene fluoride and trifluoroethylene copolymers. *Japanese Journal of Applied Physics*, 34(9B):5418–5423.
- [Tajitsu et al., 1980] Tajitsu, Y., Chiba, A., Furukawa, T., Date, M., and Fukada, E. (1980). Crystalline phase transition in the copolymer of vinylidene fluoride and trifluoroethylene. *Applied Physics Letters*, 36(4):286–288.
- [Tajitsu et al., 1987] Tajitsu, Y., Ogura, H., Chiba, A., and Furukawa, T. (1987). Investigation of switching characteristics of vinylidene fluoride trifluoroethylene copolymers in relation to their structures. *Japanese Journal of Applied Physics*, 26(4):554–560.
- [Takahashi et al., 2004] Takahashi, Y., Kitahama, A., and Furukawa, T. (2004). Dielectric properties of the surface layer in ultra-thin films of a VDF/TrFE copolymer. *Dielectrics and Electrical Insulation, IEEE Transactions on [see also Electrical Insulation, IEEE Transactions on]*, 11(2):227–231.
- [Tashiro, 1995] Tashiro, K. (1995). Crystal structure and phase transition of PVDF and related copolymers. In Nalwa, H. S., editor, *Ferroelectric Polymers*, pages 63–181. Marcel Dekker Inc., New York.
- [Tashiro et al., 1984] Tashiro, K., Takano, K., Kobayashi, M., Chatani, Y., and Tadokoro, H. (1984). Structure and ferroelectric phase transition of vinylidene fluoride-trifluoroethylene copolymers: 2. VDF 55 % copolymer. *Polymer*, 25(2):195–208.
- [Tashiro and Tanaka, 2006] Tashiro, K. and Tanaka, R. (2006). Structural correlation between crystal lattice and lamellar morphology in the ferroelectric phase transition of vinylidene fluoride-trifluoroethylene copolymers as revealed by the simultaneous measurements of wide-angle and small-angle x-ray scatterings. *Polymer*, 47(15):5433–5444.

- [Taylor et al., 1996] Taylor, D., Brooks, K., Kholkin, A., Damjanovic, D., and Setter, N. (1996). Thickness dependence of electrical and electromechanical properties of sol-gel derived PZT thin films. In Baptista, J., Labrincha, J., and Vilarinho, P., editors, *Electroceramics V, International Conference on Electroceramics and Applications*, volume 1, pages 341–344, Aviero, Portugal.
- [Tiedke et al., 2001] Tiedke, S., Schmitz, T., Prume, K., Roelofs, A., Schneller, T., Kall, U., Waser, R., Ganpule, C. S., Nagarajan, V., Stanishevsky, A., and Ramesh, R. (2001). Direct hysteresis measurements of single nanosized ferroelectric capacitors contacted with an atomic force microscope. *Applied Physics Letters*, 79(22):3678–80.
- [Tieke, 1997] Tieke, B. (1997). *Makromolekulare Chemie: eine Einführung*. VCH, Weinheim.
- [Tikhomirov et al., 2000] Tikhomirov, O., Red'kin, B., Trivelli, A., and Levy, J. (2000). Visualization of 180° domain structures in uniaxial ferroelectrics using confocal scanning optical microscopy. *Journal of Applied Physics*, 87(4):1932–1936.
- [Tomashpolski et al., 1974] Tomashpolski, Y. Y., Sevostianov, M. A., Pentegova, M. V., Sorokina, L. A., and Venevtsev, Y. N. (1974). Ferroelectric vacuum deposits of complex oxide type structure. *Ferroelectrics*, 7(1):257–258.
- [Tybell et al., 2002] Tybell, T., Paruch, P., Giamarchi, T., and Triscone, J.-M. (2002). Domain wall creep in epitaxial ferroelectric $\text{Pb}(\text{Zr}_{0.2}\text{Ti}_{0.8})\text{O}_3$ thin films. *Physical Review Letters*, 89(9):097601–1–097601–4.
- [Unni et al., 2004] Unni, K. N. N., de Bettignies, R., Dabos-Seignon, S., and Nunzi, J.-M. (2004). A nonvolatile memory element based on an organic field-effect transistor. *Applied Physics Letters*, 85(10):1823–1825.
- [Valasek, 1921] Valasek, J. (1921). Piezo-electric and allied phenomena in rochelle salt. *Physical Review*, 17:475–481.
- [von Korff Schmising et al., 2007] von Korff Schmising, C., Bargheer, M., Kiel, M., Zavoronkov, N., Woerner, M., Elsaesser, T., Vrejoiu, I., Hesse, D., and Alexe, M. (2007). Coupled ultrafast lattice and polarization dynamics in ferroelectric nanolayers. *Physical Review Letters*, 98(25):257601–4.
- [Wang et al., 1995] Wang, Y. G., Zhong, W. L., and Zhang, P. L. (1995). Lateral size effects on cells in ferroelectric films. *Physical Review B*, 51(23):17235.
- [Wu et al., 1994] Wu, P. K., Yang, G. R., Ma, X. F., and Lu, T. M. (1994). Interaction of amorphous fluoropolymer with metal. *Applied Physics Letters*, 65(4):508–510.
- [Wu, 1974] Wu, S.-Y. (1974). A new ferroelectric memory device, metal-ferroelectric-semiconductor transistor. *Electron Devices, IEEE Transactions on*, 21(8):499–504.
- [Xia and Zhang, 2003] Xia, F. and Zhang, Q. (2003). Influence of metal electrodes on the ferroelectric responses of poly(vinylidene fluoridetrifluoroethylene) copolymer thin films. In *Materials Research Society Fall Meeting*, volume 734 of *Mat. Res. Soc. Proc.*, page B9.20, Boston. Materials Research Society.

- [Xu et al., 2001] Xu, F., Trolrier-McKinstry, S., Ren, W., Xu, B., Xie, Z.-L., and Hemker, K. J. (2001). Domain wall motion and its contribution to the dielectric and piezoelectric properties of lead zirconate titanate films. *Journal of Applied Physics*, 89(2):1336–1348.
- [Yagi et al., 1980] Yagi, T., Tatemoto, M., and Sako, J.-i. (1980). Transition behavior and dielectric properties in trifluoroethylene and vinylidene fluoride copolymers. *Polymer Journal*, 12(4):209–223.
- [Yamauchi, 1986] Yamauchi, N. (1986). A metal-insulator-semiconductor (MIS) device using a ferroelectric polymer thin film in the gate insulator. *Japanese Journal of Applied Physics*, 25(4):590–594.
- [Yoon and Ishiwara, 2001] Yoon, S.-M. and Ishiwara, H. (2001). Memory operations of 1T2C-type ferroelectric memory cell with excellent data retention characteristics. *Electron Devices, IEEE Transactions on*, 48(9):2002–2008.
- [Zayats and Smolyaninov, 2004] Zayats, A. V. and Smolyaninov, I. I. (2004). Near-field second-harmonic generation. *Philosophical Transactions of the Royal Society A: Mathematical, Physical and Engineering Sciences*, 362(1817):843–860.
- [Zhang et al., 1998] Zhang, Q. M., Bharti, V., and Zhao, X. (1998). Giant electrostriction and relaxor ferroelectric behavior in electron-irradiated poly(vinylidene fluoride-trifluoroethylene) copolymer. *Science*, 280(5372):2101–2104.
- [Zhang et al., 1989] Zhang, Q. M., Jang, S. J., and Cross, L. E. (1989). High-frequency strain response in ferroelectrics and its measurement using a modified Mach-Zehnder interferometer. *Journal of Applied Physics*, 65(7):2807–2813.
- [Zhu and Cao, 1997] Zhu, S. and Cao, W. (1997). Direct observation of ferroelectric domains in LiTaO_3 using environmental scanning electron microscopy. *Physical Review Letters*, 79(13):2558.

Acknowledgements

I am grateful to Prof. Nava Setter who offered me a PhD position in her laboratory and gave me the opportunity to learn a lot about science and research as well as to perform scientific work in a well-equipped and inspiring environment. Her sense for the right directions and her useful questions and suggestions were very helpful.

Most of all, I would like to express my gratitude to Dr. Alexander Tagantsev and Dr. Igor Stolichnov. I appreciated the important input, profound knowledge of the physics of ferroelectricity, and the support and explanations from my thesis co-director Dr. Alexander “Sasha” Tagantsev. Additionally, he was a very efficient, careful and supportive reader of all manuscripts. My supervisor Dr. Igor Stolichnov helped me a lot in experimental questions and scientific writing; his efficiency and his clear thinking were inspiring. Both, Sasha and Igor found a good balance between freedom and guidance for my research activities in the exciting field of ferroelectrics — большое спасибо.

I would like to thank the members of my thesis jury: Prof. Ioannis Botsis, Prof. Adrian M. Ionescu, Dr. Elisabeth Soergel, and Prof. Harry Joseph Trodahl.

I am very grateful to Dr. Tomoaki Yamada, not only for providing me with many (pulsed laser deposited) samples, but mainly for being a personally and scientifically great office partner. His kind, responsible, and dedicated character is exemplary. Furthermore, it was a great pleasure to share the office — and worries — with Naama Klein and Jin Wang. They are great friends and were always ready to give me support in whatever I needed.

I am grateful for the interesting (Swiss German) discussions and the various suggestions from Prof. Paul Muralt. He, as well as Dr. Dragan Damjanovic, were role models of good scientists and impressed me with their ideas and understanding. Additionally, Dragan provided me with instructive demonstrations for my teaching activities and he helped me with higher harmonic dielectric measurements. I would like to thank Prof. Pavel Mokry for helpful discussions on the modelling the polarisation reversal in ferroelectric polymers. It was a pleasure for me to collaborate with Dr. Dong Su. I would like to thank him for the TEM sample preparation and investigations as well as the introduction to Chinese culture and cuisine. I am indebted to Dr. Scott Harada, who corrected the manuscripts and for sharing his thoughts and opinions with me as a good friend.

During the thesis writing, there were many occasions to remember the valuable and competent help by Dr. Hirotake Okino, mainly concerning AFM and dielectric measurements. With his great heart and his enthusiasm for life, he should never have passed away so young in the tragic accident on July 27th 2006.

I would like to thank Dr. Yongli Wang, Dr. Enrico Colla, Dr. Vladimir Sherman, and Dr. Sandrine Traversa Gentil. They were always open for questions and did many services for the lab community. I would also like to thank Janine Conde (at the time of the film depositions: Janine Antifakos) for the PZT film sputtering. I would like to thank: Dr. Cosmin Sandu for many hints on what science should be like and, together with Zlatko

Mickovic, for the X-ray studies in the Physics Department; Giancarlo Corradini and the *Laboratory of Microengineering for Manufacturing 2* for the help with microbonding; the members of the “*atelier des matériaux*”, who were always helpful in finding solutions for technical problems; Dr. Jeroen Steen for the collaboration concerning his AFM tips and the common “suffering” at the AFM.

Je remercie Lino Olivetta, Jacques Castano et Julien Maret pour toutes les “boîtes” et leur assistance technique ainsi que le “*bonjour*” matinal. I would like to thank our office secretaries, Eva Favre and Yuko Kagata Spitteler, who were — despite their work load — always very friendly, competent, and helpful. I would like to thank the *Centre of Microscopy* (CIME) of EPFL and especially Dr. Marco Cantoni, Fabienne Bobard, and Danièle Laub for their prompt help at the microscopes and the introductions to various sample preparation and microscopy techniques. I would like to thank the people at the “centre of micro/nanotechnology” for their flexibility concerning my special needs with small samples and Michaël Pavius for his patience when we prepared samples on the brand new dual beam machine.

I would like to acknowledge Prof. Joe Trodahl, Dr. Samuel Terrettaz and Nadja Franz for the introduction to the Langmuir-Blodgett (LB) deposition technique and instrumentation and Prof. H.A. Klok who allowed us the use of the LB facilities.

Concerning the collaboration for the ferroelectric transistors, I would like to acknowledge the collaboration with the *NANOLAB - Electronics Laboratory 2*, especially Giovanni Salvatore, Didier Bouvet, and Prof. Mihai Adrian Ionescu.

I also gratefully acknowledge funding from the Swiss National Science Foundation.

I would like to thank all present and former LC friends: Dr. Guido Gerra, Andreas Nöth, Sebastian Riester, Li Jin, Evgeny Milyutin, Samuel Rey-Mermet, Alvaro Artieda, Dr. Marko Budimir, Dr. Matthew Davis, Dr. Simon Bühlmann, Dr. Roman Lanz, Dr. Anna Infortuna, Dr. Kyle Brinkman, Dr. Lisa Malin, Dr. Evelyn Hollenstein. They all contributed to fruitful collaborations and to the enjoyable and international atmosphere in the LC.

I also would like to thank the numerous football and floorball players, who made it possible to remain in good physical shape, even during the writing period. I am grateful to all my friends in the Service Civil International (SCI), who enriched my leisure time and unforgettable holidays. Thanks to all my flatmates and my friends, who gave me insight to worlds outside materials science and EPFL.

Vielen Dank, *Katrin*, für deine grosse Unterstützung und die zahlreichen gemeinsamen Erlebnisse, die mir grosse Abwechslung zur alltäglichen Arbeit gaben. Soviel Wissenschaftliches ich mit der Diss gelernt habe, soviel Nicht-Wissenschaftliches habe ich mit dir gelernt.

Un grand merci à ma copine *Caroline* pour son amour, son soutien et sa patience avec moi pendant toute la rédaction de la thèse ainsi que son aide pour la correction et pour le résumé en français.

Und am Schluss möchte ich meiner Familie für die bedingungslose Unterstützung während meiner ganzen Ausbildung danken und dafür, dass “nach Hause fahren” immer eine Quelle neuer Energie (nicht nur in Form von Früchten und Gemüse) für mich darstellt.

List of Publications

1. Gysel, R.; Stolichnov, I.; Tagantsev, A.K.; Mokry, P.; Setter, N., Restricted Domain Growth and Polarization Reversal Kinetics in Ferroelectric Polymer Thin Films. *Journal of Applied Physics* 2008, 103, (8), 084120-10.
2. Wang, J.; Sandu, C.S.; Colla, E.; Wang, Y.; Ma, W.; Gysel, R.; Trodahl, H.J.; Setter, N.; Kuball, M., Ferroelectric domains and piezoelectricity in monocrystalline $\text{Pb}(\text{Zr,Ti})\text{O}_3$ nanowires. *Applied Physics Letters* 2007, 90, (13), 133107-3.
3. Gysel, R.; Tagantsev, A. K.; Stolichnov, I.; Setter, N.; Pavius, M., Ferroelectric film switching via oblique domain growth observed by cross-sectional nanoscale imaging. *Applied Physics Letters* 2006, 89, (8), 082906-3.
4. Gysel, R.; Stolichnov, I.; Tagantsev, A. K.; Setter, N. Cross-Sectional Imaging of Polarization Reversal in Ferroelectric Films, *Proceedings of the 15th IEEE International Symposium on the Applications of Ferroelectrics (ISAF 2006), Sunset Beach, NC, USA* 2006; pp 273-276.
5. Suyal, G.; Colla, E.; Gysel, R.; Cantoni, M.; Setter, N., Piezoelectric Response and Polarization Switching in Small Anisotropic Perovskite Particles. *Nano Letters* 2004, 4, (7), 1339-1342.

Curriculum Vitae

Roman Gysel

Date of birth: 8.8.1978

Nationalities: Swiss and Fürstentum Liechtenstein

Citizen of: Wilchingen (SH) and Schellenberg (FL)

Education

1998–2003 ETH Zürich, Materials Department
Master's degree in materials engineering

2001–2002 Chalmers Institute of Technology, Gothenburg, Sweden
awarded by an Erasmus exchange scholarship

1993–1998 Kantonsschule Schaffhausen, Matura Typus C (science and mathematics)

Academic and Industrial Experience

2003–2008 Ceramics Laboratory, Prof. N. Setter and
Doctoral School of Materials Science, EPF Lausanne
PhD student and assistant

2003 Master thesis
director: Prof. L. Gauckler, Ceramics Laboratory, ETH Zürich,
supervisor: Prof. A.N. Tiwari, Thin-Film Physics Group, ETH Zürich,
Characterisation of inorganic Thin-Film Solar Cells with ZnS Buffer Layers

2002 Twelve week internship at Sulzer Hexis AG, Winterthur
DC Conductivity characterisation of ceramic powders for solid oxide fuel cells

1998 Six week internship at Renggli AG, Schaffhausen
Injection moulding of polymers